Engineering Steels Under Combined Cyclic and Static Stresses[1]

By H. J. GOUGH,[2] LONDON, ENGLAND

The Testing Machine

A BRIEF description of the operating principles will be given.[4] Cyclic loading moments are produced by the centrifugal forces of unbalanced weights attached to revolving disks driven by a synchronous motor. The setting angle, θ, between the vertical planes containing the loading arm and the longitudinal axis of the specimen, determines the ratio of the imposed cyclic bending and torsional moments. A suspensory spring system takes care of the inertia of the remaining vibrating and rotating parts. Initial deflections can be given independently to each pair of springs, which then impose on the specimen the required static bending and, or alternatively, static torsional moment.

The principle of the loading system is illustrated diagrammatically in Fig. 1. The rear ends of each pair (right and left) of springs are held rigidly in a massive steel clamp which can slide, independently, vertically (and horizontally) in a casting attached to the base plate; these clamps can be locked in any desired relative position corresponding to deflections, d_1 and d_2, as shown in Fig. 1. The required values of d_1 and d_2 are preset very precisely, using measuring microscopes and an accurate static calibration.

Next, after setting the specimen to the required θ value, the lengths of the side arms shown in Fig. 1 are adjusted accurately so as to bring the disk axle back to an exactly horizontal position[5] co-axial with fixed headstock centers which provide a fixed datum line for the spring-loading system in relation to the base plate of the machine.

The machine is then ready for use, the static bending and, or alternatively, static torsional stresses applied to the specimen being determined by the spring settings d_1 and d_2, the ratio of f/q by θ, and the actual values of f and q by the weights W and the (constant) speed of the revolving disk. Fig. 2 shows the general arrangement of the machine and Fig. 3 a side view.

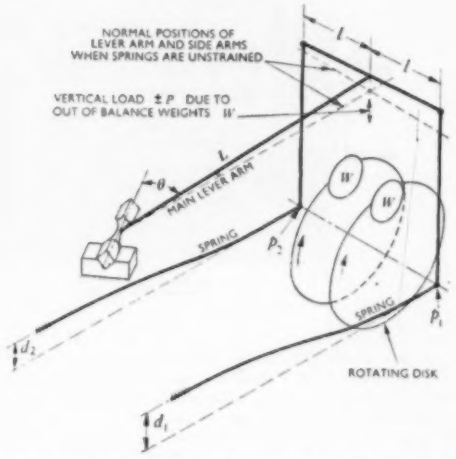

FIG. 1 LOADING SYSTEM OF THE COMBINED STRESS-FATIGUE TESTING MACHINE

Test Material

This was a nickel-chromium-molybdenum-vanadium steel to BS Specification S65A for 65-ton nickel-chromium steel. To provide for future tests on full-sized specimens, a special 32½-ton cast was made of this alloy steel. An interesting metallurgical investigation of one of the forty-seven ingots forming the cast has been published (4). Particulars concerning this material are given in Table 1. The recorded tensile strength of 65 (64.8) tons per sq in. is the normal value for this steel, which possesses excellent ductility (67 per cent reduction of area) and notched-bar Izod value (90 ft-lb). The material exhibits a well-marked drop at the upper yield point of 61.3 tons per sq in.

TABLE 1 PARTICULARS CONCERNING S65A STEEL

Chemical analysis:	
Carbon 0.24 per cent; silicon 0.20 per cent; manganese 0.57 per cent; sulphur 0.004 per cent; phosphorus 0.015 per cent; nickel 3.06 per cent; chromium 1.29 per cent; molybdenum 0.54 per cent; vanadium 0.25 per cent	
Heat-treatment:	
Normalized 900 deg C; oil-hardened from 850 deg C; tempered 640 deg C; air-cooled	
Mechanical properties:	
Tensile limit of proportionality, tons per sq in.	47.0
Upper yield point in tension, tons per sq in.	61.3
Ultimate tensile strength, tons per sq in.	64.8
Elongation at fracture ($l = 4\sqrt{A}$), per cent	23½
Reduction of area at fracture, per cent	67
Young's modulus, E, psi × 10^{-6}	29.1
Brinell hardness number (2-mm ball 120-kg load)	325
Torsional limit of proportionality, tons per sq in.	31.4
Yield point in torsion, tons per sq in.	46.3
Torsional modulus of rupture, tons per sq in.	57.3
Total twist at fracture (L/d = 8½), deg	2085
Modulus of rigidity, G, psi × 10^{-6}	11.5
Izod notched-bar value, ft-lb	90

Final machining operations on all the test specimens were made after the rough-machined blanks had been heat-treated. A

---

[1] A paper on this subject was scheduled for the ASME Annual Meeting in New York, N. Y., November 29, 1949. The paper consists of two parts: Stage 1—combined fatigue stresses; cyclic bending and cyclic torsion. Stage 2—combined stresses; cyclic bending, cyclic torsion, static bending, and static torsion. Since it is not possible to publish the entire paper and since most of the material of Stage 1 has been published previously (1, 2),[3] it has been decided to limit the present account to Stage 2. An account of both stages is to be found in Dr. Gough's Presidential Address which will appear in the Proceedings of The Institution of Mechanical Engineers (1949). A more detailed account will be published later (3).

[2] President of The Institution of Mechanical Engineers, and Engineer-in-Chief, Lever Brothers & Unilever Limited.

[3] Numbers in parentheses refer to the Bibliography at the end of the paper.

[4] A detailed description of the machine and its calibration will be published elsewhere.

[5] The final close adjustment of the axle height is effected by height and slip gages from an accurately machined surface on the upper surface of the base plate.

Discussion of this paper should be addressed to the Secretary, ASME, 29 West 39th Street, New York, N. Y., and will be accepted until July 10, 1950, for publication at a later date. Discussion received after the closing date will be returned.

NOTE: Statements and opinions advanced in papers are to be understood as individual expressions of their authors and not those of the Society.

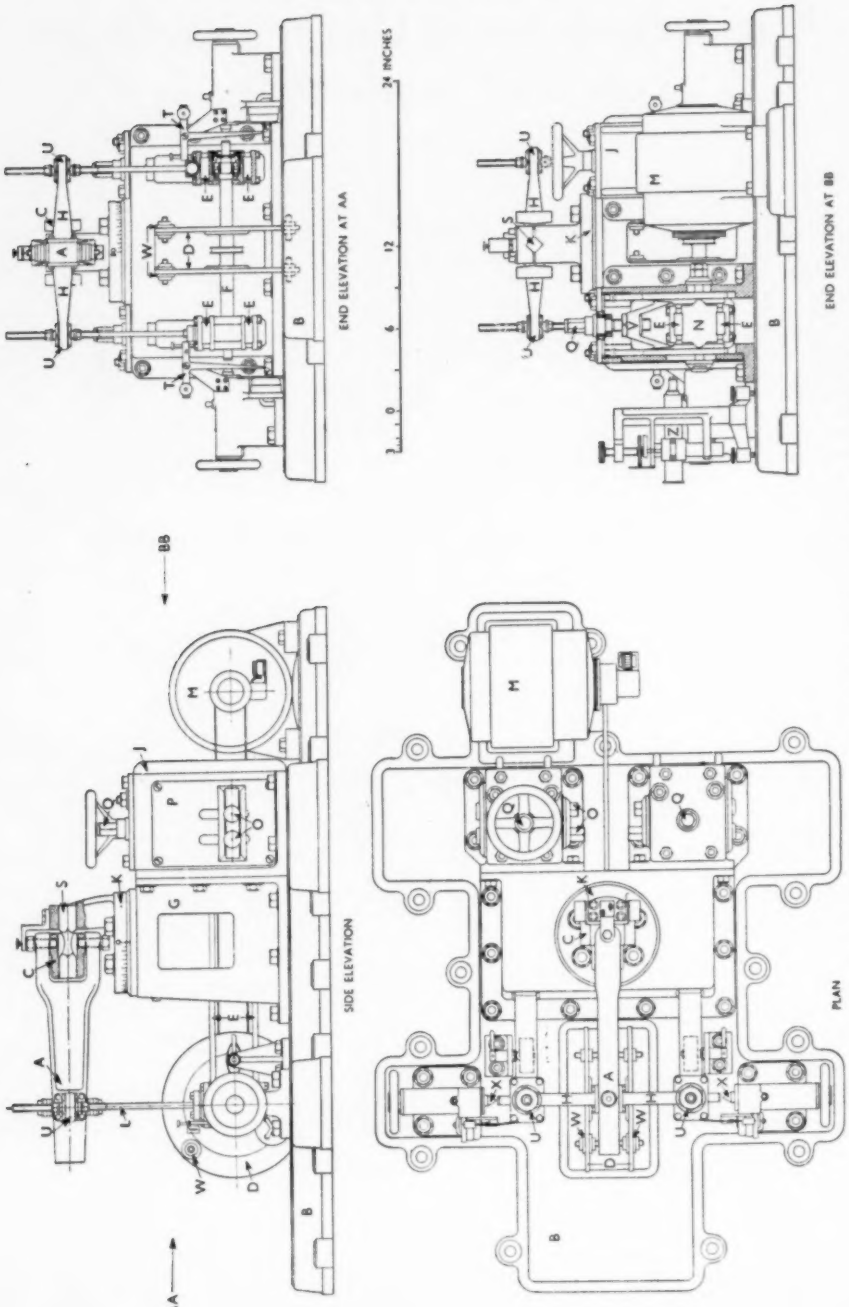

FIG. 2 GENERAL ARRANGEMENT OF THE COMBINED STRESS-FATIGUE TESTING MACHINE

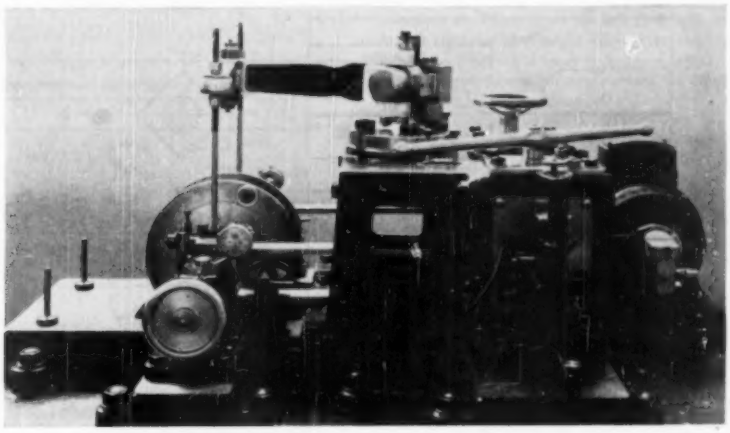

FIG. 3 COMBINED STRESS-FATIGUE TESTING MACHINE

batch method of heat-treatment was unavoidable, but every precaution was taken to preserve constant conditions for each batch; nevertheless, small differences within a batch were sometimes revealed, under the searching conditions of the fatigue tests, by "scatter" on some of the S/N diagrams. The amount of this scatter is not excessive for a heat-treated, high-alloy steel, for, of the seventy-one fatigue determinations, sixty are classed as "D," nine as "LD," and two only as "I."

TEST PROGRAM

The program of combined stress-fatigue tests divides naturally into two parts; that carried out on solid specimens of circular cross section, and that carried out on each of three selected forms of discontinuity of section.

(*a*) *Tests on Solid Specimens.* The form and dimensions of the specimens are shown in Fig. 4(*a*). The fatigue limit of a metal under cyclic reversed stresses is dependent on the superimposed static stress, which can have any value between zero and the ultimate strength of the material.

In the present investigation in which two kinds of superimposed static stress, bending and shear, were to be explored, it was, therefore, necessary to select a series of values of each kind of stress (bending or shear). It was decided to build a program around three values of each kind of superimposed static stress; also, to couple with each combination of these three values not more than five combinations (i.e., five values of θ) of reversed bending and reversed torsional cyclic stresses.

The five values selected were $\theta = 0, 29.7, 53.1, 75.9$, and 90 deg, corresponding to $\pm f/\pm q = \infty$ ($q = 0$), $3^1/_2$, $1^1/_2$, $^1/_2$, and 0($f = 0$). The maximum value of f_s and q_s selected were one half the fatigue limits for repeated cycles of stress (in which the stress varied cyclically between zero and a maximum) under bending and torsion, respectively. These repeated stress limits were determined experimentally in the combined stress machine; their values were

Repeated stress-fatigue limit (bending) = 0–69 tons per sq in., i.e., $34^1/_2 \pm 34^1/_2$.

Repeated stress-fatigue limit (torsion) = 0–$44^1/_2$ tons per sq in., i.e., $22^1/_4 \pm 22^1/_4$.

Based upon these results, the values of superimposed static stress selected for investigation were $f_s = 34^1/_2$, $17^1/_4$, and 0; $q_s = 22^1/_4$, 11, and 0. The program built up round these static stresses is expressed schematically in Table 2. Each of the nine squares, numbered in Roman numerals, covers a series of combined stress-fatigue tests in which the superimposed static stresses, given by the headings of the vertical and horizontal columns in which the particular square is situated, are held constant. In each square, the fatigue limits to be determined are sufficiently specified by a statement of the f/q ratio; each test is numbered for reference purposes.

TABLE 2 SCHEMATIC REPRESENTATION OF THE TEST PROGRAM CARRIED OUT ON SOLID SPECIMENS (S65A)

Superimposed static torsional stress, tons per sq. in.	Superimposed static bending stress, tons per sq. in. $f_s = 0$	$f_s = 17\frac{1}{4}$	$f_s = 34\frac{1}{2}$
$q_s = 0$	(1) $f/q = \infty$ ($q = 0$) (19) $f/q = 3\frac{1}{2}$ (20) $f/q = 1\frac{1}{2}$ (21) $f/q = \frac{1}{2}$ (4) $f/q = 0$ ($f = 0$) **I**	(2) $f/q = \infty$ (28) $f/q = 1\frac{1}{2}$ (13) $f/q = 0$ **II**	(3) $f/q = \infty$ (14) $f/q = 0$ **III**
$q_s = 11$	(7) $f/q = \infty$ (29) $f/q = 1\frac{1}{2}$ (5) $f/q = 0$ **IV**	(9) $f/q = \infty$ (22) $f/q = 3\frac{1}{2}$ (23) $f/q = 1\frac{1}{2}$ (24) $f/q = \frac{1}{2}$ (15) $f/q = 0$ **V**	(11) $f/q = \infty$ (16) $f/q = 0$ **VI**
$q_s = 22\frac{1}{4}$	(8) $f/q = \infty$ (6) $f/q = 0$ **VII**	(10) $f/q = \infty$ (17) $f/q = 0$ **VIII**	(12) $f/q = \infty$ (25) $f/q = 3\frac{1}{2}$ (26) $f/q = 1\frac{1}{2}$ (27) $f/q = \frac{1}{2}$ (18) $f/q = 0$ **IX**

The importance of the stress combinations represented by squares I, V, and IX merited the full series of five values of reversed bending stresses/reversed torsional stresses. In the remaining cases, considerations of economy in the testing time and numbers of specimens led to smaller numbers, three for squares II and IV, two for squares III, VI, VII, and VIII.

Each of the twenty-nine separate fatigue limits involved was determined, on one of the combined-stress-type machines, by the

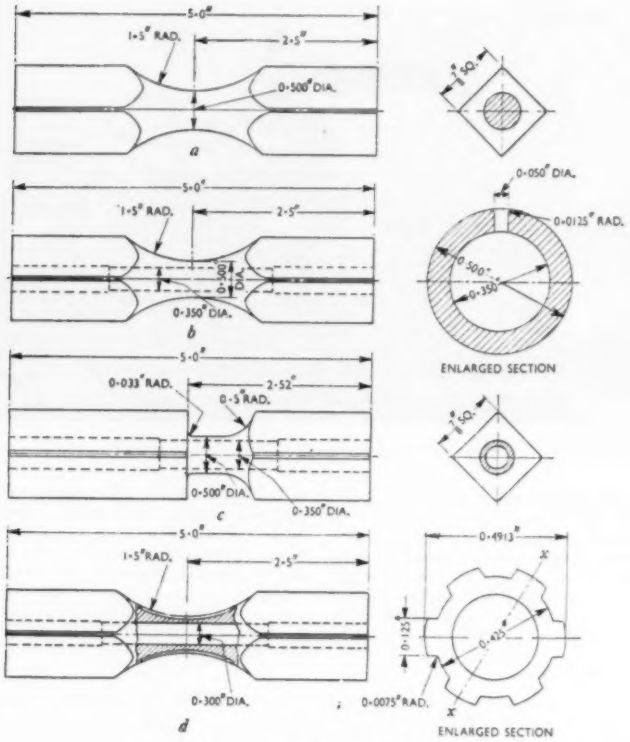

FIG. 4 COMBINED FATIGUE-STRESS SPECIMENS

usual method of endurance testing on a minimum basis of 10^7 cycles. A trip gear stopped the machine when a sensible increase occurred in the cyclic range of strain of the specimen; all tests were thus stopped in the very early stage of fatigue cracking.

(b) Tests on Specimens Containing Discontinuities of Section. The three types[6] of specimen are as follows:

Hollow specimen[7] having a drilled radial oil hole, Fig. 4(*b*).

Hollow specimen having a transition fillet of small radius, Fig. 4(*c*).

Hollow specimen having six deep splines, based upon British Standard Specification, No. 46, Part 2, 1929, Table 14, U.K. Fit, Fig. 4(*d*).

On each type, the test program shown in Table 3 was carried out. After the explanation of the previous table, Table 3 will be self-explanatory. It was considered unnecessary, from practical design considerations, to explore values of f_s and q_s greater than 17¼ and 11 tons per sq in., respectively. In these series of tests, except where otherwise stated, all values of f, q, f_s, and q_s refer to nominal stress values, calculated in the usual way without reference to the stress-concentration effect produced by the discontinuity. The latter will be discussed separately.

RESULTS AND CONCLUSIONS

Solid Specimens. Each individual test is identified by the quoted reference number from Table 2.

Commencing with the influence of superimposed static stress, of a similar and dissimilar type (bending and torsion) singly and in combination, on the fatigue limits under simple reversed bending and torsional stresses, the results merit detailed examination as they determine the two-dimensional framework on which this field of combined stresses will be erected; for this purpose, Fig. 5 has been prepared. Fig. 5(*a*) shows the effect on the fatigue limit under simple reversed bending stresses: Fig. 5(*b*) shows the effect on the fatigue limit under simple reversed torsional stresses.

Consider first the influence of similar types of stress. In Fig. 5(*a*), the reversed bending fatigue limit is ±37.8 tons per sq in. (test 1); superimposing static bending stresses only of 17¼ and 34½ tons per sq in., reduces the fatigue limit to values

[6] A hollow form of specimen was adopted as representing a nearer approach to a practical engine component in which such discontinuities are present. The results may not be strictly comparable with the intrinsic fatigue strength of the material as exhibited by solid specimens, but these hollow specimens are "thick-walled," and the "form" effect is probably small. It is certainly very small in comparison with the reduction in strength due to the presence of the discontinuity.

[7] When under test, all specimens containing the oil hole were mounted in the fatigue testing machine so that the axis of the hole lay exactly in the vertical plane of the applied bending moment. The splined-shaft specimens were all mounted so that this plane passed through the centers of an opposite pair of spline crests, although preliminary fatigue tests had, in fact, shown that the same fatigue limit was obtained with the specimens mounted in the alternative position in which the vertical plane of the applied bending moment passed through the centers of an opposite pair of spline troughs.

TABLE 3 SCHEMATIC REPRESENTATION OF TEST PROGRAM CARRIED OUT ON HOLLOW SPECIMENS CONTAINING ONE OF THREE FORMS OF DISCONTINUITY OF SECTION

Superimposed static torsional stress, tons per sq. in.		Superimposed static bending stress, tons per sq. in. $f_s = 0$	Superimposed static bending stress, tons per sq. in. $f_s = 17\frac{1}{2}$
	$q_s = 0$	(1) $f/q = \infty$ ($q = 0$) (13) $f/q = 3\frac{1}{2}$ (9) $f/q = 1\frac{1}{2}$ (14) $f/q = \frac{1}{2}$ (5) $f/q = 0$ ($f = 0$) I	(2) $f/q = \infty$ (10 $f/q = 1\frac{1}{2}$ II (6) $f/q = 0$
	$q_s = 11$	(3) $f/q = \infty$ (11) $f/q = 1\frac{1}{2}$ (7) $f/q = 0$ III	(4) $f/q = \infty$ (12) $f/q = 1\frac{1}{2}$ IV (8) $f/q = 0$

of ±35.8 (test 2) and ±34.5 tons per sq in. (test 3), a maximum reduction of 8.7 per cent only.

In Fig. 5(*b*) the reversed torsional fatigue limit is ±24.0 tons per sq in. (test 4); superimposing static torsional stresses of 11 and 22¼ tons per sq in. reduces the fatigue limit to ±22.0 (test 5) and ±22.2 tons per sq in. (test 6), a maximum reduction of 8.3 per cent only. Thus the effect of superimposing quite high values of static stresses of the same kind is definite but quite small, and this is an important characteristic from the general design aspect.

It would be idle to attempt to express in terms of stress only the shape of these M/R curves for this material, for it is well established that the M/R relation varies both with the material under test and the type of applied stressing. With increasing values of M, the value of R diminishes, in general, much more rapidly for soft, ductile, nonferrous metals than with steels, and more sharply under direct stresses than with flexural or torsional stresses for most metals and alloys; the shape of the static load-elongation diagram to fracture is also a factor. Nevertheless, as far as engineering steels are concerned, the effect of mean stress is much less than is often assumed.

As an extreme example, a series of tests (5) made on a dead-mild steel under cyclic direct stresses may be recalled; the results are summarized in Fig. 6(*a*). Under the extensive series of stress ranges which yielded the six fatigue limits represented by the points *A*, *B*, *C*, *D*, *E*, and *F*, the elastic limit and yield point of the material were exceeded and the ultimate tensile strength very closely approached; very considerable deformations of the specimens occurred. Yet, until the maximum stress of the cycle was nearly equal to the ultimate tensile strength, the drop in fatigue strength, although quite definite, was surprisingly small. Neither the "Gerber parabola" nor the linear "modified Goodman relation" predicts the fatigue resistance of this material. In fact, one would not expect any such relation to have a general application even to the group of engineering steels. The result of a study (5, 6) of deformation characteristics of metals, using x-ray precision methods, leads to the conclusion that the total damage suffered is probably directly attributable to the combined effects of the applied range of stress and the damage caused to the crystalline structure by the deformation due to the maximum stress of the cycle; the latter factor involves the stress-strain deformation characteristics of the material.

Thus, viewed against this background, it is not surprising to find that the present S65A steel, with its high ratio of yield/ultimate tensile strength[5] and especially when tested under flexure

[5] The values of the upper yield point and tensile strength of this material were, respectively, 61.3 and 64.8 tons per sq in.

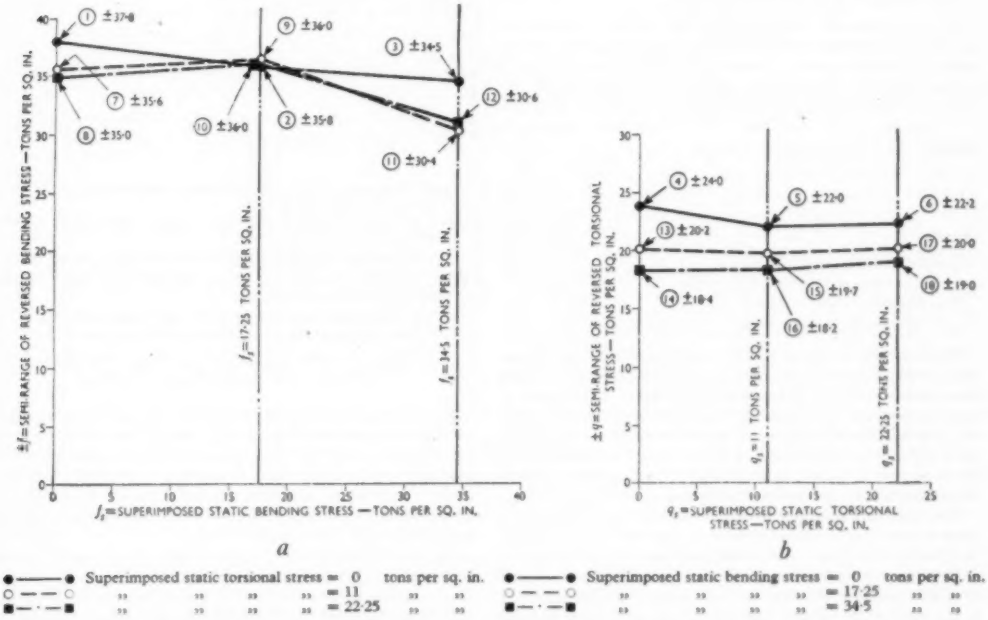
±f = SEMI-RANGE OF REVERSED BENDING STRESS — TONS PER SQ. IN.
f_s = SUPERIMPOSED STATIC BENDING STRESS — TONS PER SQ. IN.
f_s = 17·25 TONS PER SQ. IN.
f_s = 34·5 TONS PER SQ. IN.
① ±37·8
⑨ ±36·0
③ ±34·5
⑫ ±30·6
⑦ ±35·6
⑧ ±35·0
⑩ ±34·0
② ±35·8
⑪ ±30·4
a
±g = SEMI-RANGE OF REVERSED TORSIONAL STRESS — TONS PER SQ. IN.
q_s = SUPERIMPOSED STATIC TORSIONAL STRESS — TONS PER SQ. IN.
q_s = 11 TONS PER SQ. IN.
q_s = 22·25 TONS PER SQ. IN.
④ ±24·0
⑤ ±22·0
⑥ ±22·2
⑬ ±20·2
⑰ ±20·0
⑭ ±18·4
⑮ ±19·7
⑯ ±18·2
⑱ ±19·0
b
Superimposed static torsional stress = 0 tons per sq. in.
= 11
= 22·25
Superimposed static bending stress = 0 tons per sq. in.
= 17·25
= 34·5

FIG. 5 EFFECTS OF SUPERIMPOSED STATIC STRESSES, SINGLY AND IN COMBINATION, ON FATIGUE LIMITS UNDER REVERSED CYCLIC STRESSES; SOLID SPECIMENS, S65A STEEL

(The encircled figures are the test reference numbers as stated in Table 2.)

and torsion, shows relatively small drops in fatigue resistance under even very high values of applied static stresses of similar kinds.

In Fig. 5 the influence of dissimilar types of static stress, also of combinations of similar and dissimilar types, merit detailed scrutiny. Tests 1, 7, and 8 in Fig. 5(*a*) show the effect of imposing static torsional stresses on the reversed bending fatigue limit; adding 11 and $22^1/_4$ tons per sq in. reduces the fatigue limit from ± 37.8 tons per sq in. (test 1) to ± 35.6 (test 7) and ± 35.0 (test 8) tons per sq in., respectively, a maximum reduction of 7.4 per cent only.

From Fig. 5(*b*) the effect of adding $17^1/_4$ and $34^1/_2$ tons per sq in. bending stress reduces the reversed torsional fatigue limit from ± 24 tons per sq in. (test 4) to ± 20.2 (test 13) and ± 18.4 (test 14) tons per sq in., or a maximum reduction of 23.4 per cent, an appreciable amount which is, in fact, the greatest reduction produced by any combination of superimposed static stresses used in the investigation. These two series of tests may be compared with certain criteria which have been suggested.

Davies, Nimhanmimie, and Huitt[9] made some tests on mild steels and alloy steels to study the effect of static torsion superimposed on reversed bending stresses and obtained results which fitted closely to the empirical relation

$$\frac{f^2}{f_r^2} + \frac{q_s}{Q} = 1$$

where

$\pm f$ = safe range of direct stress due to the cyclic bending stresses
q_s = corresponding syperimposed static torsional stress
$\pm f_r$ = fatigue range under reversed bending stresses only
Q = ultimate static torsional strength

Fig. 6(*b*) shows the foregoing expression plotted in relation to the strength properties of the S65A steel, together with the actual results of tests 1, 7, and 8. These results do not conform to the proposed relation. Hohenemser and Prager (7) investigated the effect of static tensile stress superimposed on alternating torsional stresses, using a mild steel. They found their results conformed to the ellipse-quadrant relation

$$\frac{q^2}{q_r^2} + \frac{f_s^2}{F^2} = 1$$

where

$\pm q$ = fatigue limit of cyclic stress
f_s = superimposed static tensile stress
F = ultimate tensile strength
$\pm q_r$ = fatigue range under reversed shear stresses only

The conditions of the present test are not quite comparable, as static bending stresses have been employed in place of the static direct stresses used by Hohenemser and Prager. As a matter of interest, however, an ellipse quadrant has been drawn in Fig. 6(*c*), through the point F, denoting tensile ultimate strength, as the bending ultimate strength of S65A is not determinate. The results of tests 4, 13, and 14 are shown on the diagram but clearly do not conform to the quadrant relation shown.

The remaining test data plotted in Fig. 5 relate to combinations of superimposed static stresses of dissimilar kinds. In Fig. 5(*a*), tests 9 and 10 show that adding torsional stresses of either 11 or $22^1/_4$ tons per sq in. to a previously applied bending stress of $17^1/_4$ tons per sq in. produces no appreciable additional reduction in the value of the fatigue limit under reversed bending stresses.

[9] See discussion of paper by Gough and Follard (1) p. 66.

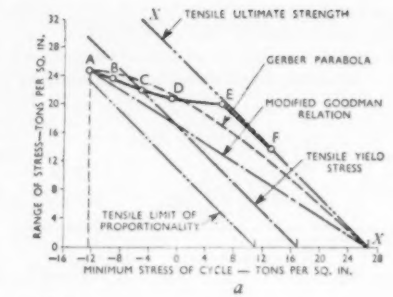

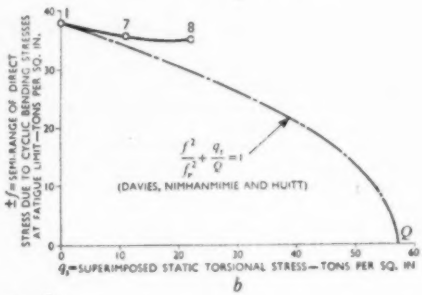
1
7
8
Q
$\frac{f^2}{f_r^2} + \frac{q_s}{Q} = 1$
(DAVIES, NIMHANMIMIE AND HUITT)
±f=SEMI-RANGE OF DIRECT STRESS DUE TO CYCLIC BENDING STRESSES AT FATIGUE LIMIT—TONS PER SQ. IN.
q_s=SUPERIMPOSED STATIC TORSIONAL STRESS—TONS PER SQ. IN
b

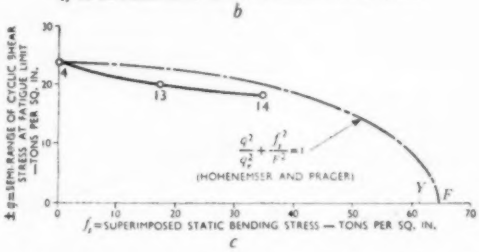

a Fatigue resistance of normalized mild steel under cyclic direct stresses (Gough and Wood).
b Effect of static torsional stress on fatigue limit under reversed bending stresses (S65A steel).
Q = torsional modulus of rupture = 57·3 tons per sq. in.
c Effect of static bending stress on fatigue limit under reversed torsional stresses (S65A steel).
F = ultimate tensile strength = 64·8 tons per sq. in.
Y = yield point in tension = 61·3 tons per sq. in.

FIG. 6 EFFECT OF MEAN STRESS ON MILD STEEL AND S65A STEEL, AND COMPARISON WITH CERTAIN CRITERIA

A greater effect is produced when either of these same torsional stresses is superimposed on a static bending stress of $34^1/_2$ tons per sq in., as shown by tests 11 and 12; the most severe stress conditions of test 12, i.e., $34^1/_2$ tons per sq in. bending, allied with $22^1/_4$ tons per sq in. torsion, reduce the original reversed bending fatigue limit from ± 37.8 (test 1) to ± 30.6 tons per sq in., a total reduction of 19.1 per cent only.

Fig. 5(*b*) shows the same general effect on the reversed torsional fatigue limit, as disclosed by the results of tests 15, 16, 17, and 18. The most severe stress conditions of test 18, i.e., $34^1/_2$ tons per sq in. bending, allied with $22^1/_4$ tons per sq in. torsion, reduce the original reversed torsional fatigue limit from ± 24 (test 4) to ± 19 tons per sq in., a reduction of 20.8 per cent.

Reviewing this complete series of results, one finds the data are satisfactorily regular and consistent and can be used reliably by interpolation, to deduce the safe range of reversed bending or reversed torsional stress under any required combination of superimposed static stresses within the wide limits investigated. Therefore that part of the combined-stress field has been surveyed satisfactorily for design purposes in regard to the S65A steel; the same general trend of results would probably be exhibited by other high-yield-ratio alloy steels of this type.

The effect of the addition of one static stress, or a combination, is quite definite and regular, but the amount of the reduction, caused even by static stresses which are high in relation to the ultimate strengths of the material, is relatively small. The effect of superimposing static bending stresses on cyclic torsional stresses is more damaging than that of static torsional stresses imposed on cyclic bending stresses.

We can now consider the results of those series of tests in which values of the static stresses are held constant and the fatigue strength is determined under various combinations of cyclic bending and torsional stresses.

There are three principal series in each of which the fatigue ranges have been determined for five values of f/q; these are shown in squares I, V, and IX of Table 2, the superimposed static stress system held constant during each series being: $f_s = 0$, $q_s = 0$ (series I); $f_s = 17^1/_4$, $q_s = 11$ (series V); $f_s = 34^1/_2$, $q_s = 22^1/_4$ (series IX). The cyclic-bending and shearing-stress components of these at the fatigue limits are plotted in Fig. 7(*a*).

Using the method of least squares, the best-fitting ellipse quadrant has been drawn for each series of data; the corresponding ellipse arcs are also shown for series I and IX. In series I the data conform closely to the ellipse-quadrant curve; the quadrant and the arc are not widely separated, but the quadrant provides the better fit. The results of this series, in which the mean stress of each kind of stress cycle has zero value, thus provide a further confirmation of the previous general investigation of stage I,[1] i.e., that the f/q relation of ductile steels, when tested in the form of specimens free from discontinuities of section, is represented by an ellipse quadrant. It will be seen from Fig. 7(*a*) that the results of series V, when static stresses ($f_s = 17^1/_4$, $q_s = 11$) are in operation, are also closely represented by the corresponding ellipse quadrant; it is unnecessary to show the corresponding ellipse arc as this obviously cannot provide so good a fit to the test data as the quadrant.

The data of series IX ($f_s = 34^1/_2$, $q_s = 22^1/_4$) are somewhat irregular but, within the accuracy of these data, are satisfactorily represented by the quadrant. In this case the arc and quadrant are not widely divergent and either curve could, without serious error, be said to fit the irregular data; but, in view of the weight of evidence now obtained that solid specimens of the ductile steels conform much more closely to the quadrant relation, it is justifiable to assume that, in this case also, the quadrant relation holds.

Thus a further and most important conclusion emerges from these tests. The effect of superimposing up to very considerable values of static bending and torsional stress merely affects the actual values of the "end points" b and t; the f/q relation remains the ellipse quadrant. When these "end-point" values have been determined experimentally for any required values of f_s and q_s, the fatigue limit for any required ratio f/q is simply calculated, a fact which should be of considerable value for design purposes. In fact, as reliable data regarding the M/R relations of many metals and alloys are already available in the literature, rational design of many engineering components should now be facilitated merely by using published data and the new principles now established.

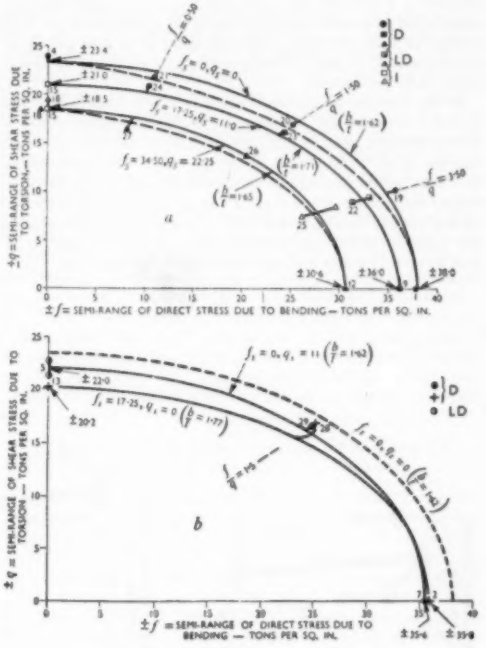

a Test sections I, V, and IX of Table 2
——————— Ellipse quadrants
— — — — Ellipse arcs
b Test sections II and IV of Table 2
——————— Ellipse quadrants
— — — — Curve reproduced from Fig. 7(*a*), for comparison

FIG. 7 EFFECT OF SUPERIMPOSED STATIC STRESS ON THE f/q RELATION; S65A STEEL, SOLID SPECIMENS

The foregoing discussion has included the results of all the tests shown in Table 2 with two exceptions—tests 28 and 29. Clearly, no definite conclusions can be drawn regarding the form of the f/q relations under the static stress conditions of series II and IV as, in each case, only three fatigue ranges have been determined. However, these results are worth a brief examination, and they have been plotted to give Fig. 7(*b*).

An ellipse quadrant has been drawn through each pair of end-point values. In series II ($f_s = 17^1/_4$, $q_s = 0$), test point 28 falls well outside the relevant quadrant, which, therefore, provides a safe design basis, while in series IV ($f_s = 0$, $q_s = 11$) test point 29 is very close to its predicted curve. It can certainly be said that, making allowance for small variations in the physical properties of the steel from batch to batch, there is nothing in these isolated tests to throw serious doubt on the general applicability of the ellipse quadrant to any values of f_s and q_s within the wide limits investigated.

Specimens Containing Discontinuities of Section. Each individual test will be identified by the reference number quoted from Table 3.

(*a*) *Effect of superimposed static stresses, singly and in combination, on the fatigue limits under reversed cyclic stresses:* The data relating to the tests made on specimens containing a radial hole are plotted in Figs. 8(*a*) and (*b*).

In Fig. 8(*a*), the fatigue limit under simple reversed bending stresses is ±16.8 tons per sq in. (test 1); this value is slightly

reduced to ±15.4 tons per sq in. (test 2), i.e., by 8.3 per cent, by superimposing a static bending stress of 17¼ tons per sq in. The further addition of a static torsional stress of 11 tons per sq in. (tests 3 and 4) to each of these conditions, produces no appreciable further reduction.

In Fig. 8(*b*) the fatigue limit under reversed torsional stresses is ±11.7 tons per sq in.; imposing a static torsional stress of 11 tons per sq in. reduces this value, by 3.4 per cent only, to ±11.3 tons per sq in. (test 7). The further addition of 17¼ tons per sq in. static bending stress has no appreciable effect, the recorded fatigue limit being ±11.2 tons per sq in. (test 8). The effect of adding a static bending stress of 17¼ tons per sq in. only reduces the simple reversed torsional limit from ±11.7 tons per sq in. (test 5) to ±11.0 tons per sq in. (test 6), i.e., by 6 per cent.

The data relating to the fillet specimens have been plotted similarly in Figs. 8(*c*) and (*d*). As shown in Fig. 8(*c*), the fatigue limit under simple reversed bending stresses is ±22.5 tons per sq in. (test 1), and superimposing a static bending stress of 17¼ tons per sq in. (test 2) has no effect. The further addition of a static shearing stress of 11 tons per sq in. reduces the fatigue limit to ±20.6 tons per sq in. (test 4), or a total reduction of 8½ per cent. Superimposing a static torsional stress only of 11 tons per sq in. apparently slightly raises the fatigue limit to ±23.4 tons per sq in. (test 3), but this result must be due to slight differences in the material, and it can be assumed that this static stress has, in fact, no effect.

In Fig. 8(*d*) the fatigue limit under simple reversed torsional stresses is ±17.5 tons per sq in. (test 5). Superimposing a static

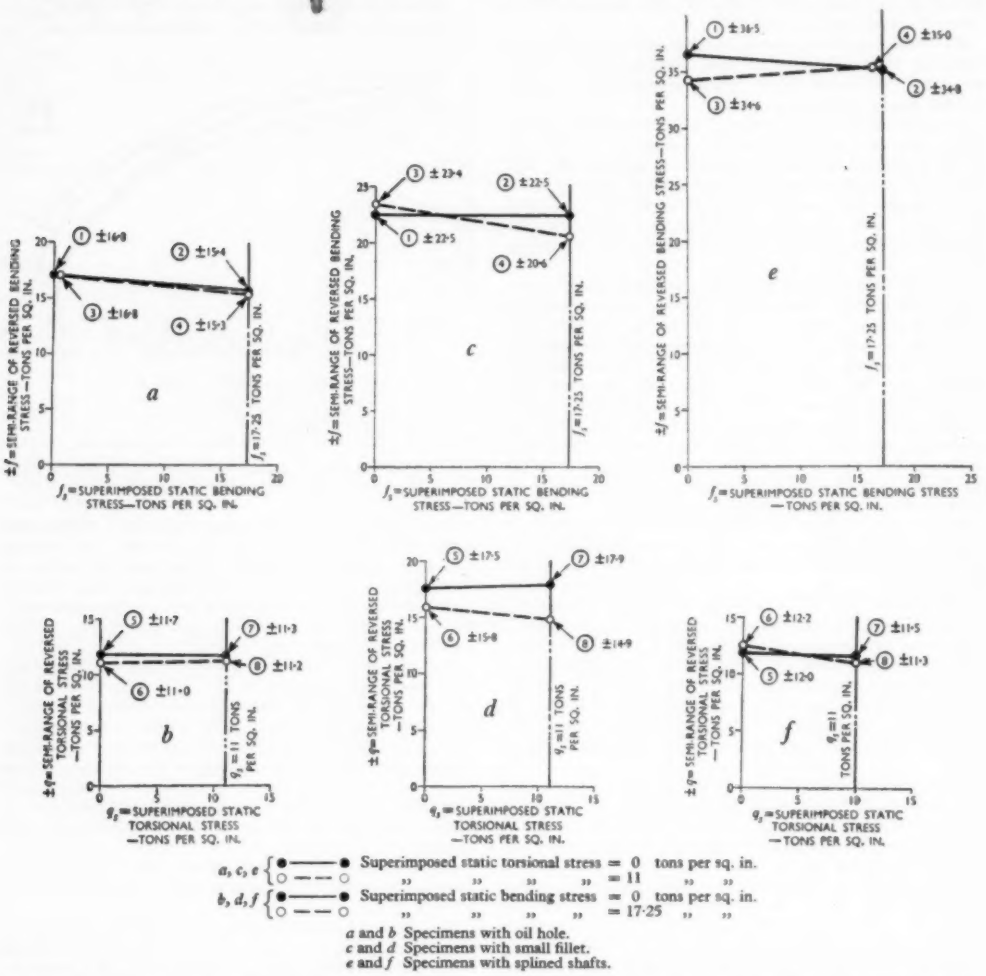

FIG. 8 EFFECTS OF SUPERIMPOSED STATIC STRESSES, SINGLY AND IN COMBINATION, ON FATIGUE LIMITS UNDER REVERSED CYCLIC STRESSES; S65A STEEL

(The encircled figures are the test reference numbers as stated in Table 3.

shear stress of 11 tons per sq in. apparently raises the fatigue limit slightly to ±17.9 tons per sq in. (test 7), which can also be ignored as a real effect. A static bending stress of 17¼ tons per sq in. reduces the fatigue limit to ±15.8 tons per sq in. (test 6), while the combined effect of imposing 17¼ tons per sq in. static bending and 11 tons per sq in. static torsional stress reduces the fatigue limit to ±14.9 tons per sq in. (test 8), or a total reduction of 14.9 per cent.

Lastly, in Figs. 8(*e*) and (*f*) are plotted the data relating to the splined-shaft specimens. The fatigue limit under simple reversed bending stresses, ±36.5 tons per sq in. (test 1) is slightly reduced to ±34.8 tons per sq in. (test 2), i.e., by 4.7 per cent, by superimposing 17¼ tons per sq in. static bending stress. The further addition of 11 tons per sq in. static shear produces no further reduction (test 4). This shear stress acting alone reduces the fatigue limit to ±34.6 tons per sq in. (test 3), a reduction of 5.2 per cent.

In Fig. 8(*f*) the fatigue limit under simple reversed shearing stresses is reduced from ±12.0 tons per sq in. (test 5) to ±11.5 tons per sq in. (test 7), i.e., by 4.2 per cent, by superimposing 11 tons per sq in. static torsional stress; and the further addition of 17¼ tons per sq in. static bending stress produces only a very slight further reduction to ±11.3 tons per sq in. (test 8), or a total reduction of 5.8 per cent. Adding 17¼ tons per sq in. static bending stress alone has no effect on the fatigue limit under simple reversed shearing stresses.

To summarize, these results show that in the presence of a radial hole, the effect on the fatigue limits under reversed bending or torsional stresses of superimposing static stress of either kind singly or both kinds simultaneously is small; the maximum reduction in fatigue strength is 8.3 per cent. When a small transition fillet is present, the effect of the superimposition is more definite, particularly on the reversed torsional fatigue limit, which suffered a maximum reduction of 14.9 per cent. The effect of superimposing the same values of static stresses on the model splined shafts was extremely small, the maximum reduction in fatigue strength being 5.8 per cent. It will be seen, however, that these same forms of discontinuity are very sensitive to cyclic stresses, and this entirely different response to static and cyclic stressing is of the greatest significance to design; the majority of fatigue failures in practice occur at such discontinuities of contour or cross section.

It is convenient first to discuss the stress-concentration effects caused by the three forms of discontinuity before examining the form of f/q relation disclosed by the test data.

(*b*) *Theoretical and actual effects of discontinuities on fatigue strength:*

1 *Radial Oil Hole.* The stress system and theoretical stress-concentration factor produced by the presence of a cylindrical hole have attracted the attention of many investigators using analytical, photoelastic, and strain-measurement methods. Many of the cases investigated relate only to thin plates subjected to simple stressing actions, but a consideration of selected investigations has enabled approximate estimates to be made of values of K_t which probably relate sufficiently closely to the present stress system and form of specimen as to afford a useful comparison of theory and experiment. As shown by Kirsch (8), under uniform tensile stress and at the boundary of the hole, two of the principal stresses vanish, the third principal stress—a circumferential tensile stress—operating on a plane containing a diameter of the oil hole.

Cox (9), in the course of a general investigation into the effect of elliptical holes, has extended this case to that of combined direct stress and shear, and has shown that, when these stresses become reversed cyclic stresses, the analysis reveals that the limiting condition for failure is such that the f/q relation should be an ellipse arc. Further, if fatigue failure occurs on the plane subjected to the greatest range of principal stress, then by the analyses of Kirsch and Cox, the fatigue cracks should be initiated at the boundary of the oil hole on a plane making an angle of $\frac{1}{2}\theta$ with a transverse section of the specimen. In the present tests the inclination of the trace of every fatigue crack at its point of initiation was measured and the agreement with the value of $\frac{1}{2}\theta$ was so close that there is little doubt that the plane of fracture is as indicated by theory.

The work of Kirsch and Cox relates to the assumed conditions of a hole having a diameter infinitesimally small in relation to the specimen size; other investigators have shown that the value of the theoretical stress-concentration factor, K_t, is dependent upon the ratio of the diameter of the hole, d, to that of the specimen, D. The actual values of K_t given by the analyses of Kirsch and Cox are not, therefore, directly applicable, but consideration of the work of Frocht (10, 11), Wahl and Beeuwkes (12), Peterson and Wahl (13), Thum and Kirmser (14), indicates that the following approximate values apply to the present specimen, where $d/D = 1/10$:

K_t (reversed bending stresses) = about 2.5−2.7, say, 2.6
K_t (reversed torsional stresses) = about 2.0

In the present specimens, the intersection of the oil hole with the outside surface of the shaft is rounded off with a small radius, but this radius would not be expected to have any appreciable strengthening effect. Its value in practice is to remove machining burrs, as these would cause a definite reduction in fatigue strength.

For comparison of K_t with the actual reduction in fatigue strength caused by the presence of the oil hole, the experimental values of the "fatigue-strength reduction factor," K_f, are listed in Table 4, where the figures in brackets refer to the test reference numbers of Table 3. As K_f is obtained by dividing two experimentally determined quantities (fatigue strength of solid specimens/fatigue strength of specimens with oil hole) each of which is subject to errors arising from small variations in material, which may be cumulative, large variations in K_f might occur. In spite of this, the values for each value of θ are remarkably constant, leading to two main conclusions as follows:

1 That the average value of K_f for reversed bending stresses is about 2.25 and 1.95 for reversed torsional stresses, with a fairly regular change between the end values. Comparison with the approximate values of K_t (2.6 for bending, 2 for torsion) shows that the presence of the oil hole produces, in this steel, a reduction in fatigue strength such that K_f/K_t = 86½ and 97½ per cent, respectively; the theoretical effect is largely realized.

2 That the value of K_f is determined primarily by the applied

TABLE 4 FATIGUE STRENGTH REDUCTION FACTORS, K_f: SPECIMEN WITH OIL HOLE

Superimposed static stress, tons per sq. in.		Values of K_f (uncorrected)				
Bending, f_s	Torsion, q_s	$\theta = 0$	$\theta = 29{\cdot}7$	$\theta = 53{\cdot}1$	$\theta = 75{\cdot}9$	$\theta = 90$
0	0	2·25 (1)	2·49 (13)	2·23 (9)	1·95 (14)	2·05 (5)
17¼	0	2·32 (2)	—	2·42 (10)	—	1·84 (6)
0	11	2·12 (3)	—	2·30 (11)	—	1·95 (7)
17¼	11	2·35 (4)	—	2·62 (12)	—	1·75 (8)
Average values		2·26	2·49	2·39	1·95	1·91

cyclic stresses and is not affected appreciably by the superimposed static stress; a very important conclusion, even if one to be expected from general knowledge of fatigue characteristics.

2 *Small Transition Fillet.* Nearly all the specimens failed similarly, by a transverse crack situated at the junction of the fillet with the parallel central portion of the test piece or slightly removed from that junction and within the fillet.

By strain-measurements, photoelastic methods, and the use of the electrical analogy, the work of Peterson and Wahl (13), Frocht (10), and Jacobsen (15) indicates the following approximate values of the stress-concentration factor for the form and dimensions of the present fillet specimens:

$$K_t \text{ (reversed bending stresses)} = 2.1$$
$$K_t \text{ (reversed torsional stresses)} = 1.6$$

The experimental values of K_f are listed in Table 5. If the average uncorrected values of K_f for reversed bending and reversed torsional stresses are taken as 1.65 and 1.35, respectively, or $K_f/K_t = 78^1/_2$ and $84^1/_2$ per cent, the agreement with approximate theory is not quite as close as with the oil hole. But, as when the oil hole was present, the previous conclusion again emerges clearly, that the effect of the superimposed static stresses is extremely small, the cyclic stresses being primarily responsible for the reduction in strength.

TABLE 5 FATIGUE STRENGTH REDUCTION FACTORS, K_f: FILLET SPECIMENS

Superimposed static stress, tons per sq. in.		Values of K_f (uncorrected)				
Bending, f_s	Torsion, q_s	$\theta = 0$	$\theta = 29.7$	$\theta = 53.1$	$\theta = 75.9$	$\theta = 90$
0	0	1·68 (1)	1·77 (13)	1·53 (9)	1·37 (14)	1·37 (5)
17½	0	1·59 (2)	—	1·54 (10)	—	1·28 (6)
0	11	1·52 (3)	—	1·65 (11)	—	1·23 (7)
17½	11	1·75 (4)	—	1·73 (12)	—	1·32 (8)
Average values		1·63	1·77	1·61	1·37	1·30

3 *Six Splines.* The case of the splined shaft is of very special interest. When tested under reversed bending stresses, theoretically no stress-concentration effect is present; under reversed torsional stresses, a marked reduction in strength should occur, somewhere between $\theta = 0$ deg and $\theta = 90$ deg. Therefore a marked change, of a discontinuous nature, should occur in the method of failure and the fatigue resistance, not a gradual change as in the case of the oil hole and fillet. Very definite visual evidence of this was afforded by the method of cracking of the specimens. All specimens tested at $\theta = 0$ deg and $\theta = 29.7$ deg, entirely irrespective of the nature and amounts of the superimposed static stresses, failed by transverse fatigue cracks which commenced at the crest of a spline and propagated, with slight deviations, on the same transverse plane. But at $\theta = 53.1$, 75.9, and 90 deg, every fatigue crack started at the inner corner of a spline as a shear failure and followed that longitudinal direction for some distance before deteriorating into a transverse fracture.

Cox (16) has made an analytical study of the torsion of long uniform shafts containing discontinuities, including splines. He found that the stress-concentration factor at the inner corner of a spline, representing as it does a form of half-groove, is given, approximately, by $(1 + {}^1/_2\sqrt{d/r})$, where d is the depth of the spline and r is the average radius of curvature of its root. In the present case, d is 0.03315 in., and r is 0.0075 in., giving $K_t = 2.1$. The analysis relates to a long shaft free from restraint; the end restraint present in the combined stress specimens may tend to reduce the value of K_t.

The uncorrected experimental values of K_f are listed in Table 6.

TABLE 6 FATIGUE STRENGTH REDUCTION FACTORS, K_f: SPLINED SHAFTS

Superimposed static stress, tons per sq. in.		Values of K_f (uncorrected)				
Bending, f_s	Torsion, q_s	$\theta = 0$	$\theta = 29.7$	$\theta = 53.1$	$\theta = 75.9$	$\theta = 90$
0	0	1·04 (1)	1·09 (13)	1·47 (9)	1·76 (14)	2·0 (5)
17½	0	1·03 (2)	—	1·56 (10)	—	1·66 (6)
0	11	1·03 (3)	—	1·51 (11)	—	1·86/1·96 (7)
17½	11	1·03 (4)	—	1·50 (12)	—	1·67/1·83 (8)
Average values		1·03	1·09	1·51	1·76	1·83

Under reversed bending stresses ($\theta = 0$ deg), the experimental values of K_f are very near to unity, while the single result at $\theta = 29.7$ deg also shows almost a complete absence of stress-concentration effect. This is in accordance with the observed nature of the fractures. But an unmistakable reduction in strength occurs at $\theta = 53.1$ deg, and a greater one at $\theta = 75.9$ deg; under reversed torsional stresses ($\theta = 90$ deg), the fatigue resistance of the material is reduced to, approximately, one half its intrinsic strength by the presence of the splines. Comparison with the approximate value of $K_t (< 2.1)$ indicates that the full theoretical effect is approached

As with the oil hole and the fillet, the reduction in fatigue strength, caused by the discontinuity, is primarily due to the applied cyclic stressing; superimposed static stress has little, if any, effect.

The actual and comparative effects on the fatigue strength of the material caused by the three forms of discontinuity investigated—the oil hole, the fillet, and the splines—on this S65A material are shown in Fig. 9 where corrected values of K_f are plotted. The corrections have been made by using values calculated on the assumptions that the f/q relation for solid specimens is the ellipse quadrant, the ellipse are throughout for the oil hole and the fillet specimens, and a combination of the quadrant and arc—which will be referred to later—for the splined shafts. All three curves relate to series I of Table 3 where $f_s = q_s = 0$.

(c) *Form of the f/q relation in presence of a discontinuity:*

1 *Oil Hole.* The results of the five tests of series I (Table 3), in which no static stresses were superimposed, are plotted in Fig. 10. The relevant ellipse quadrant and arc, drawn through the end points, are shown. Tests 13 and 14 seem to be irregular but, if this is ascribed to small variations in the material, the ellipse arc certainly provides the best fit for the series and will be taken to represent the f/q relation.

There remains for examination the results of series II, III, and IV of Table 3, in each of which three fatigue-limit determinations only were made. In each case, the experimental value of the intermediate test point ($\theta = 53.1$ deg) is compared, in Table 7, with the calculated value of the radial ordinate of the quadrant and arc drawn through the experimental end points. Expressing the results in terms of maximum shear stress is a convenient way of making the comparison. The data fit the arc better than the quadrant. In two cases (tests 10 and 11), the deviation from the

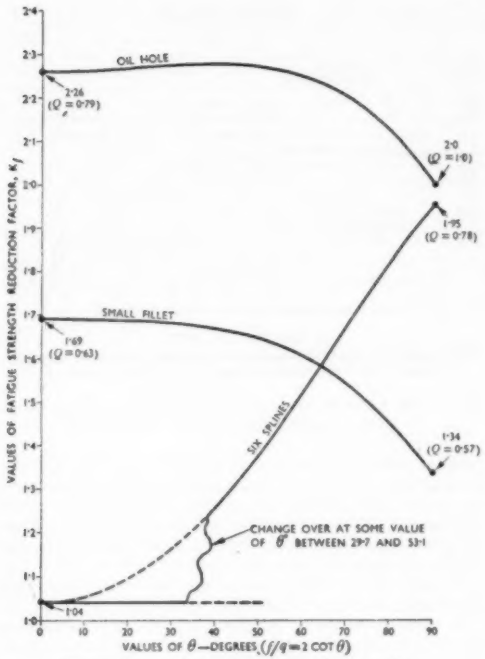

Corrected values for test series where $f_s = q_s = 0$.

Q = fatigue notch-sensitivity index $= \frac{K_f - 1}{K_t - 1}$.

Discontinuity	Approximate values of theoretical stress concentration factor, K_t	
	Reversed bending	Reversed torsion
Oil hole	2·6	2·0
Fillet	2·1	1·6
Splines	1·0	<2·1

FIG. 9 FATIGUE-STRENGTH REDUCTION FACTORS FOR THREE FORMS OF DISCONTINUITY; S65A STEEL

arc value does not exceed the accuracy of the determination; the deviation is more serious, by 14 per cent, in the third. Although more data must be obtained before definite conclusions are drawn, tests 10 and 11 support the view that when static stresses are superimposed, the ellipse arc represents the f/q relation satisfactorily when the discontinuity is present.

2 *Small Fillet.* The five test results of series I (Table 3), in which no static stresses were superimposed, are plotted in Fig. 11. One point (test 13) falls very close to the arc, tests 9 and 14, between the two curves. The ellipse arc provides the better fit and a safer guide to design and may be accepted as a satisfactory relation. The intermediate points of series II, III, and IV, in which static stresses were in operation, are briefly examined, as before, in Table 8. The ellipse arc is definitely the better fit and none of the deviations from the arc values is serious. The ellipse arc thus affords a satisfactory basis for design even when considerable static stresses are imposed.

3 *Splined Shaft.* The five test results of series I (Table 3), in

TABLE 7 INFLUENCE OF STATIC STRESS: OIL-HOLE SPECIMENS

Series	Test No. (see Table 3)	Range of maximum shear stress at fatigue limit					
		Experimental		Ellipse quadrant		Ellipse arc	
		tons per sq. in.	ratio	tons per sq. in.	ratio	tons per sq. in.	ratio
II: $f_s = 17\frac{1}{2}, q_s = 0$	10	±8·6	100	±9·38	109	±8·47	98·5
III: $f_s = 0, \quad q_s = 11$	11	±9·0	100	±9·92	110	±9·35	104
IV: $f_s = 17\frac{1}{2}, q_s = 11$	12	±7·7	100	±9·42	122	±8·76	114

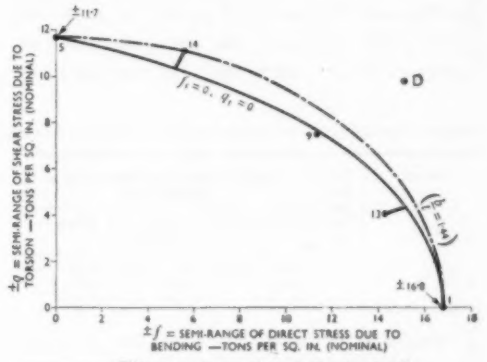
±11·7
14
$f_s = 0, \ q_s = 0$
D
9
13
(Q = 1·44)
±16·0
1
±q = SEMI-RANGE OF SHEAR STRESS DUE TO TORSION —TONS PER SQ. IN. (NOMINAL)
±f = SEMI-RANGE OF DIRECT STRESS DUE TO BENDING —TONS PER SQ. IN. (NOMINAL)

——— Ellipse arc drawn through "end-points".
— · — Ellipse quadrant drawn through "end-points".

FIG. 10 f/q RELATION FOR SPECIMENS WITH OIL HOLE; S65A STEEL

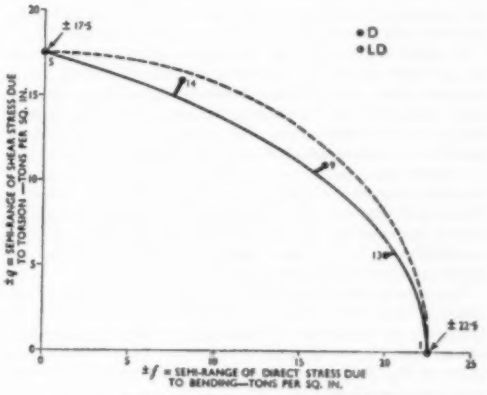

——— Ellipse arc drawn through "end-points".
— — — — Ellipse quadrant drawn through "end-points".

$b/t = 1{\cdot}286$. $\qquad f_s = q_s = 0$.

FIG. 11 f/q RELATION FOR SPECIMENS WITH SMALL FILLET; S65A STEEL

which no static stresses were in operation, are plotted in Fig. 12. As discussed previously, the fractures showed that at values of $\theta = 0$ and 29.7 deg, and also probably up to some higher, and unknown value, failure did not occur due to the stress-concentration effect of the splined contour; hence, from all previous experience of ductile steels tested in the form of solid specimens, tests 1 and 13 should conform to an ellipse quadrant; the same value as

TABLE 8 INFLUENCE OF STATIC STRESS: FILLET SPECIMENS

Series	Test No. (see Table 3)	Range of maximum shear stress at fatigue limit					
		Experimental		Ellipse quadrant		Ellipse arc	
		tons per sq. in.	ratio	tons per sq. in.	ratio	tons per sq. in.	ratio
II: $f_s = 17\frac{1}{2}, q = 0$	10	±13·5	100	±13·6	101	±12·7	94
III: $f_s = 0, \quad q = 11$	11	±12·7	100	±14·7	116	±13·6	107
IV: $f_s = 17\frac{1}{2}, q = 11$	12	±11·7	100	±12·6	108	±11·4	97

TABLE 9 INFLUENCE OF STATIC STRESS: SPLINED SHAFTS

Series	Test No. (see Table 3)	Range of maximum shear stress at fatigue limit					
		Experimental		Ellipse quadrant		Ellipse arc	
		tons per sq. in.	ratio	tons per sq. in.	ratio	tons per sq. in.	ratio
II: $f_s = 17\frac{1}{2}, q = 0$	10	±13·3	100	±13·5	102	±14·9	112
III: $f_s = 0, \quad q_t = 11$	11	±13·7	100	±12·9	94	±14·4	105
IV: $f_s = 17\frac{1}{2}, q_t = 11$	12	±13·5	100	±12·7	94	±14·3	106

found for solid plain specimens, $b/t = 1.62$ (Fig. 7*a*) may reasonably be assumed. A portion of this quadrant is shown on Fig. 12, and test point 13 is seen to fall satisfactorily near the curve.

In regard to the remaining test points 5, 14, and 9, the value of the end point *t* is, of course, given by the value of point 5, but, to compare these data with the corresponding quadrant and arc, some value of *b* must be taken as the second end point through which to draw these curves. But no such second end point is provided by the test data, for, under bending stresses (cyclic and, or alternatively, static), fracture is not influenced by the discontinuities of the section of the splined shaft. In fact, as θ changes from 0 to 90 deg, two quite different kinds of fatigue damage are, in turn, encountered. In this difficulty, the only other end point available—test 1—has been used and a quadrant and an arc drawn in between this and test point 5.

The data of tests 9 and 14 fall between the two curves, with either of which they could be associated with small error. All previous tests on specimens containing a discontinuity have conformed to an f/q relation expressed by an arc, but whether the arc shown in Fig. 12 is the correct one certainly cannot be decided from the present tests.

If, for the time being and without prejudice to future more definite findings, it is accepted that a portion of that arc represents those tests in which failure occurs at the inner corners of the splines, the fatigue behavior of the splined shafts over the whole

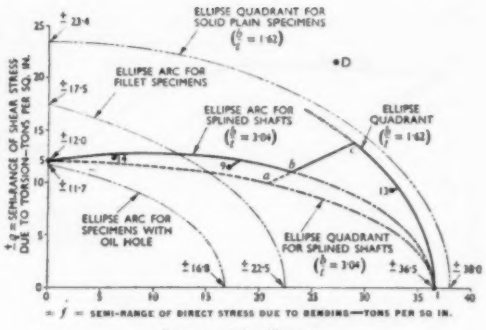

$f_s = q_t = 0$ in all cases.

The position of the radial line *abc* is arbitrarily chosen. It is merely known to lie somewhere between the test points 9 and 13.

FIG. 12 PROBABLE f/q RELATION FOR SPLINED SHAFTS: S65A STEEL (Other curves assembled for general comparison.)

range is probably represented by that portion of the arc[10] extending from test point 5 to *b*, followed by an abrupt change to the portion of the "solid" ellipse quadrant extending from *c* to the test point 1. The position of the radial line *abc* in Fig. 12 has been chosen quite arbitrarily. All that is established is that it is situated somewhere between tests 9 and 13.

A much closer experimental and analytical study of this interesting practical case would be well worth while.

In these circumstances, an examination of the three isolated results in which static mean stresses are in operation can have little real value but, to afford a comparison similar to that already given for the oil hole and fillet, the calculated data of Table 9 are recorded.

Test 10 practically falls on the quadrant, tests 11 and 12 fall intermediate between the quadrant and arc and are about 5 per cent only from either curve. It might, perhaps, be considered surprising if this particular form of discontinuity did not fall into line with the groove, oil hole, and fillet in the respect that the ellipse arc affords a satisfactory design basis, but it will be apparent that the splined shaft is a very special case and, moreover, it is not clear which ellipse arc it is justifiable to adopt.

CONCLUSION

In closing, it may be mentioned that the fatigue strength of an assembly of a splined shaft with its mating member, in which the drive is transmitted from one component to the other, may be less than that of the splined shaft alone; the stress distribution in the two cases is quite different. A few experiments of this type have been made (17) and give an indication of the different behaviors that may occur; more work in this field is required.

The f/q curves, relating to the solid plain, the fillet, and the oil-hole specimens are also indicated in Fig. 12; the assembly shows at a glance the relative reduction in fatigue strength caused by the three forms of discontinuity.

BIBLIOGRAPHY

1 "The Strength of Metals Under Combined Alternating Stresses," by H. J. Gough and H. V. Pollard, Proceedings of The Institution of Mechanical Engineers, London, England, vol. 131, 1935, p. 3.

2 "The Effect of Specimen Form on the Resistance of Metals to

[10] Or by the portion of the quadrant extending from test point 5 to *a*, or by some curve intermediate between the quadrant and arc.

Combined Alternating Stresses," by H. J. Gough and H. V. Pollard, Proceedings of The Institution of Mechanical Engineers, London, England, vol. 132, 1936, p. 549.

3 "Some Experiments on the Resistance of Metals to Fatigue Under Combined Stresses," by H. J. Gough (a monograph in course of publication by His Majesty's Stationery Office).

4 "Study of a Ni-Cr-Mo-Va Steel Ingot," by W. S. Hatfield, *Journal of the Iron and Steel Institute*, Special Report No. 25, Section 5, Eighth Report on the Heterogeneity of Steel Ingots, 1939.

5 "Deformation and Fracture of Mild Steel Under Cyclic Stresses in Relation to Crystalline Structure," by H. J. Gough and W. A. Wood, Proceedings of The Institution of Mechanical Engineers, London, England, vol. 141, 1939, p. 175, and vol. 142, p. 175.

6 "The Deformation and Fracture of Metals," by H. J. Gough and W. A. Wood, *Journal of the Institution of Civil Engineers*, vol. 8, 1938, p. 249.

7 "The Problem of Fatigue Strength Under Complex Stresses," by K. Hohenemser and W. Prager, Metallwirtschaft, vol. 12, 1933, p. 342.

8 G. Kirsch, *Zeitschrift Verein deutscher Ingenieure*, vol. 42, 1898, p. 797.

9 "The Effect of Holes on the Strength of Materials Under Complex Stress Systems," by H. L. Cox (in course of publication).

10 "Factors of Stress Concentration Photoelastically Determined," by M. M. Frocht, JOURNAL OF APPLIED MECHANICS, Trans. ASME, vol. 57, 1935, p. A-67.

11 "Photoelasticity," by M. M. Frocht, Chapman and Hall, London, England, 1948.

12 "Stress Concentrations Produced by Holes and Notches," by A. M. Wahl and R. Beeuwkes, Trans. ASME, vol. 56, 1934, p. 617.

13 "Two- and Three-Dimensional Cases of Stress Concentration and Comparison With Fatigue Tests," by R. E. Peterson and A. M. Wahl, JOURNAL OF APPLIED MECHANICS, Trans. ASME, vol. 58, 1936, p. A-15.

14 "Superimposed Alternating Stresses," by A. Thum and W. Kirmser, *VDI Forschungsheft*, vol. 419, 1943.

15 "Torsional Stresses in Shafts Having Grooves or Fillets," by L. S. Jacobsen, JOURNAL OF APPLIED MECHANICS, Trans. ASME, vol. 57, 1935, p. A-154.

16 "Stress Concentration in Twisted Shafts," by H. L. Cox (in course of publication).

17 "The Effect of Keyways Upon the Strength and Stiffness of Shafts Subjected to Torsional Stresses," by H. J. Gough, Aeronautical Research Committee, Reports and Memoranda No. 864, 1925. (His Majesty's Stationery Office.)

Some Experiments on the Interaction of Shock Waves With Boundary Layers on a Flat Plate[1]

By F. W. BARRY,[2] A. H. SHAPIRO,[3] AND E. P. NEUMANN,[4] CAMBRIDGE, MASS.

Experimental results are presented in the form of schlieren and interferometer photographs showing the interaction of oblique shocks with laminar and turbulent boundary layers on a flat plate in a supersonic stream. The effects of variations in shock intensity and boundary-layer thickness were studied through a Mach number range of 2.0 to 2.5. A greater variety of shock boundary-layer interactions was discovered than had hitherto been suspected. The nature of the interaction was found not to be solely dependent upon whether the boundary layer is laminar or turbulent. A laminar layer proved to be more greatly affected by an incident oblique shock than a turbulent layer. With relatively intense shocks the boundary layer was influenced far upstream of the point of incidence. Injection of a high-speed air stream into a turbulent boundary layer altered significantly the manner of reflection of an incident shock.

Introduction

RECENT developments in aerodynamics, high-speed flight and propulsion, and fluid-flow machinery have emphasized the need for an improved understanding of flow with supersonic velocities. Almost without exception supersonic-flow patterns include shock waves, and of course boundary layers near solid bodies.

Prandtl's original concept of the boundary layer, a concept which has been amply verified for subsonic flow, postulated that the potential part of the flow pattern is substantially independent of the flow in the boundary layer, so that the potential pattern and the boundary layer may be analyzed independently. Thus unless separation of the boundary layer occurs, friction has only a secondary influence on the flow pattern outside the boundary layer.

When shock waves exist, it appears that viscosity may be of primary significance in the determination of the flow pattern. Both shock waves and boundary layers may be thought of as semidiscontinuities in which viscosity and heat conduction play a major role. It is the interaction between these semidiscontinuities which, experiment has shown (2, 3), makes the boundary layer so important to the flow pattern as a whole. The large pressure gradients in the neighborhood of shock waves distort the boundary-layer flow. These distortions, which are propagated both upstream and downstream, in turn influence the conditions outside the boundary layer by means of expansion and compression waves generated by the disturbed boundary layer.

Object

The general object of this investigation was to provide data on the reflection of an oblique shock from a boundary layer on a flat plate in a uniform, parallel, supersonic stream and, further, to determine the influence of shock strength and Reynolds number on the nature of the interaction.

Previous Work

Liepmann (2) and Ackeret, Feldmann, and Rott (3, 4) studied the shock boundary-layer interaction for transonic flow over a curved surface and reached similar conclusions indicating that the boundary-layer regime is a critical factor. With a laminar boundary layer, lambda shocks, comprising a normal shock preceded by an oblique shock, were observed. With a turbulent boundary layer, approximately normal shocks, rather than lambda shocks, were observed.

These investigations failed to make clear how the shock waves originated. Perhaps the shock configurations of Liepmann and of Ackeret, Feldmann, and Rott are characteristic of frictionless transonic flow past curved surfaces, which suggests the possibility of the shocks arising from limit-line effects. Or perhaps the presence of the viscous boundary layer is responsible for the shocks, so that without viscosity the flow pattern would be shock-free. Because no independent control of shock strength and of Mach number prior to the shock was possible, the interpretation of the results was made correspondingly more difficult.

Apparatus

In the studies reported here, an attempt was made to avoid the difficulties of previous experimenters by designing the apparatus so that the location of the shock, the shock strength, and the Mach number before the shock were all under control and could be varied independently. The general arrangement of the apparatus is shown in Fig. 1. Flow conditions in the test section were steady, first, because of the atmospheric inlet, and second, because fluctuations in ejector performance were not transmitted upstream to the test section. An oblique shock was generated by a wedge, the location and turning angle of which could be varied. For the study of thick turbulent boundary layers, the shock was made to impinge on one of the walls of the test section. For the study of thin, laminar layers, a flat plate was supported in the test section, and the shock was made to impinge upon the boundary layer at various distances from the leading edge of the plate.

The results are presented in the form of schlieren[5] and inter-

[1] This paper is based upon reference (1). Numbers in parentheses refer to the Bibliography at the end of the paper.

[2] Research Assistant in Mechanical Engineering, Gas Turbine Laboratory, Massachusetts Institute of Technology. Jun. ASME.

[3] Associate Professor of Mechanical Engineering, Massachusetts Institute of Technology. Mem. ASME.

[4] Assistant Professor of Mechanical Engineering, Massachusetts Institute of Technology. Jun. ASME.

Contributed by the Applied Mechanics Division and presented at the Annual Meeting, New York, N. Y., November 27–December 2, 1949, of THE AMERICAN SOCIETY OF MECHANICAL ENGINEERS.

Discussion of this paper should be addressed to the Secretary, ASME, 29 West 39th Street, New York, N. Y., and will be accepted until July 10, 1950, for publication at a later date. Discussion received after the closing date will be returned.

NOTE: Statements and opinions advanced in papers are to be understood as individual expressions of their authors and not those of the Society. Paper No. 49—A-3.

[5] Taken with the apparatus described in (5).

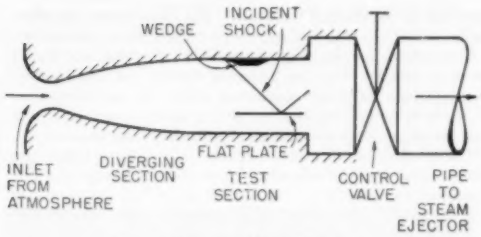

FIG. 1 SCHEMATIC FLOW DIAGRAM
(The nozzle produced a reasonably uniform parallel stream in a square test section measuring 1.292 in. on each side.)

ferometer photographs together with a sketch showing the authors' interpretation of each flow pattern.

Compression waves are indicated in the sketches by solid lines, expansion waves by dashed lines, and the edge of the boundary layer by a dotted line.

The following data are given with each figure:

(*a*) Reynolds number **R** at the point of incidence of the shock, based upon the free-stream velocity, density, and viscosity, and on the distance from the leading edge of the plate.

(*b*) Boundary-layer regime at the point of incidence of the shock.

(*c*) Wedge angle θ.

(*d*) Orientation of the schlieren knife-edge.

(*e*) Time of exposure.

(*f*) Free-stream Mach number **M**.

ANALYTICAL CONSIDERATIONS OF REFLECTION OF A SHOCK FROM A BOUNDARY LAYER

Mathematical techniques for analyzing and predicting the complex flow patterns of the shock boundary-layer interaction have not yet been developed. Therefore some of the elements entering into the observed flow patterns will be discussed in a qualitative way.

Two simple theoretical solutions exist for the reflection of an oblique shock in a parallel, uniform, supersonic flow. When the shock is incident on a solid plane wall, a possible solution is the reflection of the shock as another shock, preserving the stream direction at the wall, as in Fig. 2(*a*). This configuration, which is called "regular reflection," is impossible if the initial Mach number is too small or if the incident shock is too strong, because the maximum turning angle of a second shock is not sufficient to turn the flow direction back to that of the wall. It appears from various experimental data that the configuration then often takes the form of Fig. 2(*b*) in which the shocks are curved near the point of mutual intersection.

When the shock is incident on an interface or boundary at constant pressure, a possible solution is the reflection of the shock as an expansion wave, preserving uniform pressure at the boundary, as in Fig. 2(*c*). This pattern has often been observed at the edge of a free jet.

If an oblique shock is incident on a boundary layer or, more simply, on a region of parallel but varying velocity, the shock

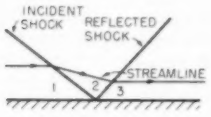

FIG. 2(*a*) REFLECTION FROM PLANE WALL

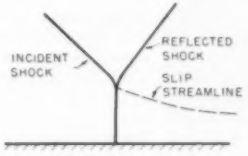

FIG. 2(*b*) REFLECTION FROM PLANE WALL

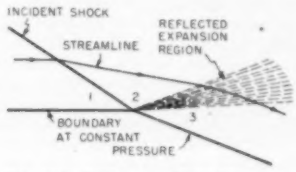

FIG. 2(*c*) REFLECTION FROM CONSTANT-PRESSURE SURFACE

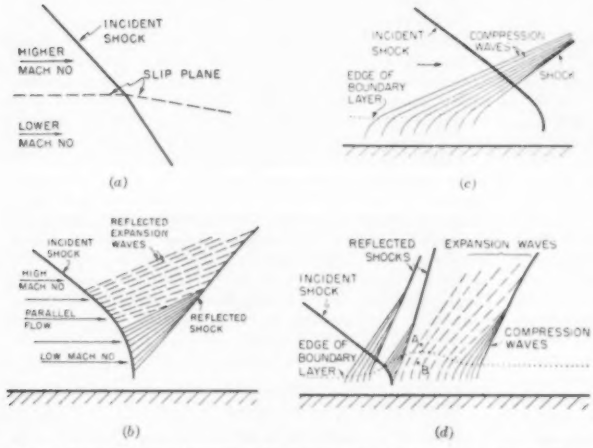

FIG. 3 SOME POSSIBLE ASPECTS OF REFLECTION OF A SHOCK FROM A PLANE WALL WITH BOUNDARY LAYER

is refracted as it passes through the region of varying velocity. As a consequence, wavelets must be generated in a continuous way along the curved part of the shock and may be thought of as part of the reflected shock system. A rigorous analysis of this process is extremely difficult, but a crude analysis (6) indicates that the reflected wavelets may in some circumstances be compressions and in others expansions, as illustrated in Fig. 3(*b*), for example.

At least part of the pressure rise occurring across the shock system will be present in the subsonic portion of the boundary layer. Therefore, unless separation occurs, the subsonic sublayer will thicken in traversing the adverse longitudinal pressure gradient. Part of the resulting streamline curvature away from the wall might occur upstream of the incident shock and generate compression waves in the supersonic stream. The compression wavelets, in turn, might coalesce into a shock originating upstream of the point of incidence of the original shock, as shown in Fig. 3(*c*).

The subsonic portion of the boundary layer

cannot sustain large longitudinal pressure gradients such as occur in the shock system. Near the wall, the longitudinal pressure gradient must be smaller than in the free stream, and hence lateral pressure gradients are likely to exist. The lateral pressure gradient is in turn associated with the streamline curvature arising from the general thickening of the boundary layer as it traverses the region of steep longitudinal pressure gradients.

It seems most probable that the pressure at A would exceed that at B (Fig. 3d) because the stream at A would have passed through a shock of greater strength. Such a pressure gradient will cause the streamlines to turn back toward the wall. This streamline curvature will in turn produce expansion waves in the supersonic flow. The flow direction where the pressure requirements for parallel flow are satisfied is not necessarily that of the wall, so that a shock shown downstream of the expansion region may in some cases be necessary in order to have the downstream flow parallel to the wall.

The wave patterns observed in the photographs, and discussed later, contain in various combinations the elementary configurations previously discussed. It will be seen that the interactions are usually very complex and that many different patterns are possible.

Reflection of Oblique Shock From a Laminar Boundary Layer

Figs. 4, 5, and 6 show representative results for an oblique shock incident upon a laminar boundary layer.

Inspection of the illustrations reveals certain general features of the shock boundary-layer interactions. The boundary layer is thickened upstream of the point of incidence of the shock. When the shock is strong, the thickening may generate oblique shocks upstream of the point of incidence, as shown in Figs. 4 and 5. Also, for strong shocks the boundary layer may separate from the wall upstream of the point of incidence, as Figs. 5 and 6 might indicate. The reflection of the shock may take several forms. In Fig. 4 the reflection comprises an expansion region followed by a shock; whereas in Figs. 5 and 6 the reflection comprises a shock followed by a wedge-shaped expansion zone and ending finally with a second shock. The boundary-layer thickness in most cases decreases for a short distance downstream of the interaction zone, probably because of the expansion region previously mentioned, and gives the appearance of a bump in the boundary layer near the point of incidence.

The effects just summarized are at least qualitatively in accord with the concepts illustrated in Fig. 3.

As regards the effect of shock strength, it was found, as might be expected, that the magnitude of the interaction is in proportion to the shock strength. With small deflection angles, Fig. 4, the boundary layer is thickened only slightly, and the reflection is in the form of a weak expansion followed by a weak shock. From the appearance of the edge of the boundary layer, it seems that even with weak shocks the boundary layer becomes turbulent almost immediately following the interaction.

With large deflection angles, Figs. 5 and 6, the boundary layer undergoes a very considerable thickening, both upstream of the point of incidence and near the point of incidence itself. In a few extreme cases, e.g., Fig. 6, the boundary layer seems to lift from the wall rather abruptly at some distance upstream of the point of incidence; at the point of abrupt thickening, the turning of the stream generates a shock which crosses the incident shock. The reflection of a strong shock takes the form of a weak compression wave followed by an expansion region and ending in an oblique shock. It seems clear from Figs. 5 and 6 that not only does the shock make the boundary layer change from laminar to turbulent (as judged by the apparent sharpness of the edge of the boundary layer), but that in some cases the transition occurs upstream of the point of incidence. The illustrations also show the formation of a new laminar sublayer following the interaction.

Comparison between Figs. 4 and 5, as a group, and Fig. 6 seems to indicate that the Reynolds number did not, in these tests at least, have any significant effect on the interaction. It might be noted here that for Fig. 6 the boundary layer was near transition, at least as judged by the Reynolds number.

The flow patterns and wave patterns of Figs. 5 and 6 illustrate how complex the shock boundary-layer interaction may be. The conditions represented by Fig. 5 were selected as an interesting flow pattern for which some additional results might be presented.

Fig. 5(b) was taken simultaneously with Fig. 5(a), using the light-splitting arrangement described in reference (5). Since the schlieren knife-edge was horizontal for Fig. 5(a), this view shows lateral density gradients, and thus the boundary layer is clearly evident. Fig. 5(b), on the other hand, shows longitudinal density gradients, corresponding to a vertical knife-edge. A comparison of the two illustrations shows that both are in agreement as to details of the flow pattern. Of course the one with the horizontal knife-edge shows the boundary-layer phenomena much more clearly and therefore is preferable for this kind of study.

To illustrate a typical difference between a flash photograph (5×10^{-6} sec) and a time exposure ($^1/_{75}$ sec), Figs. 5(a) and 5(c) which are otherwise alike, may be compared. The general features of these two photographs are the same, but much of the detail of the interaction is lost in the time exposure because the camera records only the average of highly fluctuating conditions. It might be queried whether a number of flash exposures at different times show the detailed pattern to change significantly with time. Several comparisons of spark photographs taken at different times with the same over-all flow conditions seem to show that while the flow is somewhat unsteady near the interaction, the details of the interaction are qualitatively constant.

Fig. 5(d) is an interferogram photograph corresponding to the schlieren photographs of Figs. 5(a), 5(b), and 5(c). An interferogram permits quantitative interpretation by counting the fringe shifts from the condition of no flow or by superposing negatives taken first with flow and then without flow. Fig. 5(e) shows lines of constant density ratio found from the interferogram of Fig. 5(d), the air density in the free stream approaching the wedge being used as a reference.

The theoretical solution for an oblique two-dimensional shock in a frictionless flow with an approach Mach number of 2.55 and a wedge angle of 15 deg yields a density ratio across the shock of 1.88, and a shock-wave angle of 36.4 deg. The shock-wave angle measured from Figs. 5(a), 5(b), and 5(d) agrees with the latter value within the accuracy to which the angle can be measured in the photographs. The agreement as to density ratio, e.g., 1.7 against 1.88, is only fair, according to Fig. 5(e).

The quantitative information supplied by the interferogram substantiates and amplifies the qualitative information supplied by the schlieren photographs. Fig. 5(e) shows clearly the density rise (and, presumably, the pressure rise) in the boundary layer upstream of the point of incidence of the oblique shock. The density downstream of the oblique shock seems to reach appreciably higher values in the neighborhood of the point of incidence than outside the boundary layer. Immediately downstream of the zone of interaction there is a strong expansion region, as shown by the rapid decrease in density.

Reflection of Oblique Shock From a Turbulent Boundary Layer

Typical flow patterns for a turbulent boundary layer of considerable thickness are shown in Figs. 7 and 8. With a very weak shock, Fig. 7 shows that the boundary layer is affected only

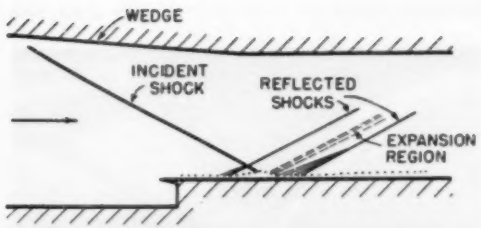

FIG. 4 $R = 1.9 \times 10^5$; LAMINAR; $\theta = 5$ DEG; KNIFE-EDGE HORIZONTAL; 5×10^{-6} SEC; $M = 2.55$

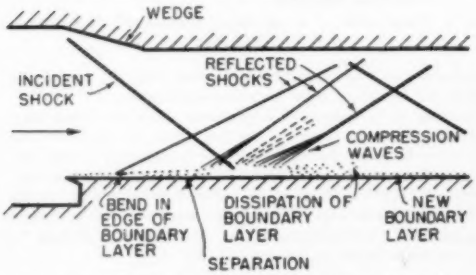

FIG. 5 $R = 3.3 \times 10^5$; LAMINAR; $\theta = 15$ DEG; $M = 2.55$

FIG. 5(a) KNIFE-EDGE HORIZONTAL; 5×10^{-6} SEC

FIG. 5(b) KNIFE-EDGE VERTICAL; 5×10^{-6} SEC

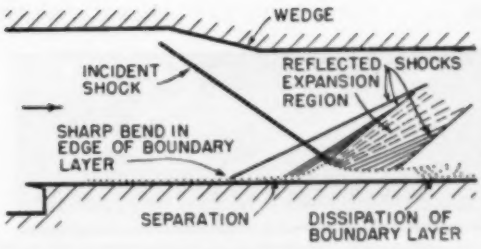

FIG. 6 $R = 5.6 \times 10^5$; $\theta = 15$ DEG; KNIFE-EDGE HORIZONTAL; 5×10^{-6} SEC; $M = 2.55$

FIG. 5(c) KNIFE-EDGE HORIZONTAL; $1/_{10}$ SEC

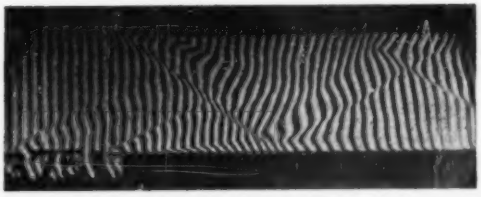

FIG. 5(d) INTERFEROGRAM; $1/_{10}$ SEC

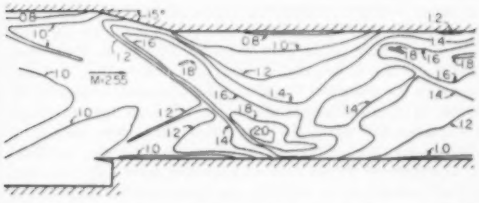

FIG. 5(e) LINES OF CONSTANT DENSITY RATIO OBTAINED FROM INTERFEROGRAM IN FIG. 5(d)
(Densities are referred to density of free stream approaching wedge.)

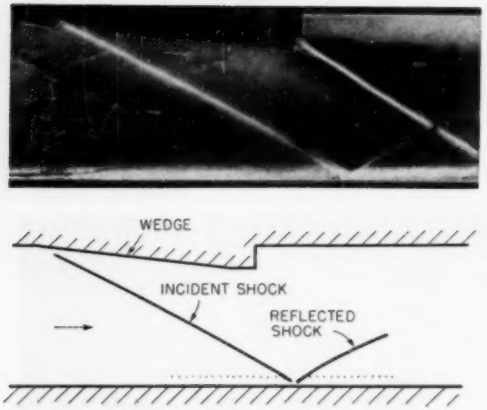

FIG. 7 TURBULENT; $\theta = 5$ DEG; KNIFE-EDGE HORIZONTAL; 5×10^{-6} SEC; $\mathbf{M} = 2.35$

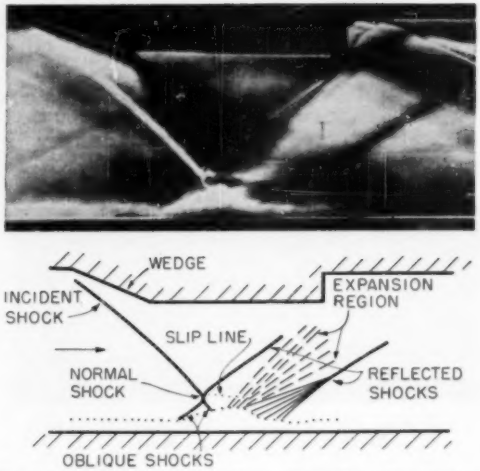

FIG. 8 TURBULENT; $\theta = 20$ DEG; KNIFE-EDGE HORIZONTAL; 5×10^{-6} SEC; $\mathbf{M} = 2.3$

slightly and that the incident shock is reflected as an oblique shock. With a relatively strong shock, on the other hand, Fig. 8 shows that the incident shock bifurcates near the wall. The thickening of the boundary layer produces a reflected oblique shock which originates well upstream of the point of incidence of the original shock. Both the incident shock and the oblique shock generated in the boundary layer are reflected as oblique shocks at the ends of a short normal shock. What appears to be a slip line extends downstream from the intersection of the normal and incident shocks. An expansion region and another oblique shock may be seen downstream. Fage and Sargent (7), using Mach numbers up to about 1.5, also observed that a strong incident shock bifurcates near a turbulent boundary layer on a plane wall.

For incident shocks of intermediate strength, a normal shock near the wall has not been observed. Instead, the oblique shock generated upstream of the point of incidence crosses the incident shock without a large change in direction. As in Fig. 7, the boundary layer did not thicken appreciably in passing the region of interaction.

COMPARISON BETWEEN LAMINAR AND TURBULENT LAYERS

Comparing the interaction of an oblique shock with a laminar and turbulent boundary layer, respectively, it appears that on the whole the interaction is of greater magnitude for the laminar boundary layer. No special correlation was observed, however, as to the relation between the reflected wave pattern and the boundary-layer regime.

It seems worthy of mention that the effect of the boundary-layer regime noted here and the other effects found by previous investigators may be in part illusory. Dr. H. S. Tsien has pointed out[6] that in the neighborhood of the interaction, shearing stresses in the boundary layer may be negligible compared to pressure stresses and inertia effects. If this is so, the boundary-layer regime will affect the interaction phenomena only in a secondary way, i.e., only in so far as the Mach number distribution is influenced by the type of boundary layer. In this connection, it might be noted that the Mach number distribution in the boundary layer depends not only on whether the boundary layer is laminar or turbulent but also on the longitudinal pressure gradients and wall curvature associated with the surface on which the boundary layer had previously grown.

In order to investigate this hypothesis, tests were made on a turbulent boundary layer by injecting a high-speed stream into it from a slit placed before the point of intersection of the incident oblique shock (8). Variation of the injection flow, and therefore of the velocity profile, altered the character of the reflection considerably. The results seem to confirm Tsien's suggestion of the importance of the velocity profile, at least for the turbulent boundary layer.

CONCLUSIONS

The results of previous investigators showing a pronounced interaction between a shock-wave system and flow in a boundary layer were confirmed. However, the possible varieties of interaction were found to be more numerous than was hitherto reported, depending not only on the boundary-layer regime but also on the curvature of the solid boundary, manner of origin of the shock, and shock strength.

The present state of knowledge concerning the shock boundary-layer interaction depends almost exclusively on experimental data, rather than on mathematical formulation. To reach a satisfactory understanding of these complicated phenomena will require the development of mathematical techniques of analysis, but additional experimentation may be necessary to achieve this end.

ACKNOWLEDGMENT

This work was carried out as part of the Guided Missiles Program of the Massachusetts Institute of Technology, and was sponsored by the Navy Department, Bureau of Ordnance.

The project was carried on in the M.I.T. Gas Turbine Laboratory. The co-operation of the staff of the laboratory is acknowledged with thanks.

Some of the work reported here was taken from the Master's theses of Mr. D. M. Poole and Mr. W. A. Loeb (8, 9).

BIBLIOGRAPHY

1 "Some Experiments on the Interaction of Shock Waves With Boundary Layers on a Flat Plate," by A. H. Shapiro, E. P. Neumann, and F. W. Barry, Project Meteor Report No. 29, October, 1948.

[6] In a verbal discussion.

2 "The Interaction Between Boundary Layer and Shock Waves in Transonic Flow," by H. W. Liepmann, *Journal of the Aeronautical Sciences*, vol. 13, December, 1946, pp. 623–637.

3 "Investigations of Compression Shocks and Boundary Layers in Gases Moving at High Speed," by J. Ackeret, F. Feldmann, and N. Rott, NACA TM, No. 1113, January, 1947.

4 "Untersuchungen an Verdichtungsstossen und Grenzschichten in schnell bewegten Gasen," by J. Ackeret, F. Feldmann, and N. Rott, *Mitteilungen aus dem Institut für Aerodynamik an der Eidgenossischen Technischen Hochschule*, No. 10, Zurich, Switzerland, 1946.

5 "An Improved Schlieren Apparatus," by F. W. Barry and G. M. Edelman, *Journal of the Aeronautical Sciences*, vol. 15, June, 1948, pp. 364–365.

6 "Interaction of Shock Waves and Boundary Layers," by F. W. Barry, Master's Thesis in Course II, Massachusetts Institute of Technology, January, 1947.

7 "Shock-Wave and Boundary-Layer Phenomena Near a Flat Surface," by A. Fage and R. F. Sargent, *Proceedings of the Royal Society*, vol. 190, series A, No. 1020, June 17, 1947, pp. 1–20

8 "Interaction of Shock Waves and Boundary Layer," by W. A. Loeb, Master's Thesis in Course II, Massachusetts Institute of Technology, June, 1947.

9 "Interaction of Shock Waves and Boundary Layers," by D. M. Poole, Master's Thesis in Course II, Massachusetts Institute of Technology, September, 1946.

10 "Introduction to the Aerodynamics of a Compressible Fluid," by H. W. Liepmann and A. E. Puckett, John Wiley & Sons, Inc., New York, N. Y., first edition, 1947, pp. 58–62.

Critical Load of Columns of Varying Cross Section

By W. T. THOMSON,[1] MADISON, WIS.

A method is developed for determining the critical load of a pin-ended long column of n different cross sections and lengths. For n less than 5, the method results in a simple equation for the critical load. Specific examples for columns of 2, 3, and 4 sections are given, and experimental data are presented for comparison.

Nomenclature

The following nomenclature is used in the paper:

l_i = length of ith section
I_i = moment of inertia of ith section
x_i = x-co-ordinate at end of ith section
y_i = deflection at end of ith section
y_i' = slope at end of ith section

$$\beta_i = \sqrt{\frac{P}{EI_i}}$$

E = Young's modulus of elasticity
P = column load
l = total length of column
M_0 = applied moment at $x = 0$

Development of Equations

Fig. 1 shows a pin-ended column of n sections. The column is assumed to be long so that failure tends to take place by lateral instability rather than by direct compression.

Starting with the differential equation for the long column

$$\frac{d^2y}{dx^2} = -\left(\frac{P}{EI}\right) y \quad \ldots\ldots [1]$$

and using the method of Laplace transformation, the solution can be written in terms of the point boundary conditions. Thus for the ith section the deflection is

$$y(x) = y_{i-1}' \frac{\sin \beta_i(x - x_{i-1})}{\beta_i} + y_{i-1} \cos \beta_i(x - x_{i-1}) \quad \ldots [2]$$

$$x_{i-1} \leq x \leq x_i$$

The foregoing solution enables one to write the equations for the deflection and slope at any position i in terms of the corresponding quantities at $i - 1$

$$\left.\begin{aligned} y_i &= y_{i-1} \frac{\sin \beta_i l_i}{\beta_i} + y_{i-1} \cos \beta_i l_i \\ y_i' &= y_{i-1}' \cos \beta_i l_i - y_{i-1} \beta_i \sin \beta_i l_i \end{aligned}\right\} \quad \ldots\ldots [3]$$

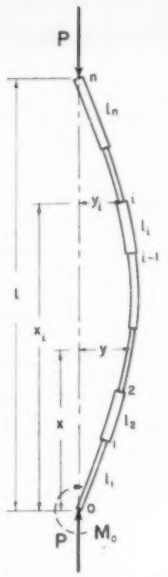

Fig. 1 Column of n Sections

Dividing each equation by $y_{i-1}' \cos \beta_i l_i$ we obtain the following reduction formula

$$\frac{y_i}{y_i'} = \frac{\dfrac{\tan \beta_i l_i}{\beta_i} + \left(\dfrac{y_{i-1}}{y_{i-1}'}\right)}{1 - \left(\dfrac{y_{i-1}}{y_{i-1}'}\right) \beta_i \tan \beta_i l_i} \quad \ldots\ldots [4]$$

We now apply the boundary condition of zero deflection at each end. We will also introduce temporarily a moment M_0 at $x = 0$ which will modify the solution at $i = 1$ as follows

$$\left.\begin{aligned} y_1 &= y_0' \frac{\sin \beta_1 l_1}{\beta_1} - \frac{M_0}{EI_1\beta_1^2}(1 - \cos \beta_1 l_1) \\ y_1' &= y_0' \cos \beta_1 l_1 - \frac{M_0}{EI_1\beta_1} \sin \beta_1 l_1 \end{aligned}\right\} \quad \ldots\ldots [5]$$

Dividing as before, we obtain

$$\frac{y_1}{y_1'} = \frac{\dfrac{\tan \beta_1 l_1}{\beta_1} - \dfrac{M_0}{y_0' EI_1\beta_1^2}\left(\dfrac{1 - \cos \beta_1 l_1}{\cos \beta_1 l_1}\right)}{1 - \dfrac{M_0}{y_0' EI_1 \beta_1} \tan \beta_1 l_1} \quad \ldots\ldots [6]$$

---

[1] Associate Professor of Mechanics, University of Wisconsin. Mem. ASME.

Contributed by the Applied Mechanics Division and presented at the Annual Meeting, New York, N. Y., November 27–December 2, 1949, of The American Society of Mechanical Engineers.

Discussion of this paper should be addressed to the Secretary, ASME, 29 West 39th Street, New York, N. Y., and will be accepted until July 10, 1950, for publication at a later date. Discussion received after closing date will be returned.

Note: Statements and opinions advanced in papers are to be understood as individual expressions of their authors and not those of the Society. Paper No. 49—A-1.

At the critical load, the ratio M_s/y_s' becomes equal to zero, reducing Equation [6] to

$$\frac{y_1}{y_1'} = \frac{\tan \beta_1 l_1}{\beta_1} \quad \ldots\ldots [7]$$

At the other end $i = n$, we let $y_n = 0$ in Equations [3] and obtain

$$\frac{\tan \beta_n l_n}{\beta_n} = -\frac{y_{n-1}}{y_{n-1}'} \quad \ldots\ldots [8]$$

Starting with Equation [7] and applying the reduction Equation [4] $n - 2$ times, we obtain the right side of Equation [8] and the equation for the critical load.

Critical Loads for Specific Cases

By the use of Equations [8], [7], and [4], the following formulas for the critical load are derived

$n = 1$

$$\tan \beta_1 l_1 = 0 \quad \ldots\ldots [9]$$

$n = 2$

$$\frac{\tan \beta_2 l_2}{\beta_2} = -\frac{\tan \beta_1 l_1}{\beta_1} \quad \ldots\ldots [10]$$

$n = 3$

$$\frac{\tan \beta_3 l_3}{\beta_3} = -\left(\frac{\dfrac{\tan \beta_1 l_1}{\beta_1} + \dfrac{\tan \beta_2 l_2}{\beta_2}}{1 - \dfrac{\beta_2}{\beta_1} \tan \beta_1 l_1 \tan \beta_2 l_2} \right) \quad \ldots\ldots [11]$$

$n = 4$

$$\frac{\tan \beta_4 l_4}{\beta_4} = -\left(\frac{\dfrac{\tan \beta_1 l_1}{\beta_1} + \dfrac{\tan \beta_2 l_2}{\beta_2} + \dfrac{\tan \beta_3 l_3}{\beta_3} - \dfrac{\beta_2}{\beta_1 \beta_3} \tan \beta_1 l_1 \tan \beta_2 l_2 \tan \beta_3 l_3}{1 - \dfrac{\beta_2}{\beta_1} \tan \beta_1 l_1 \tan \beta_2 l_2 - \dfrac{\beta_2}{\beta_1} \tan \beta_1 l_1 \tan \beta_3 l_3 - \dfrac{\beta_2}{\beta_2} \tan \beta_2 l_2 \tan \beta_3 l_3} \right) \quad \ldots\ldots [12]$$

These equations are solved for the critical load in the following manner: Using Equation [11] as an example and letting $\varphi = \beta_1 l_1$, we have on rewriting

$$\tan \frac{\beta_3}{\beta_1} \frac{l_3}{l_1} \varphi = -\left(\frac{\dfrac{\beta_2}{\beta_1} \tan \varphi + \dfrac{\beta_3}{\beta_2} \tan \dfrac{\beta_2}{\beta_1} \dfrac{l_2}{l_1} \varphi}{1 - \dfrac{\beta_2}{\beta_1} \tan \varphi \tan \dfrac{\beta_2}{\beta_1} \dfrac{l_2}{l_1} \varphi} \right) \quad \ldots\ldots [13]$$

When the column is specified, the ratios of β_s' and l_s' are known; that is

$$\frac{\beta_2}{\beta_1} = \sqrt{\frac{I_1}{I_2}}$$

Thus, by plotting each side of the equation against φ, the critical load can be determined. In some specific cases the solution can be carried out algebraically as shown under illustrative examples.

General Procedure for Large n

When n is greater than 4, the equation for the critical load becomes rather long and complicated, and a numerical method of tabular computation somewhat on the order of Holzer's method for torsional systems is preferable. For instance, we start by first choosing a value of β_1, which establishes y_1/y_1' from Equation [7]. Terms β_2, β_3, etc., are then known from the relation $\beta_2 = \beta_1 \sqrt{I_1/I_2}$, etc., and hence from Equation [4] y_2/y_2', y_3/y_3', etc., are successively computed. The critical load is established when Equation [8] is satisfied.

Illustrative Examples

1 Determine the critical load of a two-section column of rectangular cross section if $l_1 = l_2 = l/2$, and the thickness ratio $h_1/h_2 = 2$.

Solution: Writing Equation [10] in the form

$$\tan \frac{\beta_2}{\beta_1} \frac{l_2}{l} \beta_1 l = -\frac{\beta_2}{\beta_1} \tan \frac{l_1}{l} \beta_1 l$$

and substituting

$$\frac{\beta_2}{\beta_1} = \sqrt{\frac{I_1}{I_2}} = \sqrt{\left(\frac{h_1}{h_2}\right)^3} = 2.82$$

$$\frac{l_1}{l} = \frac{l_2}{l} = \frac{1}{2}$$

we have

$$\tan 2.82 \frac{\beta_1 l}{2} = -2.82 \tan \frac{\beta_1 l}{2}$$

A few trials result in the solution

$$\frac{\beta_1 l}{2} = \frac{l}{2} \sqrt{\frac{P_{cr}}{EI_1}} = 0.698$$

$$P_{cr} = 1.95 \left(\frac{EI_1}{l^2}\right)$$

The critical load of a column of the same length with uniform cross section I_1 is

$$P_1 = \pi^2 \left(\frac{EI_1}{l^2}\right)$$

Thus the reduction in the critical load of a rectangular column due to cutting down half the length to half the thickness is $1.95/\pi^2 = 0.197$.

2 Determine the critical load of a three-section column where the middle third is cut down in cross section in the ratio

$$\frac{\beta_2}{\beta_1} = \sqrt{\frac{I_1}{I_2}} = 2$$

Solution: Using Equation [13] and substituting the following quantities

$$\frac{\beta_3}{\beta_1} = 1$$

$$l_1 = l_2 = l_3 = \frac{l}{3}$$

$$\frac{\beta_2}{\beta_1} = 2$$

we obtain

$$\tan \varphi = -\left(\frac{\tan \varphi + \dfrac{1}{2} \tan 2\varphi}{1 - 2 \tan \varphi \tan 2\varphi} \right)$$

Replacing $\tan 2\varphi$ by

$$\frac{2 \tan \varphi}{1 - \tan^2 \varphi}$$

TABLE 1 RESULTS ON TESTS ON DOUGLAS FIR EXPERIMENTAL COLUMNS

Col. no.	l_1/l	l_2/l	l_3/l	k_2/k_1	k_3/k_1	β_2/β_1	β_3/β_1	P_{cr}/P_1 (theoretical)	Experimental P_1 lb	Experimental P_{cr} lb	Computed P_{cr} lb	Error, per cent
1	1/3	1/3	1/3	0.628	1	2	1	0.346	50 3/4	16 1/4	17.4	3.9
2	1/4	1/2	1/4	1.59	1	0.5	1	0.442	49 1/4	23.0	21.8	5.2
3	1/4	1/2	..	1/2	..	2.82	..	0.197	54 1/2	10.5	10.7	1.9

NOTE:
P_1 = critical load of uniform column I_1, l.
I_1 = moment of inertia before reduction.

and solving, we obtain

$$\tan \varphi = 0.707$$

$$\varphi = \frac{l}{3}\sqrt{\frac{P_{cr}}{EI_1}} = 0.616$$

$$P_{cr} = 3.43\left(\frac{EI_1}{l^2}\right)$$

Thus the reduction in the critical load, compared to a uniform column of the same length is $3.43/\pi^2 = 0.346$.

3 Show that if $l_1 = l_2 = l_3 = l_4 = l/4$, and $\beta_1 = \beta_2 = \beta_3 = \beta_4$, Equation [12] for four sections gives the critical load of a uniform column of length l.

Substituting the given quantities into Equation [12], we obtain the equation

$$1 = -\frac{3 - \tan^2 \beta_1 \frac{l}{4}}{1 - 3\tan^2 \beta_1 \frac{l}{4}}$$

which on solving results in

$$\tan \frac{\beta_1 l}{4} = 1$$

$$\beta_1 \frac{l}{4} = \frac{l}{4}\sqrt{\frac{P_{cr}}{EI_1}} = \frac{\pi}{4}$$

$$P_{cr} = \pi^2\left(\frac{EI_1}{l^2}\right)$$

Experimental Verification

Three experimental columns of clear Douglas fir (see Fig. 2), were built up to verify special cases of the formulas derived in this paper. The approximate dimensions of each column were 1 in. × 1/2 in. × 6 ft, and the critical load of each was determined before and after cutting. The results are given in Table 1. The per cent error is not large when one considers the nonhomogeneity of wood.

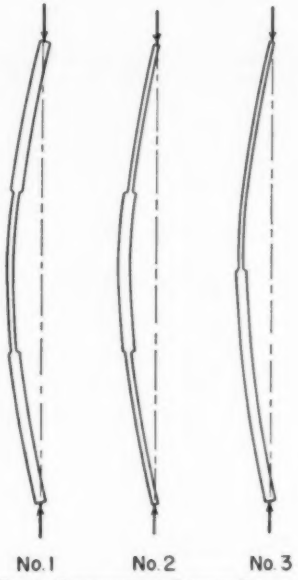

FIG. 2 EXPERIMENTAL COLUMNS TESTED

Conclusions

The critical load of a pin-ended long column of n sections can be determined by the general method outlined in this paper. The tabular method is somewhat analogous to Holzer's method for torsional vibration or Myklestad's method for beam vibration in that a reduction formula relating the quantities at position i to that at position $(i-1)$ is necessary. For n less than 5, simple formulas for the critical loads are readily obtained. Similar procedure can be applied to columns with other types of end fixity.

Stress Studies on Piping Expansion Bellows

By F. J. FEELY, JR.,[1] and W. M. GORYL,[2] ELIZABETH, N. J.

As a result of numerous and costly failures of the stainless-steel bellows used to take up thermal expansion in the piping of petroleum and chemical processing equipment, a basis has been developed for designing these bellows to operate within reasonable stresses. A formula has been derived to show the total stress induced in the material as a result of the combined effects of pressure and movement. The validity of the approximations used in this formula has been verified by laboratory strain-gage measurements on an experimental bellows. A relationship between several variables in the design of the disks has also been determined and serves as a basis for dimensioning them to achieve the most economical proportions. When this relationship is satisfied, the maximum permissible movement per disk can be obtained. This is shown graphically. Several supplementary formulas are given for determining bellows characteristics which may affect the design of adjacent piping. The problem of designing an expansion joint for high-pressure service is discussed briefly, and some preliminary laboratory data are presented on a commercial joint of this type.

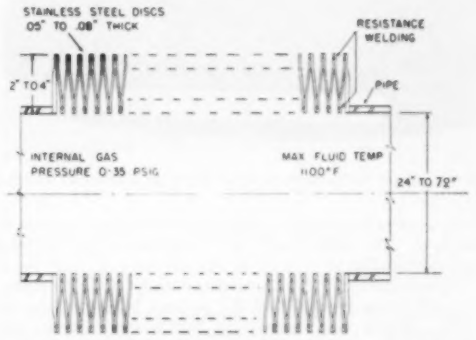

Fig. 1 Section of Typical Expansion Bellows, Showing Size Ranges and Design Conditions Most Frequently Encountered

Introduction

In petroleum and chemical processing plants where high-temperature low-pressure piping frequently is used, common practice has been to install flexible steel bellows to absorb the thermal expansion which, due to the rigidity of certain piping systems, cannot be taken up in deflection. These bellows, commonly known as expansion joints, are built to a number of different designs. This paper deals with joints which are constructed by crimping thin stainless-steel disks into shallow cones which are resistance-welded together at their inner and outer edges. The details of a typical joint of this type are shown in Fig. 1. This figure also shows the size ranges and design conditions most frequently encountered in commercial applications.

Quite frequently, thermal movements can be accommodated by providing a bellows to act as a hinge in the piping. Fig. 2 illustrates a typical commercial construction of this type commonly called a hinge joint. Other joints combining the features of both rotation and axial movement are known as universal joints. An example of this design is shown in Fig. 3.

Joints of this design were used extensively in fluid-catalyst cracking plants built by Standard Oil Company (New Jersey) which have been in operation since 1942. In these units, expansion and hinge joints are utilized in large-diameter piping (24 in. to 72 in.) carrying oil vapors and flue gas at temperatures ranging from 900 to 1100 F. A considerable number of failures

Fig. 2 Typical Hinge Joint

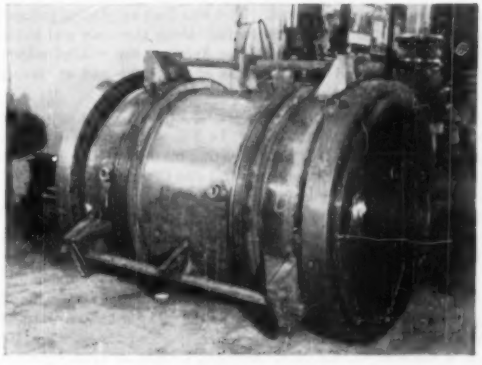

Fig. 3 Universal Expansion Joint

[1] Esso Engineering Department, Standard Oil Development Company.

[2] Esso Engineering Department, Standard Oil Development Company. Jun. ASME.

Presented at the National Meeting of the Applied Mechanics Division, Ann Arbor, Mich., June 13–15, 1949, of The American Society of Mechanical Engineers.

Discussion of this paper should be addressed to the Secretary, ASME, 29 West 39th Street, New York, N. Y., and will be accepted until July 10, 1950, for publication at a later date. Discussion received after the closing date will be returned.

Note: Statements and opinions advanced in papers are to be understood as individual expressions of their authors and not those of the Society. Paper No. 49—APM-22.

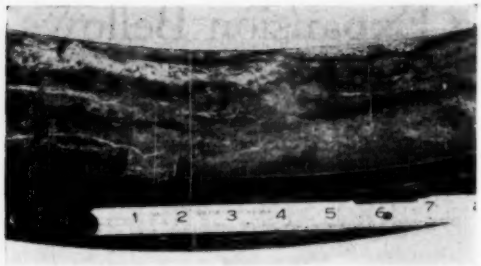

FIG. 4 BELLOWS-ELEMENT FAILURE SHOWING NATURE OF CRACKS

have occurred in this service owing to the formation of cracks in the disks. The cracks usually run circumferentially in the disks as is shown in Fig. 4.

Microscopical examinations of failed disks led to the conclusion that the cracks resulted from the material being subjected to acidic corrosion in the presence of high stresses. It was also recognized that this corrosion occurs only during periods when the plants are shut down, and the piping and joints are cool. During these periods, weak acids are formed from various corrosive compounds dissolved in condensed purging steam. Since little could be done about these conditions, attention was given to the question of stresses in the disk material resulting from the pressure and movements to which the bellows are subjected. It was then found that no information was available from manufacturers on the magnitude of these stresses or the factors affecting them.

LABORATORY STRESS DETERMINATIONS

In order to secure information on the magnitude of the stresses set up in an expansion joint, laboratory tests were made on a typical expansion bellows subjected to pressure and movement.

Description of Equipment. The joint tested was of the universal type consisting of two bellows, each having ten stainless-steel disks 0.052 in. thick and 2.50 in. wide. It was rated to take 4 in. axial compression as an expansion joint or 4 deg 53 min angularity per bellows as a hinge joint. The design pressure was 25 psig.

A total of 34 SR-4 $^1/_8$-in. strain gages were cemented to the disks in such a way that the directions and magnitudes of all primary and secondary anticipated stresses could be determined, and their uniformity checked. This was done by placing pairs of gages (one radial and one tangential) along the inner and outer edges of disks as well as midway between the welded edges. Gages were located on both sides of the disks and at 90-deg intervals around the circumference of the joint.

Figs. 5 and 6 show the joint set up in the testing apparatus with all strain gages attached. In Fig. 5 the joint is shown mounted in a laboratory tensile-testing machine which was used to produce the axial compression and also to maintain the desired face to face when internal pressure was applied. Fig. 6 shows the arrangement used to measure the effects of angular movement.

Tests and Results. The first test performed consisted of a double cycle of axial compression and release over the full range of 4 in., during which readings were taken at approximately 1-in. intervals. The greatest strains were measured on the radial gages adjacent to the resistance welds. These strains were as high as 7000 microinches per in. which, if a modulus of 28.5×10^6 psi is assumed, would mean indicated stresses of approximately 200,000 psi. Since the psuedoelastic limit of the 18-8 Cr-Ni

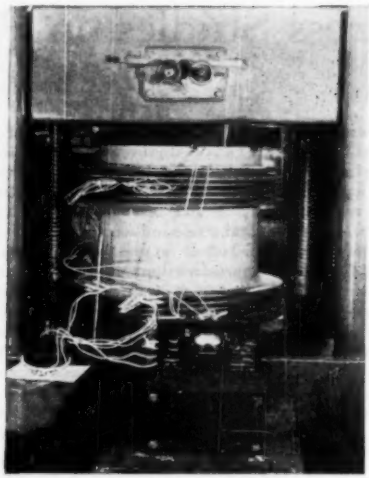

FIG. 5 EXPERIMENTAL EXPANSION JOINT SHOWN IN TESTING MACHINE WITH STRAIN GAGES ATTACHED

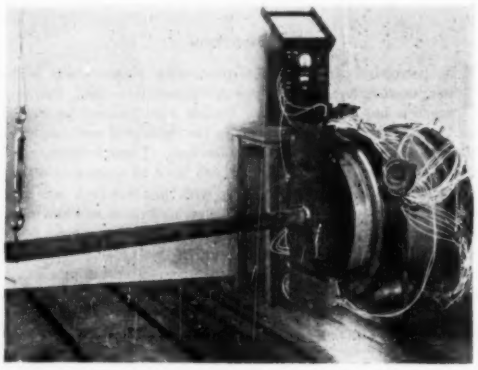

FIG. 6 EXPERIMENTAL JOINT SET UP FOR ANGULAR-MOVEMENT TESTS

disk material is less than 15,000 psi, the joint obviously was being stressed well into the plastic range. This was verified by the failure of the joint to return to its initial length after the applied forces were released. Circumferential stresses were found to be small enough to be neglected.

The next test consisted of loading the joint in a vertical position with lead weights in 50-lb increments until about 650 lb were applied. This produced a movement of 0.754 in., of which 0.118 in. remained as permanent set when the load was removed. The results of this test are shown in Fig. 7 from which it can be seen that there is a straight-line relationship between compressive force and joint movement in the range covered. No strain-gage readings were taken during this test.

Strain measurements were then taken as the joint was rotated through the design angle. In this test, strains were measured at corresponding points of maximum movement on the tension and compression sides as the bellows was rotated by a force on the

extended arm. Readings were taken at movements of 2 deg 26 min and 4 deg 53 min. When the weight was released from the arm, the bellows did not return to its original no-load position, thus again indicating a permanent set in the disk material. The maximum indicated stresses for this type movement, however, did not exceed about 50,000 psi, or somewhat less than one quarter the values obtained in the axial-compression tests. This test confirmed the belief that hinge joints were more conservatively rated than expansion joints, a belief which had been based on the excellent service record of hinge joints as compared to expansion joints.

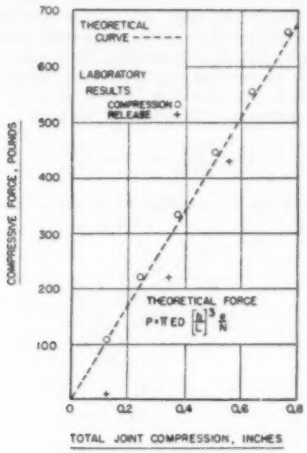

FIG. 7 THEORETICAL VERSUS ACTUAL EXPANSION-JOINT COMPRESSIVE FORCE

A final series of strain-gage readings was taken as the joint was subjected to internal air pressure of 25 psig while being restrained from axial movement. Because of some distortion of the bellows during the previous tests, it was necessary to apply pressure several times before the strain readings indicated by the various gages became reasonably uniform at similar locations. The results of this test indicated that the stresses due to the 25-psig pressure were generally less than 15,000 psi or reasonably near the elastic limit of the material.

APPROXIMATE THEORETICAL FORMULAS

Basic Stress Equations. To establish a basis for further studies of expansion-joint stresses, a theoretical analysis was made. As a first approximation, the disks were assumed to be flat plates, thus neglecting the slight coning introduced for ease of fabrication. Following a remark by Timoshenko[3] and studies on circular plate stresses by Wahl and Lobo,[4] the disks were considered as beams, since for most commercial joints the diameter is large in comparison with the disk width.

Inasmuch as the disks are semirigidly held by welding at the inner and outer edges, they were treated as fixed-end beams. Two loadings are then assumed. The loading due to internal pressure is shown in Fig. 8(*a*), and the loading due to expansion

[3] "Theory of Plates and Shells," by S. Timoshenko, McGraw-Hill Book Company, Inc., New York, N. Y., 1940, p. 68.

[4] "Stresses and Deflections in Flat Circular Plates With Central Holes," by A. M. Wahl and G. Lobo, Jr., JOURNAL OF APPLIED MECHANICS, Trans. ASME, vol. 52, 1930, p. A-29.

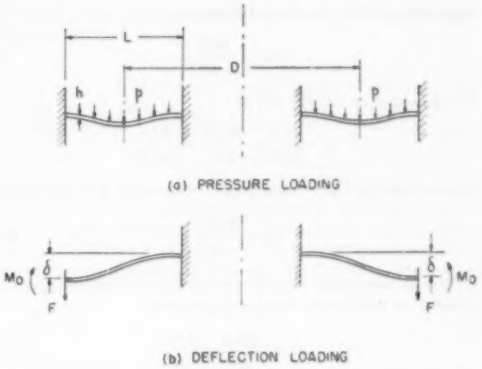

FIG. 8 BEAM CONCEPT APPLIED TO DISKS OF EXPANSION BELLOWS

or compression is shown in Fig. 8(*b*). Equations for the stresses resulting from these two loadings are then derived using normal beam theory.

In these equations the following nomenclature is used:

S_p = stress due to pressure loading, psi
S_δ = stress due to deflection, psi
S_t = total stress in disk material, psi
p = internal pressure, psig
L = Free disk width, or distance between inner and outer welds on a disk, in.
h = disk thickness, in.
E = Young's modulus of disk material, psi
δ = deflection per disk, in.
D = mean diameter of disks, in.

Referring to Fig. 8(*a*) for pressure loading, the end moment is

$$M = \frac{qL^2}{12}$$

where q, the load per unit length is

$$q = \pi Dp$$

Also, the stress is

$$S_p = \frac{M}{I}\frac{h}{2}$$

where the moment of inertia is

$$I = \pi\frac{Dh^3}{12}$$

Substituting for M and I, we have

$$S_p = \frac{pL^2}{2h^2} \quad \ldots\ldots\ldots\ldots\ldots\ldots\ldots\ldots [1]$$

Referring to Fig. 8(*b*), for loading due to deflection, we can assume a force F, and a moment, M_0 to keep the end horizontal. The slope at the end will then be

$$\frac{M_0 L}{EI} - \frac{FL^2}{2EI} = 0 \text{ or } M_0 = \frac{FL}{2}$$

Also the stress is

$$S_\delta = \frac{M_0}{I}\frac{h}{2}$$

Again, substituting for M_0 and I, we have

$$S_\delta = \frac{3FL}{\pi Dh^2}$$

The deflection at the end will be

$$\delta = \frac{FL^3}{3EI} - \frac{M_0L^2}{2EI} = \frac{FL^3}{12EI}$$

Substituting for I and eliminating F between the last two results

$$S_\delta = \frac{3Eh\delta}{L^2} \quad \text{[2]}$$

Since at some point these stresses are always additive, the expression for total stress in the disk material is

$$S_t = \frac{3Eh\delta}{L^2} + \frac{L^2p}{2h^2} \quad \text{[3]}$$

An exact expression for the disk stresses was also obtained by combining several fundamental cases for which solutions had been worked out by Wahl and Lobo. This exact solution is very similar in form to Equation [3], but contains coefficients which must be computed for various joint sizes. Most commercial bellows, however, fall within a size range which is covered with sufficient accuracy by Equation [3]. Variations between theoretical and actual values will be discussed later.

Useful Supplementary Equations. In some instances, the force exerted by a joint in compression or extension may be critical in the design of the adjacent piping. An expression containing this force was obtained in the last step of the derivation of the deflection stress equation. This expression is

$$F = \frac{\pi EDh^3}{L^3}\delta$$

For a bellows containing N disks, this force becomes

$$P = \pi\frac{EDh^3e}{L^3N} \quad \text{[4]}$$

where

P = compression or extension force, lb
e = total axial movement, in.
N = number of disks

In the case of hinge joints where angular motion is involved, the deflection of the disks is calculated from a geometric relationship between the sine of the angle and the diameter of the joint. This is shown in Fig. 9.

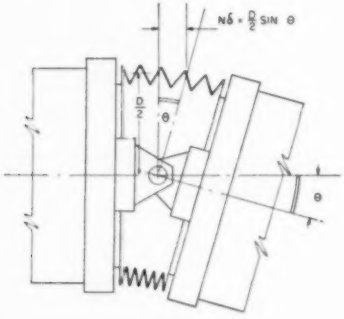

FIG. 9

Thus by substituting the value of δ in terms of joint angularity in Equation [3], the following expression for stress in a hinge joint is obtained

$$S_t = \frac{3Eh}{L^2}\frac{D}{2N}\sin\theta + \frac{L^2p}{2h^2} \quad \text{[5]}$$

where

θ = joint angularity, deg

The maximum deflection in a hinge joint, however, occurs at only two points 180 deg apart, while the intermediate positions of the disks are deflected and stressed to a lesser extent.

To determine the moment necessary to rotate a hinge joint, the deflection forces which vary around the circumference must be multiplied by corresponding moment arms and integrated.

From the derivation of Equation [2], we have

$$\delta = \frac{FL^3}{12EI} \quad \text{or} \quad F = \frac{\delta 12EI}{L^3}$$

Referring to Fig. 10, consider the elemental force df at any

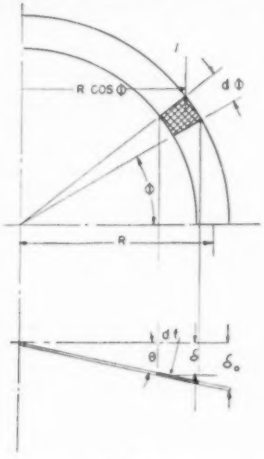

FIG. 10

location on the joint. Then

$$df = \frac{\delta 12EI}{L^3}$$

and

$$I = \frac{Rh^3\,d\phi}{12}$$

Then

$$df = \frac{\delta ERh^3d\phi}{L^3}$$

Also from Fig. 10 it can be seen that

$$\delta = \delta_0\frac{R\cos\phi}{R}$$

Substituting we have

$$df = \delta_0 \frac{ER h^3 \cos \phi d\phi}{L^3}$$

Multiplying this force by the moment arm $R \cos \phi$ to determine the elemental moment dm we have

$$dm = \delta_0 \frac{ER^2 h^3}{L^3} \cos^2 \phi d\phi$$

Integrating over one quadrant of the joint

$$m = \delta_0 \frac{ER^2 h^3}{L^3} \frac{\pi}{4}$$

Since the moment necessary to rotate a complete disk will be 4 times m, and since the total hinge-joint moment will vary inversely with the number of disks we have

$$M = \delta_0 \frac{ER^2 h^3}{L^3} \frac{\pi}{N}$$

From Fig. 10 it can be seen that $\delta_0 = R \sin \theta$
Therefore

$$M = \frac{ER^2 h^3}{L^3} \frac{\pi}{N} \sin \theta \quad [6]$$

m = moment necessary to rotate one quadrant of a single disk hinge joint through angle θ, lb-in.
M = moment necessary to rotate a hinge joint through angle θ, lb-in.
R = mean radius of disk, in.
$d\phi$ = angle subtending small section of disk, radians
df = force to deflect small section of disk, lb
dm = moment to deflect small section of disk, lb-in.

Comparison Between Laboratory and Theoretical Results. The laboratory stress data obtained on the experimental joint were checked against theoretical values computed from the stress equations. Good agreement was obtained for all types of loading. Fig. 7, for example, illustrates how close this agreement was for calculated values of compressive force compared with the actual weights applied in the laboratory to compress the joint a given amount.

It is actually quite surprising that the theoretical work checked the laboratory data as closely as it did in view of the approximations made in the analysis, some variations in disk thickness, the effect of the stresses introduced by the resistance welding, and the fact that the joint was frequently stressed beyond the elastic limit. These variations between theoretical and actual conditions revealed themselves in rippling of the outer edges of several disks when the joint was compressed to any great extent.

Development of Optimum Design

While the basic equations permitted the determination of stresses in existing joints, they did not offer any practical solution to the expansion-joint problem, since it was found that the existing joints were so highly stressed that approximately 10 times as many disks would be required to reduce the stress due to movement to a reasonable value. Furthermore, as shown in the laboratory tests, the pressure stress alone for a typical joint was essentially equal to the elastic limit of the material.

Accordingly, an analysis of the basic formula was made to determine the effect of variations in the physical dimensions.

Optimum Joint Dimensions. The most important feature of joint design revealed by this analysis is that there is an optimum relationship for the dimensions of the disks (L and h), which will permit the maximum movement for a given pressure and allowable stress. This optimum condition is found by solving the basic Equation [3] for δ

$$\delta = \left[S_t L^3 - \frac{pL^4}{2h^2} \right] \frac{1}{3hE} \quad [7]$$

If δ is then differentiated with respect to L, then

$$\frac{d\delta}{dL} = \left[2 S_t L - \frac{4pL^3}{2h^2} \right] \frac{1}{3hE}$$

S_t, E, p, and h are considered constants in this differentiation since they are dependent upon service conditions, suitable materials, and manufacturing facilities. By setting the differentiated equation equal to zero and reducing, the optimum relationship is secured

$$\frac{L}{h} = \sqrt{\frac{S_t}{p}} \quad [8]$$

By designing a joint to satisfy this equation, the maximum deflection can be obtained with given values of design pressure and allowable stress. Fig. 11 illustrates how the L/h ratio varies with the deflection per disk and shows graphically where the maximum point occurs. It can also be seen that the allowable deflection is increased in proportion to the thickness. Another interesting feature of this relationship is that for the optimum conditions, the stress due to pressure is equal to the stress due to movement.

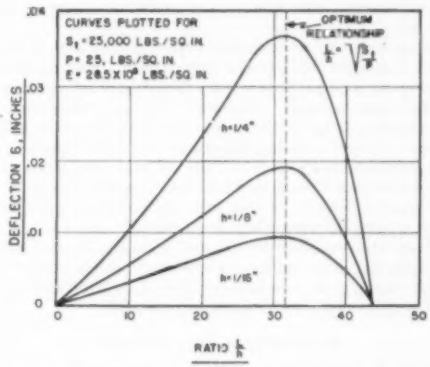

Fig. 11 Curves Showing Importance of Correct Disk Dimensions

Effect of Variables. In order to find an expression for the maximum deflection permissible under the optimum conditions, Equation [8] was solved for L^2 and substituted in Equation [7]

$$L^2 = \frac{h^2 S_t}{p}$$

$$\delta = \left[S_t \frac{h^2 S_t}{p} - \frac{p h^4 S_t^2}{2h^2} \right] \frac{1}{3E}$$

This reduces to

$$\delta = \frac{S_t^2 h}{6pE} \quad [9]$$

From this equation the effects of the several variables became readily apparent. It can be seen that the maximum deformation per disk varies as the square of the design stress, directly with the

thickness of the disks and inversely with the pressure and modulus.

Practical Design Limitations

In selecting the most satisfactory bellows material, the effects of stress and modulus in Equation [9] were considered along with the requirement that the material be as little susceptible as possible to stress corrosion-cracking. After a careful study had been made, including bellows temperature measurements, and a review of all past joint experience, 18 per cent Cr-8 per cent Ni type 347 stainless steel was chosen as the material possessing the most desirable properties for expansion-joint construction. Laboratory and plant experience with this material were used as the basis for selecting a design stress of 25,000 psi. Young's modulus was taken as 28.5×10^6 psi.

Since increasing the disk thickness provides another means for achieving larger deflections, this possibility was discussed with joint manufacturers. While some increase in disk thickness was found possible, further steps in this direction have been limited by the fact that available manufacturing facilities for resistance-welding expansion-joint bellows are limited to handling 0.078-in-thick disks. The reason for limiting the construction to resistance welding is that the uniformity of the product is considered superior, thus reducing the possibility of stress concentrations.

In applying the new formulas, close attention is given to the exact expansion and pressure requirements. For example, in determining piping expansion, only the actual or estimated metal temperatures are used. Emergency condition movements are considered in fixing limit stops, etc., but are not used for bellows design. Normal operating pressure is used in the equation, and all possible efforts are made to locate the joint in a position where it will be subjected to the least pressure. Another change in normal practice has been to limit joint test pressures to the design value to prevent unnecessary overstressing.

When these principles are followed, it has been found practical to design expansion and hinge joints which operate within a reasonable stress range, providing the internal pressure is low (30 psi maximum), and the movement is not excessive.

High-Pressure Bellows Design

While the flat-disk-type expansion joints are widely used in low-pressure piping, they are not applicable for high-pressure service.

In view of this and the need for a high-pressure joint to operate within reasonable stresses, preliminary investigations have been made of several commercial designs for such service. Again using simple beam formulas, in combination with membrane stress relations, a qualitative comparison was made between the stresses likely to occur in each variety of high-pressure joint. Based on these comparisons, the "torus" design of joint shown in Fig. 12 was selected as offering the best possibilities for reasonably low-stress operation and so was chosen for further investigation.

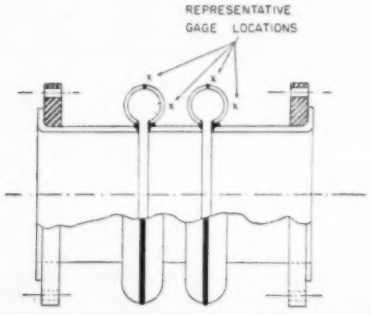

Fig. 12 Omega Joint—Design and Construction Details

To check the order of magnitude of the stresses calculated for this design, strain-gage measurements were made on an experimental joint.

Description of Equipment. The joint tested consisted of three cylindrical pipe sections $12^{13}/_{16}$ in. OD, joined by two stainless-steel torus bellows elements having semicircular cross sections. These torus sections were approximately 4.25 in. diam with 0.062-in-thick walls. The joint was stress-relieved and was rated to take 1 in. axial compression with an internal pressure of 250 psig. When received, the joint was distorted so that the flanges were not parallel by about $^3/_{16}$ in. This distortion was corrected by holding one flange and pulling the other until they became parallel. It was recognized that this procedure resulted in the introduction of unknown locked-up stresses, but it was believed the strain measurements would still indicate the type and magnitude of stresses resulting from the various tests.

For extension and compression tests, the joint was placed in the same tensile-testing machine used for the flat disk-type joint. Later, the joint was fitted with blind flanges and fittings for hydrostatic-pressure testing. It is shown in this position in Fig. 13.

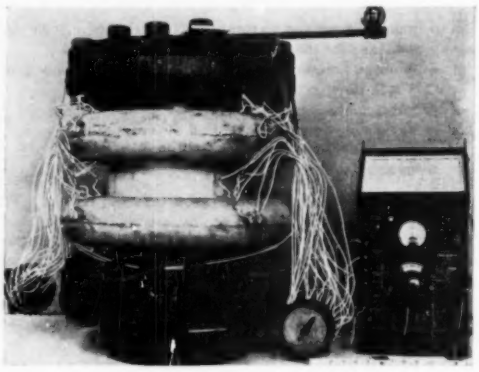

Fig. 13 Experimental Omega Joint Shown With Strain Gages and Hydraulic Fittings Attached

Out of a total of sixteen pairs of gages on the joint, eight pairs were installed on each torus. Of these eight, two pairs were placed at each quadrant designated, A, B, C, and D. One of the pairs was located as near as possible to the weld joining the sections of torus, and the other pair was placed midway between this weld and the weld joining the torus to the cylindrical portions of the joint. One gage in each pair was arranged to measure strains in a radial direction from the center of the joint (actually circumferential to a cross section of the torus), and the other was located to measure strains in a circumferential direction. Typical locations are shown in Fig. 12.

Tests and Results. The first test consisted of an axial compression of 0.38 in. When released, a permanent set of 0.16 in. remained. Further tests were then made for movements of only 0.2 in. in an attempt to secure data on operations below the elastic limit. Column 1 in Table 1 presents typical results for these tests. Columns 2 and 3 show readings taken for 0.2-in. movements at 25 and 250 psi, respectively. Column 4 indicates the effect of increasing the hydrostatic pressure from 25 psi to 250 psi while the joint was prevented from moving.

TABLE 1 TEST RESULTS

Gage location	Quadrant	Strain-gage readings,[a] microinches per in. Comp. 0.2 in. at 0 psig Column 1	Ext. 0.2 in. at 25 psig Column 2	Ext. 0.2 in. at 250 psig Column 3	Pressure increase 25 to 250 psig, no movement Column 4
Radial gages at weld	A		70	70	240
	B	—110	90	80	130
	C		80	110	150
	D	—100	60	90	110
Circumferential gages at weld	A		—60	100	100
	B	90	—80	—110	90
	C		—90	—110	120
	D	80	—80	—100	20
Radial gages at center	A		—590	—560	280
	B	210	—750	—700	240
	C		200	—670	—30
	D	—270	—820	—770	—40
Circumferential gages at center	A		560	650	160
	B	—530	—440	—480	340
	C		550	450	130
	D	—350	380	290	240

[a] Compressive strains are marked minus (—). Tensile strains are unmarked.

From a study of these data, the following conclusions seem justified:

1 Large discrepancies exist between readings on gages similarly located in different quadrants. This is believed due to irregularities in the fabrication of the torus sections.

2 Strains due to movements of as little as 0.2 in. far exceeded strains due to internal pressure of 250 psig.

3 Strains due to deflection at 25 psig showed no significant difference from those at 250 psig so long as the movement was the same.

4 When the direction of movement was reversed, strains generally reversed.

5 Contrary to results predicted from equations based upon beam theory, the maximum stresses were circumferential in direction instead of radial, and these occurred in the center portions of the torus sections rather than near the inner and outer welds.

Future Work. In spite of the somewhat disappointing results of these tests, the torus joint seems to offer good possibilities for use under relatively high pressures. Therefore further work is planned along the lines of developing a more uniformly constructed torus section and, if possible, a fairly accurate theoretical stress analysis of this design of joint.

Acknowledgment

Acknowledgment is made of the work done by Prof. J. P. Den Hartog of the Massachusetts Institute of Technology, in developing the basic stress equation and for his helpful suggestions in preparing this paper.

Acceleration of the Instant Center

By W. J. CARTER,[1] AUSTIN, TEX.

The acceleration of the members of a mechanism having a "floating link," such as that in Fig. 2, are not obtainable by the method of relative accelerations. Beskin[2] has given a solution for this problem which involves the determination of the center of trajectory of points on a connecting link. The method presented in this paper makes use of the acceleration of the instant center of velocity, the acceleration of which is dependent only on the velocity of the linkage elements. The method developed may also be used to obtain the accelerations for linkages which normally require the use of Coriolis' law.

THE four-bar linkage in Fig. 1(*a*) has two cranks, links 2 and 4, and a connecting rod, link 3. The frame of the linkage is represented by 1. Fixed centers of rotation are represented by concentric circles and pin joints, connecting moving links, by a single circle. The crossing of the extension of the center lines of links 2 and 4 define a point q_3. The point q_3 should be thought of as a moving point not on link 3. At the instant considered, q_3 defines a coincident point x_3, on link 3 extended. Point x_3 is the instant center of link 3 at this instant and has zero velocity. It is the purpose of this paper to derive a method for obtaining the linear acceleration of point x_3 and to show that the acceleration of this point is independent of the angular accelerations of any of the members of the four-bar linkage.

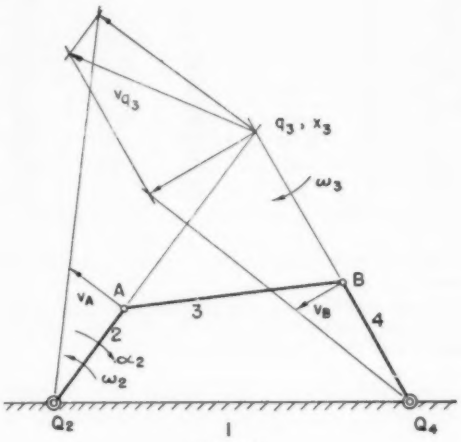

FIG. 1(*a*)

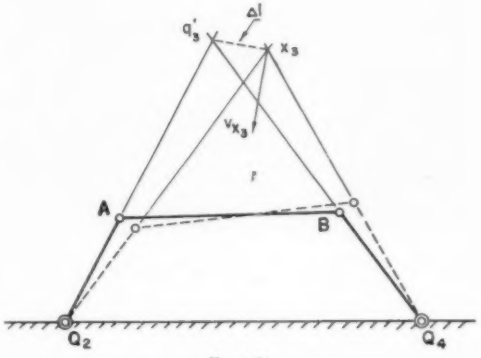

FIG. 1(*b*)

DETERMINATION OF ACCELERATION OF INSTANT CENTER

Point q_3, defined by the crossing of the extension of the center lines of links 2 and 4, has a velocity v_{q3}, which is determined in the conventional manner. After a small time interval Δt, has elapsed, the mechanism will have moved to the position shown in Fig. 1(*b*). Then q_3 will have moved to a new position q'_3 on link 3, defining a new point on link 3 as the instant center. Point x_3, the original instant center, will be a distance Δl from q'_3 and will now have a velocity v_{x3}. If ω_3 is the angular velocity of link 3 for the position in Fig. 1(*a*), the angular velocity ω'_3 for the position in Fig. 1(*b*), is found as follows

$$\omega'_3 = \omega_3 + \alpha_3 \, \Delta t$$

where α_3 is the angular acceleration of link 3 during the time interval Δt. The distance Δl, Fig. 1(*b*), is the distance between x_3 and the new instant center q'_3. The distance Δl may be found

$$\Delta l = \left(v_{q3} \; +\!\!\rightarrow \Delta v_{q3} \, \frac{\Delta t}{2} \right) \Delta t = v_{q3} \, \Delta t \; +\!\!\rightarrow \Delta v_{q3} \, \frac{\Delta t^2}{2}$$

where Δv_{q3} is the rate of change of v_{q3} in the time interval Δt. The vector-plus sign is used in the addition since v_{q3}, in general, will be changing in both magnitude and direction.

The velocity v_{x3}, may be found as the product of ω'_3 and Δl

$$v_{x3} = v_{q3} \, \Delta l(\omega_3 + \alpha_3 \, \Delta t) \; +\!\!\rightarrow \Delta v_{q3} \, \frac{\Delta t^2}{2} \, (\omega_3 + \alpha_3 \Delta t)$$

$$= (v_{q3}\omega_3 \Delta_t + v_{q3}\alpha_3 \, \Delta t^2) \; +\!\!\rightarrow \left(\Delta v_{q3}\omega_3 \, \frac{\Delta t^2}{2} + \Delta v_{q3}\alpha_3 \, \frac{\Delta t^3}{2} \right)$$

The acceleration of x_3 may be obtained by dividing v_{x3} by Δt since the velocity of x_3 was zero at the beginning of the time interval Δt

$$a_{x3} = (v_{q3} \, \omega_3 \; +\!\!\rightarrow v_{q3}\alpha_3 \Delta t) \; +\!\!\rightarrow \left(v_{q3}\omega_3 \, \frac{\Delta t}{2} + \Delta v_{q3}\alpha_3 \, \frac{\Delta t^2}{2} \right)$$

---

[1] Assistant Professor, Department of Mechanical Engineering, The University of Texas.

[2] "Simplified Method Shortens Acceleration Analysis," by Leon Beskin, *Machine Design*, vol. 16, June, 1944, pp. 113–116.

Contributed by the Applied Mechanics Division and presented at the Annual Meeting, New York, N. Y., November 27–December 2, 1949, of THE AMERICAN SOCIETY OF MECHANICAL ENGINEERS.

Discussion of this paper should be addressed to the Secretary, ASME, 29 West 39th Street, New York, N. Y., and will be accepted until July 10, 1950, for publication at a later date. Discussion received after the closing date will be returned.

NOTE: Statements and opinions advanced in papers are to be understood as individual expressions of their authors and not those of the Society. Paper No. 49—A-9.

As the time interval Δt, approaches zero, all terms except the first vanish and

$$a_{x3} = v_{q3}\omega_2 \ldots\ldots\ldots\ldots\ldots\ldots\ldots [1]$$

The direction of a_{x3} is perpendicular to v_{q3}. If the observer looks in the direction of v_{q3}, the direction of a_{x3} will be toward the right if ω_2 turns counterclockwise, and toward the left if ω_2 turns clockwise.

Equation [1] may be used to determine the acceleration of the instant center of any link in any machine. It is to be noted that Equation [1] does not involve the angular acceleration. Thus for any machine having n links, the acceleration of the n instant centers of velocity may be determined from the results of a similar velocity analysis as given. Obviously, some of the n instant centers of velocity will be fixed centers of velocity, such as Q_2 in Fig. 1(*a*) and consequently will have no acceleration.

Acceleration Analysis for Mechanism With Floating Link

The linkage in Fig. 2 has six members. Link 5 is sometimes referred to as a floating link since one end of the link, in this case point C, does not move in a circular path. If the accelerations of one of links 2, 3, or 4 are specified, the accelerations for all other parts of the linkage may be obtained by a straightforward application of the method of relative accelerations. If, however, the motions of link 6 are the given data, an acceleration analysis is impossible by means of relative accelerations alone. The difficulties encountered may be seen from an inspection of the following vector equation

$$a_C{}^n + \rightarrow a_C{}^t = a_D{}^n + \rightarrow a_D{}^t + \rightarrow a_{CD}{}^n + \rightarrow a_{CD}{}^t \ldots\ldots [2]$$

Equation [2] is the relative acceleration equation. It expresses the fact that if two points, such as C and D, are on the same link in a mechanism, the acceleration of a point C equals the acceleration of the point D plus the acceleration of C relative to D. Since the acceleration of either point may have two components, a normal component and a tangential component, the relative acceleration equation may have six terms.

Of the right-hand members of the equation, $a_{CD}{}^t$ is unknown in magnitude since a_5 is unknown, but its direction is known to be perpendicular to link 5. Of the left-hand members of the equation, nothing may be determined. The velocity of C may be determined but $a_C{}^n$ cannot be determined, since C does not move in a circular path. The direction and magnitude of $a_C{}^t$ are also unknown.

By the use of the additional condition provided by Equation [1], the solution of this problem may be found. Since points C and x_3 of the mechanism in Fig. 2 are on the same link, the following equation may be written

$$a_C{}^n + \rightarrow a_C{}^t = a_{x3} + \rightarrow a_{Cx3}{}^n + \rightarrow a_{Cx3}{}^t \ldots\ldots\ldots [3]$$

Equation [3] is the relative acceleration equation for points C and x_3.

The simultaneous solution of Equations [2] and [3] yields a_C. Once a_C is known, the acceleration of other points in links 2, 3, or 4 may be determined by conventional procedures.

Example. To demonstrate the use of the principle of Equation [1] an acceleration analysis will be made for the linkage in Fig. 2. Crank 6 has an angular velocity of 6.5 radians per sec clockwise, and an angular acceleration of 50 radians per sec^2 clockwise.

Solution. The linkage is drawn to scale. (Original, 1 in. = 1 ft.) A convenient velocity and acceleration scale is chosen. (Original, 1 in. = 6 fps and 1 in. = 36 fps^2.)

$$v_D = \omega_6 \times \overline{Q_6 D} = 6.5 \times 1.5 = 9.75 \text{ fps}$$

Knowing the velocity of D, the velocities of other parts of the linkage may be found by drawing a velocity polygon. The polygon is shown in Fig. 2(*a*). The following results are obtained from the velocity polygon

$v_A = 6.78$ fps
$v_B = 7.68$ fps
$v_C = 6.72$ fps
$v_{CD} = 7.40$ fps
$v_{AC} = 4.80$ fps

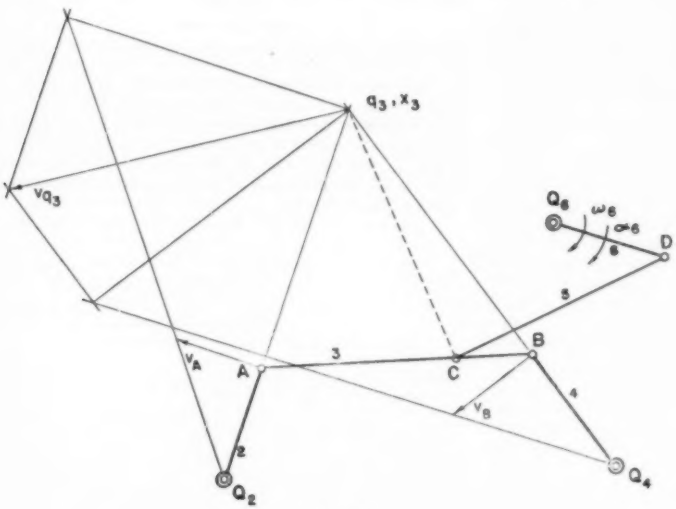

Fig. 2

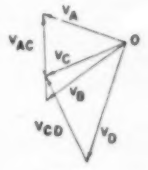

Fig. 2(*a*)

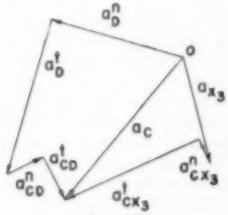

Fig. 2(*b*)

$$\omega_5 = \frac{v_{CD}}{\overline{CD}} = \frac{7.40}{3} = 2.47 \text{ radians per sec clockwise}$$

$$\omega_3 = \frac{v_{AC}}{\overline{AC}} = \frac{4.80}{2.5} = 1.92 \text{ radians per sec clockwise}$$

q_3 is located, and its velocity is determined as shown in Fig. 2

$$v_{q3} = 4.46 \times 6 = 26.8 \text{ fps}$$
$$a_{x3} = v_{q3} \times \omega_3 = 26.8 \times 1.92 = 51.5 \text{ fps}^2$$

The direction of a_{x3} is determined by the rule previously stated.

The acceleration components necessary for the simultaneous solution of Equations [2] and [3] may now be computed

$a_D^n = (\omega_6)^2 \times \overline{Q_6D} = (6.50)^2 \times 1.5 = 63.3 \text{ fps}^2$
$a_D^t = \alpha_6 \times \overline{Q_6D} = 50 \times 1.5 = 75 \text{ fps}^2$
$a_{CD}^n = (\omega_5)^2 \times \overline{CD} = (2.47)^2 \times 3 = 18.3 \text{ fps}^2$
a_{CD}^t = is unknown in magnitude but is known to be perpendicular to $\overline{CD}$
$a_{x3} = 51.5 \text{ fps}^2$
$a_{Cx3}^n = (\omega_3)^2 \times \overline{Cx_3} = (1.92)^2 \times 3.48 = 12.83 \text{ fps}^2$
a_{Cx3}^t is unknown in magnitude, but is known to be perpendicular to Cx_3

Equations [2] and [3] may now be solved by drawing the acceleration polygon, Fig. 2(*b*). The intersection of the lines representing a_{Cx3}^t and a_{CD}^t determines the end of the vector representing a_C; $a_C = 87$ fps^2. With the acceleration of C known, the acceleration of other points in the mechanism may be determined by conventional methods.

Acceleration Analysis of Quick-Return Linkage

A procedure similar to that used in solving the foregoing problem may be employed to determine the accelerations in machines having a sliding pair, such as a quick-return mechanism, shown in Fig. 3(*a*).

The motion of link 2 is specified, and it is desired to determine the angular motion of link 4. By the principle of inversion, it is known that the same relative motion results between the links if link 2 be considered fixed and ω_2 reversed is given to the frame, link 1. In Fig. 3(*b*) the inversion is shown with q_4 defining the instant center of link 4. As before, ω_4 and v_{q4} may be determined for the inverted mechanism. The product of ω_4 and v_{q4} in the inverted mechanism determines the acceleration of x_4 relative to link 2, which is fixed in the inverted mechanism.

Returning to the original linkage, Fig. 3(*a*), the acceleration of the point x_2 in link 2 extended, coincident with x_4, may be found as follows

$$a_{x2} = (\omega_2)^2 \times \overline{Q_2x_2} \; +\!\!\rightarrow \; \alpha_2 \times \overline{Q_2x_2}$$

The acceleration of x_4 may now be expressed

$$a_{x4} = a_{x2} \; +\!\!\rightarrow \; a_{x4x2} \quad \ldots\ldots\ldots\ldots\ldots\ldots\ldots\ldots [4]$$

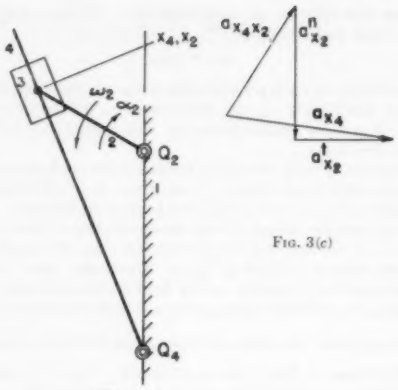

Fig. 3(*c*)

Fig. 3(*a*)

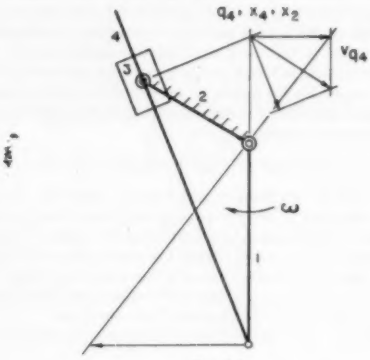

Fig. 3(*b*)

where a_{x4x2} is the product of v_{q4} and ω_4 for the inverted mechanism. It will be noted that the Coriolis' component does not need be added to the right side of Equation [4], since the relative velocity between the coincident points x_4 and x_2 is zero.

The solution of Equation [4] is shown in Fig. 3(*c*). Term α_4 may be found by taking the component of a_{x4} perpendicular to the line $\overline{Q_4x_4}$ and dividing by the distance $\overline{Q_4x_4}$. With α_4 known, the accelerations of other parts of the linkage may be determined by conventional methods.

Atomization of Liquids by Means of a Rotating Cup

By J. O. HINZE[1] and H. MILBORN[1]

Liquid, supplied through a stationary tube to the inner part of a rotating cup widening toward a brim, flows viscously in a thin layer toward this brim and is then flung off, all by centrifugal action. The flow within this layer and the disintegration phenomena occurring beyond the brim have been studied, experimentally as well as theoretically. A formula has been derived for the thickness and for the radial velocity of the liquid layer within the cup, which proved to agree reasonably well with experimental results. Three essentially different types of disintegration may take place around and beyond the edge of the cup designated, respectively, by: (*a*) the state of direct drop formation; (*b*) the state of ligament formation; and (*c*) the state of film formation. Which one of these is realized depends upon working conditions. Transition from state (*a*) into (*b*), or of state (*b*) into state (*c*) is promoted by an increased quantity of supply, an increased angular speed, a decreased diameter of the cup, an increased density, an increased viscosity, and a decreased surface tension of the liquid. The experimental results have been expressed in relationships between relevant dimensionless groups. For the state of ligament formation a semiempirical relationship has been derived between the number of ligaments and dimensionless groups determining the working conditions of the cup. Results of drop-size measurements made for the state of ligament formation as well as for the state of film formation show that atomization by mere rotation of the cup is much more uniform than commonly achieved with pressure atomizers.

Nomenclature

The following nomenclature is used in the paper:

D = maximum diameter of cup
φ_0 = semicone angle of cup
$\xi, \vartheta, \varphi, \psi$ resp. = co-ordinates used in liquid layer within cup
r = co-ordinate in radial direction
ω = angular speed of cup
v_ξ, v_ϑ, v_φ = velocity components in liquid layer
$v_{\xi(1)}$ = maximum value of v_ξ
$v_{\xi(m)}$ = mean value of v_ξ across layer
ρ = density of liquid
μ = dynamic viscosity of liquid
σ = surface tension of liquid
Q = quantity of liquid supply to cup
δ = thickness of liquid layer
p = static pressure within liquid
$\Delta\xi$ = distance between two subsequent windings of spiral described by particles in liquid layer
δ_t = thickness of liquid torus
h = distance of farthermost point of torus to edge of cup
x, ϑ = co-ordinates used in liquid torus
t = time
v_D = radial velocity at edge of cup
$v_{r(h)}$ = radial velocity at distance h from edge of cup
ζ = momentary value of a surface disturbance on liquid torus
λ = wave length of surface disturbance on liquid torus
β = logarithmic increment of surface disturbance
z = number of ligaments
δ_l = thickness of ligaments
v_l = velocity within ligament
g = gravitational acceleration
k = constant
d = diameter of drop
d_l = linear mean diameter
d_s = mean diameter by surface
d_v = mean diameter by volume
N = cumulative per cent by number
V = cumulative per cent by volume
$\bar{d}$ = absolute-size constant
q = distribution constant

Introduction

In the year preceding World War II, the rotating cup as a means of atomizing liquids had become the subject of an investigation by the Delft Laboratory in order to apply this cup in a burner for small capacities (a delivery of about 1 gph, say).

The use of a rotating cup in burners for domestic heating is well known (1, 2).[2] Besides such applications, a rotating cup is also used in other spraying devices as, for instance, for drying purposes.

After the war the investigation by the Delft Laboratory was renewed, but now carried out upon a more fundamental basis. The need for such a fundamental study, particularly concerning the mechanism of the disintegration process became apparent during the prewar investigations; no results of such a study could be traced in the literature.

Although, generally, a more or less strong blast of air in the axial direction past the cup is applied when the latter is used in a burner or in a spray drying device, the investigation has been started without such a forced air flow.

For this case, the present paper discusses the results of experimental and theoretical investigations concerning the flow of the liquid within the rotating cup and concerning various mechanisms of disintegration occurring at and beyond the edge of the cup. Drop sizes and drop-size distribution of the atomization obtained with these various mechanisms of disintegration are also discussed.

[1] "Delft" Laboratory, Royal Dutch/Shell Group, Delft, Holland.

Contributed by the Applied Mechanics Division and presented at the Semi-Annual Meeting, San Francisco, Calif., June 27–30, 1949, of The American Society of Mechanical Engineers.

Discussion of this paper should be addressed to the Secretary, ASME, 29 West 39th Street, New York, N. Y., and will be accepted until July 10, 1950, for publication at a later date. Discussion received after closing date will be returned.

Note: Statements and opinions advanced in papers are to be understood as individual expressions of their authors and not those of the Society. Paper No. 49—SA-2.

[2] Numbers in parentheses refer to the Bibliography at the end of the paper.

General Description

Liquid is supplied through a stationary tube to the inner part of a rotating cup widening toward a brim. Friction between the liquid and the wall of the cup will cause the liquid to attain the same rotational speed as that of the cup. Centrifugal forces set up in the liquid will cause a flow of liquid toward the brim of the cup. At sufficiently high angular speeds of the cup, the layer of liquid formed at the inner wall of the cup is very thin. A viscous flow of liquid toward the sharp edge of the cup is obtained. Fig. 1 illustrates, schematically, this case.

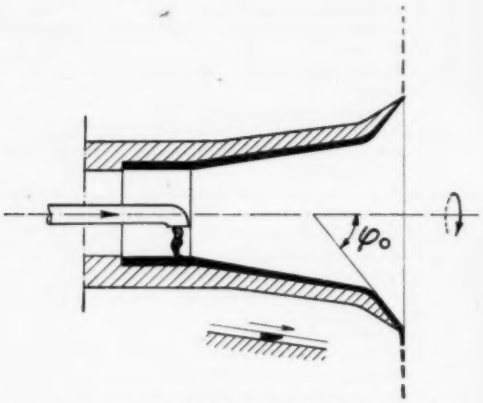

Fig. 1 Supply and Flow of Liquid Within Rotating Cup

Three essentially different types of phenomena may take place around and beyond the edge of the cup. Which one of these is realized depends on working conditions, i.e., quantity of supply, angular speed, and dimensions of the cup; and on properties of the liquid, i.e., density, viscosity, and surface tension. For a brief description of these phenomena it is sufficient to cover the case of a given cup rotating with a fixed angular speed while different quantities of the same liquid are supplied to the cup.

State I. At a very small supply rate a liquid torus is formed around the edge. The diameter of this torus is determined mainly by equilibrium conditions between centrifugal and surface-tension forces. Because of disturbances the torus will be varicosely deformed. Incidentally, drops will be formed singly at one or more bulges of the torus by the action of centrifugal forces; these drops are flung off from the edge, see Fig. 2. This phenomenon may be called "disintegration by direct drop formation."

State II. At an increased rate of supply, the state of formation of drops singly at the bulges of the torus may transit into the formation of complete thin jets or ligaments. The number of these ligaments increases with increasing rate of supply up to a maximum value, after which the number remains constant, irrespective of the rate of supply. Apparently, in this state the ligaments grow in thickness with increasing rate of supply. The ligaments themselves are unstable for disturbances and break up into drops at some distance from the edge of the cup, see Fig. 3. This phenomenon may be called "disintegration by ligament formation."

State III. Still further increasing the rate of supply, a condition is reached where the number of ligaments can increase no more, nor can they grow in thickness. The ligaments are unable to consume all the liquid supplied to the cup. The result is that, roughly speaking, the torus will be flung off the edge and a film will be formed extending to a certain distance from the edge where it breaks up in an irregular way into ligaments and clots of liquid. The thickness of the film just beyond the edge is practically equal to that of the liquid layer within the cup at the edge, see Fig. 4. This phenomenon may be called "disintegration by film formation."

Fig. 2 Disintegration by Direct Drop Formation

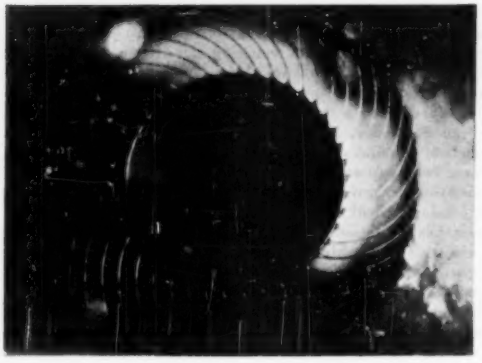

Fig. 3 Disintegration by Ligament Formation

It is recommendable to produce a liquid layer of uniform thickness within the cup, and consequently also a liquid torus or a film of uniform thickness around the circumference of the cup. In the state of ligament formation this then results in ligaments of equal thickness and equally spaced around the edge. In order to insure such a uniform thickness the following requirements must be satisfied:

1 Gravitational effects must be negligible; this means that centrifugal acceleration must be very great with respect to gravitational acceleration ($\omega^2 r > 10\ g$, say).

2 A rotation completely free from vibrations.

3 A uniform supply of liquid.

4 A supply of liquid to the cup wall at a point where the cup is only very slightly conical, preferably cylindrical.

5 A smooth surface of the wall of the cup, particularly if the liquid layer within the cup is very thin.

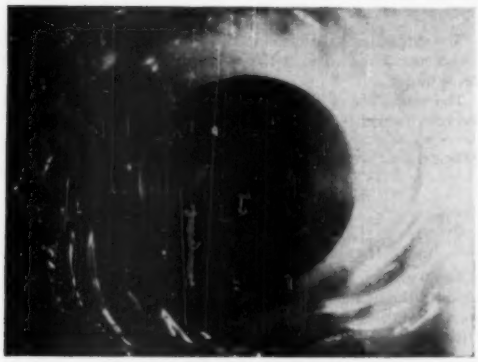

FIG. 4 DISINTEGRATION BY FILM FORMATION

DIMENSIONAL ANALYSIS

An exact theoretical treatment of the process of ligament formation and of the transition into the state of film formation seems hardly possible, seeing how complex are the boundary conditions for the flow of liquid beyond the edge of the cup in these cases. Yet it appears possible, as will be shown later on in the theoretical analysis, by simple reasoning to form a conception of the flow conditions in the state of ligament formation. With this as a base, a relationship can be derived between the number of ligaments and dimensionless groups which affect this number, in which relationship occur only two unknown parameters that can be determined easily by experiment.

It appears possible to treat in a similar way the transition of the state of ligament formation into the state of film formation.

The relevant dimensionless groups also may be obtained in a formal way by applying the well-known procedure of dimensional analysis to the quantities involved.

Thus the number of ligaments z, may be affected by the following:

1 Diameter D of brim of cup.
2 Cone angle $2\varphi_0$ of cup.
3 Angular speed ω of cup.
4 Quantity of delivery Q.
5 Density of liquid ρ.
6 Surface tension of liquid σ.
7 Dynamic viscosity of liquid μ.

Because the main variables at the experiments with a given cup are the quantity Q, the angular speed ω, and the viscosity μ, it is recommended to form the dimensionless group in such a way that each group contains only one of them. Taking the quantities D, ρ, and σ as fundamental quantities, each of the main variables Q, ω, and μ can be rendered dimensionless by them.

The result is that the general relationship between z and the dimensionless groups reads

$$z = f\left(\frac{\rho Q^2}{\sigma D^3}, \frac{\rho\omega^2 D^3}{\sigma}, \frac{\mu^2}{\rho\sigma D}, \varphi_0\right) \quad [1]$$

In a similar way one may obtain for the transition of the state of ligament formation into the state of film formation, the general relationship

$$g\left(\frac{\rho Q^2}{\sigma D^3}, \frac{\rho\omega^2 D^3}{\sigma}, \frac{\mu^2}{\rho\sigma D}, \varphi_0\right) = 0 \quad [2]$$

Dimensional analysis has not been applied to the internal flow within the cup, because for this case a solution of the hydrodynamical equation has been obtained.

CALCULATION OF FLOW IN LAYER OF LIQUID WITHIN CUP

The calculation is based on the following assumptions:

1 Thickness of the layer is very small compared with the dimensions of the cup.
2 Flow within the layer is completely viscous.
3 Flow within the cup is rotationally symmetric.

By comparing the order of magnitude of the various terms occurring in the hydrodynamical equations for viscous flow, the following may be shown:

1 The static pressure p is practically constant across the layer.
2 The velocity component v_φ is very small with respect to the component v_ξ.
3 The velocity component v_ϑ is very small with respect to the component v_ξ; this implies that the path described by any liquid particle with respect to the cup is practically straight and radial. The liquid has practically the same rotational speed as that of the cup.

Hence, with the assumption of a constant static pressure and neglecting the velocity components v_φ and v_ϑ, the equation of motion and the boundary conditions read, Fig. 5

$$\frac{\partial^2 v_\xi}{\xi^3 \partial\psi^2} + \frac{\rho\omega^2\xi}{\mu}\sin^2\varphi_0 = 0 \quad [3]$$

$$\left.\begin{aligned} v_\xi &= 0 \quad \text{at the wall} \quad (\psi = 0) \\ \frac{\partial v_\xi}{\xi\partial\psi} &= 0 \quad \text{at the free surface} \quad (\psi = \psi_1) \end{aligned}\right\} \quad [4]$$

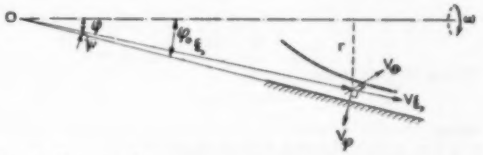

FIG. 5 VELOCITY COMPONENTS IN LAYER OF LIQUID WITHIN CUP

The solution of the differential equation, which satisfies the boundary conditions, is

$$v_\xi = \frac{\rho\omega^2}{\mu}\sin^2\varphi_0\left(\xi_1^3\psi_1\psi - \xi^3\frac{\psi^2}{2}\right)$$

where ξ_1 is the value of ξ at the free surface. The value ψ_1 is determined by the condition that the total quantity of liquid flowing through the layer toward the brim of the cup must be equal to the quantity Q supplied to the cup.

This condition gives

$$Q = \int_0^{\psi_1} 2\pi r\,\xi\,d\psi v_\xi = \frac{2\pi\rho\omega^2\xi_1^5\sin^3\varphi_0\cdot\psi_1^3}{3\mu}$$

or, with

$$\xi_1\psi_1 = \delta$$

and

$$\xi_1\sin\varphi_0 = r$$

$$Q = \frac{2\pi\rho\omega^2 r^3\delta^3\sin\varphi_0}{3\mu} \quad [5]$$

whence

$$\delta = \left(\frac{3 \mu Q}{2 \pi \rho \omega^2 r^2 \sin \varphi_0} \right)^{1/3} \quad \ldots\ldots\ldots\ldots [6]$$

The values of the maximum radial velocity $v_{\xi(0)}$ and of the mean radial velocity $v_{\xi(m)}$ are, respectively

$$v_{\xi(0)} = \left(\frac{9 \rho \omega^2 \sin \varphi_0 Q^2}{32 \pi^2 \mu r} \right)^{1/3} \quad \ldots\ldots\ldots\ldots [7]$$

and

$$v_{\xi(m)} = \left(\frac{\rho \omega^2 \sin \varphi_0 Q^2}{12 \pi^2 \mu r} \right)^{1/3} \quad \ldots\ldots\ldots\ldots [8]$$

The condition for the validity of the simplifications introduced is

$$\psi_1 << 1$$

or

$$\frac{\delta}{\xi_1} << 1$$

or

$$\left(\frac{\mu Q \sin^2 \varphi_0}{\rho \omega^2 r^5} \right)^{1/3} << 1 \quad \ldots\ldots\ldots\ldots [9]$$

When the path described by a single liquid particle with respect to the cup is considered, it has been shown that this path is practically a straight line in the radial direction. For a stationary observer, however, the path is a spiral. An identical spiral will be described by liquid supplied at a stationary point to the cup. The shape of this spiral is determined by the ratio: Rotational speed ωr divided by radial velocity v_ξ. Hence the differential equation of the spiral, if described in terms of the co-ordinates ξ and θ, is

$$\frac{d\xi}{r\, d\theta} = \frac{v_\xi}{\omega r}$$

Taking for v_ξ the value

$$v_\xi = k v_{\xi(0)}$$

where
$0 \leqslant k \leqslant 1$, the differential equation reads

$$\frac{d\xi}{d\theta} = A \xi^{-1/3}$$

where

$$A = k \left(\frac{9 \rho Q^2}{32 \pi^2 \mu \omega} \right)^{1/3}$$

The equation of the spiral then is

$$\xi = \left(\frac{4}{3} A \theta \right)^{1/4}$$

where the constant of integration has been put equal to zero.

From this expression it follows that the distance $\Delta\xi$ between two subsequent windings is equal to

$$\Delta\xi = \left(\frac{8 \pi A}{3} \right)^{1/4} = \left(k^3 \frac{16 \pi \rho Q^2}{3 \mu \omega} \right)^{1/4} \quad \ldots\ldots [10]$$

From this expression it is concluded that $\Delta\xi$ is independent of the cone angle φ_0 of the cup, and of ξ, that is, $\Delta\xi$ has a constant value from the point of supply up to the brim of the cup. The experimental determination of $\Delta\xi$ offers a possibility to check the theory.

Experimental Determination of $\Delta\xi$

The experiments pertinent to this case have been carried out with a cup having a diameter $D = 10$ cm (4 in.), and a cone angle $2\varphi_0 = 60$ deg.

The properties of the liquids used in these experiments are shown in Table 1.

TABLE 1 PROPERTIES OF LIQUIDS USED IN DETERMINING $\Delta\xi$

Liquid	Density, ρ, g-cm^{-3}	Viscosity at 60 F, μ, g-sec^{-1} cm^{-1}	Surface tension, σ, g-sec^{-2}
A	0.885	14.15	29.5
B	0.856	0.985	29.5

Fig. 6 gives an example of the spirals formed by a dyed liquid supplied through a stationary pipe. Photographs of identical spirals occurring in rotating cups have already been shown by Hickman (3).

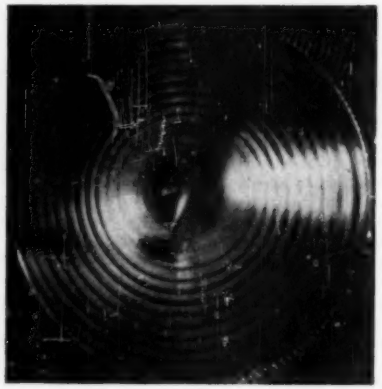

Fig. 6 Spirals Formed by Dyed Liquid Supplied From Stationary Point to Liquid Layer

In order to prevent slipping effects of the dyed liquid with respect to the original liquid layer, the end of the pipe for the dyed liquid had to be dipped into the original liquid layer at the experiments; thus the dyed liquid is introduced within the original layer. This implies that the radial velocity of the dyed liquid within the liquid layer will have a value, certainly smaller than the maximum value $v_{\xi(0)}$. Consequently, for these spirals the value of k must be smaller than unity.

Equation [10] suggests plotting the experimental data in a graph of the dimensionless group $\Delta\xi/D$ versus the dimensionless group $\rho Q^2/\mu\omega D^4$.

The mean curve through the experimental data shown in Fig. 7 is given by the equation

$$\frac{\Delta\xi}{D} = 0.95 \left(\frac{\rho Q^2}{\mu \omega D^4} \right)^{1/4} \quad \ldots\ldots\ldots\ldots [11]$$

which is qualitatively in satisfactory agreement with the predicted theoretical relationship, Equation [10]. A quantitative comparison of Equations [10] and [11] yields for k the value 0.39, which is a rather low value ($k = 0.67$, if v_ξ would be equal to $v_{\xi(m)}$).

Experimental Results Concerning Ligament Formation and Transition Into Film Formation

The experiments pertinent to this investigation have been

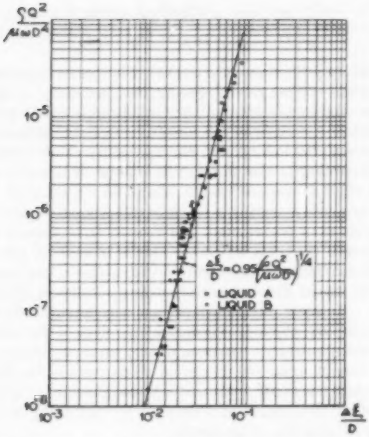

FIG. 7 EFFECT OF WORKING CONDITIONS OF CUP ON DISTANCES OF SUBSEQUENT SPIRALS

carried out with three cups of different sizes, namely, with diameters D of 1 cm (0.4 in.), 2.5 cm (1 in.), and 10 cm (4 in.), respectively; all cups have the same cone angle of $2\varphi_0 = 60$ deg. The liquids used in these experiments are given in Table 2.

TABLE 2 PROPERTIES OF LIQUIDS USED IN LIGAMENT FORMATION EXPERIMENTS

Liquid	Density, ρ, g-cm^{-3}	Viscosity at 60 F, μ, g-sec^{-1} cm^{-1}	Surface tension, σ, g-sec^{-2}
A	0.885	14.15	29.5
C	0.945	2.36	28.5
B	0.856	0.985	29.5
D	0.910	0.246	27.5
E	0.866	0.078	29.5

Each of the quantities Q and the angular speed ω have been varied to such an extent that all three of the different states, namely, the state of direct drop formation, the state of ligament formation, and the state of film formation, have been achieved.

In the following, however, we will confine ourselves to the results pertaining to the state of ligament formation, and to the transition into the state of film formation, these being of greatest importance for practical applications of the rotating cup. Moreover, in the case of ligament formation, only those data will be considered pertaining to the cases where the quantity Q has no effect on the number z of ligaments.

Fig. 8 shows the graphs where this number z has been plotted against the dimensionless group $(\rho\omega^2D^3/\sigma)^{1/2}$ with the dimensionless groups $(\mu^2/\rho\sigma D)$ and $(\rho Q^2/\sigma D^3)$ as parameters. Only the results with the 1-cm cup are given here. The results with the 2.5-cm, and 10-cm cups, and with other liquids are included in the graph in Fig. 11.

The graphs in Fig. 8 show that within the range of values of the dimensionless groups the number z indeed is practically independent of the quantity Q. The general trend shown by the data in the graphs suggests a linear relationship between the number z and the angular speed ω. As will be shown hereafter, a more detailed investigation discloses that z does not vary linearly with ω, but with the $^5/_4$ power of this speed.

In Fig. 9 the experimental data of the beginning of transition from the state of ligament formation into the state of film formation are shown. The dimensionless group $(\rho Q^2/\sigma D^3)^{1/2}$ has been plotted against the dimensionless group $(\rho\omega^2D^3/\sigma)^{1/2}$ while the

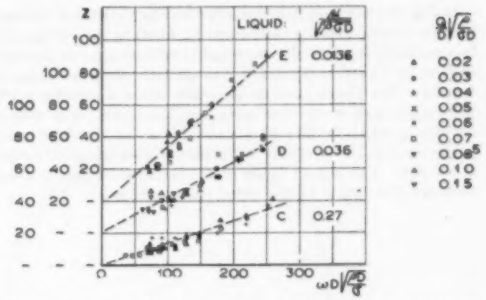

FIG. 8 NUMBER OF LIGAMENTS AS A FUNCTION OF $\omega D(D/\sigma)^{1/2}$ FOR VARIOUS VISCOSITY EFFECTS

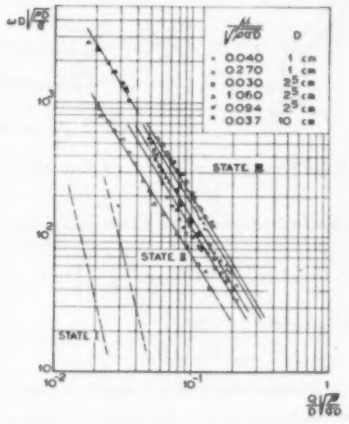

FIG. 9 TRANSITION CURVES BETWEEN STATE OF LIGAMENT FORMATION AND STATE OF FILM FORMATION

dimensionless group $(\mu^2/\rho\sigma D)$ occurs as a parameter. The figure shows that the tendency to the formation of a film is advanced by an increased value of either of the groups $\rho Q^2/\sigma D^3$, $\rho\omega^2D^4/\sigma$, and $\mu^2/\rho\sigma D$.

THEORETICAL ANALYSIS

The theoretical analysis will be based on the concept of the mechanism of the processes occurring beyond the edges of the cup, as described very roughly in the general description. At the same time we will focus our attention mainly on the state of ligament formation, particularly when the number z is independent of the quantity Q, and on the transition into the state of film formation.

According to the concept mentioned, in the state of ligament formation it is assumed that a toruslike liquid column is formed around the edge of the cup, from which torus the maximum number of ligaments originates in the case that the quantity Q has no influence on the number of ligaments. These ligaments grow in thickness with increasing quantity Q up to a maximum value, after which a transition into the state of film formation is likely to occur.

In order to estimate the thickness δ_1 of the liquid torus, the following simple reasoning will be followed. Fig. 10 shows a plausible shape for the cross section of the torus.

In Fig. 10 the liquid particles, after leaving the edge of the cup, have (*a*) a radial-velocity component v_D, which on the average will be practically equal to the mean radial velocity $v_{\xi(m)}$ at the edge as given by Equation [8], and (*b*) a tangential-velocity component $^1/_2(\omega D)$. The liquid particles generally follow a straight path, and collide against the free surface of the liquid torus with a velocity v_h, which in the case of a nonviscous liquid will be equal to the total absolute velocity of the particle just beyond the edge of the cup. The impact forces on the farthermost points of the torus are determined by the radial component $v_{r(h)}$.

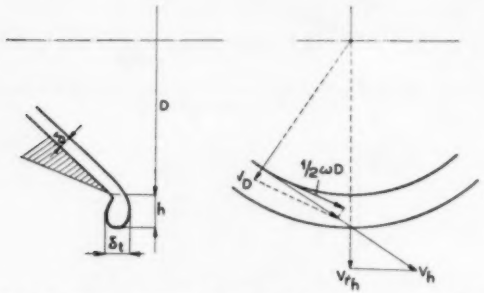

FIG. 10 FLOW CONDITIONS IN TORUS OF LIQUID AROUND EDGE OF CUP

Simple geometry shows that (for a nonviscous liquid)

$$v_{r(h)}^2 = \frac{\omega^2 D^2}{4}\left[1 - \frac{D^2}{(D+2h)^2}\right] + v_D^2$$

or because, generally, $h << D$

$$v_{r(h)}^2 \simeq \omega^2 D\, h + v_D^2 \quad \ldots\ldots [12]$$

Now, the following simplifying assumptions have been made:

1 The radius of curvature in the farthermost point of the torus is practically equal to $^1/_2(\delta_t)$.

2 The effect of the radius of curvature $^1/_2(D + 2h)$, being great with respect to $^1/_2(\delta_t)$, will be neglected.

3 The length h is proportional to δ_t, with a factor of proportionality independent of the quantity Q, the viscosity μ, and the angular speed ω. Actually, such a dependency may be expected, because it is likely that the factor of proportionality depends on the ratio δ_t/δ, which ratio is affected by the foregoing quantities.

4 In Equation [12] the term v_D^2 may be neglected with respect to the term $\omega^2 Dh$; this is justified because generally v_D is small compared with $\omega(Dh)^{1/2}$.

5 The effect of viscosity on $v_{r(h)}$ will be accounted for by a simple power law of the Reynolds number $\rho v_{r(h)}\delta_t/\mu$.

Consequently, we put

$$v_{r(h)}^2 \alpha\, \omega^2 D\delta_t \left[\frac{\rho v_{r(h)}\delta_t}{\mu}\right]^n \quad \ldots\ldots [13]$$

The condition for equilibrium between the impact forces and surface-tension forces in the farthermost points of the liquid torus yields

$$\rho v_{r(h)}^2 \alpha\, \frac{\sigma}{\delta_t} \quad \ldots\ldots [14]$$

From Relations [13] and [14], the value of δ_t can be solved, giving

$$\frac{\delta_t}{D} \alpha \left(\frac{\sigma}{\rho\,\omega^2 D^3}\right)^{\frac{2}{4+n}} \left(\frac{\mu^2}{\rho\,\sigma\,D}\right)^{\frac{n}{4+n}} \quad \ldots\ldots [15]$$

In order to determine the number z of ligaments, a simplified calculation will be given. Seeing that, generally, $\delta_t/D << 1$, and that the cross section of the torus is approximately circular, it is plausible to consider the torus as a straight column of liquid and to apply to this column the instability theory of Rayleigh (4). According to this theory, the column of liquid is unstable by the effect of surface tension alone, for disturbances of rotational symmetry, having a wave length λ greater than π times the diameter of the column. Moreover, an optimum value of wave length exists for which the rate of increase of the disturbance is a maximum, so it is likely that the column has a preference to break up in droplets corresponding to this optimum wave length. However, instability of such a column, by the effect of surface tension alone, exists only in the case of disturbances of rotational symmetry. Because disturbances of rotational symmetry cannot occur on the liquid torus considered, Rayleigh's theory does not apply. Moreover, account must be taken of the effect of the foregoing impact forces on the instability of the torus, leading to formation of ligaments.

In order to account for this latter effect, the following approximate calculation for a nonviscous liquid is given:

Assume a disturbance on the free surface of the torus of the following form

$$\zeta = \zeta^* e^{\beta t} \cos\frac{2\pi x}{\lambda} \cos s\,\vartheta \quad \ldots\ldots [16]$$

Consider the pressures acting in the farthermost points of the torus (that is, for $\vartheta = 0$).

The impact forces cause an excess pressure equal to $^1/_2(\rho\omega^2 D\zeta)$.

The excess internal pressure to accelerate the liquid may be given by

$$-\cdot \text{ number} \cdot \delta_t \rho \frac{\partial^2 \zeta}{\partial t^2}$$

The surface tension causes an excess pressure (5)

$$\sigma\left(\frac{4}{\delta_t^2} + \frac{4}{\delta_t^2}\frac{\partial^2}{\partial\vartheta^2} + \frac{\partial^2}{\partial x^2}\right)\zeta$$

The equilibrium condition at the free surface between these pressures then gives

$$-\text{number}\ \delta_t\rho\frac{\partial^2\zeta}{\partial t^2} + \frac{1}{2}\rho\omega^2 D\zeta + \sigma\left(\frac{4}{\delta_t^2} + \frac{4}{\delta_t^2}\frac{\partial^2}{\partial\vartheta^2} + \frac{\partial^2}{\partial x^2}\right)\zeta = 0 \quad \ldots\ldots [17]$$

Substitution of Equation [16] into [17] yields

$$-\text{number}\ \delta_t\rho\beta^2 + \frac{1}{2}\rho\omega^2 D + \frac{4\sigma}{\delta_t^2}\left(1 - s^2 - \frac{\pi^2\delta_t^2}{\lambda^2}\right) = 0 \quad \ldots\ldots [18]$$

The disturbance increases if β has a positive value, that is, if

$$\frac{\pi^2\delta_t^2}{\lambda^2} < \frac{\rho\omega^2 D\delta_t^2}{8\sigma} + 1 - s^2 \quad \ldots\ldots [19]$$

If all the bulges of the disturbance grow out into ligaments, the relation between the number z of ligaments and the wave length λ reads

$$z = \pi D/\lambda \quad \ldots\ldots [20]$$

The right-hand term of the Inequality [19] has approximately a constant value because δ_t is approximately inversely propor-

tional to ω; this suggests assuming a constant value for λ/δ_l. The maximum number of bulges will then be proportional to D/δ_l.

If the shape of the torus between two adjacent ligaments is visualized (see, for instance, Fig. 3), it is apparent that the maximum number of ligaments cannot be equal to the maximum number of bulges, but must have a smaller value. If it is still assumed that the minimum possible spacing for the ligaments is proportional to δ_l, so that $z \propto D/\delta_l$, one obtains from Expression [15]

$$z \propto \left(\frac{\rho\omega^2 D^3}{\sigma}\right)^{\frac{2}{4+n}} \left(\frac{\rho\sigma D}{\mu^2}\right)^{\frac{n}{4+n}} \quad \ldots\ldots\ldots [21]$$

In this expression the parameter n has to be determined by experiment. The results of the experiments made, yield a value $n \simeq 4/5$.

Fig. 11 shows a graph of the experimental data and the semiempirical relation according to Expression [21] with $n = 4/5$

$$z = 0.215 \left(\frac{\rho\omega^2 D^3}{\sigma}\right)^{5/12} \left(\frac{\rho\sigma D}{\mu^2}\right)^{1/6} \quad \ldots\ldots\ldots [22]$$

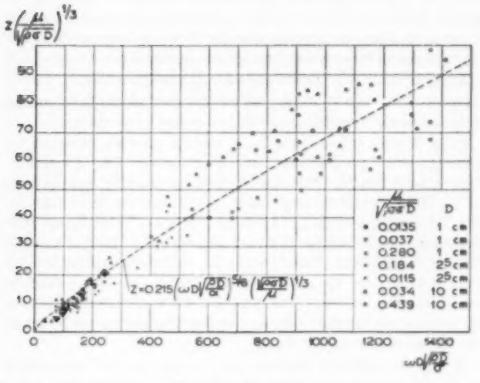

Fig. 11 Experimental Data on Number of Ligaments Grouped Around a Semiempirical Curve

The shape of the ligaments is roughly an involute. Neglecting any initial radial-velocity component, when the liquid leaves the cup edge, neglecting also any effect of resistance (external or internal) on the development of the ligament, which means, if the liquid particles persist in their initial tangential velocity, the shape of the ligament is exactly an involute. This may be elucidated by referring to Fig. 12.

Fig. 12 gives various stages of the development of one single ligament. A liquid particle which leaves at a point 1 the edge of the cup in a tangential direction, causes a protuberance in point 2. In the absence of any counteracting action the liquid particle continues its motion in the same direction with the same speed. At stage 4 the particle has reached the point A^{III}; at the same time point 1 of the edge of the cup has arrived in point 4. The liquid particle at B^I has left the edge of the cup at point 3.

Fig. 12 shows also that during the further development of the involutely shaped ligament a stretching process of the ligament takes place (the length $A^{III}B^I$ at stage 4 increases to the length $A^{IV}B^{II}$ at stage 5). Actually this stretching process will be counteracted by viscous stresses and surface tension.

For the transition into the state of film formation the (rather arbitrary) assumption is made that the maximum thickness of

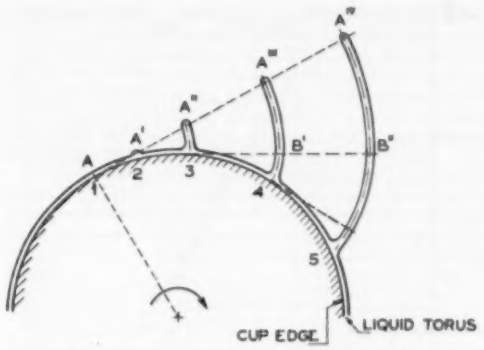

Fig. 12 Geometrical Development of Ligaments

the ligaments is roughly equal to the thickness of the torus $\delta_{l(\max)} \propto \delta_l$.

Transition occurs if

$$Q > \text{number } z\delta^2_{l(\max)}\, v_l = \text{number } z\delta_l^2 v_l \ldots\ldots [23]$$

Put

$$v_l \propto v_{r(A)} \left(\frac{\rho v_l \delta_l}{\mu}\right)^m$$

or, with Expression [14]

$$v_l \propto \sqrt{\frac{\sigma}{\rho\delta_l}} \left(\frac{\rho v_l \delta_l}{\mu}\right)^m \quad \ldots\ldots\ldots [24]$$

With $\delta_l \propto D/z$, Equations [23] and [24] yield

$$\frac{\rho Q^2}{\sigma D^3} \cdot z^{\frac{1}{1-m}} \left(\frac{\mu^2}{\rho\sigma D}\right)^{\frac{m}{1-m}} > \text{number} \ldots\ldots [25]$$

Taking for z the Relation [22], Expression [25] becomes

$$\frac{\rho Q^2}{\sigma D^3} \cdot \left(\frac{\rho\omega^2 D^3}{\sigma}\right)^{\frac{7}{16(1-m)}} \left(\frac{\mu^2}{\rho\sigma D}\right)^{\frac{8m-1}{8(1-m)}} > \text{number} \ldots [26]$$

The graph in Fig. 13 shows that the Relation [26] fits quite well the trend shown by the experimental data if $m \simeq 0.25$; the equation of the curve in Fig. 13, corresponding to the Relation [26] reads

$$\frac{\rho Q^2}{\sigma D^3} \left(\frac{\rho\omega^2 D^3}{\sigma}\right)^{0.438} \left(\frac{\mu^2}{\rho\sigma D}\right)^{0.188} = 1.77 \ldots\ldots [27]$$

Atomization

It is plausible that the atomization of the liquid, as a result of the disintegration process, will be different for the three different states of disintegration. In the state of direct formation of droplets, the droplets are formed singly from protuberances originating from the bulges of the varicosely deformed liquid torus around the edge of the cup. The moment at which the droplets are split off from these protuberances generally will be different for the various droplets; this means that the protuberances will have different thicknesses and heights at the moment of splitting off a droplet. Consequently the various droplets will not have the same size; it is likely, however, that they will have a diameter roughly of the same magnitude as the thickness

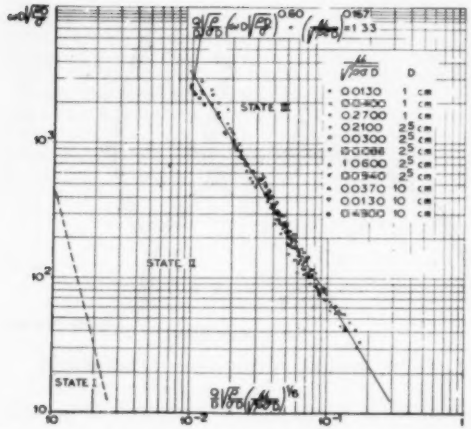

FIG. 13 EXPERIMENTAL DATA ON TRANSITION OF STATE II INTO STATE III AS GROUPED AROUND A SEMIEMPIRICAL CURVE

of the liquid torus; the Expression [15] may then serve as a rough estimation of the mean drop size.

In the state of ligament formation, the ligaments break up into droplets by disturbances of rotational symmetry. This process of breaking up, identical with that of a straight liquid column and agreeing with Rayleigh's instability theory, is clearly shown in Fig. 3.

If all the ligaments have the same diameter, if they all break up at the same distance from the edge of the cup, if this occurs by disturbances with the optimum value of wave length, and if there is no effect of the stretching process of the ligaments on their breaking up, all droplets formed would have the same diameter.

Actually, the drops are not all of equal size. The reason is mainly that not all ligaments break up at the same distance from the edge of the cup, so that the diameter of the ligaments at the place of breaking up is unequal for various ligaments. Also, breaking up occurs very often by singular disturbances not according to the optimum wave length. Fig. 3 shows a few cases of breaking up by such singular disturbances. Particularly in the latter case, the stretching process of the ligament causes bigger drops to form than according to optimum wave length, a thin thread of liquid at the same time trailing behind. This thin thread of liquid breaks up into very small droplets. The effect on atomization is that in a few cases, the distribution curve by number of drop sizes shows two definite peaks pointing to two definite size groups.

Nevertheless, the atomization is still more uniform if compared with results obtained with other methods of disintegration.

In the state of film formation, air forces and other disturbing forces deform the film, tears arise, and surface-tension action causes disruption into many irregular ligaments and clots of liquid, the latter mostly interconnected by thin threads of liquid which break up in fine droplets. It is reasonable to expect, generally, a less uniform atomization than that occurring in the state of ligament formation. Because this less uniformity is mainly caused by a greater number of drops of very small size, the difference between both atomizations will be more pronounced if distribution curves by number are compared. In order to find a simple measure for the uniformity of the distribution of drop sizes, the distribution curves have been approximated by the mathematical equation first applied to distribution curves of powdered coal by Rosin and Rammler (5, 6). For the distribution curves by number and by volume, respectively, the equation reads

$$N = 100e^{-(d/\bar{d}_n)^{q_n}} \quad \ldots\ldots\ldots\ldots\ldots\ldots [28]$$

and

$$V = 100e^{-(d/\bar{d}_v)^{q_v}} \quad \ldots\ldots\ldots\ldots\ldots\ldots [29]$$

where N is the cumulative per cent by number of drops of diameter greater than d; V is the cumulative per cent by volume of drops of diameter greater than d; $\bar{d}$ and q, respectively, are the "absolute size constant," and the "distribution constant."

A higher value of q implies a more uniform atomization.

Distribution curves of drop sizes have been obtained by means of the well-known catching method on sooted glass plates (7).

Table 3 gives a few examples of the atomization obtained by disintegration by ligament formation and by film formation. This table shows that, for distribution by number, atomization by ligament formation is generally more uniform than that by film formation (compare the values of q_n). This lesser uniformity by film formation is mainly caused by the greater number of small droplets, the effect of which on the distribution by volume is very small; so the reverse conclusion is sometimes reached concerning the uniformity of atomization if distribution curves by volume are compared instead of distribution curves by number (compare the values of q_v).

It may be useful to mention that in the case of atomization by means of pressure nozzles, the distribution constants q_v generally vary between 2 and 3, which denotes a much less uniform atomization.

The various mean diameters given in Table 3 are defined as follows:

Linear mean diameter

$$d = \frac{\Sigma nd}{\Sigma n}$$

Mean diameter by surface

$$d_s = \left(\frac{\Sigma nd^2}{\Sigma n}\right)^{1/2}$$

TABLE 3 EXAMPLES OF ATOMIZATION

Liquid	$\frac{\mu}{\sqrt{\rho\sigma D}}$	$\frac{Q}{D}\sqrt{\frac{\rho}{\sigma D}}$	$\omega D\sqrt{\frac{\rho D}{\sigma}}$	d_l micr.	d_s micr.	d_v micr.	SMD micr.	$\bar{d}_n$ micr.	q_n	$\bar{d}_v$ micr.	q_v
				LIGAMENT FORMATION							
D	0.028	0.0314	1130	42	49	55	71	51	2.86	95	4.32
D	0.0134	0.0233	2140	66	88	103	134	71	2.07	156	8.66
D	0.0134	0.0171	2610	66	80	89	111	71	2.48	130	8.00
B	0.0374	0.0068	2450	73	88	98	120	83	2.60	140	9.4
				FILM FORMATION							
D	0.028	0.070	1130	65	83	97	144	73	2.24	164	7.25
D	0.0134	0.0383	2610	66	88	109	140	64	1.88	166	8.55
B	0.0374	0.0234	2450	61	87	116	154	58	1.55	180	7.85

Mean diameter by volume

$$d_v = \left(\frac{\Sigma n d^3}{\Sigma n}\right)^{1/3}$$

Sauter mean diameter

$$SMD = \frac{\Sigma n d^3}{\Sigma n d^2}$$

Until now the effect of air flow relative to the liquid flung off by the cup has been considered only in so far as it plays a part on the deformation of the film. This is because at low circumferential speeds of the cup, say, below 15 m per sec (40 fps), the effect of air forces on splitting up of drops and on the break-up of ligaments is very small. At appreciably greater circumferential speeds, say, 30 m per sec (100 fps) and greater, however, air forces substantially affect atomization. Ultimately, at extremely high circumferential speeds, atomization will be determined predominantly by the air forces, eventually reaching the state of so-called true air atomization.

As has already been mentioned, in many technical appliances an additional blast of air in the axial direction past the edge of the cup is used. This blast of air may affect appreciably atomization. Particularly in the state of film formation where breaking up by mere rotation of the cup would take place at a certain distance beyond the edge of the cup, the additional forced air flow causes atomization within this distance. It is evident that then the results of atomization given in the foregoing do not hold.

Final Remarks

It may be noticed from the various graphs given that the experimental data show a rather great spread with respect to a general law which they tend to follow, and which laws obtained a physical meaning by the theoretical analysis. Particularly the scatter of the number of ligaments z is striking (see Fig. 11). This, however, becomes quite obvious if one visualizes that there is more than one possibility for the liquid to be carried off the cup through the ligaments, namely, by either an increase in number or an increase of thickness, or by both. In fact, the number of ligaments tends to persist, if the angular speed of the cup is varied, even within wide limits. Moreover, the theories developed and based upon simplifying assumptions show clearly the many possibilities for deviations from the general relationship resulting from those theories.

Notwithstanding all that, the experimental data, statistically stated, are in fair agreement with the theoretically predicted relations; this justifies the conclusion that the actual mechanism of the processes would appear to be mainly in agreement with the concept underlying the hypotheses and assumptions made in the theory.

Acknowledgment

The authors express their thanks to N. V. De Bataafsche Petroleum Maatschappij (Royal/Dutch Shell Group) for permission to publish this paper.

BIBLIOGRAPHY

1 "Oil Burning," by H. A. Romp, Martinus Nijhoff, The Hague, Netherlands, 1937.

2 "New Ways of Burning Liquid Fuel," by W. L. van de Putte and H. K. J. van den Bussche. Paper read before the World Power Conference at The Hague, Sept. 2–9, 1947.

3 "High-Vacuum Short-Path Distillation. A Review," by K. C. D. Hickman, *Chemical Reviews*, vol. 34, 1944, p. 70.

4 "Hydrodynamics," by H. Lamb, Dover Publications, New York, N. Y., sixth edition, 1945, p. 472.

5 "The Laws Governing the Fineness of Powdered Coal," by P. O. Rosin and E. Rammler, *Journal of the Institute of Fuel*, vol. 7, 1933–1934, p. 29.

6 "Methods of Representing Distribution of Particle Size," by J. B. Austin, *Industrial and Engineering Chemistry*, Analytical Edition, vol. 11, 1939, p. 334.

7 "The Effect of Nozzle Design and Operating Conditions on the Atomization and Distribution of Fuel Sprays," by D. W. Lee, NACA Report No. 425, 1932.

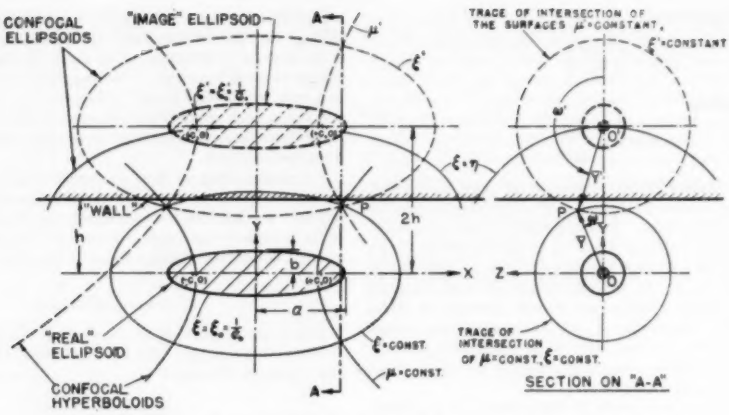

FIG. 1 MODEL FOR CALCULATING FLOW ABOUT AN ELLIPSOID NEAR A PLANE WALL

An Approximate Solution for Incompressible Flow About an Ellipsoid Near a Plane Wall[1]

BY PHILLIP EISENBERG,[2] WASHINGTON, D. C.

Using the method of successive images, an approximate solution for the velocity potential is obtained in closed form for incompressible flow about an ovary ellipsoid near a plane wall. The velocity distribution is computed from this solution in two ways. The first computation properly predicts differences in velocities on opposite half-meridians of the ellipsoid. A second method results in a symmetric velocity distribution but is useful for rapid estimates of the average wall effect. Pressure distributions calculated by this theory are compared with values measured on 4:1 and 6:1 ellipsoid models.

INTRODUCTION

THE inherent difficulties in obtaining the solution for the flow about arbitrary bodies of revolution near a plane wall usually preclude an exact evaluation of the effect of wall proximity on the pressure distribution. However, in many engineering applications it may be sufficient to replace the actual body with an ovary ellipsoid as an approximation. For this purpose, it is desired to obtain an approximate solution for the velocity potential for the flow about an ellipsoid near a plane wall.

Using the method of successive images, the evaluation of the image potentials or potentials of the equivalent source distributions) and the restoring images will be approximated by expansions in series which are equivalent to rectilinear flows. The velocity distributions will be derived in two ways, the first of which properly predicts differences in velocities on opposite half meridians of the ellipsoid. The second computation, which corresponds to an expansion in associated Legendre polynomials of zero order, results in a symmetric distribution, but is useful for rapid estimates of the average wall effect, and corresponds most closely to the distribution on the meridian parallel to the wall.

The solution is obtained in closed form with expressions for the velocity distributions that may be easily applied to specific cases. The applicability of the solution was tested by measurements of the pressure distributions on two ellipsoid models. Comparisons of the calculated and measured values for the models at various distances from a single wall are included.

DERIVATION OF THE VELOCITY POTENTIAL

The potential flow about an ellipsoid near a plane wall is known if the flow is known for the case of two ellipsoids of the same size moving abreast at the same speed. Here the plane of symmetry between the two forms is a stream surface and may be replaced by a solid "wall" without disturbing the motion.

The model used for the computation is shown in Fig. 1, wherein the unprimed ellipsoidal co-ordinates refer to the "real" ellipsoid and the primed co-ordinates refer to the "image" ellipsoid. The origin of co-ordinates is chosen to coincide with the center of the real ellipsoid having foci in Cartesian co-ordinates placed at $x =$

---

[1] This paper is abstracted from a thesis in partial fulfillment of the requirements for the Professional Degree of Civil Engineer, California Institute of Technology, Pasadena, Calif., May, 1948.

[2] David Taylor Model Basin.

Contributed by the Applied Mechanics Division and presented at the Annual Meeting, New York, N. Y., November 27–December 2, 1949, of THE AMERICAN SOCIETY OF MECHANICAL ENGINEERS.

Discussion of this paper should be addressed to the Secretary, ASME, 29 West 39th Street, New York, N. Y., and will be accepted until July 10, 1950, for publication at a later date. Discussion received after the closing date will be returned.

NOTE: Statements and opinions advanced in papers are to be understood as individual expressions of their authors and not those of the Society. Paper No. 49—A-7.

$*c$, $y = z = 0$. The ovary ellipsoidal co-ordinates, μ, ξ, ω, are then defined by the set of equations

$$\left.\begin{aligned} x &= c\mu\xi \\ \bar{y} &= c\sqrt{(1-\mu^2)(\xi^2-1)} \\ \omega &= \omega \end{aligned}\right\} \quad \ldots\ldots\ldots\ldots [1]$$

It is clear that $\bar{y}$ is the distance perpendicular to the x-direction in the meridional plane $\omega = \text{const}$, and that the Cartesian co-ordinate $y = \bar{y}\cos\omega$. The surfaces $\xi = \text{const}$ constitute a set of ellipsoidal surfaces confocal with the real ellipsoid and having semimajor axes equal to $c\xi$ and semiminor axes equal to $c\sqrt{\xi^2-1}$. The surfaces $\mu = \text{const}$ are a set of confocal hyperboloids with foci at $x = \pm c$ and semiaxes $c\mu$ and $c\sqrt{1-\mu^2}$. It is readily shown that the equation of continuity in these co-ordinates is

$$\frac{\partial}{\partial\mu}\left[(1-\mu^2)\frac{\partial\Phi}{\partial\mu}\right] + \frac{\partial}{\partial\xi}\left[(\xi^2-1)\frac{\partial\Phi}{\partial\xi}\right] + \frac{\xi^2-\mu^2}{(1-\mu^2)(\xi^2-1)}\frac{\partial^2\Phi}{\partial\omega^2} = 0 \quad \ldots\ldots\ldots [2]$$

where Φ is the velocity potential of the entire flow (1, 2).[3]

The ellipsoids, which have semimajor diameters a, and semiminor diameters b, are assumed to be separated by a distance $2h$. From Equation [1] and the triangle $OO'P$ in Fig. 1, it is seen that the two co-ordinate systems are related by

$$x = c\mu\xi = c\mu'\xi' \quad \ldots\ldots\ldots\ldots [1a]$$

and

$$\bar{y}'^2 = \bar{y}^2 + 4h^2 - 4h\bar{y}\cos\omega \quad \ldots\ldots\ldots\ldots [3]$$

The solution of Equation [2] for the flow about an ovary ellipsoid moving parallel to its major axis in a fluid of infinite extent, which forms the starting point of the present investigation, is given by Lamb (1). The boundary condition at the surface of the ellipsoid, $\xi = \xi_0 = 1/e_0$, where e_0 is the eccentricity of the ellipsoid, is

$$\frac{\partial\Phi}{\partial\xi} = -U\frac{\partial x}{\partial\xi} = -Uc\mu \quad \ldots\ldots\ldots\ldots [4]$$

where U is the velocity of the body. With this condition and the condition that the fluid be stationary at infinity, the solution is

$$\Phi_\infty = AP_1(\mu)Q_1(\xi) = A\mu\left(\frac{1}{2}\,\xi\ln\frac{\xi+1}{\xi-1} - 1\right) \quad \ldots [5]$$

where

$$A = Uc\left(\frac{e_0}{1-e_0^2} - \frac{1}{2}\ln\frac{1+e_0}{1-e_0}\right)^{-1} \quad \ldots\ldots\ldots [6]$$

This solution is given in terms of the so-called zonal surface harmonics of the first kind or Legendre coefficients $P_n(\mu)$, and the zonal harmonics of the second kind, $Q_n(\xi)$, in each case (3) with $n = 1$. In this case the flow pattern is symmetrical with respect to any axis of the ellipsoid.

The velocity potential Φ, which is a solution of Equation [2] for the flow about two ellipsoids, may be written in the form

$$\Phi = \varphi + \varphi' \quad \ldots\ldots\ldots\ldots [7]$$

where the potential φ is the solution of the problem of the real ellipsoid passing a stationary image, and φ' is the solution for the image passing the stationary real ellipsoid, both evaluated at the instant the ellipsoids are abreast. In order that the model be undeformed, there must be no crossflow through the surfaces of the two ellipsoids. This requirement and the boundary condition, Equation [4], impose the boundary conditions on the real ellipsoid, $\xi = \xi_0 = 1/e_0$

$$\frac{\partial\varphi}{\partial\xi} = -Uc\mu, \quad \text{and} \quad \frac{\partial\varphi'}{\partial\xi} = 0 \quad \ldots\ldots\ldots [8]$$

and on the image ellipsoid, $\xi' = \xi_0' = 1/e_0$

$$\frac{\partial\varphi}{\partial\xi'} = 0 \quad \text{and} \quad \frac{\partial\varphi'}{\partial\xi'} = -Uc\mu' \quad \ldots\ldots\ldots [9]$$

The exact solution of the present problem can be accomplished by an expansion of Φ in the associated Legendre (4) polynomials, $P_n^m(\mu)$, $P_n^m(\xi)$, and $Q_n^m(\xi)$, since this case is not one of symmetry in the sense of the single ellipsoid in an infinite stream. However, the extreme complexity of the expressions which must be considered in the evaluation of the successive images by such an exact expansion, if not entirely impracticable, will certainly lead to very unwieldy expressions with a resultant loss in attractiveness for applications. As a result, a procedure has been adopted which leads to an approximate solution that approaches the exact solution in the limit as the ellipsoid recedes from the wall. This approximation is essentially an evaluation in a power series of associated Legendre polynomials but with $n = 1$ and $m = 0$.

Starting with the solution for the flow about an ellipsoid in an infinite stream, Equation [5], the potential function φ in the neighborhood of the image, assuming for the moment that the image is at rest, is, with the aid of Equation [1a]

$$\varphi_1 = A\frac{\mu'\xi'}{\xi}\left(\frac{1}{2}\,\xi\ln\frac{\xi+1}{\xi-1} - 1\right) \quad \ldots\ldots\ldots [10]$$

In place of an exact evaluation of φ_1 over the surface of the image, assume, instead, that the image ellipsoid lies entirely on a portion of the ellipsoidal surface confocal with the real ellipsoid[4] and which passes through the center of the image. The semiminor diameter of this surface is $c\sqrt{\xi^2-1} = 2h$, so that, since $c = ae_0$

$$\xi = \sqrt{1 + \frac{4}{e_0^2}\left(\frac{h}{a}\right)^2} = \eta \text{ (say)} \quad \ldots\ldots\ldots [11]$$

Therefore, in the neighborhood of the image, the induced velocity potential due to the real ellipsoid is, approximately

$$\varphi_1 = A\mu'\xi'\left(\frac{1}{2}\ln\frac{\eta+1}{\eta-1} - \frac{1}{\eta}\right) \quad \ldots\ldots\ldots [12]$$

This potential produces a normal velocity on the surface of the image proportional to

$$\frac{\partial\varphi_1}{\partial\xi'} = A\mu'\left(\frac{1}{2}\ln\frac{\eta+1}{\eta-1} - \frac{1}{\eta}\right) \quad \ldots\ldots\ldots [13]$$

It is easily verified that the term Equation [13] is canceled by addition of the potential

[3] Numbers in parentheses refer to the Bibliography at the end of the paper.

[4] This method of approximation is somewhat analogous to the first steps in the solution shown by Lamb (1) for the flow about two spheres. However, to the same degree of approximation, the present solution might be expected to give better comparative results, since the image ellipsoid "fits" the ellipsoidal surface confocal with the real ellipsoid better than the image sphere on the spherical surface concentric with the real sphere. Of course as $e_0 \to 0$, this advantage disappears.

$$\varphi_1' = -A\mu' \left(\frac{\frac{1}{2}\ln\frac{\eta+1}{\eta-1} - \frac{1}{\eta}}{\frac{1}{2}\ln\frac{1+e_0}{1-e_0} - \frac{e_0}{1-e_0^2}} \right) \left(\frac{1}{2}\xi' \ln\frac{\xi'+1}{\xi'-1} - 1 \right) \quad [14]$$

and that φ_1' satisfies the equation of continuity. Equation [14] represents the potential of the first equivalent source image in the image ellipsoid.

Using the assumption, Equation [11], the potential φ_1', in the neighborhood of the real ellipsoid, takes on the value

$$\varphi_1' = -A\mu\xi \frac{\left(\frac{1}{2}\ln\frac{\eta+1}{\eta-1} - \frac{1}{\eta}\right)^2}{\left(\frac{1}{2}\ln\frac{1+e_0}{1-e_0} - \frac{e_0}{1-e_0^2}\right)} \quad [15]$$

which, in turn, is canceled by the potential

$$\varphi_2 = A\mu \left(\frac{\frac{1}{2}\ln\frac{\eta+1}{\eta-1} - \frac{1}{\eta}}{\frac{1}{2}\ln\frac{1+e_0}{1-e_0} - \frac{e_0}{1-e_0^2}} \right)^2 \left(\frac{1}{2}\xi \ln\frac{\xi+1}{\xi-1} - 1 \right) \quad [16]$$

The law of formation of the successive images is now clear. Remembering that an exactly similar process must be carried through, starting with the image ellipsoid and holding the real ellipsoid at rest, the potential function for the entire flow, after evaluating all the images in the foregoing manner is, approximately

$$\Phi = \varphi + \varphi' = A\left[\mu\left(\frac{1}{2}\xi \ln\frac{\xi+1}{\xi-1} - 1 \right) + \mu'\left(\frac{1}{2}\xi' \ln\frac{\xi'+1}{\xi'-1} - 1 \right) \right] \times \sum_{\lambda=0}^{\infty} (-1)^\lambda \left(\frac{\frac{1}{2}\ln\frac{\eta+1}{\eta-1} - \frac{1}{\eta}}{\frac{1}{2}\ln\frac{1+e_0}{1-e_0} - \frac{e_0}{1-e_0^2}} \right)^\lambda \quad [17]$$

For the infinite series to be absolutely convergent, it is sufficient to require only that $1/\eta > e_0$, since, from Equation [11], $\eta^2 \geq 1$ for all values of h/a, and $0 \leq e_0 \leq 1$, i.e., the series converges absolutely for all values

$$\frac{h}{a} > \frac{1}{2}\sqrt{1-e_0^2} \quad [18]$$

Furthermore, with this requirement, the solution converges everywhere on all ellipsoids $0 \leq e_0 \leq 1$ and everywhere in the field.

Finally, by applying the formula for the sum of an absolutely convergent geometric series, and putting in the value of the constant A from Equation [6], the expression

$$\Phi = -Uc \left[\frac{\mu\left(\frac{1}{2}\xi \ln\frac{\xi+1}{\xi-1} - 1 \right) + \mu'\left(\frac{1}{2}\xi' \ln\frac{\xi'+1}{\xi'-1} - 1 \right)}{\frac{1}{2}\ln\left(\frac{\eta+1}{\eta-1}\right)\left(\frac{1+e_0}{1-e_0}\right) - \left(\frac{e_0}{1-e_0^2} + \frac{1}{\eta}\right)} \right] \quad [19]$$

is obtained. This is the desired approximate solution for the velocity potential of the flow about an ellipsoid near a plane wall.

Derivation of Pressure Distribution

To determine the pressure distribution on the real ellipsoid, it is convenient to carry out the computation in Cartesian coordinates. Let

$$\alpha = 1 + \left(\frac{x}{c}\right)^2 + \left(\frac{y}{c}\right)^2 + \left(\frac{z}{c}\right)^2 \quad [20]$$

$$\beta = \sqrt{\alpha^2 - 4\left(\frac{x}{c}\right)^2} \quad [21]$$

$$\gamma = \alpha + 4\left(\frac{h}{c}\right)^2 - 4\frac{hy}{c^2} \quad [22]$$

$$\zeta = \sqrt{\gamma^2 - 4\left(\frac{x}{c}\right)^2} \quad [23]$$

With this notation

$$\xi = \sqrt{\frac{\alpha+\beta}{2}} \quad [24]$$

and

$$\xi' = \sqrt{\frac{\gamma+\zeta}{2}} \quad [25]$$

Superposing a uniform velocity potential to transform the motion to one of flow past a stationary model, the equation of the potential becomes[b]

$$\Phi_1 = Ux + BU\frac{x}{c}\left[\frac{1}{2}\ln\left(\frac{\xi+1}{\xi-1}\right)\left(\frac{\xi'+1}{\xi'-1}\right) - \left(\frac{1}{\xi} + \frac{1}{\xi'}\right) \right] \quad [26]$$

where

$$B = -c\left[\frac{1}{2}\ln\left(\frac{\eta+1}{\eta-1}\right)\left(\frac{1+e_0}{1-e_0}\right) - \left(\frac{e_0}{1-e_0^2} + \frac{1}{\eta}\right) \right]^{-1} \quad [27]$$

The velocity components in the direction of increasing x, y, and z are, then

$$\left.\begin{aligned} \frac{u_x}{U} &= -\frac{1}{U}\frac{\partial\Phi_1}{\partial x} = -1 - \frac{B}{c}\left[\frac{1}{2}\ln\left(\frac{\xi+1}{\xi-1}\right)\left(\frac{\xi'+1}{\xi'-1}\right) - \left(\frac{x}{c}\right)^2\left(\frac{1}{\beta\xi^2} + \frac{1}{\zeta\xi'^2}\right) - \left(\frac{1}{\xi} + \frac{1}{\xi'}\right) \right] \\ \frac{u_y}{U} &= -\frac{1}{U}\frac{\partial\Phi_1}{\partial y} = \frac{B}{c}\left(\frac{x}{c}\right)\left\{ \frac{y}{c}[\beta(\xi^2-\xi)]^{-1} + \left(\frac{y}{c} - 2\frac{h}{c}\right)[\zeta(\xi'^2-\xi')]^{-1} \right\} \\ \frac{u_z}{U} &= -\frac{1}{U}\frac{\partial\Phi_1}{\partial z} = \frac{B}{c}\left(\frac{x}{c}\right)\left(\frac{z}{c}\right)\{[\beta(\xi^2-\xi)]^{-1} + [\zeta(\xi'^2-\xi')]^{-1}\} \end{aligned}\right\} \quad [28]$$

[b] This procedure is equivalent to finding correctly the effects of each image potential but carrying out the successive cancellations by means of the approximation $\xi' = \eta$, $\mu' = \mu\xi/\eta$.

The pressure distribution, in nondimensional form, is

$$\frac{p-p_\infty}{\frac{1}{2}\rho U^2} = 1-\left[\left(\frac{u_x}{U}\right)^2+\left(\frac{u_y}{U}\right)^2+\left(\frac{u_z}{U}\right)^2\right] \quad \ldots\ldots[29]$$

where p is the pressure at the surface of the ellipsoid, p_∞ is the pressure in the undisturbed stream, and ρ is the mass density of the fluid.

To calculate the pressure distribution on any ellipsoid surface confocal with the real ellipsoid, it is only necessary to replace e_0 by e and ξ by $1/e$ where e is the eccentricity of the confocal ellipsoid. In addition, the values of α and β reduce to

$$\alpha_{\xi=\frac{1}{e}} = \frac{1}{e^2}+\left(\frac{x}{a}\right)^2$$

and

$$\beta_{\xi=\frac{1}{e}} = \frac{1}{e^2}-\left(\frac{x}{a}\right)^2$$

Otherwise, the substitutions, Equations [20] through [25], must be used.

Derivation of an "Average" Pressure Distribution

To the same degree of approximation as the original calculation of the image effects, the potential, Equation [19], with a superposed uniform flow, is

$$\Phi_2 = U\mu\left\{c\xi+B\left[\frac{1}{2}\ln\left(\frac{\xi+1}{\xi-1}\right)\left(\frac{\eta+1}{\eta-1}\right)-\left(1+\frac{\xi}{\eta}\right)\right]\right\} \quad \ldots\ldots[30]$$

Since this function is essentially an expansion in a series of $P_1(\mu)\,Q_1(\xi)$, the velocity field will be a symmetric one. Nevertheless, Φ_2 may be expected to give an approximately correct average distribution over the entire surface, and, because of the simplicity of the expression for the pressure distribution, appears worth while for rapid estimates of an average wall effect. This approximation will underestimate the effects near the center and overestimate toward the two ends. That this is the case can be seen from the fact that the expansion of images by approximations of the type, Equation [12], is equivalent to a rectilinear flow, which evidently will give velocities that are too low at the center and too high at the leading and trailing ends. In general, it might be expected that the velocity distribution will most closely approximate that along the meridian parallel to the wall.

The velocity components in the direction of increasing μ, ξ, and ω, in the neighborhood of the real ellipsoid, are

$$\left.\begin{aligned}
\frac{u_\mu}{U} &= -\frac{1}{Uc}\sqrt{\frac{1-\mu^2}{\xi^2-\mu^2}}\frac{\partial\Phi_2}{\partial\mu} = -\sqrt{\frac{1-\mu^2}{\xi^2-\mu^2}}\left\{\xi\right.\\
&\quad\left.+\frac{B}{c}\left[\frac{1}{2}\xi\ln\left(\frac{\xi+1}{\xi-1}\right)\left(\frac{\eta+1}{\eta-1}\right)-\left(1-\frac{\xi}{\eta}\right)\right]\right\}\\
\frac{u_\xi}{U} &= -\frac{1}{Uc}\sqrt{\frac{\xi^2-1}{\xi^2-\mu^2}}\frac{\partial\Phi_2}{\partial\xi} = -\sqrt{\frac{\xi^2-1}{\xi^2-\mu^2}}\\
&\quad\left\{1+\frac{B}{c}\left[\frac{1}{2}\ln\left(\frac{\xi+1}{\xi-1}\right)\left(\frac{\eta+1}{\eta-1}\right)-\left(\frac{\xi}{\xi^2-1}+\frac{1}{\eta}\right)\right]\right\}\\
\frac{u_\omega}{U} &= -\frac{1}{Uc\sqrt{(1-\mu^2)(\xi^2-1)}}\frac{\partial\Phi_2}{\partial\omega} = 0
\end{aligned}\right\} \quad \ldots[31]$$

Evaluating Equations [31] on the surface of the ellipsoid, $\xi_0 =$

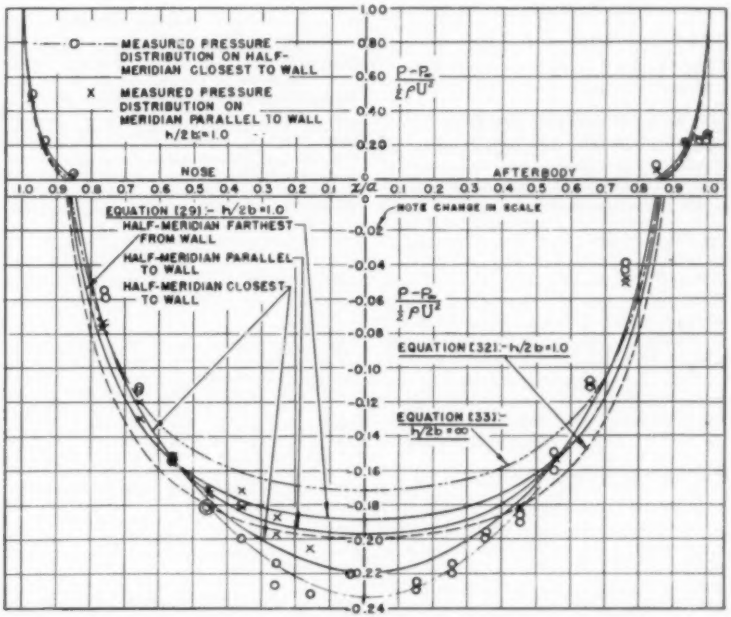

Fig. 2 Calculated and Measured Pressure Distributions on a 4:1 Ellipsoid

$1/e_0$, and putting $\mu = x/c\xi_0 = x/a$, only the tangential component remains

$$\frac{u_\mu}{U}\bigg|_{\xi=\frac{1}{e_0}} = -\frac{B}{a}\left(\frac{e_0^2}{1-e_0^2}\right)\sqrt{\frac{1-(x/a)^2}{1-e_0^2\,(x/a)^2}} \quad \ldots\ldots [31a]$$

To this degree of approximation, then, the pressure distribution is

$$\frac{p-p_\infty}{\frac{1}{2}\rho U^2} = 1 - \left[\frac{Be_0^2}{a(1-e_0^2)}\right]^2 \sin^2\theta \quad \ldots\ldots\ldots [32]$$

where

$$\sin^2\theta = \frac{1-\left(\frac{x}{a}\right)^2}{1-e_0^2\left(\frac{x}{a}\right)^2}$$

and θ is the angle between the normal to the surface of the ellipsoid and the direction of motion.

As $\eta \to \infty$, Equations [29] and [32] reduce to the familiar result for an ovary ellipsoid in an infinite stream

$$\frac{p-p_\infty}{\frac{1}{2}\rho U^2} = 1 - \left(\frac{Ae_0^2}{Ua(1-e_0^2)}\right)^2 \sin^2\theta \quad \ldots\ldots\ldots [33]$$

Velocity Distribution on the "Wall"

For any point on the wall, put $y = h$, $\gamma = \alpha$, $\zeta = \beta$, $\xi = \xi'$, in Equations [28], so that, on the wall

$$\left.\begin{aligned}
\frac{u_x}{U}\bigg|_{y=h} &= -1 - \frac{B}{c}\left[\ln\frac{\xi+1}{\xi-1} - \frac{2}{\beta\xi^3}\left(\frac{x}{c}\right)^3 - \frac{2}{\xi}\right] \\
\frac{u_y}{U}\bigg|_{y=h} &= 0 \\
\frac{u_z}{U}\bigg|_{y=h} &= 2\,\frac{B}{c}\left(\frac{x}{c}\right)\left(\frac{z}{c}\right)\{\beta(\xi^3-\xi)\}^{-1}
\end{aligned}\right\} \quad \ldots [34]$$

Comparison With Experimental Results

Experiments to check the solutions were carried out in the free surface water tunnel of the Hydrodynamics Laboratory of the California Institute of Technology (5). Pressures were measured on ellipsoid models having length-diameter ratios of 4 and 6, which were held at various distances from a plate simulating a wall. For these forms, the measurable pressure defects due to viscous flow are confined to the after 25 or 30 per cent of the length independently of the Reynolds number. The boundary-layer thickness of the plate was negligible for the separations between plate and model in these tests. For facility in mounting the models, it was necessary to use a straight cylindrical middle body over 7 per cent of the 4:1 ellipsoid and 5 per cent of the 6:1 ellipsoid, with resulting discontinuities in the slopes and curvatures of the surface at the ends of these cylinders.

TABLE 1 COMPARISON OF MEASURED AND COMPUTED VALUES OF MINIMUM PRESSURE COEFFICIENTS ($x/a = 0$) ON THE HALF-MERIDIAN CLOSEST TO THE WALL

Ellipsoid mode	Distance from wall in diam $h/2b$	Measured (faired) values $\frac{p-p_\infty}{\frac{1}{2}\rho U^2}$	Equation [29] $\frac{p-p_\infty}{\frac{1}{2}\rho U^2}$	Equation [29] Per cent deviation	Equation [32] $\frac{p-p_\infty}{\frac{1}{2}\rho U^2}$	Equation [32] Per cent deviation
4:1	0.75	−0.295	−0.264	−10.5	−0.221	−25
	1.0	−0.233	−0.219	− 6	−0.199	−14.6
	1.5	−0.199	−0.193	− 3	−0.181	− 9
	2.0	−0.182	−0.178	− 2.2	−0.175	− 4
	∞		−0.1707		−0.1707	
6:1	1.0	−0.145	−0.137	− 5.5	−0.123	−15

Although these discontinuities are such as to increase the deviation between theory and experiment in this region, the values obtained are sufficient to indicate the ranges of usefulness of the solutions.

An example of data is shown in Fig. 2 in which are compared the measured and computed pressure distributions for the 4:1 ellipsoid at a distance of 1 diam between the plate and center of the model (1 radius separation). Since the largest deviations may be expected to occur at the point of minimum pressure on the meridian closest to the wall, the computed and measured data are compared for this point; the results are given in Table 1 for all measurements.

BIBLIOGRAPHY

1 "Hydrodynamics," by H. Lamb, Cambridge University Press, London, England, sixth edition, 1932, pp. 139–143.

2 "Aerodynamic Theory," by W. F. Durand, Julius Springer, Berlin, Germany, vol. 1, div. C, 1934, p. 277.

3 "A Course of Modern Analysis," by E. T. Whittaker and G. N. Watson, Cambridge University Press, London, England, fourth edition, 1927, pp. 317–319.

4 Loc. cit., pp. 323–326.

5 "The Hydrodynamics Laboratory of the California Institute of Technology," by R. T. Knapp, Joseph Levy, J. Pat O'Neill, and F. B. Brown, Trans. ASME, vol. 70, 1948, pp. 419–435.

Influence of the Dimensional Factors on Mode of Yielding and Fracture in Medium-Carbon Steel—II[1]

The Size of the Round Tensile Bar

By JULIUS MIKLOWITZ,[2] ANN ARBOR, MICH.

Test results show an increase in axial strain, average true stress, and maximum true stress at the minimum section of the neck of a round tension bar at fracture when the size of the bar is decreased. An explanation is given for this size effect on the axial strain. It suggests that the restraint on the flowing material at the heart of the neck, created by lateral stresses induced by the adjacent stagnant material, is dependent upon the diameter of the stagnant material; hence the bar diameter. Some metallurgical variations in the data are analyzed and discussed.

Introduction

PART I (1)[3] of this investigation was devoted to a study of the effects of geometry and size variation on the mode of yielding and fracture in flat tension bars of medium-carbon steel. This work was further extended to include a group of tests on round tensile bars of the same steel where size was varied under geometric similarity.

The local necking phenomenon associated with the fracture of a round tension bar is well known. It was the purpose of this work to investigate the effects of size variation on this fracture process.

The body of this paper reports observations and calculations made on the stress and strain values associated with the progressive necking process and fracture. The linear size range covered was 16 to 1, the largest specimen reaching a diameter of 3 in.

Specimens and Material

The testing machines used in this investigation already have been discussed (1). The round tensile piece is shown in Fig. 1. A series of ten of these specimens (two of each size) were used. Later two additional large bars were prepared (specimens Nos. 11 and 12) and tested. The diameters of the bars tested were 3, 1.5, $^3/_4$, $^3/_8$, and $^3/_{16}$ in., chosen according to a geometric progression, each specimen being one half the size of the one larger than it. Geometric similarity was kept in all by making the gage length 5 times, and gage radius 4.25 times the diameter. The larger specimens were undercut 1 per cent of the diameter at the center of the gage length to control the fracture location. To prevent any concentration of stress the profile of the undercut was made a large circular arc.

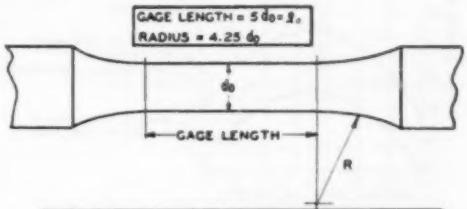

SPECIMEN NO.	DIMENSIONS (INCHES)		
	d_0	ℓ_0	RADIUS
9 10	3.000	15.000	12.750
7 8	1.500	7.500	6.375
1 2	0.750	3.750	3.188
3 4	0.375	1.875	1.594
5 6	0.188	0.938	0.797

THE LARGER SPECIMENS WERE UNDER CUT 1% IN DIA. AT THE CENTER OF THE GAGE TO CONTROL THE FRACTURE LOCATION.

Fig. 1 Round Bars for Series on Size Variation

The round bars were cut from the same heat of material as the flat specimens of Part I (1). Billets $4^1/_2 \times 4^1/_2$ in. in cross section served the purpose.

Measurement of Stresses and Strains

In the round tensile bar the average true stress in the axial direction on a particular cross section is given by $\sigma = P/A$, where P is the tensile load, and A the area of the section when the bar is under this load. The data for the stress were easily obtained by measuring with micrometers the particular diameters of interest, after the load was dropped off a little from the value recorded. The data on diameters was also useful for cal-

[1] Parts I and II of this work have partially fulfilled the requirements for the degree of Doctor of Philosophy at the University of Michigan. The experimental work of this investigation was carried out at the Westinghouse Research Laboratories, East Pittsburgh, Pa., during 1945 and 1946, under a contract with the David Taylor Model Basin of the Navy Department, Bureau of Ships, Washington, D. C.

[2] Formerly Research Engineer, Westinghouse Research Laboratories, East Pittsburgh, Pa.; on leave at the University of Michigan.

[3] Numbers in parentheses refer to the Bibliography at the end of the paper.

Presented at the National Meeting of the Applied Mechanics Division, Ann Arbor, Mich., June 13–15, 1949, of The American Society of Mechanical Engineers.

Discussion of this paper should be addressed to the Secretary, ASME, 29 West 39th Street, New York, N. Y., and will be accepted until July 10, 1950, for publication at a later date. Discussion received after the closing date will be returned.

Note: Statements and opinions advanced in papers are to be understood as individual expressions of their authors and not those of the Society. Paper No. 49—APM-20.

culating the mean value of unit conventional strain in the axial direction, since this is given by the relation $\epsilon = (A_0/A) - 1$, where A_0 is the original area of the strained section A (d_0 is the diameter of section A_0). The sections along the bar were circularly marked to facilitate measuring them.

Fig. 2 is a reproduction of a figure (Fig. 7) of a paper by Davidenkov and Spiridonova (2), showing the distribution of the stresses in the minimum section of the neck of a round tension

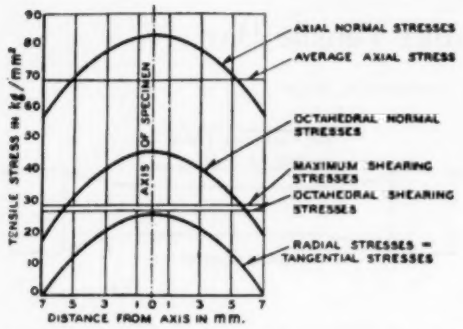

FIG. 2 DISTRIBUTION OF STRESSES IN MINIMUM SECTION OF NECK OF ROUND TENSILE SPECIMEN
(According to Davidenkov and Spiridonova, reference 2.)

specimen. The maximum true stress in the axial direction, it can be seen, comes at the center of the bar, at the peak of a parabola representing the axial true stresses. The relation representing this function is given as

$$\sigma_m = \sigma \left[\frac{R + 0.5\,a}{R + 0.25\,a} \right]$$

where a is the radius of the minimum section of the neck and R the radius of curvature, at and near the minimum section, of the contour of the neck in the meridional section. This relation was used in the present work; a and R were measured photographically.

In Fig. 2 the octahedral shearing stress is seen to be a constant over the entire section. The octahedral shearing stress is defined by the relation

$$\tau_0 = \frac{1}{3}\sqrt{(\sigma_1 - \sigma_2)^2 + (\sigma_2 - \sigma_3)^2 + (\sigma_3 - \sigma_1)^2}$$

where σ_1, σ_2, and σ_3 are the principal stresses. In the quoted work (2), it was found that at any point in the minimum section, the radial and tangential stresses are equal. The relation for octahedral shearing stress therefore becomes

$$\tau_0 = \frac{1}{3}\sqrt{2(\sigma_1 - \sigma_2)^2}$$

where σ_1 is the axial and σ_2 the radial or tangential stress. The quantity $(\sigma_1 - \sigma_2)$ is sometimes called the effective stress and is a constant over the minimum section of the neck. If we denote the effective stress by σ_e, we have $\tau_0 = 0.47\,\sigma_e$. The effective stress is given by the relation

$$\sigma_e = \frac{\sigma}{1 + \dfrac{a}{4R}}$$

The octahedral shearing stresses τ_0 in the present work were calculated using these relations.

STRESS AND STRAIN IN THE NECK AS INFLUENCED BY SIZE OF BAR

The results of the tests are presented in Table 1, the quantities in this table being reproduced for various sizes of the specimens (various diameters) in Figs. 3 and 4. As shown by the large differences in the values of Table 1, the size of the test bar influenced the local necking process and the accompanying stresses and strains. Over the 16-fold range of the increase in size, the variance in average true stress at the ultimate load is slight and no general trend is evident. Since the stress-strain curves were very flat in the vicinity of the ultimate stress, a choice in strain had to be made to compare the stresses at the ultimate load. A unit conventional axial strain of 0.22 was used for the values appearing in Table 1.

Table 1 and Figs. 3 and 4 show that, with an increase of bar size, the average true and the maximum true stress at fracture, and the unit axial strain at fracture decrease. The octahedral shearing stress at fracture decreases slightly.

TABLE 1 SIZE INFLUENCE ON STRESS AND STRAIN IN MINIMUM SECTION OF NECK OF A ROUND TENSION BAR

Specimen no.	Size, diam, in.	Average true stress at ultimate load[a] Value, psi	Average true stress at ultimate load[a] 2 Spec. avg, psi	Average true stress at fracture[b] Value, psi	Average true stress at fracture[b] 2 Spec. avg, psi	Maximum true stress at fracture[b] Value psi	Maximum true stress at fracture[b] 2 Spec. avg, psi	Octahedral shearing stress at fracture[b] Value, psi	Octahedral shearing stress at fracture[b] 2 Spec. avg, psi	Unit axial strain at fracture Value	Unit axial strain at fracture 2 Spec. avg
5	5/16	81600	82100	144000 ↑ [c]	147000 ↑	173000 ↑	175,500 ↑	54200	55800	1.70 ↑	1.75 ↑
6		82600		150000 ↑		178000 ↑		57400		1.80 ↑	
3	3/8	78700	78700	137000 ↓	135800	162500 ↓	160000 ↓	52600	52600	1.83 ↓	1.80 ↓
4		78700		134500		157500		52600		1.76	
1	1/4	83700	84500	136000 ↓	134500 ↓	159500 ↓	158300 ↓	53000	52100	1.58 ↓	1.52 ↓
2		85200		133000 ↓		157000 ↓		51200		1.46 ↓	
7	1 1/2	80200	80500	[c]	113000	[c]	127000 ↑	[c]	46700	[c]	1.05 ↑
8		80700		113000 ↑		127000 ↑		46700		1.05 ↑	
9	3	79800	80100	90500 ↑	90500 ↑	93200 ↑	93200 ↑	41300	41300	0.47 ↑	0.46 ↑
10		80300		90500 ↑		93200 ↑		41300		0.45 ↑	
11[d]	3	84500	84500	133800	133800	155500	155500	51600	51600	1.28	1.27
12[d]		84500		(97800)		(144200)		(38000)		1.26	

[a] These stresses were calculated at an axial strain value of 0.22.
[b] These stresses were calculated by the use of the relations derived by Davidenkov and Spiridonova (2).
[c] Specimen 7 was not broken. The comparison of 7 and 8 at the necking load of 100,000 lb (just before fracture) is as follows:

	Average true stress in min. section of neck, psi	Unit axial strain in min. section of neck
Specimen 7	105500	0.82
Specimen 8	107000	0.86

[d] Later tests by Julius Aronofsky.
[e] The arrow indicates how the value should be corrected (increased ↑ or decreased ↓) if the specimen's position in the cross section of the original billet is taken into account. A specimen from the billet center showed lower true stresses and axial strain than the specimen taken from the outside portion of the billet section (see Table 2 and Fig. 5).

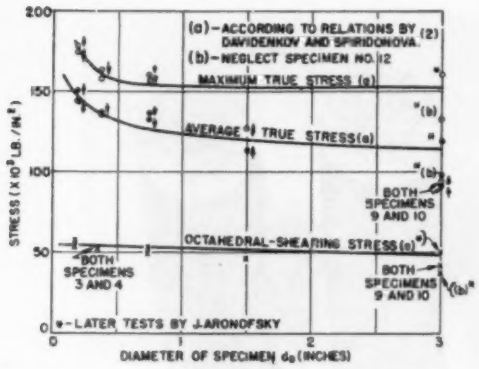
(a)-ACCORDING TO RELATIONS BY (2) DAVIDENKOV AND SPIRIDONOVA
(b)-NEGLECT SPECIMEN NO. 12
MAXIMUM TRUE STRESS (a)
AVERAGE TRUE STRESS (a)
OCTAHEDRAL-SHEARING STRESS (a)
BOTH SPECIMENS 3 AND 4
BOTH SPECIMENS 9 AND 10
BOTH SPECIMENS 9 AND 10
* - LATER TESTS BY J. ARONOFSKY
STRESS (X 10³ LB./IN.²)
DIAMETER OF SPECIMEN d_0 (INCHES)

FIG. 3 INFLUENCE OF SIZE OF SPECIMEN ON STRESS IN MINIMUM SECTION OF NECK OF ROUND TENSION BAR AT FRACTURE

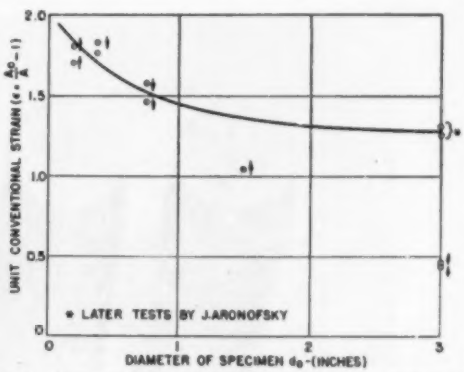

FIG. 4 MAXIMUM STRAIN AT FRACTURE IN MINIMUM SECTION OF NECK AS A FUNCTION OF SPECIMEN SIZE

These stress and strain values (with the exception of the octahedral shearing stress) have been influenced by the position of the specimen in the original cross section of the billet from which the specimens were cut. Fig. 5 shows the cutting plan. Specimens Nos. 1 and 2 ($^3/_4$ in. diam) and 3 ($^3/_8$ in. diam) were cut from the outside parts of the billet, whereas specimens Nos. 4 ($^3/_8$ in. diam) and 5 and 6 ($^3/_{16}$ in. diam) were cut from the central parts. As a check on position, bars A and B, shown in Fig. 5, were pulled to fracture. Table 2 gives the results.

If we assume that the average of values given in Table 2 of specimens A and B are the values of a specimen unaffected by position in the billet (this specimen lying between A and B), then the stress and strain values at fracture of each of bars 1, 2, and 3 are somewhat high, and bars 5 and 6 low. Bar 4 lying between A and B probably was not affected by position. If the values in Table 1 were corrected for position, specimens 5 and 6 would have higher and 1, 2, and 3 lower stresses and strains. A further check on position is given by the specimens 3, 4, 5, and 6. Comparing 3 and 4 in Table 1, 3 shows the higher values; this represents not a great difference, but one that is in line with the tendency shown by the position of specimens A and B. Comparing specimens 5 and 6, 6 shows the higher values, which again is in the right direction. At a first glance, the differences in the strain values for the $^3/_8$-in. (3 and 4) and the $^3/_{16}$-in-diam specimens (5 and 6) might be attributed to the position effect, but if this were so, specimens 1 and 2 (also from the outside of the billet) would have to show larger values than specimens 5 and 6. A glance at the rest of the table verifies the size effect. On the basis of the position influence, specimens 7, 8, 9, and 10 show somewhat low values, since they were cut from the center of the $4^1/_2 \times 4^1/_2$-in. billet. Bar 8, being only $1^1/_2$ in. diam as against 3 in. for bars 9 and 10, would be affected more. The position influence is indicated in Table 1. There is an arrow alongside each value indicating how the value should be corrected for position. An upward arrow (↑) signifies a higher, and a downward arrow (↓) a lower value. Table 1 corrected for position shows, in a much more pronounced form, the size effect on stress and strain values. In Figs. 3 and 4 arrows similar to those in Table 1 are shown.

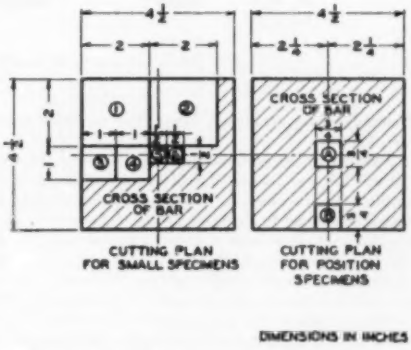
CROSS SECTION OF BAR
CROSS SECTION OF BAR
CUTTING PLAN FOR SMALL SPECIMENS
CUTTING PLAN FOR POSITION SPECIMENS
DIMENSIONS IN INCHES

FIG. 5 CUTTING PLANS FOR SMALL SPECIMENS

TABLE 2 INFLUENCE OF POSITION OF SPECIMEN IN ORIGINAL BILLET ON STRESS AND STRAIN IN MINIMUM SECTION OF NECK OF A ROUND TENSION BAR

Specimen no.	Size, diam. in.	Average true stress at fracture, psi	Maximum true stress at fracture,[a] psi	Octahedral shearing stress at fracture,[a] psi	Unit axial strain at fracture
A (bar center)	0.357	137000	155500	56000	1.58
B (bar outside)	0.357	140000	162000	55000	1.80

[a] Calculated according to Davidenkov and Spiridonova (2).

Specimens 11 and 12 were tested by Mr. Julius Aronofsky[4] almost 2 years after the tests on the identical specimens 9 and 10 had been made. Premature fracture of the latter two was the reason for the additional tests with specimens 11 and 12 of the largest-size bars. As Table 1 shows, considerably great differences were found in the stresses and strains between the earlier and later tests. The fractures were entirely different. This will be discussed later. Specimens 11 and 12, identical in shape to 9 and 10, came from the same heat of steel as 9 and 10. It should be mentioned that the load observations at fracture made for 12

[4] Research Engineer, Westinghouse Research Laboratories, East Pittsburgh, Pa.

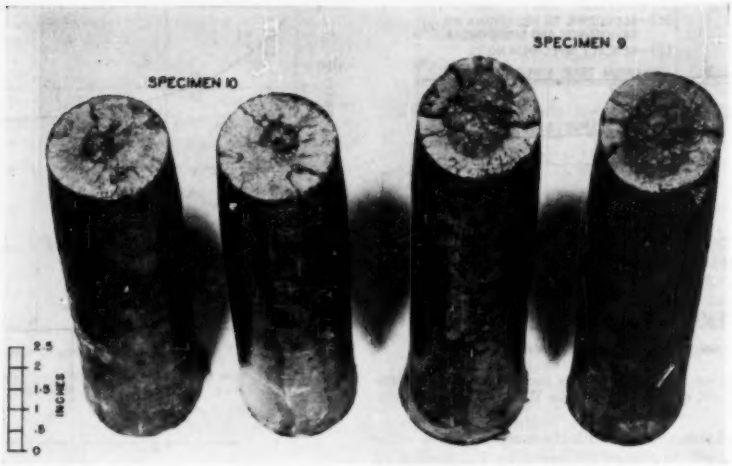

FIG. 6 FRACTURE SURFACES OF TWO 3-IN-DIAM TENSILE SPECIMENS
(Gage length, 15 in.)

are believed to be erroneous, hence the probable incorrect stresses.

The influence of the position of the specimens in the original billet, it was felt, was associated with a nonhomogeneity of structure in the billet cross section. The premature fracturing of the large specimens 9 and 10 gave convincing evidence of this. Fig. 6 shows the fracture surfaces of these two large bars. In specimen No. 9, particularly, a lighter ringlike outer region surrounds a dark central region of seemingly different structure. The same, but not as large, central region is shown by specimen No. 10. It was not the purpose of this investigation to enter into the metallurgical details involved, but the outstanding discrepancies, such as the position effect and the abnormal fractures in bars 9 and 10, suggested some research along metallurgical lines.

Schane (3) has noted central "dark spots," as they were called, similar to those exhibited by bars 9 and 10, in fractures of smaller specimens of structural steel. It was shown that this condition and the accompanying low ductility were due to a coarse grain size in the steel in its as-rolled condition.

The perfect cup-and-cone fractures exhibited by bars 11 and 12 (11 is shown in Fig. 7), along with their large maximum-strain values in the neck at fracture, suggested the search for possible metallurgical causes for the differences observed in the fractures of bars 9 and 10 and the later tests 11 and 12. Comparisons of bars 10 and 11 were made. Cross-sectional slices, taken from points of the gage length of these bars which had undergone 0.20 unit conventional axial strain, served as specimens for producing macroetches. The results are shown in Figs. 8(*a*) and (*b*). A comparison of the sulphur prints in Fig. 8(*a*), reveals a faint square-shaped segregation zone in the case of specimen 10. (The large white spots are due to air bubbles and should not be taken into consideration.) Fig. 8(*b*) exhibits the same slices after they were subjected to another method of etching. The same segregation zone for specimen 10 is evident.

Mention should be made of the fact that the fracture surface of 10 was coincident with a machined line (surface scratch which had been applied for measuring purposes). The possibility that a stress concentration, induced by this machined line, influenced the premature fracture exists. However, specimen No. 9, which had a similar machined line on its gage surface, also broke prematurely and at a strain almost equivalent to that of 10. The line seemingly did not influence the fracture of 9. To eliminate these surface scratches in the later tested bars, a photogrid was applied (on bars 11 and 12). The author attaches more importance to the nonuniformity of the structure due to the segregation zone as the reason for the premature fractures in bars 9 and 10.

FIG. 7 FRACTURE SURFACE OF SPECIMEN NO. 11

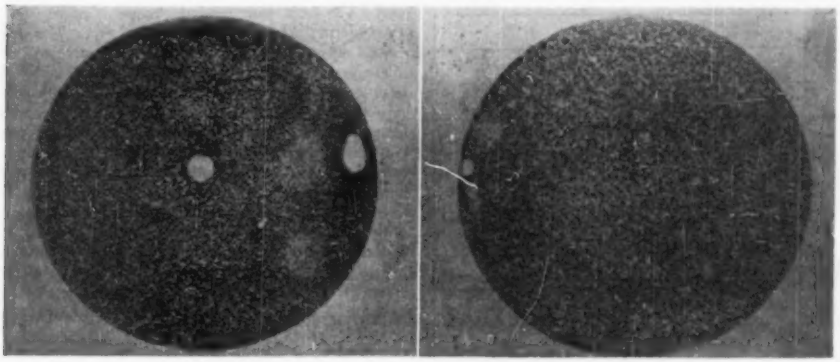

Specimen No. 10 Specimen No. 11

FIG. 8(a) COMPARISON OF SULPHUR PRINTS OF CROSS SECTIONS OF LARGE BARS

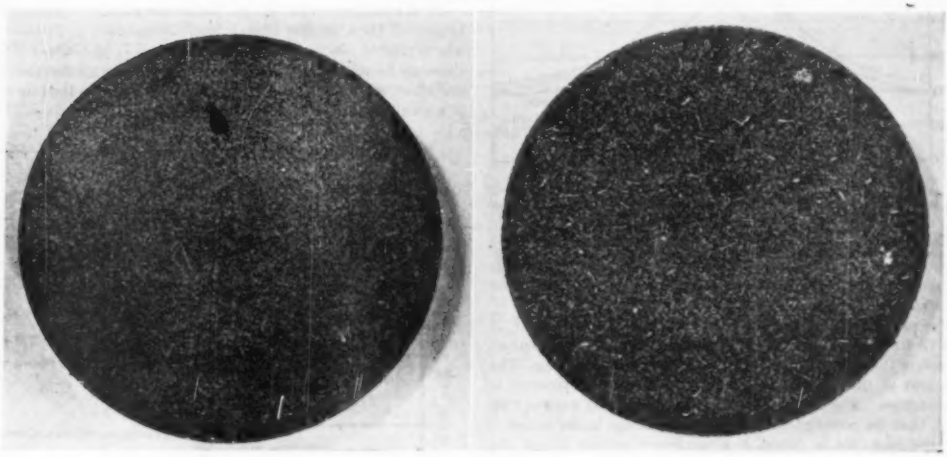

Specimen No. 10 Specimen No. 11

FIG. 8(b) COMPARISON OF MACROETCHES OF CROSS SECTIONS OF LARGE BARS

That segregation is an important factor in ductility studies has been pointed out by others. Recent OSRD work by Mehl, Wells, and Fetters (4) and a second report by the first two authors (5) contain information along these lines. Their work entailed a study of the ductility associated with different-type fractures in tensile bars of steel used in gun tubes (alloy steels). They defined four types of fractures, which in order of decreasing ductility are the cup and cone, angular, irregular, and laminated brittle. Specimens 11 and 10 of this work would fall into the first and last, respectively, of the quoted categories. Bar No. 8 of this work, which showed a comparatively low strain value (see Table 1), probably would fit into the "irregular" fracture type. No record of this exists, however. They state that the brittle fracture is commonly caused by the presence and segregation of extraneous refractory inclusions. Mention is made that the inclusions tend to localize into one part of the ingot and are responsible for low ductility.

This, then, seems to be a possible explanation for the square-shaped segregation zone and its influence in specimen 10. The shape of the zone evidently was produced by the rolling of the billet. The large number of tests made by the authors (4, 5) showed that only 60 per cent of the tests produced a pure cup-and-cone fracture. Hence in this there is the suggestion that a large number of tests should be made in an investigation of the size effect, and that only specimens exhibiting cup-and-cone fractures (optimum ductility) should be compared. In the present work, then, only specimens 11 and 12 (cup-and-cone fracture), along with the smaller-sized specimens, have been considered in the plots in Figs. 3 and 4.

The distribution of the axial strain in the neck as a function of size is brought out in Fig. 9. If the curve of specimen 1 and that of bars 11 and 12 are compared, the size of specimen seems to influence the strain values along the gage length (in the vicinity of the deepest portions of the neck) in a manner similar to its in-

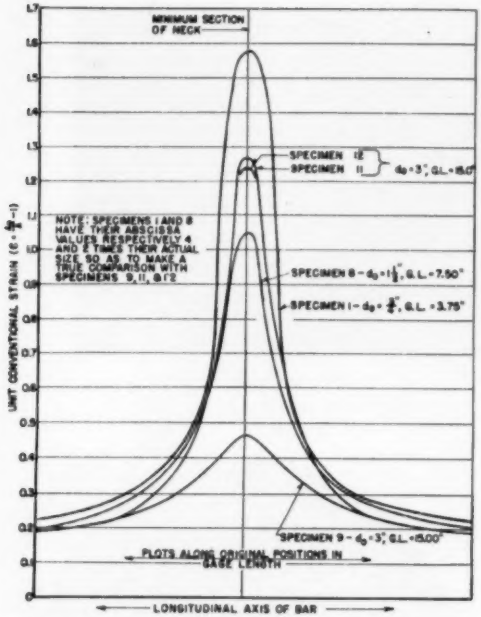
MINIMUM SECTION OF NECK
SPECIMEN 12
SPECIMEN 11
NOTE: SPECIMENS 1 AND 8 HAVE THEIR ABSCISSAE VALUES RESPECTIVELY 4 AND 2 TIMES THEIR ACTUAL SIZE SO AS TO MAKE A TRUE COMPARISON WITH SPECIMENS 9, 11, & 12
SPECIMEN 8 - $d_0 = 1\frac{1}{2}$", G.L. = 7.50"
SPECIMEN 1 - $d_0 = \frac{3}{4}$", G.L. = 3.75"
SPECIMEN 9 - $d_0 = 3$", G.L. = 15.00"
PLOTS ALONG ORIGINAL POSITIONS IN GAGE LENGTH
UNIT CONVENTIONAL STRAIN $\epsilon = \frac{\Delta l}{l_0} = \frac{l - l_0}{l_0}$
LONGITUDINAL AXIS OF BAR

FIG. 9 DISTRIBUTION OF AXIAL STRAIN IN NECK OF ROUND TENSION BAR AS A FUNCTION OF SIZE OF BAR
(All bars at fracture.)

fluence on the maximum values; the smaller the bar the higher the strains.

The progressive axial-strain diagrams for specimens 1, 8, 9, 11 and 12 are shown in Figs. 10, 11, and 12. The numbered curves in each of the figures reflect the successive stages of necking. The abscissas of the smaller specimens have not been increased in these figures. The curves indicate, as in the flat-bar work of Part I (1), that the restraint on the gage material due to the action of the specimen heads produces a minimum section before the ultimate load is reached. They also show the localization phenomenon, that is, the straining tends more and more to become restricted to the immediate vicinity of the minimum section of the neck as the necking process continues.

Figs. 13 (*a*) and (*b*) show the fractured necks. The photographs of the smaller specimens have been magnified.

That the size effect is a recognized factor in the plastic flow and fracture of metals, has been brought out by others. In a recent survey for the Navy Department of the literature on the fracture problem, Gensamer, Saibel, Ransom, and Lowrie (6) mentioned the more important approaches toward explaining size phenomena. Significance is attached to a statistical-theory explanation.

A paper by Brown, Lubahn, and Ebert (7) has a detailed discussion on this work. This, together with a paper by Davidenkov, Shevandin, and Wittman (8) do much toward establishing the "statistical theory" as the most probable explanation for the size effect. Paper (7) describes the statistical theory.

It will be recognized in reading the foregoing literature that the focus of attention in size phenomena has been directed toward notched-bar testing (both bending and tensile) in which a stress gradient is dealt with. Brittle materials under high speeds of testing form the bulk of the work. The paper (7) emphasizes that the size effect is a property of ductile materials also.

The present work has brought out a size effect in ordinary uniform tension bars of a ductile material. On the basis of what was stated in Part I (1) of this paper, the author favors explaining this influence of size in an analogous manner to that presented for flat bars in Part I. The localization of straining more and more toward the vicinity of the minimum section of the neck, as necking progressed, was brought out in Figs. 10 and 11. The production of a thinner and thinner disk of flowing material at the heart of the neck is probable. It is believed that the contraction of this disk diameter depends greatly on the lateral stresses in the plane of the disk, which are created by the restraint of the adjacent stagnant material on the disk, and which increase with the increase of diameter of the bar (diameter of adjacent stagnant material depends on this bar diameter).

The curves in Figs. 3 and 4 seem to indicate that the greatest change due to size variation is in the range of smaller specimens. An actual limit of dimensional influence is suggested by each curve, except the octahedral shearing stress which is only slightly affected in its entirety.

On the suggestion of Dr. A. Nadai the advice of the metallurgists of the Carnegie Illinois Steel Corporation in Pittsburgh was requested. Messrs. W. T. Lankford and T. M. Garvey of the Carnegie Illinois Steel Corporation, expressed the opinion that the size effect, as exhibited here, might have been due to the presence of a small quantity of occluded hydrogen gas in the steel. Mr.

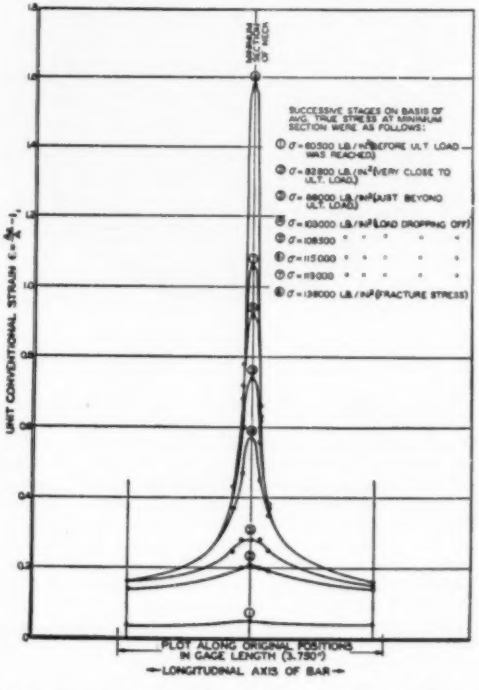
MINIMUM SECTION OF NECK
SUCCESSIVE STAGES ON BASIS OF AVG. TRUE STRESS AT MINIMUM SECTION WERE AS FOLLOWS:
① σ = 80500 LB/in² BEFORE ULT. LOAD WAS REACHED)
② σ = 82800 LB/in² (VERY CLOSE TO ULT. LOAD)
③ σ = 88000 LB/in² (JUST BEYOND ULT. LOAD)
④ σ = 103000 LB/in² (LOAD DROPPING OFF)
⑤ σ = 108500 " " " " "
⑥ σ = 115000 " " " " "
⑦ σ = 119000 " " " " "
⑧ σ = 138000 LB/in² (FRACTURE STRESS)
UNIT CONVENTIONAL STRAIN $\epsilon = \frac{\Delta l}{l_0} = \frac{l - l_0}{l_0}$
PLOT ALONG ORIGINAL POSITIONS IN GAGE LENGTH (3.750")
LONGITUDINAL AXIS OF BAR

FIG. 10 PROGRESSIVE AXIAL-STRAIN DIAGRAMS IN NECK OF ROUND TENSION BAR
(Specimen No. 1; $d_0 = \frac{3}{4}$ in.)

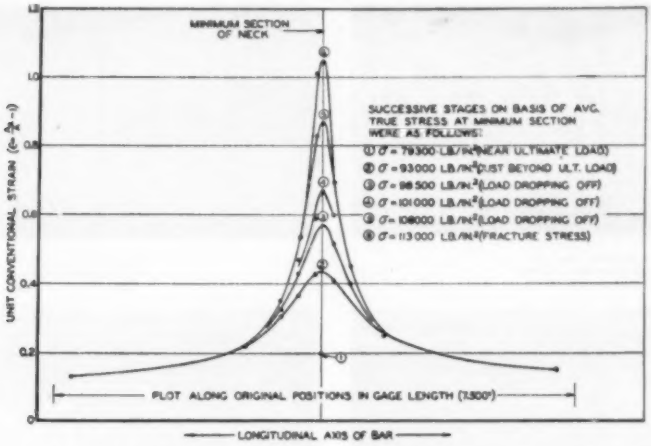
MINIMUM SECTION OF NECK
SUCCESSIVE STAGES ON BASIS OF AVG. TRUE STRESS AT MINIMUM SECTION WERE AS FOLLOWS:
① σ = 79300 LB./IN.² (NEAR ULTIMATE LOAD)
② σ = 93000 LB./IN.² (JUST BEYOND ULT. LOAD)
③ σ = 98 500 LB./IN.² (LOAD DROPPING OFF)
④ σ = 101 000 LB./IN.² (LOAD DROPPING OFF)
⑤ σ = 108000 LB./IN.² (LOAD DROPPING OFF)
⑥ σ = 113 000 LB./IN.² (FRACTURE STRESS)
UNIT CONVENTIONAL STRAIN
PLOT ALONG ORIGINAL POSITIONS IN GAGE LENGTH (7.500")
LONGITUDINAL AXIS OF BAR

FIG. 11 PROGRESSIVE AXIAL-STRAIN DIAGRAMS IN NECK OF ROUND TENSION BAR
(Specimen No. 8; $d_0 = 1^1/_2$ in.)

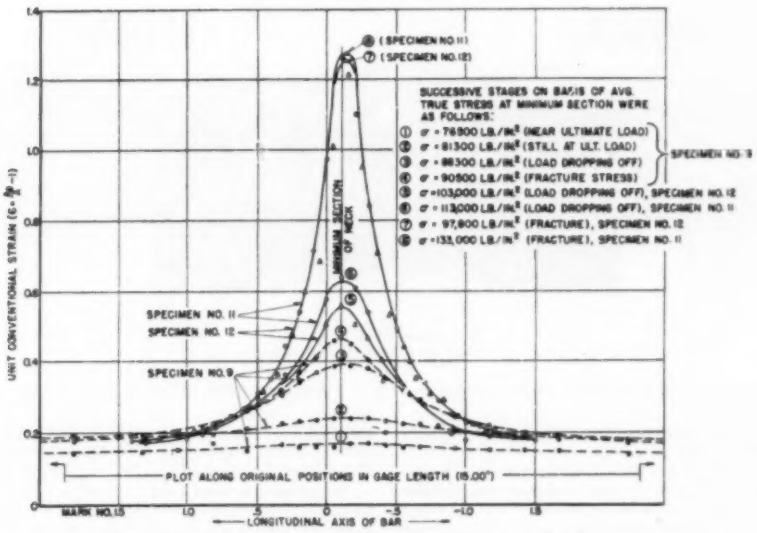
⑧ (SPECIMEN NO. 11)
⑦ (SPECIMEN NO. 12)
SUCCESSIVE STAGES ON BASIS OF AVG. TRUE STRESS AT MINIMUM SECTION WERE AS FOLLOWS:
① σ = 76900 LB./IN.² (NEAR ULTIMATE LOAD)
② σ = 81300 LB./IN.² (STILL AT ULT. LOAD)
③ σ = 88300 LB./IN.² (LOAD DROPPING OFF)
④ σ = 90500 LB./IN.² (FRACTURE STRESS)
SPECIMEN NO. 9
⑤ σ = 103,000 LB./IN.² (LOAD DROPPING OFF), SPECIMEN NO. 12
⑥ σ = 113,000 LB./IN.² (LOAD DROPPING OFF), SPECIMEN NO. 11
⑦ σ = 97,900 LB./IN.² (FRACTURE), SPECIMEN NO. 12
⑧ σ = 133,000 LB./IN.² (FRACTURE), SPECIMEN NO. 11
MINIMUM SECTION OF NECK
SPECIMEN NO. 11
SPECIMEN NO. 12
SPECIMEN NO. 9
UNIT CONVENTIONAL STRAIN
PLOT ALONG ORIGINAL POSITIONS IN GAGE LENGTH (15.00")
MARK NO. 15
LONGITUDINAL AXIS OF BAR

FIG. 12 PROGRESSIVE AXIAL-STRAIN DIAGRAM IN NECK OF ROUND TENSION BAR
(Specimens Nos. 9, 11, and 12.)

Lankford quoted Korber,[8] who discussed the possibility that a decrease in hydrogen content with time might be the cause of an increase in ductility. According to Messrs. Lankford and Garvey, the specimens tested a short time after the steel rolling had a low ductility because of their relatively high hydrogen content. After some time, hydrogen diffused out of the steel and the ductility increased. They believe that the hydrogen diffused out of the smaller specimens with sufficient speed to enable these to show high ductility while the hydrogen in the two 3-in-diam bars (Nos. 9 and 10) had not yet escaped at testing. Contrastingly, the similar specimens Nos. 11 and 12, tested after a time interval of 2 years, had lost the occluded hydrogen. Statement is made that the time necessary to reach maximum ductility varies roughly as the square of the linear dimensions of the bar cross section.

[8] ASTM Proceedings, Part A, 1937.

REFERENCES TO THE LITERATURE

The amount of literature on the size effect in the static testing of round uniform tension bars is small. As has been stated, most of the work on size phenomena has been directed toward notched-

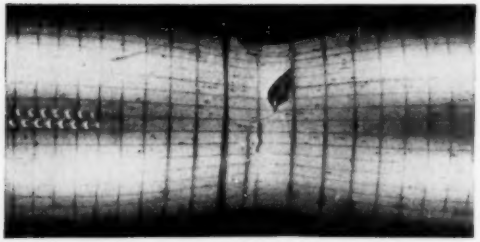

Specimen No. 11
Original diam, 3 in.
Gage length, 15 in.

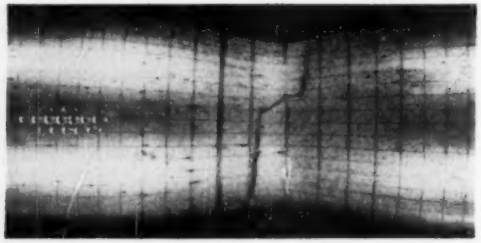

Specimen No. 12
Original diam, 3 in.
Gage length, 15 in.

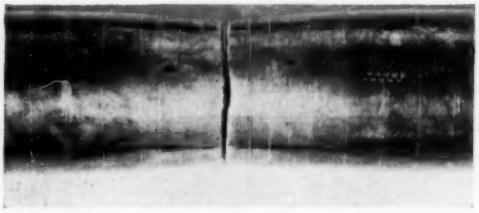

Specimen No. 10
Original diam, 3 in.
Gage length, 15 in.

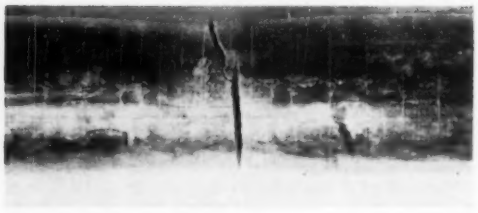

Specimen No. 9
Original diam, 3 in.
Gage length, 15 in.

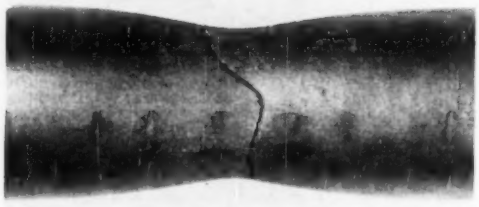

Specimen No. 8
Original diam, 1½ in.
Gage length, 7½ in.

FIG. 13(*a*) SHAPE OF NECK OF ROUND TENSILE BAR AS INFLUENCED BY SIZE OF BAR

bar testing, static and dynamic. Reference (7) covers a great deal of the literature on this.

Lyse and Keyser (9) report early findings of Bach (10) concerned with the size effect in uniform tension testing in round bars. Bach noted that: (*a*) strength decreased slightly with a diameter increase; (*b*) elongation was independent of diameter and gage length as long as the gage length-to-diameter ratio remained constant; and (*c*) reduction in area was independent of diameter. These of course are not in line with the present findings. Lyse and Keyser (9) report on their own results that the reduction of area remained constant when bar diameter was varied.

Duwez, Wood, and Clark (11), working with annealed copper wires, report that stress-strain curves for different-sized wires indicate an increase in ultimate strength as wire size decreases. In fact, all stress ordinates along the curves show the same trend. The elongation was not affected by size. The range of wire sizes was from 0.20 to 0.05 in. (4-1).

In a second paper by these authors (12), static tests were run on geometrically similar specimens of annealed SAE 1020 steel. The gage-length-to-diameter ratio was 26.6. They varied the size by a factor of 2 only. For comparable hardness values (approximately 73 Rockwell B) they found that: (*a*) ultimate strength increased; (*b*) elongation decreased; and (*c*) reduction in area decreased as bar diameter decreased. The latter two are evidence of a trend opposite to that in the present work. It suggests that perhaps the absolute length of specimen is the important variable. In other words, with greater size, geometric similarity remaining, the absolute length is larger and possibly this means less restraint, due to the heads, over the major portion of the gage length. The authors mention their belief in attributing size variations to a nonuniform distribution of impurities in the different sections. Mention is also made of the possibility that surface characteristics might be more influential in the small specimens (possible greater strength at surface).

SUMMARY

The size of the round uniform tension bar was found to have an influence on the local necking process and its accompanying stress

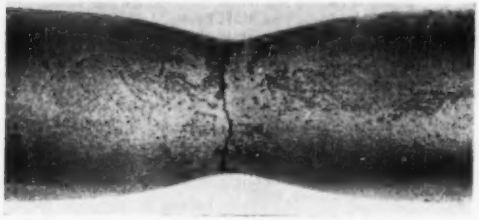

Specimen No. 1
Original diam. 3/4 in.
Gage length, 3 3/4 in.

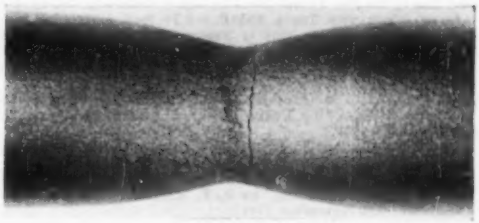

Specimen No. 2
Original diam. 3/4 in.
Gage length, 3 3/4 in.

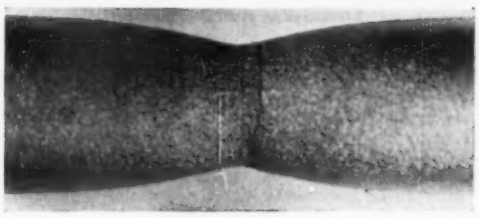

Specimen No. 3
Original diam. 3/4 in.
Gage length 1 7/8 in.

Specimen No. 4
Original diam. 3/8 in.
Gage length 1 7/8 in.

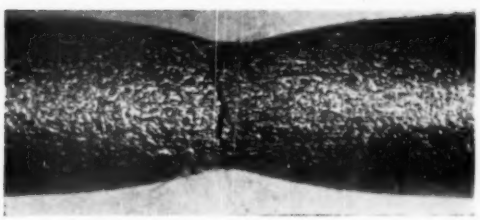

Specimen No. 5
Original diam. 3/16 in.
Gage length 15/16 in.

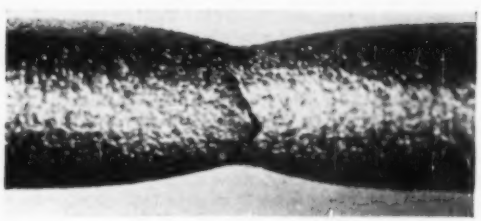

Specimen No. 6
Original diam. 3/16 in.
Gage length 15/16 in.

FIG. 13(*b*) SHAPE OF NECK OF ROUND TENSILE BAR AS INFUENCED BY SIZE OF BAR

and strain characteristics. Specifically, the test results indicated that the axial conventional strain in the minimum section of the neck at fracture increased as the specimen size decreased (geometric similarity remaining). The average true stress in this section and the maximum true stress at the center of this section at fracture also increased with a specimen-size decrease. The octahedral shearing stress, a constant over the section, showed a trend, but not as great, similar to the other stresses. The stress and strain values were influenced by the original position of the specimen in the cross section of the billet from which the specimens were cut. The foregoing stress and strain values, with the exception of the octahedral shearing stress were found to be higher in the specimen cut from the outer portions of the billet cross section. Taking this fact into account strengthened the observed size effect.

Metallurgical considerations are taken into account in explaining this position influence. The size effect on the axial strain in the minimum section of the neck at fracture is attributed to a restraint influence of stagnant material in the neck on the localized plastically flowing material adjacent to it. Inferred in this is the reasoning that the stagnant material creates restraining lateral stresses in the plane of the thin plastic disk at the heart of the neck, and these lateral stresses increase with an increase in the diameter of stagnant material. The thin disk is produced through localization of straining, that is, the tendency of the straining to become more and more restricted to the immediate vicinity of the minimum section.

ACKNOWLEDGMENT

Acknowledgment is expressed to Dr. A. Nadai of the Westinghouse Research Laboratories, for his guidance in this work, and to Mr. Julius Aronofsky of the same laboratories, for having carried out the tests with two large bars. The author appreciates the interest Messrs. W. T. Lankford and T. M. Garvey have shown in this investigation. Acknowledgment is due to the David Taylor Model Basin for permission to publish the test results, and to the personnel there for the help received in the testing of the large bars.

BIBLIOGRAPHY

1 "The Influence of the Dimensional Factors on the Mode of Yielding and Fracture in Medium-Carbon Steel—I. The Geometry

and Size of the Flat Tensile Bar," by Julius Miklowitz, JOURNAL OF APPLIED MECHANICS, Trans. ASME, vol. 70, 1948, p. 274.

2 "Mechanical Methods of Testing—Analysis of the Tensile Stress in the Neck of an Elongated Test Specimen," by N. N. Davidenkov and Miss N. I. Spiridonova, Proceedings of ASTM, vol. 46, 1946, pp. 1147–1158.

3 "Effects of McQuaid-Ehn Grain-Size on the Structure and Properties of Steel," by Phillip Schane, Jr., Trans. ASM, vol. 22, 1934, pp. 1038–1050.

4 "Steel for Gun Tubes—Progress Report," by R. F. Mehl, C. Wells, and K. F. Fetters, OSRD Report no. 731, July, 1942.

5 "Final Report on Steel for Gun Tubes, Part I—The Significance of Angular Fractures," by R. F. Mehl and C. Wells, OSRD Report no. 1009, November, 1942.

6 "Report on Fracture of Metals—Part I," by M. Gensamer, E. Saibel, and J. T. Ransom, Welding Research Supplement of the *Welding Journal*, vol. 26, 1947, pp. 443s–472s.

"Report on Fracture of Metals—Part II," by M. Gensamer, E. Saibel, and R. E. Lowrie, Welding Research Supplement of the *Welding Journal*, vol. 26, 1947, pp. 472s–484s

7 "Effects of Section Size on the Static Notch Bar Tensile Properties of Mild Steel Plate," by W. F. Brown, J. D. Lubahn, and L. J. Ebert, Welding Research Supplement of the *Welding Journal*, vol. 26, 1947, pp. 554s–559s.

8 "The Influence of Size on the Brittle Strength of Steel," by N. Davidenkov, E. Shevandin, and F. Wittman, JOURNAL OF APPLIED MECHANICS, Trans. ASME, vol. 69, 1947, p. A-63.

9 "Effects of Size and Shape of Test Specimen Upon the Observed Physical Properties of Structural Steel," by I. Lyse and C. C. Keyser, Proceedings of the ASTM, vol. 34, part 2, 1934, p. 202.

10 "Elastizität und Festigkeit," by C. Bach, fifth edition, Julius Springer, Berlin, Germany, 1905.

11 "Factors Influencing the Propagation of Plastic Strain in Long Tension Specimens," by P. E. Duwez, D. S. Wood, and D. S. Clark, OSRD Report no. 1304, March, 1943.

12 "The Influence of Specimen Dimensions and Shape on the Results of Tensile Impact Tests," by D. S. Wood, P. E. Duwez, and D. S. Clark, OSRD Report no. 3028, December, 1943.

Gaskets and Bolted Joints

By IRVING ROBERTS,[1] JEANNETTE, PA.

This paper consists of a study of the loading requirements of gaskets in bolted joints, with the object of developing a rational basis for design of such joints. Starting with an analysis of gasket conditions for tightness, the gasket factor *m* is defined, and its variation with initial gasket stress and gasket width is predicted. These trends are confirmed by a survey of the available literature data.

In a bolted joint, gasket stress becomes a function of the elastic constants of the system. Equations are derived to predict gasket and bolt stresses resulting from application of internal fluid pressure, and typical elastic recovery curves for an asbestos gasket are presented. Consideration is given to the effect of gasket creep in a bolted joint, and to the problem of distribution of bolt load, for which an approximate theory is derived.

On this basis, defects in the ASME Code are pointed out, and a tentative new design procedure is proposed. Finally, a summary of data which should be obtained for use with the new design procedure is given.

Nomenclature

The following nomenclature is used in the paper:

A_b = effective cross section of bolts, sq in.
A_g = gasket area, sq in.
A_i = internal area, sq in.
E_b = modulus of elasticity of bolts, psi
E_g = modulus of elasticity of gasket, psi
G = bolt circle diameter, in.
I = moment of inertia, in^4
P = applied load, lb
$S = \frac{t b_f E_b}{d b_g E_g}$, dimensionless
a_b = effective cross section of one bolt, sq in.
b_f = width of flange, in.
b_g = width of gasket, in.
d = thickness of flange, in.
k = modulus of the foundation, psi
l = effective bolt length, in.
m = gasket factor, dimensionless
p_i = internal pressure, psi
q = unit load on foundation, psi/in. of length
t = gasket thickness, in.
x = distance from point of concentrated load, in.
y = deflection of beam on elastic foundation, in.
$\beta = \sqrt[4]{\frac{k}{4\,EI}}$, in^{-1}
δ = deflection, in.
ϵ = strain, dimensionless
σ_b = bolt stress, psi
σ_g = gasket stress, psi
τ = bolt spacing, in.

Introduction

When considering the universal use of bolted flange connections, and the fact that there exists a set of rules for the design of bolted joints in the ASME Code, it is disconcerting to find, in a survey of American literature, not a single paper which gives either an analytical or an experimental study of the gasket conditions which make for tightness in a bolted joint. Several European experimental papers have appeared (1, 2),[2] and these are apparently the only available source of data on gasket loadings required for tightness. Published data on elastic properties or creep properties of gaskets which are important for bolted-joint design are also notable by their absence.

It is hoped that this situation will be rapidly ameliorated by the adoption of an experimental program which is now being considered by the Subgroup on Gaskets of the Boiler Code Special Committee on Rules for Bolted Flanged Connections. The present paper is intended to provide the foundation for such an experimental program in that it presents an analytical treatment of the factors which relate to joint tightness, reviews the available data, and proposes a tentative new design procedure.

Gasket Conditions for Tightness

Theoretical. It is difficult to define what is meant by a "tight" joint. The degree of tightness of a joint can be defined on the basis of the rate of leakage of the process fluid under known pressure conditions. However, the ability to measure such a rate implies that the joint is not tight, unless some arbitrary criterion is used for the maximum allowable leakage rate. Such a criterion would be determined entirely on the basis of the nature of the process occurring in the pipe or vessel. Thus it can be seen that a joint which is considered to be tight for steam or compressed-air service, for example, might not be considered tight for high-vacuum work.

However, for the great majority of services, it is commonly recognized that a flanged joint is entirely satisfactory if it passes some simple test such as the soap-bubble test with compressed air in the system. Evidently, a test of this type indicates the absence of any openings through which mass flow can occur. To try to understand this criterion of tightness, consider an opening which constitutes a large leak in a system containing a gas under pressure. If the opening is large enough, the flow through it will be turbulent in nature. As the size of the opening is decreased, the Reynolds number will decrease below the critical, and the character of the flow will become laminar. As the size of the opening is further decreased until its diameter is of the same order of magnitude as the mean free path of the molecules of gas, the flow loses its mass character and becomes diffusive, i.e., the gas molecules flow through the opening individually by random thermal motion. As a final limit, the opening may be considered to decrease below molecular size to prevent the flow of gas entirely, but this condition may not be attained in practice, as evidenced by the fact that the diffusion of gases through metals is a well-known phenomenon.

On the basis of this picture, a reasonable definition of the usual

[1] Division Engineer, Process Division, Research and Development Department, Elliott Company, Mem. ASME.

Contributed by the Applied Mechanics Division and presented at the Annual Meeting, New York, N. Y., November 27–December 2, 1949, of The American Society of Mechanical Engineers.

Discussion of this paper should be addressed to the Secretary, ASME, 29 West 39th Street, New York, N. Y., and will be accepted until July 10, 1950, for publication at a later date. Discussion received after the closing date will be returned.

Note: Statement and opinions advanced in papers are to be understood as individual expressions of their authors and not those of the Society. Paper No. 49—A-2.

[2] Numbers in parentheses refer to the Bibliography at the end of the paper.

commercially tight joint may be one in which all openings have decreased in size to the point where the leakage flow has lost its mass character, i.e., the gas flow has become entirely diffusive. For the case of liquids, where no diffusive flow occurs, this would mean that the joint would be absolutely tight, except for losses by evaporation. By this definition it can be seen that a joint which is tight by hydrostatic test will also be tight by the soap-bubble test under air pressure. At the same time the joint may be unsatisfactory for high-vacuum work where the diffusive flow of inleaking air becomes important.

Let us now consider a gasket placed between a pair of rigid flanges to which a uniform loading is applied. It is to be expected that the surfaces of both the gasket and the flanges will be rough, the degree of roughness depending on the type of gasket material and on the type of finish of the flanges. As the compressive force is applied to the flanges, high local stresses in the gasket material result, causing the material to deform and fill the openings left by the uneven surfaces. Most of this deformation will be permanent, i.e., the gasket stresses will be well above the yield strength of the material.

The possibility of a leak depends upon the chance that the process fluid will find a continuous channel between the gasket and the flange large enough for mass flow. The elimination of such channels obviously depends upon the magnitude of the initial loading of the gasket. However, even though the gasket has deformed considerably under the initial load, it is apparent that the gasket stress at a point beneath a flange projection may be higher than the average gasket stress, whereas the gasket stress in a flange depression may be lower than the average gasket stress. Then, when the gasket loading is reduced, as always occurs when internal pressure is applied to the vessel, the areas of low initial stress may separate from the flange, opening up a channel for leakage.

With higher initial stresses, it is to be expected that the gasket material will deform further, and that the distribution of stresses will become more uniform. This should result in better sealing properties, i.e., for the same internal pressure a leak will appear at a lower average gasket stress than before. The limit of this condition occurs when all fibers have been stressed beyond the yield point, and the gasket stress becomes uniform, so that reduction in gasket loading results in an equal chance that separation will occur at all points on the face of the flange.

This latter condition is of particular interest since it represents the theoretically perfect joint. To study this situation, consider that our joint consists of a pair of closed flanges without bolts which is placed in a testing machine, so that a uniform compressive load can be applied. A space is left between the halves of the joint, and this space is so connected that hydrostatic pressure can be applied internally. This type of apparatus has been used in experimental work on gaskets since it allows the compressive force on the gasket to be held constant, independent of the internal pressure which is applied to the vessel, and independent of any of the elastic constants in the system. In the usual setup, the internal pressure is increased steadily until a leak is just observed. This test is repeated under different compressive loads to determine the sealing properties of the gasket over a range.

For this apparatus, when a load P is applied by the testing machine

$$P = \sigma_{s1} A_g \quad [1]$$

where σ_{s1} is the average initial gasket stress and A_g is the gasket area. When internal pressure is applied, the following relation holds

$$\sigma_{s2} A_g = P - p_i A_i \quad [2]$$

where σ_{s2} is the new average gasket stress, p_i is the internal pressure, and A_i is the internal area based on the inside diameter of the gasket. As the internal pressure is increased, σ_{s2} decreases, and assuming uniform loading of the gasket and no sticking of the gasket to the flange, such a joint will leak when σ_{s2} becomes equal to p_i, as may be seen from the following. Assume $p_i > \sigma_{s2}$, and that a minute increment of gasket area, ΔA, is open to the internal fluid pressure. Over this increment of area, p_i will be greater than σ_{s2}, so that there will result a net force tending to open the joint. The remainder of the gasket will take on a new stress, σ_{s2}' given by the relation

$$\sigma_{s2}' (A_g - \Delta A) = P - p_i (A_i + \Delta A) \quad [3]$$

Rearranging, and substituting Equation [2]

$$\Delta A (p_i - \sigma_{s2}') = A_g (\sigma_{s2} - \sigma_{s2}') \quad [4]$$

or

$$\frac{p_i - \sigma_{s2}'}{\sigma_{s2} - \sigma_{s2}'} = \frac{A_g}{\Delta A} \quad [4a]$$

Since $A_g / \Delta A$ is finite and greater than 1, and since $p_i > \sigma_{s2}$, this equation can be satisfied only if $\sigma_{s2}' < \sigma_{s2}$. This implies that the gasket stress in the remaining area will become progressively smaller, and that the internal pressure will penetrate still further between the flange and the gasket until complete separation occurs. In other words, the condition $\sigma_{s2} = p_i$ is a critical one, at which a slight increase in p_i results in instability. Examination of Equation [4a] will show that the converse is true when $p_i < \sigma_{s2}$, i.e., σ_{s2}' must be greater than σ_{s2}, and the joint is self-stabilizing.

As a convenient measure of the efficiency of a bolted joint, a gasket factor m is defined as follows

$$m = \frac{\sigma_{s2}}{p_i} \quad [5]$$

where σ_{s2} is the average gasket stress at which a leak occurs when the internal pressure is increased to the value p_i. From the previous discussion, in general, m will vary with initial stress in the following way:

As σ_{s1} is increased from zero, m will decrease from infinity and will approach unity as a limit. The shape of this curve will obviously depend upon the particular gasket material and the roughness of the flange surfaces. Furthermore, in the region where $m > 1$, increased gasket width will cause m to be smaller for the same σ_{s1}, since the chance of finding a leakage channel will be smaller. Finally, it is to be expected that gasket thickness will not have much effect on m, assuming that the thickness is great enough to provide sufficient material to fill the depressions in the flange surface without additional local stress.

The effect of these factors on m must be determined experimentally, since no quantitative theory predicting these effects has been developed, and, indeed, none can be expected to be developed until considerable experimental data have been accumulated. The following section is devoted to a study of the data from the few literature sources available.

Literature Data. Only two papers (1, 2) have been found in which the data are of such form that m can be calculated unequivocally. In both papers the bulk of the useful data were obtained by the compression-machine technique mentioned.

The values of m for rubber from the Siebel, Hering, and Raible paper are plotted against σ_{s1}, the initial gasket stress, in Fig. 1. Within the scatter of the data, each gasket width shows a decreasing value of m, approaching the theoretical value of $m = 1$ at high initial gasket stress. Increase in gasket width shows decreasing values of m for the same σ_{s1} as is to be expected from the discussion in the preceding section. It should be noted at this

time that a plot of σ_{g2} against p_i such as that shown in the original paper is quite deceptive in that it indicates that the value of $m = 1$ can be used throughout the test range for rubber. Actually, Fig. 1 exposes the fact that m decreases steadily with increasing initial stress.

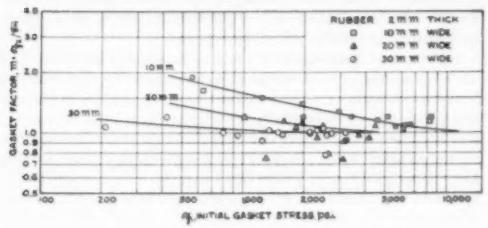
RUBBER 2 m m THICK
10 m m WIDE
20 m m WIDE
30 m m WIDE
10 m m
20 m m
30 m m
GASKET FACTOR, m = σ_{g2}/p_i
σ_{g1} INITIAL GASKET STRESS psi.

FIG. 1

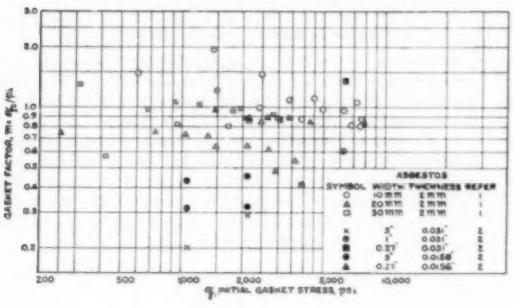

FIG. 2

Fig. 1 also shows a certain amount of scatter of m below unity. Apparently this is to be explained by "sticking" of the gasket to the flange faces, causing an additional force to be required for opening the joint beyond the pressure force available when p_i just reaches σ_g. Sticking is a commonly observed phenomenon with soft gaskets and in many cases the sticking force is so great that when a joint is taken apart the gasket tears before it can be removed from the flange faces. It is a fairly widespread practice to coat the gasket with graphite before making a joint to try to assure easier removal of the gasket at a later time. In so far as m values are concerned, this effect is evidently an erratic one, occurring with some gasket materials to a greater extent than with others.

There is another possible cause for m values lower than unity which is worthy of mention. If the toolmarks in the flange faces are concentric rings, then sealing can occur without deforming the gasket as far as would be required for a random distribution of flange projections. Furthermore, the stress concentration at the ring projections would tend to maintain a tight seal at a considerably lower average gasket stress, giving an apparent m value of less than unity. However, neither of the literature sources indicates that this type of machining of flanges was used and, for want of evidence to the contrary, it will be assumed in this paper that $m < 1$ indicates a sticking effect.

Fig. 2 is a plot of the data for asbestos from both literature sources. Most of the m values are below 1.0, indicating that the sticking effect is important for this material. This is in accord with qualitative observations of the difficulty of removal of asbestos gaskets after they have been in service.

In general, those points for which m is greater than 1.0 are obtained with the narrow gaskets, and here the trend of decreasing m with increasing σ_{g1} is apparent.

Another material tested by Siebel, Hering, and Raible was "piskatorit," apparently a commercial gasket material available in Germany. The results are plotted in Fig. 3 which shows well-defined trends of m with σ_{g1} for the narrower gaskets. In addition, much of the data are below 1.0, indicating that the sticking effect is important for this material.

The data of Siebel, Hering, and Raible for leather are plotted in Fig. 4. Leather appears to act in approximately the same manner as does piskatorit, with the data for the 30-mm gasket falling well below 1.0.

For all gasket materials the German authors carried out their measurements by the usual procedure of gradually increasing the applied load on the apparatus, measuring the internal pressure for leakage at each step. In the case of fiber gaskets, and also in the case of lead and copper, they repeated the measure-

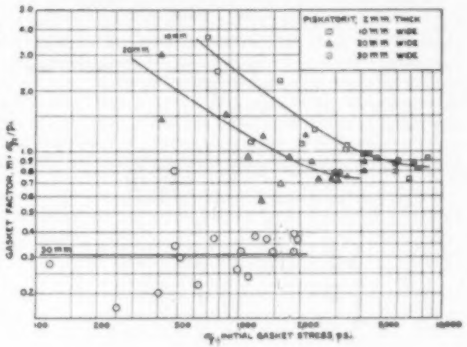
PISKATORIT, 2 m m THICK
10 m m WIDE
20 m m WIDE
30 m m WIDE
10 m m
20 m m
30 m m
GASKET FACTOR, m = σ_{g2}/p_i
σ_{g1} INITIAL GASKET STRESS psi.

FIG. 3

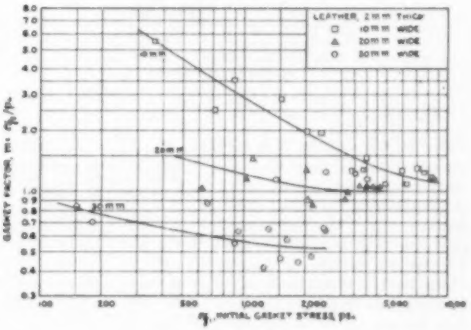
LEATHER, 2 m m THICK
10 m m WIDE
20 m m WIDE
30 m m WIDE
10 m m
20 m m
30 m m
GASKET FACTOR, m = σ_{g2}/p_i
σ_{g1} INITIAL GASKET STRESS, psi.

FIG. 4

ments while decreasing the applied load in steps, and again while increasing the load a second time.

The latter measurements cannot be of any value in bolted-joint design, since such design is based upon the use of fresh gaskets. Furthermore, measurements of this type on a precompressed gasket are of doubtful reproducibility, since they would depend upon whether the gasket reseats itself in the same way after each measurement as the load is reduced. In general, the results show lower m values for precompressed gaskets at the same σ_{g1},

as is to be expected. For the foregoing reasons, the data considered here are only those obtained during the initial compression.

The results for fiber gaskets are given in Fig. 5. For this material the m factor obeys the same general trends as for previous materials, and also shows the sticking effect at high initial stress.

In the case of lead, only the 30-mm-wide gasket is shown in the Siebel, Hering, and Raible paper to have been measured under both increasing and decreasing load. Although it is not

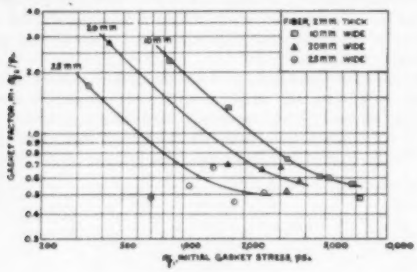

FIG. 5

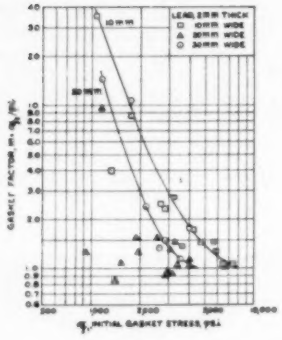

FIG. 6

stated by the authors, it is assumed that the data for the other two gasket widths were obtained during the initial compression only. The results are plotted in Fig. 6 on this basis. The data for the 20-mm gasket width are badly scattered, and do not appear to agree with the data for the other two gasket widths. However, it is interesting to note that within the apparent precision of the measurements, the limiting value of m is 1.0, indicating the absence of any significant sticking effect. This is in accord with qualitative observations of the removal of lead gaskets from flanged joints after they have been in service.

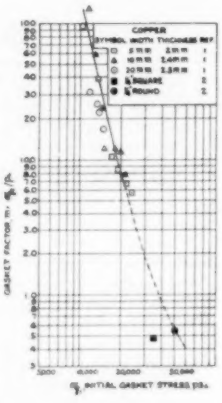

FIG. 7

The German data on copper show very high values of m throughout the entire range of measurement. On the other hand, the British data on copper consist of only two m values, both less than 1.0. This apparent conflict is resolved by Fig. 7 which shows that the British points were measured at a much higher initial gasket stress than were any of the German data. The fact that the German data show no significant difference for the three gasket widths tested is difficult to explain.

The German paper gives a series of measurements made in a bolted-joint assembly at temperatures of about 200 C and 350 C. While these results are more subject to complications because of creep than are room-temperature data, it is of interest to note that m values for soft nonmetallic gaskets are somewhat reduced on the average when compared with room-temperature results. For copper gaskets, m values drop sharply with increased temperature, and values below 1.0 are observed at 350 C in the range of σ_{g1} where m values of 10 to 100 were obtained at room temperature. This effect is undoubtedly the result of the annealing and softening of copper in this temperature range. A similar temperature effect is also observed with aluminum.

Gasket Loading in Bolted Joints

Application of Internal Pressure. Having determined the gasket stresses which are required to assure tightness, it is now important to examine how the gasket stress in a bolted joint behaves under operating conditions.

In the bolted joint shown in Fig. 8 it is assumed that the flanges are perfectly rigid and that the bolt load is uniformly distributed over the entire gasket-flange contact area. Upon initial tightening of the joint, the bolts are given an initial stress, σ_{b1}, corresponding to which the gasket takes on an average stress σ_{g1}, which may be calculated by the equation

$$\sigma_{g1} A_g = \sigma_{b1} A_b \quad \ldots\ldots\ldots\ldots\ldots\ldots\ldots\ldots [6]$$

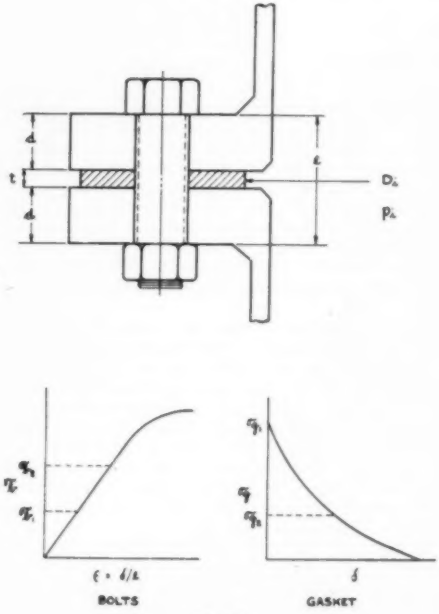

FIG. 8

where A_b is the effective cross-sectional area of the bolts.

When internal pressure p_i is applied to the vessel, the hydrostatic end force causes the bolt stress to increase to a new value, σ_{b2}, and the bolts increase in length by an amount δ. Simultaneously, the gasket increases in thickness by the same amount δ, and the gasket compressive stress is reduced to σ_{g2}. These changes are shown graphically in Fig. 8; the changes in bolt stress are shown to occur within the elastic range of the bolt material, and the $\sigma - \delta$ curve of the gasket is shown in general form. For the bolts

$$\sigma_{b2} - \sigma_{b1} = \epsilon E_b = \frac{\delta}{l} E_b \quad \ldots\ldots [7]$$

where E_b is the elastic modulus of the bolt material. For the gasket, the $\sigma - \delta$ restoration curve will, in general, be a function of σ_{g1}, so that we may write

$$\delta = f(\sigma_{g1}, \sigma_{g2}) \quad \ldots\ldots [8]$$

where this function is to be determined from measurements of the deformation properties of the gasket material.

Under this condition

$$\sigma_{g2} A_g + p_i A_i = \sigma_{b2} A_b \quad \ldots\ldots [9]$$

where A_i is the internal area based on the inside diameter of the gasket, D_i. Substituting into Equation [9] the values of σ_{b1}, σ_{b2}, and δ from Equations [6], [7], and [8], we find

$$(\sigma_{g1} - \sigma_{g2}) A_g = p_i A_i - \frac{E_b A_b}{l} f(\sigma_{g1}, \sigma_{g2}) \quad \ldots\ldots [10]$$

This equation will, in general, predict the change in average gasket stress upon application of internal pressure, if the function $f(\sigma_{g1}, \sigma_{g2})$ is known.

As a simple case we will assume a gasket material which obeys Hooke's law, so that

$$\delta = \frac{t}{E_g} (\sigma_{g1} - \sigma_{g2}) \quad \ldots\ldots [11]$$

where t is the gasket thickness and E_g is the modulus of the gasket material. Substituting in Equation [10] for $f(\sigma_{g1}, \sigma_{g2})$ we obtain

$$(\sigma_{g1} - \sigma_{g2}) A_g = \frac{p_i A_i}{1 + \dfrac{E_b A_b l}{E_g A_g l}} \quad \ldots\ldots [12]$$

By a similar derivation, it can be shown that the change in bolt stress for the case of the Hooke's law gasket is given by

$$(\sigma_{b2} - \sigma_{b1}) A_b = \frac{p_i A_i}{1 + \dfrac{E_g A_g t}{E_b A_b t}} \quad \ldots\ldots [13]$$

In design of a bolted joint, σ_{b2}, the allowable working stress of the bolts will be known, and A_b will not be known. Hence a convenient form of this relation will be

$$(\sigma_{g1} - \sigma_{g2}) A_g = \frac{p_i A_i}{1 + \dfrac{E_b l \sigma_{g2}}{E_g l \sigma_{b2}}} \quad \ldots\ldots [14]$$

A number of qualitative observations can be made from examination of Equation [12]. If E_g is very small (as, for example, with gum rubber) and the ratio $\dfrac{E_b A_b l}{E_g A_g l}$ is large, then $\sigma_{g1} - \sigma_{g2}$ will be small, indicating that the hydrostatic end force, $p_i A_i$, is taken up almost entirely by additional stress on the bolts, without significant loss of gasket stress. On the other hand, if E_g is large (metallic gasket) and the ratio $\dfrac{E_b A_b l}{E_g A_g l}$ is small compared with unity, then almost all of the hydrostatic end force is taken up by a decrease in the gasket compressive stress, with only a slight change in bolt stress. It is apparent that low modulus is a desirable characteristic of a gasket material from the point of view of maintaining gasket stress for tightness.

Elastic Properties of an Asbestos Gasket. This section summarizes some experiments carried out to determine the σ-δ curve for a typical gasket material. The material chosen for these tests was "Cranite," a compressed-asbestos gasket material sold in sheet form by the Crane Company, and used largely for high-pressure steam lines. The samples tested were 1-in. squares, $^1/_{16}$ in. thick. Each sample was placed in a tensile tester and a slight compressive load was applied. A dial gage was then set on the machine in such a way as to measure the amount of deflection under load. It was found essential to place both the gasket sample and the dial gage at the center of the movable part of the press in order to avoid errors due to cocking.

The first measurements were carried out by applying a compressive load and then measuring the retraction curve as the load was reduced. This procedure was repeated for increasing initial loads on each sample. It was soon found that such results were nonreproducible. A typical set of such measurements is shown in Fig. 9. The arrows show the direction of the load increments,

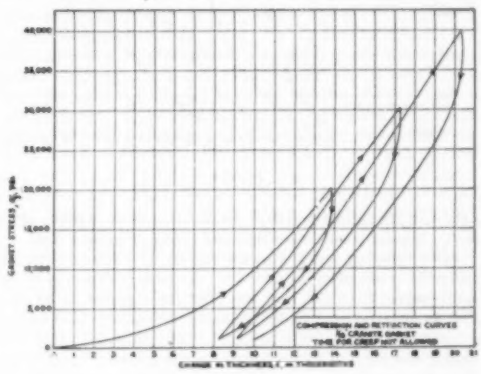

FIG. 9

i.e., compression or restoration of the gasket. It is apparent that each retraction curve did not coincide with the following compression curve, and that, when the compressive load again reached the highest previous compression stress, a decrease in thickness had occurred. This indicated that creep of the gasket was the complicating factor.

To test this possibility, a new sample was compressed to 10,000 psi, and this load was maintained while readings were taken at regular time intervals. The data taken during this period are plotted in Fig. 10. It can be seen that after about 20 min, the rate of creep became very small although not zero. After this was done the load was reduced in steps and the increase in gasket thickness was measured. At each point it was found that a five-minute period under constant load was sufficient to insure a constant dial-gage reading. Following the lowest reading at 1000 psi, the load was increased in steps up to the 10,000 psi applied initially. The resulting compression curve was found to coin-

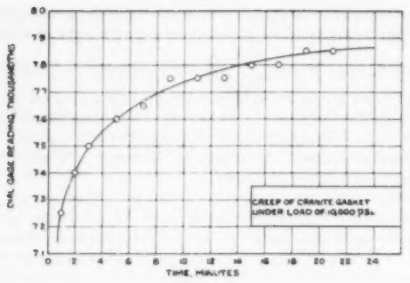

FIG. 10

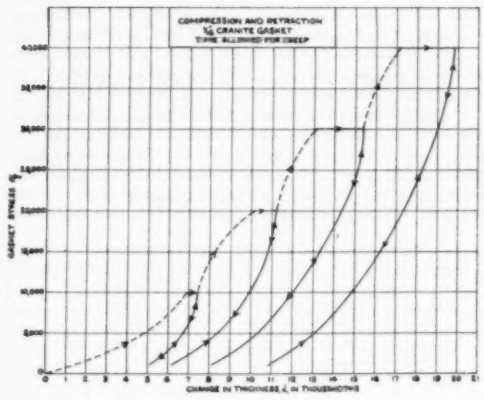

FIG. 11

cide with the retraction curve within one ten thousandth of an inch. Similar results were obtained at higher initial loads.

For a complete series of measurements on a new sample, the following procedure was adopted. At each increase in initial compressive stress the load was held for a period of 30 min. During retraction-curve measurements the load was held for five minutes at each point. Although time-consuming, this procedure was justified by the results, as can be seen from Fig. 11. Here the compression curves were always found to coincide with the previous retraction curves up to the point of initial stress. Each increment of initial stress appeared to generate a new stress-strain curve which is reproducible and independent of the previous lower-stress history of the sample.

For the purpose of calculating gasket stress in bolted joints, we are interested in the change in thickness along the retraction curve only. For simplicity of design calculations, it would be very desirable to use a constant E_g, but the proper E_g value will depend upon the range of gasket stresses occurring in the joint, and this range will be different for different vessel diameters and pressure conditions. However, it is tentatively proposed that E_g be obtained from a straight line drawn between the point of initial stress and the point at which the stress has been reduced to 50 per cent of the initial value, i.e.

$$E_g = \frac{t\,\sigma_{g1}/2}{\delta_{100\%} - \delta_{50\%}} \qquad [15]$$

where t is the initial (unstressed) gasket thickness. Use of this definition will result in safe calculations for bolted joints in which the gasket stress falls below 50 per cent of its initial value. For bolted joints in which the gasket stress lies between 50 and 100 per cent of the initial value, the error will lie in the direction of lower gasket stress, but will be a maximum of only about 12 per cent in σ_{g2} for the data of Fig. 11. This degree of accuracy will probably be considered adequate for design purposes.

By this definition the average retraction modulus for the four retraction curves of Fig. 11 is 480,000 psi.

For more rigid calculations it is possible to express the retraction data of Fig. 11 in the form of a single equation. We will set up our scale of δ starting from zero at σ_{g1} and increasing as σ_g is reduced. Furthermore, in order to place all four retraction curves of Fig. 11 on the same basis with regard to stress, we will express each value in terms of ratio σ_g/σ_{g1}, which will vary from unity to zero in all cases. On this basis the data are found to agree well with a parabola of equation

$$\left(1 - \frac{\sigma_g}{\sigma_{g1}}\right)^2 = 5.3 \times 10^5 \frac{\delta}{\sigma_{g1}^{0.8}} \qquad [16]$$

where δ is expressed in in., and σ_g and σ_{g1} in psi. In Fig. 12 the

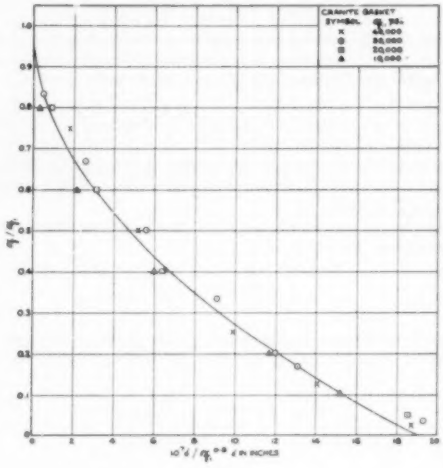

FIG. 12

actual data points are shown, and the curve is the parabola of Equation [16].

To express the stress-strain characteristics of the Cranite in terms of an elastic modulus, this may be found by differentiating Equation [16], since E_g will be a variable.

$$E_g = t\left(\frac{\partial \sigma_g}{\partial \delta}\right)_{\sigma_{g1}} = -5.3 \times 10^5 \frac{t\,\sigma_{g1}^{0.2}}{2\left(1 - \frac{\sigma_g}{\sigma_{g1}}\right)} \qquad [17]$$

where the minus sign merely expresses the fact that compressive stresses have been taken to be positive, and can be disregarded. From Equation [17] it can be seen that any one relaxation curve will show values of E_g beginning at infinity when $\sigma_g = \sigma_{g1}$, decreasing to a definite value when σ_g approaches zero. As an example, the limiting value of E_g for the 1/16-in. Cranite gasket and $\sigma_{g1} = 10{,}000$ psi, is 208,000 psi.

For calculation of gasket stress in a bolted joint using a Cranite

gasket, Equation [16] may be solved for δ and substituted for $f(\sigma_{g1}, \sigma_{g2})$ in Equation [10]. This results in a quadratic equation

$$(\sigma_{g1} - \sigma_{g2})^2 \frac{E_b A_b}{l K \sigma_{g1}^{1.5}} + (\sigma_{g1} - \sigma_{g2}) A_g - p_i A_i = 0 \quad [18]$$

where $K = 5.3 \times 10^6$, and which is the more general counterpart of Equation [12]. Similar solutions will give the non-Hooke's law equivalents of Equations [13] and [14].

Gasket Creep. With many gasket materials, the initial tightening of the bolted joint is followed by a slow reduction in gasket and bolt stress due to gasket creep. After a time the gasket stress may fall to a value below that required for sealing, at which time the bolts must be retightened. In many cases, however, retightening may not be convenient, since the flanges may not be accessible, or may be covered with insulation. For such cases it has been proposed that the joints be designed for a higher initial gasket stress so that the necessity for retightening will occur much less frequently. As the basis of such a design, a knowledge of the rate of unloading of the gasket is required and it should be possible to predict this from creep data on the gasket material.

We will assume that we have available from measurements on the gasket material in a test machine a series of curves of creep against time, each such curve corresponding to a constant value of gasket stress, σ_g. We will further assume that this family of curves can be expressed as a single continuous function of σ_g and the time, θ, i.e.

$$\epsilon_p = f(\sigma_g, \theta) \quad [19]$$

Here ϵ_p is the plastic strain, given by

$$\epsilon_p = \delta_p / t \quad [20]$$

where δ_p is the change in gasket thickness due to creep, and t is the total thickness. The assumption that Equation [19] is a continuous function of both σ_g and θ has been found to work well in predicting the creep relaxation of metals (3).

In a bolted joint, initial tightening gives

$$\sigma_{b_1} A_b = \sigma_{g1} A_g \quad [21]$$

After a time interval θ, the gasket thickness is decreased by an amount δ, due to creep. Simultaneously, the bolts decrease in length by the same amount, reducing σ_b and σ_g. With the reduction in σ_g, there is a certain amount of elastic recovery in the gasket, δ_e, which tends to compensate for the plastic change, δ_p, that is

$$\delta = \delta_p - \delta_e \quad [22]$$

The elastic change is assumed to occur independently of the plastic effect, and the flanges are assumed to be rigid. Dividing through by t

$$\epsilon = \epsilon_p - \epsilon_e \quad [23]$$

For the bolts

$$\sigma_{b_1} - \sigma_b = E_b \frac{\delta}{l} \quad [24]$$

Also

$$\sigma_b A_b = \sigma_g A_g \quad [25]$$

Substituting the values of σ_{b_1} and σ_b from Equations [21] and [25] into Equation [24], we obtain

$$\sigma_{g1} - \sigma_g = \frac{E_b A_b}{A_g l} \delta = \frac{E_b A_b t}{A_g l} \epsilon \quad [26]$$

For the gasket material, we may write

$$\epsilon_e = \frac{\sigma_{g1} - \sigma_g}{E_g} \quad [27]$$

where E_g is the elastic modulus obtained by retraction in the test machine. Substituting Equations [23] and [27] into Equation [26], we have

$$\sigma_{g1} - \sigma_g = \frac{E_b A_b t}{A_g l} \left[\epsilon_p - \frac{\sigma_{g1} - \sigma_g}{E_g} \right] \quad [28]$$

This equation, when the expression for ϵ_p is known, will allow direct calculation of σ_g as a function of time. If a constant value of E_g may not be used over the entire useful range of the data, E_g may have to be expressed as a function of σ_g and θ, thus complicating the solution.

This analysis covers the case of a bolted joint which has been merely tightened and allowed to stand. For the case in which internal pressure is applied to the joint immediately after tightening, the same derivation should hold, with the exception that σ_{g1} is reduced by an amount corresponding to the effect of the internal pressure load.

Unfortunately, there do not appear to be creep data in the literature which would be suitable for use in this problem, although data of this type should be relatively easy to obtain in a tensile-testing machine.

Distribution of Bolt Load. In our previous discussion it has been assumed that the bolt load is distributed uniformly over the entire gasket-flange contact area. In any actual case, the areas under the bolts are under concentrated load, and the efficiency of transmission of this load to the areas between bolts will be a function of the bolt spacing, the flange thickness, and the properties of the gasket material.

In bolted-joint design, the choice of a bolt spacing is made after the flanges have been designed for the internal pressure and gasket loads. Thus the total cross section of the bolts is known, and the decision to be made is that of distribution of this bolt area among few bolts of large size or more bolts of smaller size. Since this decision will not have a serious effect on the cost of the joint, only a rough theory is necessary to establish a criterion for bolt spacing. The following analysis is rough, but conservative, in that it considers straight flanges only and neglects any stiffening effect of the vessel walls such as would occur in a circular joint or at the corner of a rectangular joint.

An approach to this problem can be made by an extension of the method used by Soderberg (4) in the analysis of metal-to-metal joints. For this analysis we will assume that the gasket obeys Hooke's law, and that the flange and gasket combination represents an elastic foundation for which

$$q = -ky \quad [29]$$

where q is the unit load on the foundation, k is the modulus of the foundation, and y is the deflection (5). To determine k, assume that the joint is split in half at the center of the gasket, and that one flange and one half of the gasket are on a rigid foundation, see Fig. 13A. A load P applied uniformly over a length of flange a will cause a compressive strain in the half-gasket of $\Delta t/2$, and in the flange of Δd. However, since elastic theory is based on the deflection of the center line of the beam, the compressive strain of the flange used in calculating the modulus of the foundation is $\Delta d/2$. Hence

$$k = \frac{P}{a\left(\frac{\Delta d}{2} + \frac{\Delta t}{2}\right)} \quad [30]$$

For the flange

$$E_f = \frac{\sigma}{\epsilon} = \frac{P/ab_f}{\Delta d/d} \quad [31]$$

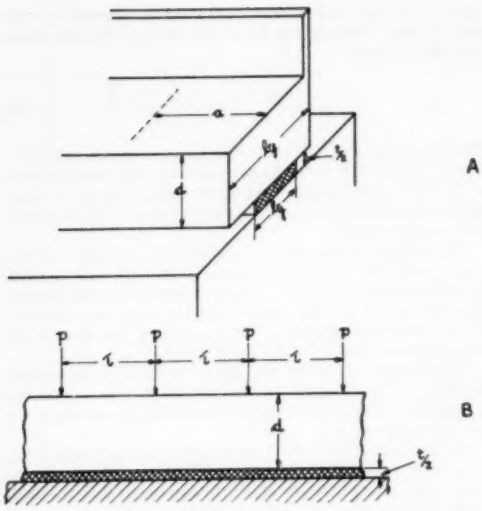

FIG. 13

and

$$\Delta d = \frac{Pd}{ab_f E_f} \quad \text{[31a]}$$

For the gasket

$$E_g = \frac{\sigma}{\epsilon} = \frac{P/ab_g}{\Delta t/t} \quad \text{[32]}$$

and

$$\Delta t = \frac{Pt}{ab_g E_g} \quad \text{[32b]}$$

Substituting in Equation [30]

$$k = \frac{2}{\dfrac{d}{b_f E_f} + \dfrac{t}{b_g E_g}} \quad \text{[33]}$$

It should be noted here that it has been assumed that the flange deflects uniformly over its entire width b_f in spite of the fact that only the width b_g rests upon the gasket. Evidently some flange width between b_g and b_f would give a more accurate approximation to the actual case, but this complicating effect has been neglected.

The theory of a beam on an elastic foundation (5) gives the following equation for the deflection y as a function of the distance x from a point of concentrated load P

$$y = \frac{P\beta}{2k} e^{-\beta x} (\cos \beta x + \sin \beta x) \quad \text{[34]}$$

where

$$\beta = \sqrt[4]{\frac{k}{4\,EI}} \quad \text{[35]}$$

in which E is the modulus of elasticity and I is the moment of inertia of the beam. Since the unit distributed load $q = -ky$, then

$$q = -\frac{P\beta}{2} e^{-\beta x} (\cos \beta x + \sin \beta x) \quad \text{[36]}$$

If we designate the unit load under the point of concentrated load P by q_0, then, since $x = 0$

$$q_0 = -\frac{P\beta}{2} \quad \text{[37]}$$

and

$$\frac{q}{q_0} = e^{-\beta x} (\cos \beta x + \sin \beta x) \quad \text{[38]}$$

We will represent our flange in Fig. 13B as a beam with a series of point loads P representing the bolts, having a spacing τ between bolts. To calculate the load intensity q at any point on the beam, the principle of superposition is used, i.e., the contribution of each bolt to the unit load at the point in question is calculated independently, and all are added together. For our case

$$\beta = \sqrt[4]{\frac{2}{\dfrac{d}{b_f E_f} + \dfrac{t}{b_g E_g}}} \Big/ 4\,E_f \times \frac{b_f d^3}{12} = \frac{1.565}{d} \sqrt[4]{\frac{1}{1+S}} \quad \text{[39]}$$

where

$$S = \frac{tb_f E_f}{db_g E_g} \quad \text{[40]}$$

In the case where $t = 0$, i.e., metal-to-metal joint, $S = 0$, and $\beta = 1.565/d$, which is the result obtained by Soderberg.

For the purpose of predicting the bolt spacing, τ, we are interested in the ratio of q at $x = \tau/2$ to q_0 at $x = 0$. It can be seen from the form of Equations [38] and [39] that τ is best expressed in terms of multiples of flange thickness, i.e., $\tau = nd$ so that for any given S, q/q_0 will vary only with the number n. Thus at $x = \tau/2$

$$\beta x = \frac{1.565}{d} \sqrt[4]{\frac{1}{1+S}} \times \frac{nd}{2} = 0.783\, n \sqrt[4]{\frac{1}{1+S}} \quad \text{[41]}$$

and q/q_0 will be a unique function of $\dfrac{\tau}{d}\sqrt[4]{\dfrac{1}{1+S}}$ which will be applicable to all gasket-flange combinations. This relation was calculated, and for high q/q_0, it was found necessary to include the contributions of as many as 15 bolts to obtain the desired accuracy. The result is shown in Fig. 14.

The question now arises as to what value of q/q_0, i.e., what ratio of the loading midway between bolts to the loading under the bolts, should be used as a criterion for bolt spacing. A choice which appears to have some support from leakage evidence in the Elliott oxygen pilot plant (6) is $q/q_0 = 0.95$. A design chart on this basis is given in Fig. 15.

The major uncertainty which occurs with the use of Fig. 15 is that of the value of E_g. For transmission of load during initial tightening of the joint, presumably some average modulus for compression should be used. When internal pressure is applied and relaxation of the gasket occurs, the effective modulus may be of an entirely different order of magnitude. Of course whatever modulus is decided upon, the value of q/q_0 which is used as a criterion will be adjusted to fit the actual results.

For analysis of the leakage evidence from the Elliott oxygen pilot plant, an average compression modulus was determined in

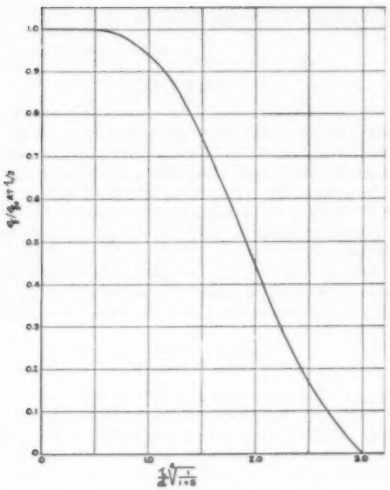

FIG. 14

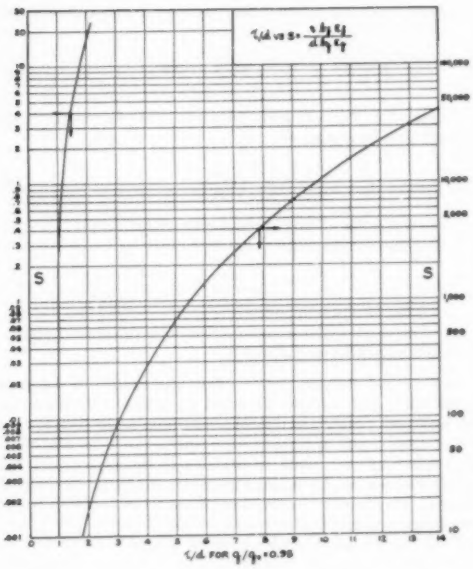

FIG. 15

the tensile tester for the range of loads used. The modulus during the initial compression was chosen because it was felt that the initial tightening was the more important phase of the problem with low-pressure joints. The tensile-tester measurements gave almost linear stress-strain curves over the ranges tested for the three gasket materials mentioned below. The following examples are based upon room-temperature leakage evidence only:

HEAT EXCHANGERS

Rubber Gaskets

Gaskets, $t = 3/16$ in., $b_g = 3/8$ in., $E_g = 7500$ psi
Flanges, $d = 1/4$ in., $b_f = 1$ in., $E_f = 30{,}000{,}000$ psi
Rectangular joints.
$S = 8000$
τ/d, actual = 6.0
τ/d, maximum allowable (Fig. 15) = 9.3
These joints showed no evidence of leakage.

Vellumoid Gaskets

Gaskets, $t = 1/16$ in., $b_g = 3/8$ in., $E_g = 19{,}000$ psi
Flanges, $d = 1/4$ in., $b_f = 1$ in., $E_f = 30{,}000{,}000$ psi
Rectangular joints.
$S = 1050$
τ/d, actual = 6.0
τ/d, maximum allowable (Fig. 15) = 5.6
These joints showed occasional leaks. It is of interest that many of these gaskets showed evidence of crushing in the areas beneath the bolts, but were soft and pliable in the areas between the bolts.

FRACTIONATING COLUMN

Top of Reboiler. Copper-Clad Asbestos Gasket

Gasket, $t = 1/8$ in., $b_g = 7/8$ in., $E_g = 20{,}000$ psi
Flanges, $d = 5/8$ in., $b_f = 2$ in., $E_f = 30{,}000{,}000$ psi
Bolt circle, $21\ 3/4$ in. diam., 20 bolts
$S = 686$
τ/d, actual = 5.5
τ/d, maximum allowable (Fig. 15) = 5.0
This joint could not be made tight, and finally the gasket was eliminated and the flanges were soldered together.

Bottom of Reboiler. Copper-Clad Asbestos Gasket

Gasket, $t = 5/32$ in., $b_g = 7/8$ in., $E_g = 20{,}000$ psi
Flanges, $d = 3/4$ in., $b_f = 2$ in., $E_f = 30{,}000{,}000$ psi
Bolt circle, $48\ 1/2$ in. diam., 48 bolts.
$S = 720$
τ/d, actual = 4.2
τ/d, maximum allowable (Fig. 15) = 5.1
This joint did not leak.

The $q/q_0 = 0.95$ criterion is considered entirely tentative, and is subject to revision after considerably more evidence is available on leakage of joints as a function of bolt pitch, and on the elastic properties of gaskets. There are refinements which may be made in this development which do not appear to be justified at the present time, in view of the gasket modulus uncertainty. These include corrections for the fact that the bolt heads and nuts actually cover a finite area rather than being point loads, and for the stiffening effect of the vessel walls on the flanges. The latter effect will be particularly important for small-diameter joints such as occur in piping. Evidently, for such joints, the use of Fig. 15 may result in considerable overdesign.

DESIGN OF BOLTED JOINTS

The design rules given in the ASME Code (7) are basically at fault for the following reasons:

1 The m values given in Table UA-8(a), corrected by the addition of 0.5 to obtain m as defined in this paper (the Code uses one half the gasket area as a design basis), range from 1.0 for gum rubber to 7.0 for stainless steel. No account is taken of the fact that all m values approach unity (or less, for gaskets which stick) with increasing initial gasket stress. No account is taken

of the variation of m with gasket width, or possible variations of m with gasket thickness or flange surface finish.

2 A yield point value y is used, evidently in implicit recognition of the fact that a certain amount of initial gasket stress is required to reduce m to a low value in the case of low-pressure joints. The reduction of m with increasing initial stress is shown by the data of Siebel, Hering, and Raible to be a gradual one, i.e., there is no unique value of initial stress which can be called a "yield value."

3 While the bolt load is designed to carry both the internal pressure force and the residual gasket stress required for tightness, no consideration is given to the elastic properties of the gasket material, and there is no assurance that the residual gasket stress or the bolt stress will be that calculated. As a corollary, it must be recognized that the initial tightening conditions will play a large part in determining operating stresses under pressure.

4 Finally, the Code provides no basis for choice of bolt spacing, specifying merely the total bolt load.

A proposed revision of Table UA-8(a) has been presented by Rossheim and Markl (8). The discussion which followed this paper (9) presents in more emphatic and detailed form some of the criticisms just given.

The criticisms of the Code given here should not be interpreted as implying that bolted joints designed in accordance with the Code will leak. While it is possible to conceive of designs where this would occur, such situations are evidently avoided in practice by the experienced designer. In many cases where the Code is used, the joints appear to be considerably overdesigned. Therefore the major contribution of any new design procedure will be to provide an accurate knowledge of the extent of the safety factor in any joint, as well as to prevent any possibility of joint leakage due to incorrect formulation of design rules.

The portion of bolted-joint design with which we are concerned consists of the calculation of the least total bolt load which assures tightness. This will result in the most economical design since it is this bolt load which determines the bending moments for which the flanges are designed.

For the new design procedure it is assumed that the following information on the available gasket materials will be available for design purposes:

1 The variation of m with initial gasket stress, gasket width, gasket thickness, and flange surface finish. It is assumed that the data will be available in the form of graphs of the type of Figs. 1 through 7, and that appropriate safety factors will have been applied to the curves to cover any uncertainties in the data.

2 Stress-strain curves of the gasket material over the useful range of gasket stress and thickness, both for compression and recovery. Any effects of creep are neglected because of the absence of data on this subject.

The design procedure consists of the following steps:

(a) Within the limitations of temperature and corrosion conditions, choose the gasket material which requires the lowest σ_{g1} for a given m value.

(b) Assume a gasket thickness, gasket width, and σ_{g1} value, and read the value of m. For any values of m which are less than unity, assume $m = 1$.

(c) Calculate σ_{g2} by the Equation

$$\sigma_{g2} = mp_i \qquad [5a]$$

The value of σ_{g2} must be less than σ_{g1}. If this is not the case, a new value of σ_{g1} must be tried. As a guide, σ_{g2} should be much less than σ_{g1} for a gasket with high modulus, and closer to σ_{g1} for a gasket with low modulus.

(d) Calculate σ_{g1} from the Equation

$$\sigma_{g1} = \sigma_{g2} + \frac{p_i A_i}{A_g\left(1 + \dfrac{E_g l}{E_g' l'}\dfrac{\sigma_{g2}}{\sigma_{g2}}\right)} \qquad [14a]$$

where σ_{b2} is the allowable working stress of the bolts. For this solution, use the value of σ_{g2} from step (c), and guess at a reasonable value of l, the effective bolt length.

(e) In general, the value of σ_{g1} calculated by step (d) will not be equal to the value initially assumed. Assume new σ_{g1} values and repeat steps (b), (c), and (d) until agreement is obtained.

(f) Repeat steps (b), (c), (d), and (e) for several different gasket widths (and thicknesses, if this produces any significant effect). A gasket width will be found for which the bolt load, given by

$$W_m = \sigma_{b2}A_b = \sigma_{g2}A_g + p_i A_i \qquad [9]$$

will be a minimum. This is the design bolt load.

(g) Design the flanges in accordance with the methods given in the ASME Code. Check the effective bolt length, l, against the value assumed in step (d). If there is a significant difference, the design must be repeated. In general, however, sizable variations in l will influence the design only slightly.

(h) Determine the number of bolts n from the gasket and flange dimensions, such that τ/d is lower than the value given by Fig. 15

$$n = \frac{\pi G}{\tau} \qquad [42]$$

where G is the bolt circle diameter. The size of the bolts will then be given by

$$a_b = \frac{A_b}{n} \qquad [43]$$

where a_b is the effective cross section of one bolt.

(i) Calculate the initial stress in the bolts by the equation

$$\sigma_{b1} = \frac{\sigma_{g1}A_g}{A_b} \qquad [6a]$$

This is the initial stress to which the bolts should be tightened in making up the joint.

This method of design, and, in fact, any method of design of bolted joints depends upon the initial tightening of the bolts to a known stress. Failure to tighten the bolts up to the design stress will of course result in leakage when internal pressure is applied. Overtightening may result in crushing of the gasket, and will generate stresses in the flange greater than assumed in the original design. The use of torque wrenches is recommended, with proper precautions as to lubrication of the threads.

While the design procedure given in this section may be considered lengthy, it is to be expected that it will be considerably shortened when basic data become available. At that time the construction of design charts or nomographs will probably be justified.

The foregoing discussions have indicated the type of data which are required for complete design of bolted joints. In summary, this consists of the measurement of gasket factors, elastic properties, and creep properties of gasket materials, as well as data on bolt load distribution. These factors should be determined for the gasket materials in common use as a function of gasket width, gasket thickness, temperature, flange surface

finish, and initial stress. This list may seem formidable, but the bulk of the data can be obtained by relatively simple and rapid compression-machine techniques.

Acknowledgment

The writer wishes to express his appreciation to Messrs. J. L. Cost, E. S. Dennison, and W. K. Bodger of the Elliott Company, and to Mr. F. C. Thorn of the Garlock Packing Company, or their co-operation and helpful discussions of these problems.

BIBLIOGRAPHY

1 "Versuche über das Verhalten von Dichtungen," by E. Siebel, W. G. Hering, and A. Raible, *Forshung auf dem Gebiete des Ingenieurwesens*, vol. 5, 1934, pp. 298–305.

2 "First Report of the Pipe Flanges Research Committee," by H. J. Gough, Proceedings of The Institution of Mechanical Engineers, vol. 132, 1936, pp. 201–340.

3 "Correlation of Tension Creep Tests With Relaxation Tests," by E. P. Popov, JOURNAL OF APPLIED MECHANICS, Trans. ASME, vol. 69, 1947, p. A-135.

4 Discussion on "Practical Aspects of Turbine Cylinder Joints," by C. Richard Soderberg, JOURNAL OF APPLIED MECHANICS, Trans. ASME, vol. 61, 1939, p. A-31.

5 "Strength of Materials," Part 2, by S. Timoshenko, D. Van Nostrand Company, New York, N. Y., second edition, 1941.

6 "The Elliott Oxygen Pilot Plant," by I. Roberts, D. Aronson, M. Atcheson, L. C. Claitor, J. L. Cost, and D. B. Crawford, to be published in *Industrial and Engineering Chemistry*.

7 "Rules for Construction of Unfired Pressure Vessels," Section VIII, ASME Boiler Construction Code, 1943, pp. 130–140.

8 "Gasket Loading Constants," by D. B. Rossheim and A. R. C. Markl, *Mechanical Engineering*, vol. 65, 1943, p. 647.

9 Discussion on "Gasket Loading Constants," *Mechanical Engineering*, vol. 66, 1944, p. 72.

A Quantitative Comparison of Flow and Deformation Theories of Plasticity[1]

By P. G. HODGE, JR.,[2] AND G. N. WHITE, JR.,[3] PROVIDENCE, R. I.

The stresses and displacements in a partly plastic, infinitely long, hollow cylinder are obtained according to the flow type of stress-strain law of Prandtl-Reuss and to the deformation law of Hencky. In both cases the Mises yield condition is used and the compressibility of the material is taken into account. It is shown that under these assumptions the two theories yield substantially the same results for this particular problem, but that one theory or the other may be preferable for computing purposes in certain cases. The results are compared with those of other investigations in which different combinations of stress-strain law, yield condition, compressibility, and end loading were assumed.

Introduction

In the investigation of the elastic behavior of materials, Hooke's law is the accepted stress-strain relation. On the other hand, for materials in a plastic state, there are many stress-strain theories available. In addition, for plastic materials some criterion of initial and continued plastic flow must be selected.

This paper considers an ideal material which is assumed to behave elastically under stresses which do not satisfy the yield condition and to flow or deform under constant stress when the yield condition is satisfied. The yield condition chosen is that of Mises (1),[4] according to which the material behaves plastically when the octahedral shearing stress reaches a certain critical value. Such a material does not exhibit strain-hardening and is called perfectly plastic. Usually such a material is assumed incompressible since permanent volume changes are known to be negligible in a fully plastic state. If, however, a study of the elastic-plastic behavior is to be made, the total strain in the plastic region is considered to consist of a reversible elastic strain, obeying Hooke's law, and a permanent plastic strain which is not accompanied by any volume changes. To simplify the mathematical work the elastic volume changes are often neglected. In the following, however, the elastic compressibility of the material will be taken into account.

The most important theoretical difference between the theories of a perfectly plastic material is that manifested by the various stress-strain laws. These fall into two distinct categories; "deformation"[5] laws, which involve only the instantaneous states of stress and strain, and "flow"[5] laws, which involve the strain rates as well.[6] The usually accepted law of the flow type for elastic-plastic problems of a perfectly plastic material is that of Prandtl (4) and Reuss (5), while the usual deformation law is that of Hencky (6). For the elementary cases of simple tension or of torsion of cylindrical bars, the two theories give identical predictions.

On the other hand, the mathematical difficulties presented by the most general problems are too great to permit a general comparison of the two theories. For the particular case of plane strain with radial symmetry, however, a mathematical difference is observed. In this paper a typical problem of plane strain will be solved by each of the two theories. The results will be compared with each other and with the solutions obtained by other authors.

Basic Relations

The basic equations for this problem are well known Let the tube be referred to a set of cylindrical co-ordinates r, θ, z, such that the z-axis coincides with the axis of the tube. The radial, tangential, and normal stress will be denoted by σ_r, σ_θ, and σ_z, respectively; a similar notation will be used for the strains. Since the tube is in a state of plane strain with rotational symmetry, the following relations are valid (7, 8)

$$\left.\begin{aligned} &\sigma_r = \sigma_r(r,\rho), \quad \sigma_\theta = \sigma_\theta(r,\rho), \quad \sigma_z = \sigma_z(r,\rho) \\ &\tau_{r\theta} = \tau_{zr} = \tau_{z\theta} = 0 \\ &u_r = u(r,\rho), \quad u_\theta = u_z = 0 \\ &\epsilon_r = \frac{\partial u}{\partial r}, \quad \epsilon_\theta = \frac{u}{r}, \quad \epsilon_z = 0 \\ &\gamma_{r\theta} = \gamma_{z\theta} = \gamma_{zr} = 0 \end{aligned}\right\} \quad \ldots\ldots [1]$$

where ρ is some parameter which is characteristic of the state of deformation or flow.

The only equilibrium equation which is not satisfied identically reduces to

$$\frac{\partial \sigma_r}{\partial r} + \frac{\sigma_r - \sigma_\theta}{r} = 0 \quad \ldots\ldots [2]$$

If the three equations of Hooke's law are added to Equation [2], there are then four equations for the four unknown functions u, σ_r, σ_θ, and σ_z in the elastic region. In the plastic region, although there are only two independent stress-strain relations, the yield condition provides the necessary fourth equation.

If a hollow cylinder of inner radius a and outer radius b is subjected to an internal pressure p, then the boundary conditions for the problem are

$$\sigma_r(a) = -p, \quad \sigma_r(b) = 0 \quad \ldots\ldots [3]$$

---

[1] The material for this paper was obtained in the course of research conducted under Contract N7onr-358 sponsored jointly by the Office of Naval Research and the Bureau of Ships.

[2] Research Associate in Applied Mathematics, Brown University.

[3] Research Assistant in Applied Mathematics, Brown University.

[4] Numbers in parentheses refer to the Bibliography at the end of the paper.

Contributed by the Applied Mechanics Division and presented at the Annual Meeting, New York, N. Y., November 27–December 2, 1949, of The American Society of Mechanical Engineers.

Discussion of this paper should be addressed to the Secretary, ASME, 29 West 39th Street, New York, N. Y., and will be accepted until July 10, 1950, for publication at a later date. Discussion received after the closing date will be returned.

Note: Statements and opinions advanced in papers are to be understood as individual expressions of their authors and not those of the Society. Paper No. 49—A-5.

[5] These terms are due to Ilyushin (2).

[6] For a general discussion of the relative merits of the two types of laws, see, for instance, (2) and (3).

In addition, σ_r and σ_θ must both be continuous across any elastic-plastic boundaries.[7]

It will prove convenient to introduce stress and strain deviators defined by

$$\left.\begin{aligned} s_r &= \sigma_r - s, \quad s_\theta = \sigma_\theta - s, \quad s_z = \sigma_z - s \\ e_r &= \epsilon_r - e, \quad e_\theta = \epsilon_\theta - e, \quad e_z = \epsilon_z - e \end{aligned}\right\} \quad \ldots\ldots [4]$$

where

$$\left.\begin{aligned} s &= \frac{1}{3}(\sigma_r + \sigma_\theta + \sigma_z) \\ e &= \frac{1}{3}(\epsilon_r + \epsilon_\theta + \epsilon_z) = \frac{1}{3}\left(\frac{\partial u}{\partial r} + \frac{u}{r}\right) \end{aligned}\right\} \quad \ldots\ldots [5]$$

In terms of the stress deviator, Equation [2] becomes

$$\frac{\partial s_r}{\partial r} + \frac{\partial s}{\partial r} + \frac{s_r - s_\theta}{r} = 0 \quad \ldots\ldots [6]$$

while the strain-deviator components are given by

$$\left.\begin{aligned} e_r &= \frac{1}{3}\left(2\frac{\partial u}{\partial r} - \frac{u}{r}\right), \quad e_\theta = \frac{1}{3}\left(\frac{2u}{r} - \frac{\partial u}{\partial r}\right) \\ e_z &= \frac{1}{3}\left[-\frac{\partial u}{\partial r} - \frac{u}{r}\right] = -e \end{aligned}\right\} \quad \ldots\ldots [7]$$

Elastic Solution

For sufficiently small values of the pressure, the entire tube will behave elastically. The solution for this case is well known (7). In terms of the present variables it may be written

$$\left.\begin{aligned} s_r &= p_e\left[\frac{G}{G+3K} - \frac{b^2}{r^2}\right], \quad s_\theta = p_e\left[\frac{G}{G+3K} + \frac{b^2}{r^2}\right] \\ \sigma_r &= p_e\left[1 - \frac{b^2}{r^2}\right], \quad \sigma_\theta = p_e\left[1 + \frac{b^2}{r^2}\right], \\ \sigma_z &= p_e\left[\frac{3K-2G}{G+3K}\right] \\ u &= \frac{3}{2}p_e\left[\frac{r}{G+3K} + \frac{b^2}{3Gr}\right], \\ J_2 &= p_e^2\left[3\left(\frac{G}{G+3K}\right)^2 + \frac{b^4}{r^4}\right] \end{aligned}\right\} \quad \ldots [8]$$

where

$$p_e = \frac{pa^2}{b^2 - a^2} \quad \ldots\ldots [9]$$

Here G is the modulus of rigidity and K the bulk modulus. Equations [8] will be the solution for all values of the pressure such that the octahedral shearing stress does not exceed the critical value at any point, i.e., such that

$$J_2 = s_r^2 + s_\theta^2 + s_r s_\theta < k^2 \quad \ldots\ldots [10]$$

where k is the yield stress in pure shear. Obviously, this condition will first be violated at the inner surface $r = a$, the necessary pressure being

$$p_1 = k\,\frac{b^2 - a^2}{a^2}\left[\frac{b^4}{a^4} + 3\left(\frac{G}{G+3K}\right)^2\right]^{-1/2} \quad \ldots\ldots [11]$$

[7] Although the stress and strain rates may be discontinuous across an elastic-plastic boundary, the components themselves must be continuous. The proof of this is based upon the fact that a given material particle is only on the elastic-plastic boundary for an infinitesimal length of time. Since the stress and strain rates are continuous in the elastic and in the plastic domains, and, since the discontinuities at boundary must be finite, it follows that the integrated components will be continuous throughout the tube.

For pressures slightly greater than p_1 a plastic zone will form which will extend from the inner surface $r = a$ to some surface $r = \rho$ (elastic-plastic boundary). Although the equilibrium equations and stress-strain law in the elastic region ($\rho < r < b$) remain the same for this elastic-plastic state, the boundary conditions are now given by

$$\left.\begin{aligned} J_2 &= s_r^2 + s_\theta^2 + s_r s_\theta = k^2 \quad \text{at } r = \rho \\ \sigma_r &= 0 \quad \text{at } r = b \end{aligned}\right\} \quad \ldots\ldots [12]$$

It is readily verified that the solution is still given by Equations [8] provided that the value of p_e is replaced by

$$p_p = k\left[\frac{b^4}{\rho^4} + 3\left(\frac{G}{G+3K}\right)^2\right]^{-1/2} \quad \ldots\ldots [13]$$

The Prandtl-Reuss Solution

The plastic problem will first be solved for a material obeying the Prandtl-Reuss stress-strain law

$$\left.\begin{aligned} 2G\frac{\partial e_r}{\partial \rho} &= \frac{\partial s_r}{\partial \rho} + \lambda s_r, \quad 2G\frac{\partial e_\theta}{\partial \rho} = \frac{\partial s_\theta}{\partial \rho} + \lambda s_\theta, \\ 2G\frac{\partial e_z}{\partial \rho} &= \frac{\partial s_z}{\partial \rho} + \lambda s_z \\ s &= 3Ke \end{aligned}\right\} \quad \ldots [14]$$

Here λ is a function of the rate of plastic work of deformation, and ρ, the radius of the elastic-plastic boundary, is a characteristic parameter of the plastic flow. The elimination of λ from Equations [14] leads to the relations

$$\left.\begin{aligned} 2G\left(\frac{\partial e_r}{\partial \rho}s_\theta - \frac{\partial e_\theta}{\partial \rho}s_r\right) &= s_\theta\frac{\partial s_r}{\partial \rho} - s_r\frac{\partial s_\theta}{\partial \rho} \\ s &= 3Ke \end{aligned}\right\} \quad \ldots\ldots [15]$$

For the plastic domain the stress components must also satisfy the Mises yield condition

$$J_2 = s_r^2 + s_\theta^2 + s_r s_\theta = k^2 \quad \ldots\ldots [16]$$

If Equation [16] is solved for one of the stress-deviator components, there appears to be a certain ambiguity of sign; thus

$$s_\theta = -\frac{s_r \pm \sqrt{4k^2 - 3s_r^2}}{2} \quad \ldots\ldots [17]$$

However, in the elastic domain

$$2s_\theta + s_r = p_e\left(\frac{3G}{G+3K} + \frac{b^2}{r^2}\right) > 0 \quad \ldots\ldots [18]$$

Since s_θ and s_r are to be continuous across any elastic-plastic boundary, the upper sign in Equation [17] must hold in the plastic zone as well. The remaining necessary equation for the plastic problem is of course the equilibrium Equation [6].

It is found convenient to set up the problem in terms of the mean normal strain e and a new variable φ, defined by

$$\varphi = \frac{1}{3}\left(\frac{\partial u}{\partial r} - \frac{u}{r}\right) \quad \ldots\ldots [19]$$

If u is eliminated from Equations [5] and [19], it is seen that φ and e must satisfy the "compatibility condition"

$$\frac{\partial e}{\partial r} - \frac{\partial \varphi}{\partial r} = \frac{2\varphi}{r} \quad \ldots\ldots [20]$$

If the Mises yield condition, Equation [17], and the variables e and φ are substituted into the Prandtl-Reuss stress-strain law

Equations [15], the resulting equation is

$$\frac{\partial s_r}{\partial \rho} - \frac{G}{4k^2}\left(4k^2 - 3s_r^2 - 3s_r\sqrt{4k^2 - 3s_r^2}\right)\frac{\partial e}{\partial \rho} - \frac{3}{4}\frac{G}{k^2}\left(4k^2 - 3s_r^2 + s_r\sqrt{4k^2 - 3s_r^2}\right)\frac{\partial \varphi}{\partial \rho} = 0 \quad \ldots [21]$$

In terms of the same variables, the equilibrium Equation [2] becomes

$$\frac{\partial s_r}{\partial r} + 3K\frac{\partial e}{\partial r} = -\frac{3s_r + \sqrt{4k^2 - 3s_r^2}}{2} \quad \ldots [22]$$

Equations [20], [21], and [22] form a hyperbolic system of three quasi-linear first-order partial differential equations with independent variables r and ρ, and dependent variables s_r, e, and φ. These equations are to be solved in the domain $a \leq r \leq \rho$, $a \leq \rho \leq b$. The necessary boundary values are given by the values of e, φ, and s_r on $r = \rho$ as determined by the solution for the elastic domain. Although these equations cannot be solved in closed form, they can be transformed to a system of difference equations and solved numerically.

The Hencky Solution

Hencky's stress-strain law expresses the fact that the principal stress-deviator components are in the same ratio as the principal strain-deviator components; thus

$$s_r : s_\theta : s_z = e_r : e_\theta : e_z \quad \ldots [23]$$

or equivalently

$$s_r e_\theta = s_\theta e_r \quad \ldots [24]$$

In view of Equation [17], the Hencky stress-strain law may be written in the form

$$s_r(e - 3\varphi) = -\frac{s_r + \sqrt{4k^2 - 3s_r^2}}{2}(e + 3\varphi) \quad \ldots [25]$$

If Equation [25] is solved for e, and the result substituted into Equations [20] and [22], a system of two first-order ordinary differential equations is obtained. These equations, like those of the Prandtl-Reuss solution, must be solved by numerical methods.

Comparison of Results

The problem of a thick-walled tube under internal pressure, being one of the more accessible plasticity problems, has been studied from a variety of viewpoints. However, to the authors' knowledge, this problem has not yet been used to compare the flow and deformation theories when all other factors are the same. In the present section the results furnished by these two theories will be compared with each other and with the results of other authors.[9] The chief points of difference in investigating this problem are the stress-strain law, the yield condition, the allowance for compressibility, and the assumption concerning the axial strain. A summary of the theories analyzed is presented in Table 1, and the results are presented graphically in Figs. 1 to 4, inclusive. For the purpose of comparison a particular problem has been solved by numerical methods according to both the Prandtl-Reuss and Hencky theories. The following numerical values were assigned to the parameters involved

$$b/a = 2, \quad \rho/a = 1.5$$

$$\nu = 0.3, \quad k/G = 0.003$$

In Table 1 and in Figs. 1 to 4, inclusive, curve A shows the re-

[9] Other comparisons of published results are to be found in articles by D. G. Sopwith (9) and Beliaev and Sinitski (10).

TABLE 1. THEORIES OF PLASTICITY APPLIED TO A THICK-WALLED TUBE UNDER INTERNAL PRESSURE

Curve	Stress-strain law	Yield condition	Compressibility: Elastic	Compressibility: Plastic	Axial strain	Reference
A	Prandtl-Reuss	Mises	Comp.	Comp.	$\epsilon_z = 0$	
B	Prandtl-Reuss	Tresca	Comp.	Comp.	$\epsilon_z = 0$	(11)
C	Hencky	Mises	Comp.	Comp.	$\epsilon_z = 0$	
D	Hencky	Mises	Comp.	Comp.	$\epsilon_z \neq 0$	(13)
E	Either[a]	Either[a]	Comp.	Incomp.	$\epsilon_z = 0$	(14)
F	Either[a]	Either[a]	Incomp.	Incomp.	$\epsilon_z = 0$	(15)

[a] Under the assumption of plastic incompressibility, the two stress-strain laws and the two yield conditions coincide.

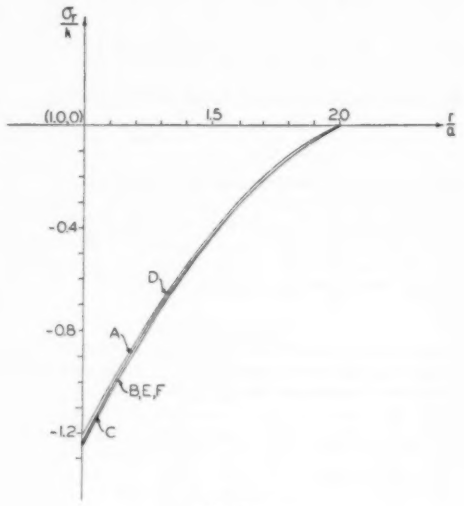

Fig. 1

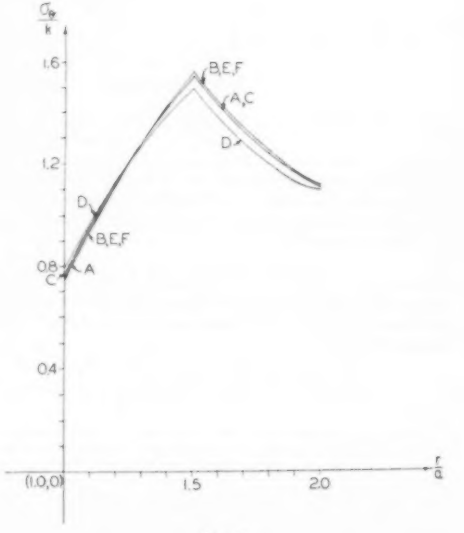

Fig. 2

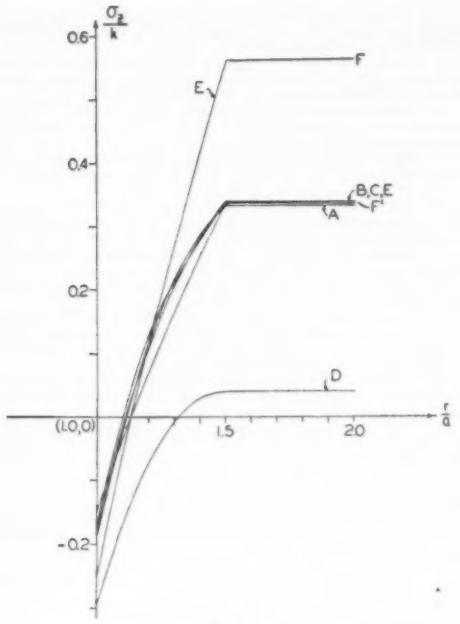

FIG. 3

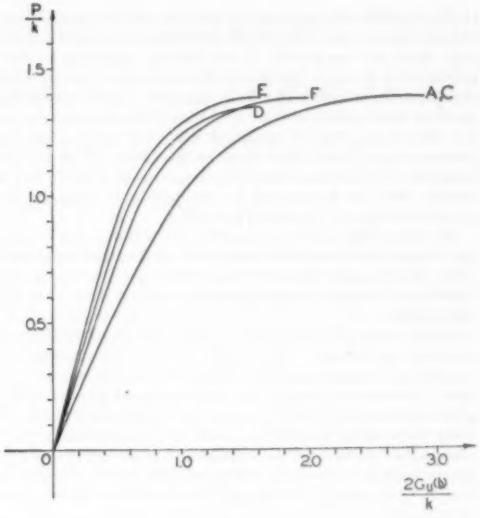

FIG. 4

sults of the Prandtl-Reuss stress-strain law with the Mises yield condition obtained from the solution of Equations [20], [21], and [22]. Curve *B* was obtained by Hill, Lee, and Tupper (11) using the Prandtl-Reuss law with the Tresca (12) yield condition, according to which plastic flow takes place when the maximum shear reaches a certain critical value. This simplifies the problem considerably, as the equilibrium equation reduces to

$$\frac{\partial \sigma_r}{\partial r} = \frac{\sigma_\theta - \sigma_r}{r} = \frac{2k}{r} \quad \ldots\ldots\ldots\ldots\ldots\ldots\ldots\ldots [26]$$

and hence σ_r and σ_θ can be found directly. However, it is still necessary to use numerical methods to find σ_z and u. Hill, Lee, and Tupper predicted on a theoretical basis that the results, according to the two yield conditions, would differ by less than 3 per cent. In the example considered this prediction is certainly verified, the differences being barely perceptible on the scale used.

Curve *C* presents the results of the Hencky solution, determined by Equations [20], [22], and [25]. The external displacement u_b is precisely the same as that predicted by the Prandtl-Reuss solution, while the values of the stress components agree quite closely.

Curve *D* was obtained by MacGregor, Coffin, and Fisher (13) for a closed-end tube, that is, instead of $\epsilon_z = 0$, they assumed the tube to be closed by rigid plates at either end, and computed the end load corresponding to the excess internal pressure. The variation of boundary conditions is seen to have little effect upon σ_r, σ_θ, or the radial displacement, but an extremely large difference is obtained for the values of the axial stress. The solution of MacGregor, Coffin, and Fisher was found under the assumptions of the Hencky stress-strain law and the Mises yield condition. To the authors' knowledge no solution to the problem of the closed-end tube has been obtained by the Prandtl-Reuss law. It would be interesting to see if the close correlation between the two theories also held in this case.

Curve *E* presents the results of Nadai (14), obtained by neglecting compressibility in the plastic part of the tube. This assumption plus that of plane strain produces a statically determinate problem for σ_r and σ_θ; hence Nadai's results are identical with those of Hill, Lee, and Tupper.

Curve *F* shows the values obtained by assuming an incompressible material throughout (15). Although under this assumption σ_z is continuous, its value appears to be at marked variance with the more exact results obtained by the other theories.

To correct this difficulty, an artificial solution is obtained as follows: The values of σ_r, σ_θ, and u of the incompressible solution are retained, but the value of σ_z is computed from the incompressible $\sigma_{z(i)}$ by the relation

$$\sigma_z = \frac{\nu}{0.5}\,\sigma_{z(i)} \quad \ldots\ldots\ldots\ldots\ldots\ldots\ldots\ldots [27]$$

This value is plotted as curve *F'* in Fig. 3 and is seen to agree quite well with both the elastic and plastic parts of the exact compressible-solution curves.

CONCLUSION

A study of the plastic-elastic behavior of an infinite hollow cylinder under internal pressure has been made by means of the two types of stress-strain law, deformation and flow, for a perfectly plastic material. In each case the material was assumed to satisfy Mises yield criterion, and account was taken of compressibility of the material in the plastic region. A numerical solution for the stress distribution and displacements was obtained for a particular case and compared with the results of other authors. The comparison of the results shows that for this particular problem of plane strain with rotational symmetry, either the Prandtl-Reuss or Hencky theory gives essentially the same results.

Although the Hencky theory uses a finite stress-strain relation,

the final differential equations are nonlinear and are more difficult to solve numerically than the Prandtl-Reuss equations. However, since the integration of the Hencky equations is independent of ρ, the stress distribution for a particular position of the elastic-plastic boundary can be computed without considering previous elastic-plastic states. The Prandtl-Reuss equations, on the other hand, must be integrated over both r and ρ, i.e., all previous elastic-plastic states must be considered. Thus the deformation theory appears preferable if a particular solution only is desired, while the flow theory is advantageous in obtaining the complete solution for a range of pressures.

As for the other solutions reviewed, the solution of Hill, Lee, and Tupper is in closest agreement with the results of the present work. In fact, since their solution is mathematically simpler, the Tresca yield condition would appear to be the preferable one for this problem.

Finally, from the viewpoint of simplicity, the "adjusted incompressible solution" gives sufficiently accurate results for many purposes and, moreover, these results are obtained in closed form. However, although this solution should give extremely good results for an infinitely long open tube (and possibly for other plane-strain problems), it will not be satisfactory for a closed tube. In fact, for an incompressible material, the solution for the open and closed tubes coincide, while the results of MacGregor, Coffin, and Fisher indicate that a large variation of σ_z is to be expected.

BIBLIOGRAPHY

1 "Mechanik der festen Körper im plastisch-deformablen Zustand," by R. von Mises, *Göttinger Nachrichten mathematisch physikalische Klasse*, 1913, pp. 582–592.

2 "Relation Between the Theory of Saint Venant-Lévy-Mises and the Theory of Small Elastic-Plastic Deformations" (Russian with English Summary), by A. A. Ilyushin, *Prikladnaia Matematika i Mekhanika*, vol. 9, 1945, pp. 207–218.

3 "On the Mechanical Behavior of Metals in the Strain-Hardening Range," by G. H. Handelman, C. C. Lin, and W. Prager, *Quarterly of Applied Mathematics*, vol. 4, 1947, pp. 397–407.

4 "Spannungsverteilung in plastischen Körpern," by L. Prandtl, *Proceedings of the First International Congress for Applied Mechanics*, Delft, Holland, 1924, pp. 43–54.

5 "Berücksichtigung der elastischen Formänderungen in der Plastizitätstheorie," by E. Reuss, *Zeitschrift für angewandte Mathematik und Mechanik*, vol. 10, 1930, pp. 226–274.

6 "Zur Theorie plastischer Deformationen und der hierdurch im Material hervorgerufenen Nachspannung," by H. Hencky, *Zeitschrift für angewandte Mathematik und Mechanik*, vol. 4, 1924, pp. 323–334.

7 "Theory of Elasticity," by S. Timoshenko, McGraw-Hill Book Company, Inc., New York, N. Y., 1934, p. 57.

8 "The Mathematical Theory of Elasticity," by A. E. H. Love, Dover Publications, New York, N. Y., 1944, p. 143.

9 "The Stresses and Strains in a Partly Plastic Thick Tube Under Internal Pressure and End Load," by D. G. Sopwith, to be published in the Proceedings of the Eighth International Congress for Applied Mechanics, Cambridge, England, 1948.

10 "Stresses and Strains in Thick-Walled Cylinders in the Elastic-Plastic State" (Russian), by N. M. Beliaev and A. K. Sinitski, *Izvestia Ak. Nauk SSSR*, vol. 2, 1938, pp. 3–54.

11 "The Theory of Combined Plastic and Elastic Deformation With Particular Reference to a Thick Tube Under Internal Pressure," by R. Hill, E. H. Lee, and S. J. Tupper, Proceedings of the Royal Society, series A, vol. 191, 1947, pp. 278–303.

12 "Mémoire sur l'écoulement des corps solides," by H. Tresca, *Mémoires présentés par divers savants*, vol. 18, 1868, pp. 733–799.

13 "Partially Plastic Thick-Walled Tubes," by C. W. MacGregor, L. F. Coffin, Jr., and J. C. Fisher, *Journal of The Franklin Institute*, vol. 245, 1948, pp. 135–158.

14 "Plasticity, a Mechanics of the Plastic State of Matter," by A. Nadai, McGraw-Hill Book Company, Inc., New York, N. Y., 1931.

15 "Theory of Plasticity" (mimeographed lecture notes), by W. Prager, Brown University, Providence, R. I., 1942.

Free Periodic Motions of an Undamped Two-Degree-of-Freedom Oscillatory System With Nonlinear Unsymmetrical Elasticity

By WALTER W. SOROKA,[1] BERKELEY, CALIF.

Precise solutions are presented for a two-degree-of-freedom oscillatory system containing a preset spring. Such a system is characteristic of an aircraft propeller-engine-supercharger installation. The periodic free motions obtained indicate the possibility of highly unconventional motions when the nonlinearity is pronounced, motions which may be easily overlooked in the usual approximate treatment of nonlinear systems. The results presented in this paper show that one mass may oscillate several times while the other mass is going through one oscillation. The ratio of oscillations of one mass with respect to the other changes with amplitude.

By considering the load-deflection curve for the nonlinear spring to be a broken line, periodic motions may be obtained to any desired degree of precision by combining conventional general solutions for two-degree-of-freedom linear systems.

Statement of the Problem

PERIODIC solutions of oscillatory systems containing nonlinear elasticity are readily obtained for single-degree-of-freedom systems. References (1)[2] through (4) present a number of solutions for such systems. When more than one degree of freedom is involved, the analytical solution of a nonlinear oscillatory system becomes considerably more difficult.

This paper[3] is concerned with periodic free motions of a two-degree-of-freedom system in which one spring is nonlinear, the nonlinearity consisting of a single sharp break in the linear load-deflection characteristic, corresponding to the effect of a preset spring. In practice such a system may be found in an aircraft-engine supercharger propeller system installation wherein the supercharger rotor is connected to the crankshaft through soft preset springs.

In such systems the deflection is linear with load through given ranges of load, the deflection rate being predetermined for each load range. This "piecemeal" linearity suggests the possibility of treating multidegree-of-freedom nonlinear systems by means of linear theory. Any curved deflection characteristic may be approximated by a connected series of straight lines, so that at least in principle most nonlinear oscillatory systems may be treated by linear methods. The solution of the present case serves to show, however, that a tremendous amount of labor is involved in making such solutions; in such cases consideration should be given to the use of a differential analyzer or analog computer.

In its essentials the method of solution consists of solving the differential equations of motion for each linear piece of the deflection curve, inserting into these general solutions the conditions of continuity of displacement, velocity, and acceleration through each break in the deflection curve. These conditions determine the phase angles and amplitudes of the sets of modes representing the oscillation in its different stages.

Description of Oscillatory System

The system analyzed is shown in Fig. 1. The propeller inertia is considered to be great enough to enforce a node at that point. The equivalent stiffness of the shaft between propeller and engine rotary inertia is assigned the value $k_1 = 100$; that of the supercharger shaft the value $k_2 = 50$ with preset springs inactive, or the value $k_3 = 1$ when the preset springs come into play. The engine and supercharger are considered to have the same equivalent inertias.

When rotating, the twist in the supercharger shaft as a result of the power torque results in an unsymmetrical load-deflection

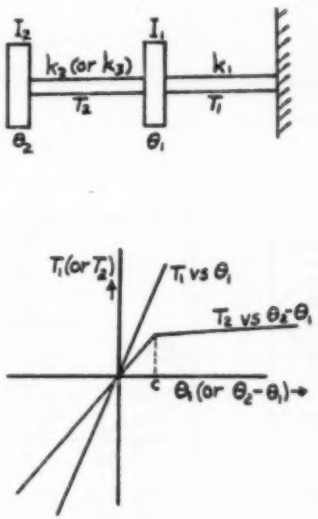

Fig. 1

[1] Associate Professor in Engineering Design, University of California.

[2] Numbers in parentheses refer to the Bibliography at the end of the paper.

[3] Based on a thesis submitted by the author to the Massachusetts Institute of Technology in 1945.

Contributed by the Applied Mechanics Division and presented at the Semi-Annual Meeting, San Francisco, Calif., June 27–30, 1949, of The American Society of Mechanical Engineers.

Discussion of this paper should be addressed to the Secretary, ASME, 29 West 39th Street, New York, N. Y., and will be accepted until July 10, 1950, for publication at a later date. Discussion received after the closing date will be returned.

Note: Statements and opinions advanced in papers are to be understood as individual expressions of their authors and not those of the Society. Paper No. 49—SA-6.

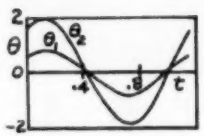

FIG. 2 $\omega = 5.352$

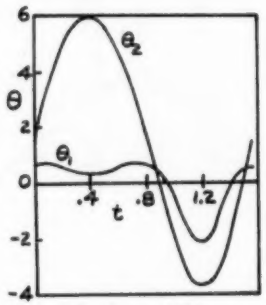

FIG. 3 $\omega = 4.064$

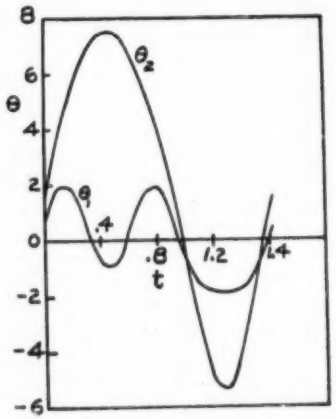

FIG. 4 $\omega = 3.876$

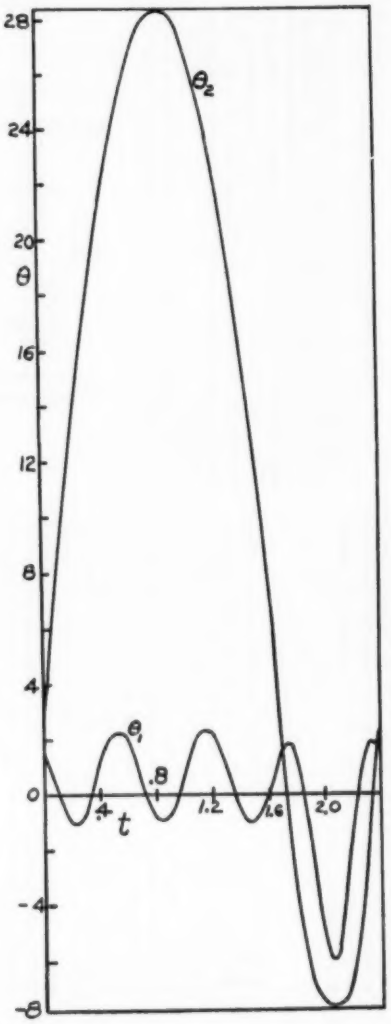

FIG. 5 (*left*) $\omega = 2.632$

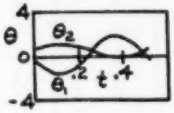

FIG. 6 $\omega = 12.056$

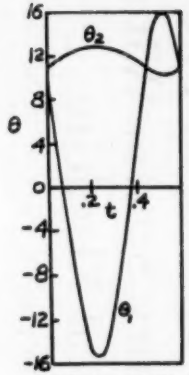

FIG. 7 $\omega = 10.404$

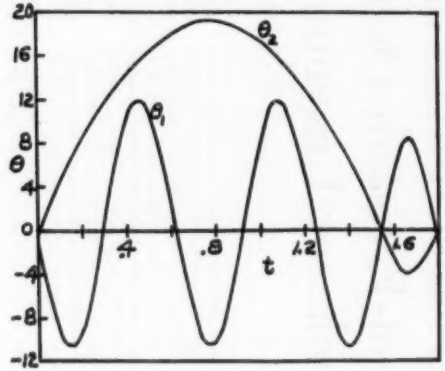

FIG. 8 $\omega = 3.506$

curve about this mean position. Consequently the analysis has been conducted for the case wherein the supercharger deflections about the steady load position do not twist the shaft beyond the effective limit of the preset springs in one direction, and, in the other direction, beyond the point where the preset springs again become effective.

The preset springs are considered to come into play when the supercharger shaft twist reaches a value of unity in the one direction. In the other direction, of course, the preset springs do not come into play at all.

Summary of Results

Results of the analysis are shown in graphical form in Figs. 2 to 8. These figures reveal curious and very interesting characteristics caused by the nonlinearity, which to the author's knowledge, have not been suggested in any other work. For example, Figs. 2 to 5 show how the wave form of the free vibration changes successively from the approximately conventional form of Fig. 2 to the unconventional forms of Figs. 3 to 5. With increase in amplitude the expected decrease in frequency occurs; but an unexpected trend is the growth of the number of oscillations of the linear shaft in a period. Such motions would be entirely overlooked by ordinary methods of analysis in which the nonlinear stiffness would be replaced by average linear stiffnesses corresponding to given amplitude ranges.

A second set of vibration wave forms is shown in Figs. 6 to 8. These might be considered as corresponding to the higher vibration mode of a linear system. At low amplitudes they are characterized by higher frequencies than those of the first set, but with increasing amplitude the frequency drops to values in the range corresponding to the first vibration mode, albeit the amplitude for the same frequency is greater.

Although forced motion results are not presented at the present time, some calculations have been made to determine the effect on the periodic free motion of a force of the same period. The condition was set that the net work done by the force over a complete cycle must be zero (undamped forced motions). It was found that for a given frequency, the forced motion differs considerably from the free motion when the amplitude of the force is comparable in magnitude to the resultant spring force acting on the forced inertia. When the force amplitude is relatively small, the forced motion apparently differs but little from the free motion. The forced motions, like the free motions, have unorthodox wave forms when the nonlinearity is pronounced.

Method of Analysis

The analysis of the general system follows.

Let

I_1 = effective engine inertia
I_2 = effective supercharger inertia (referred to engine speed)
k_1 = effective stiffness of propeller shaft (referred to engine speed)
k_2 = effective stiffness of supercharger shaft with preset springs inactive
k_3 = effective stiffness of supercharger shaft with preset springs active
θ_1 = instantaneous angular displacement of inertia I_1
θ_2 = instantaneous angular displacement of inertia I_2
c = the twist in the supercharger shaft above which the preset springs are active
T_1 = instantaneous torque in shaft k_1
T_2 = instantaneous torque in shaft k_2 (or k_3)

From the geometry of the arrangement

$T_1 = k_1\theta_1$,
$T_2 = k_2(\theta_2 - \theta_1)$ for values of $\theta_2 - \theta_1$ less than c
$= k_2(\theta_2 - \theta_1) - c(k_2 - k_3)$ for values of $\theta_2 - \theta_1$ greater than c.

Application of the conditions of equilibrium to each inertia yields the following differential equations

$$I_1\ddot{\theta}_1 + T_1 - T_2 = 0 \quad [1]$$

$$I_2\ddot{\theta}_2 + T_2 = 0 \quad [2]$$

For values of $\theta_2 - \theta_1$ less than c, Equations [1] and [2] become

$$I_1\ddot{\theta}_1 + k_1\theta_1 - k_2(\theta_2 - \theta_1) = 0 \quad [3]$$

$$I_2\ddot{\theta}_2 + k_2(\theta_2 - \theta_1) = 0 \quad [4]$$

For values of $\theta_2 - \theta_1$ greater than c, Equations [1] and [2] are

$$I_1\ddot{\theta}_1 + k_1\theta_1 - [k_3(\theta_2 - \theta_1) - c(k_2 - k_3)] = 0 \quad [5]$$

$$I_2\ddot{\theta}_2 + [k_3(\theta_2 - \theta_1) - c(k_2 - k_3)] = 0 \quad [6]$$

To put Equations [5] and [6] into the solvable form of Equations [3] and [4] it is necessary to introduce a change of variable. Let

$$k_3(\theta_2' - \theta_1) = k_3(\theta_2 - \theta_1) - c(k_2 - k_3)$$

Then

$$\theta_2' = \theta_2 - c\left(1 - \frac{k_3}{k_2}\right)$$

$$\dot{\theta}_2' = \dot{\theta}_2$$

$$\ddot{\theta}_2' = \ddot{\theta}_2$$

and Equations [5] and [6] become

$$I_1\ddot{\theta}_1 + k_1\theta_1 - k_3(\theta_2' - \theta_1) = 0 \quad [7]$$

$$I_2\ddot{\theta}_2' + k_3(\theta_2' - \theta_1) = 0 \quad [8]$$

Equations [3], [4], [7], and [8] now may be solved by usual methods to determine the natural frequencies and amplitude ratios in the intervals in which these equations are valid. Thus for the interval governed by Equations [3] and [4] the natural frequencies are

$$\beta^2 = \frac{1}{2}\left(\frac{k_1 + k_2}{I_1} + \frac{k_2}{I_2}\right) \pm \sqrt{\left[\frac{1}{2}\left(\frac{k_1 + k_2}{I_1} + \frac{k_2}{I_2}\right)\right]^2 - \frac{k_1k_2}{I_1I_2}} \quad [9]$$

Similarly, for the interval governed by Equations [7] and [8], the natural frequencies are

$$\omega^2 = \frac{1}{2}\left(\frac{k_1 + k_3}{I_1} + \frac{k_3}{I_2}\right) \pm \sqrt{\left[\frac{1}{2}\left(\frac{k_1 + k_3}{I_1} + \frac{k_3}{I_2}\right)\right]^2 - \frac{k_1k_3}{I_1I_2}} \quad [10]$$

The general solutions of Equations [3] and [4] are therefore

$$\theta_1 = C_1 \sin(\beta_1 t + \delta_1) + C_2 \sin(\beta_2 t + \delta_2) \quad [11]$$

$$\theta_2 = D_1 \sin(\beta_1 t + \delta_1) + D_2 \sin(\beta_2 t + \delta_2) \quad [12]$$

where C_1, C_2, D_1, D_2, δ_1, δ_2 are constants to be determined from initial and final conditions.

The general solutions of Equations [7] and [8] are

$$\theta_1 = A_1 \sin(\omega_1 t + \phi_1) + A_2 \sin(\omega_2 t + \phi_2) \quad [13]$$

$$\theta_2' = B_1 \sin(\omega_1 t + \phi_1) + B_2 \sin(\omega_2 t + \phi_2) \quad [14]$$

where A_1, A_2, B_1, B_2, ϕ_1, ϕ_2 are similarly to be determined.

Let t_1 represent the time interval during which $\theta_2 - \theta_1$ is greater than c, so that Equations [13] and [14] describe the motion;

let t_2 represent the time interval during which $\theta_2 - \theta_1$ is less than c, so that Equations [11] and [12] describe the motion. At the start of interval t_1, let the position of I_1 be given by $\theta_1 = K$; then the position of I_2 will be $\theta_2 = K + c$. At the end of the interval t_1, let the position of I_1 be denoted by $\theta_1 = M$; then the position of I_2 will be $\theta_2 = M + c$. The final conditions for the interval t_1 become the initial conditions for the interval t_2, and since a complete cycle is accomplished in the interval $t_1 + t_2$, the final conditions for the interval t_2 are the initial conditions for the interval t_1.

The displacements, velocities, and accelerations at the beginning and end of each interval are as follows:

First Interval

For $t = 0$

$$K = A_1 \sin \phi_1 + A_2 \sin \phi_2 \quad [15]$$

$$K + \frac{ck_2}{k_1} = B_1 \sin \phi_1 + B_2 \sin \phi_2 \quad [16]$$

$$\dot{\theta}_1 = \omega_1 A_1 \cos \phi_1 + \omega_2 A_2 \cos \phi_2 \quad [17]$$

$$\dot{\theta}_2' = \omega_1 B_1 \cos \phi_1 + \omega_2 B_2 \cos \phi_2 \quad [18]$$

$$\frac{-k_1 K + ck_2}{I_1} = -\omega_1^2 A_1 \sin \phi_1 - \omega_2^2 A_2 \sin \phi_2 \quad [19]$$

$$-\frac{ck_2}{I_2} = -\omega_1^2 B_1 \sin \phi_1 - \omega_2^2 B_2 \sin \phi_2 \quad [20]$$

For $t = t_1$

$$M = A_1 \sin (\omega_1 t_1 + \phi_1) + A_2 \sin (\omega_2 t_1 + \phi_2) \quad [21]$$

$$M + \frac{ck_2}{k_1} = B_1 \sin (\omega_1 t_1 + \phi_1) + B_2 \sin (\omega_2 t_1 + \phi_2) \quad [22]$$

$$\dot{\theta}_1 = \omega_1 A_1 \cos (\omega_1 t_1 + \phi_1) + \omega_2 A_2 \cos (\omega_2 t_1 + \phi_2) \quad [23]$$

$$\dot{\theta}_2' = \omega_1 B_1 \cos (\omega_1 t_1 + \phi_1) + \omega_2 B_2 \cos (\omega_2 t_1 + \phi_2) \quad [24]$$

$$\frac{-k_1 M + ck_2}{I_1} = -\omega_1^2 A_1 \sin (\omega_1 t_1 + \phi_1) - \omega_2^2 A_2 \sin (\omega_2 t_1 + \phi_2) \quad [25]$$

$$-\frac{ck_2}{I_2} = -\omega_1^2 B_1 \sin (\omega_1 t_1 + \phi_1) - \omega_2^2 B_2 \sin (\omega_2 t_1 + \phi_2) \quad [26]$$

Second Interval

For $t = 0$

$$M = C_1 \sin \delta_1 + C_2 \sin \delta_2 \quad [27]$$

$$M + c = D_1 \sin \delta_1 + D_2 \sin \delta_2 \quad [28]$$

$$\dot{\theta}_1 = \beta_1 C_1 \cos \delta_1 + \beta_2 C_2 \cos \delta_2 \quad [29]$$

$$\dot{\theta}_2 = \beta_1 D_1 \cos \delta_1 + \beta_2 D_2 \cos \delta_2 \quad [30]$$

$$\frac{-k_1 M + ck_2}{I_1} = -\beta_1^2 C_1 \sin \delta_1 - \beta_2^2 C_2 \sin \delta_2 \quad [31]$$

$$\frac{-ck_2}{I_2} = -\beta_1^2 D_1 \sin \delta_1 - \beta_2^2 D_2 \sin \delta_2 \quad [32]$$

For $t = t_2$

$$K = C_1 \sin (\beta_1 t_2 + \delta_1) + C_2 \sin (\beta_2 t_2 + \delta_2) \quad [33]$$

$$K + c = D_1 \sin (\beta_1 t_2 + \delta_1) + D_2 \sin (\beta_2 t_2 + \delta_2) \quad [34]$$

$$\dot{\theta}_1 = \beta_1 C_1 \cos (\beta_1 t_2 + \delta_1) + \beta_2 C_2 \cos (\beta_2 t_2 + \delta_2) \quad [35]$$

$$\dot{\theta}_2 = \beta_1 D_1 \cos (\beta_1 t_2 + \delta_1) + \beta_2 D_2 \cos (\beta_2 t_2 + \delta_2) \quad [36]$$

$$\frac{-k_1 K + ck_2}{I_1} = -\beta_1^2 C_1 \sin (\beta_1 t_2 + \delta_1) - \beta_2^2 C_2 \sin (\beta_2 t_2 + \delta_2) \quad [37]$$

$$\frac{-ck_2}{I_2} = -\beta_1^2 D_1 \sin (\beta_1 t_2 + \delta_1) - \beta_2^2 D_2 \sin (\beta_2 t_2 + \delta_2) \quad [38]$$

It can be shown that

$$\sin \phi_1 = \sin (\omega_1 t_1 + \phi_1) \quad [39]$$

$$\sin \phi_2 = \sin (\omega_2 t_1 + \phi_2) \quad [40]$$

$$\sin \delta_1 = \sin (\beta_1 t_2 + \delta_1) \quad [41]$$

$$\sin \delta_2 = \sin (\beta_2 t_2 + \delta_2) \quad [42]$$

To do this, eliminate K from Equations [15] and [16] and combine with Equation [20] in order to determine $\sin \phi_1$ and $\sin \phi_2$. Similarly, eliminate M from Equations [21] and [22] and combine with Equation [26] to determine $\sin (\omega_1 t_1 + \phi_1)$ and $\sin (\omega_2 t_2 + \phi_2)$. Thus

$$\sin \phi_1 = \frac{ck_2 \left[\left(\frac{\omega_2^2}{k_2} - \frac{1}{I_2} \right) B_2 + \frac{A_2}{I_2} \right]}{(\omega_2^2 - \omega_1^2) B_1 B_2 + \omega_1^2 A_2 B_1 - \omega_2^2 A_1 B_2} = \sin (\omega_1 t_1 + \phi_1)$$

$$\sin \phi_2 = \frac{-ck_2 \left[\left(\frac{\omega_1^2}{k_2} - \frac{1}{I_2} \right) B_1 + \frac{A_1}{I_2} \right]}{(\omega_2^2 - \omega_1^2) B_1 B_2 + \omega_1^2 A_2 B_1 - \omega_2^2 A_1 B_2} = \sin (\omega_2 t_1 + \phi_2)$$

Similarly, from Equations [27], [28], [32], and [33], [34], [38]

$$\sin \delta_1 = \frac{ck_2 \left[\left(\frac{\beta_2^2}{k_2} - \frac{1}{I_1} \right) D_2 + \frac{C_2}{I_2} \right]}{(\beta_2^2 - \beta_1^2) D_1 D_2 + \beta_1^2 C_2 D_1 - \beta_2^2 C_1 D_2} = \sin (\beta_1 t_2 + \delta_1)$$

$$\sin \delta_2 = \frac{-ck_2 \left[\left(\frac{\beta_1^2}{k_2} - \frac{1}{I_2} \right) D_1 + \frac{C_1}{I_2} \right]}{(\beta_2^2 - \beta_1^2) D_1 D_2 + \beta_1^2 C_2 D_1 - \beta_2^2 C_1 D_2} = \sin (\beta_2 t_2 + \delta_2)$$

It can be shown, also, that $M = K$. To do this, solve Equations [15] and [19] simultaneously to determine $A_1 \sin \phi_1$ and $A_2 \sin \phi_2$. From Equations [21] and [25] determine $A_1 \sin (\omega_1 t_1 + \phi_1)$ and $A_2 \sin (\omega_2 t_1 + \phi_2)$. From Equation [15]

$$A_2 \sin \phi_2 = K - A_1 \sin \phi_1$$

Substituting into Equation [19]

$$\frac{-k_1 K + ck_2}{I_1} = -\omega_1^2 A_1 \sin \phi_1 - \omega_2^2 K + \omega_2^2 A_1 \sin \phi_1$$

Whence

$$A_1 \sin \phi_1 = \frac{K \left(\omega_2^2 - \frac{k_1}{I_1} \right) + \frac{ck_2}{I_1}}{\omega_2^2 - \omega_1^2} = a_1 \quad [43]$$

and

$$A_2 \sin \phi_2 = \frac{-K \left(\omega_1^2 - \frac{k_1}{I_1} \right) - \frac{ck_2}{I_1}}{\omega_2^2 - \omega_1^2} = a_2 \quad [44]$$

From Equation [21]

$$A_2 \sin(\omega_2 t_1 + \phi_2) = M - A_1 \sin(\omega_1 t_1 + \phi_1)$$

Substituting into Equation [25]

$$\frac{-k_1 M + ck_2}{I_1} = -\omega_1^2 A_1 \sin(\omega_1 t_1 + \phi_1) - \omega_2^2 M + \omega_2^2 A_1 \sin(\omega_1 t_1 + \phi_1)$$

whence

$$A_1 \sin(\omega_1 t_1 + \phi_1) = \frac{M\left(\omega_2^2 - \frac{k_1}{I_1}\right) + \frac{ck_2}{I_1}}{\omega_2^2 - \omega_1^2}$$

$$A_2 \sin(\omega_2 t_1 + \phi_2) = \frac{-M\left(\omega_1^2 - \frac{k_1}{I_1}\right) - \frac{ck_2}{I_1}}{\omega_2^2 - \omega_1^2}$$

By virtue of Equation [39]

$$\frac{K\left(\omega_2^2 - \frac{k_1}{I_1}\right) + \frac{ck_2}{I_1}}{\omega_2^2 - \omega_1^2} = \frac{M\left(\omega_2^2 - \frac{k_1}{I_1}\right) + \frac{ck_2}{I_1}}{\omega_2^2 - \omega_1^2}$$

Therefore

$$K = M$$

By the same methods the following expressions, paralleling Equations [43] and [44] are obtained

$$B_1 \sin\phi_1 = \frac{\left(K + \frac{ck_2}{k_2}\right)\omega_2^2 - \frac{ck_2}{I_2}}{\omega_2^2 - \omega_1^2} = b_1 \quad [45]$$

$$B_2 \sin\phi_2 = \frac{-\left(K + \frac{ck_2}{k_2}\right)\omega_1^2 + \frac{ck_2}{I_2}}{\omega_2^2 - \omega_1^2} = b_2 \quad [46]$$

$$C_1 \sin\delta_1 = \frac{K\left(\beta_2^2 - \frac{k_1}{I_1}\right) + \frac{ck_2}{I_1}}{\beta_2^2 - \beta_1^2} = c_1 \quad [47]$$

$$C_2 \sin\delta_2 = \frac{-K\left(\beta_1^2 - \frac{k_1}{I_1}\right) - \frac{ck_2}{I_1}}{\beta_2^2 - \beta_1^2} = c_2 \quad [48]$$

$$D_1 \sin\delta_1 = \frac{(K+c)\beta_2^2 - \frac{ck_2}{I_2}}{\beta_2^2 - \beta_1^2} = d_1 \quad [49]$$

$$D_2 \sin\delta_2 = \frac{-(K+c)\beta_1^2 + \frac{ck_2}{I_2}}{\beta_2^2 - \beta_1^2} = d_2 \quad [50]$$

The continuity of velocity through the break in the deflection characteristic of the supercharger shaft and the fact that $K = M$ result in the equality of the velocities given, respectively, by Equations [17], [18], [23], [24] and Equations [35], [36], [29], [30]. By making use of these relationships the final equations which determine the solution of this problem are derived.

It is evident from Equations [39] through [42] that

$$\cot\phi_1 = -\cot(\omega_1 t_1 + \phi_1)$$

$$\cot\phi_2 = -\cot(\omega_2 t_1 + \phi_2)$$

$$\cot\delta_1 = -\cot(\beta_1 t_2 + \delta_1)$$

$$\cot\delta_2 = -\cot(\beta_2 t_2 + \delta_2)$$

Substituting these conditions and also the symbols a_1 through d_2 given by Equations [43] through [50] into the pairs of Equations [17] and [35], and [18] and [36], the final equations to be satisfied are

$$\omega_1 a_1 \cot\phi_1 + \omega_2 a_2 \cot\phi_2 = -\beta_1 c_1 \cot\delta_1 - \beta_2 c_2 \cot\delta_2 \quad [51]$$

$$\omega_1 b_1 \cot\phi_1 + \omega_2 b_2 \cot\phi_2 = -\beta_1 d_1 \cot\delta_1 - \beta_2 d_2 \cot\delta_2 \quad [52]$$

Exactly the same equations would result from the use of the pairs of Equations [23] and [29], and [24] and [30].

In order to use Equations [51] and [52] it is necessary to derive the relationships existing between the phase angles ϕ_1 and ϕ_2 and between the phase angles δ_1 and δ_2. Referring again to Equations [39] and [40] for values of ϕ_1 arbitrarily chosen in the first quadrant, $\omega_1 t_1 + \phi_1$ must fall in the second quadrant by virtue of Equation [39]. Or, choosing negative values of ϕ_1 in the fourth quadrant, $\omega_1 t_1 + \phi_1$ must fall in the third quadrant. Therefore, expressing the angles in degrees

$$\omega_1 t_1 + \phi_1 = 180 - \phi_1$$

or

$$t_1 = \frac{180 - 2\phi_1}{\omega_1} \quad [53]$$

Likewise, by virtue of Equation [40]

$$\omega_2 t_1 + \phi_2 = 180\, n - \phi_2$$

where n is an odd integer so chosen that ϕ_2 falls in either the first or fourth (negative values of ϕ_2) quadrants for convenience. The theory and results would be unaffected should n be so chosen as to place ϕ_2 in the second or third quadrants. Hence

$$\phi_2 = \frac{180\, n - \omega_2 t_1}{2}$$

$$= 90\, n - \frac{\omega_2}{\omega_1}(90 - \phi_1) \quad [54]$$

By the same reasoning

$$\beta_1 t_2 + \delta_1 = 180 - \delta_1$$

$$t_2 = \frac{180 - 2\delta_1}{\beta_1} \quad [55]$$

$$\delta_2 = 90\, n - \frac{\beta_2}{\beta_1}(90 - \delta_1) \quad [56]$$

Equations [51] and [52] may be solved simultaneously to express $\cot\delta_1$ in terms of $\cot\phi_1$ and $\cot\phi_2$. The resulting equation is

$$\cot\delta_1 = \frac{(a_1 d_2 - b_1 c_2)\omega_1}{(c_2 d_1 - c_1 d_2)\beta_1}\cot\phi_1 + \frac{(a_2 d_2 - b_2 c_2)\omega_2}{(c_2 d_1 - c_1 d_2)\beta_1}\cot\phi_2 \quad [57]$$

The values of ϕ_1 are determined by trial in the range -90 deg to $+90$ deg so as to satisfy either Equation [51] or [52] with the aid of Equations [54], [57], and [56].

Summary of Procedure in Determining Free Vibrations

1 Determine the two sets of natural frequencies of the system from Equations [9] and [10].

2 Assume a series of values for K (negative and positive).

3 For each K evaluate a_1, a_2, b_1, b_2, c_1, c_2, d_1, d_2 by means of Equations [43] through [50].

4 Substitute values determined in steps 1 and 3 into

Equation [57] and evaluate the coefficients of cot ϕ_1 and cot ϕ_2 for each value of K.

5 Make a table of values of ϕ_1, ϕ_2 (from Equation [54]) and their cotangents, covering the range of ϕ_1 between —90 deg and +90 deg. The interval between successive values of ϕ_1 depends on the specific problem and is subject to change after the first trial.

6 Choose one of the values of K assumed in step 1. Using the coefficients of Equation [57] for this value of K, determine for each ϕ_1 the value of cot δ_1 and then δ_1.

7 Determine δ_2 by means of Equation [56] and tabulate its cotangent.

8 Substitute cot ϕ_1, cot ϕ_2, cot δ_1, and cot δ_2 into either one of Equations [51] and [52]. For certain values of ϕ_1 the numerical magnitudes of the two sides of this equation approach each other.

9 Pick out the points which show the tendency to satisfy both sides of the chosen equation, and, by successively closer approximations, determine the values of ϕ_1 which satisfy this equation to the desired degree. This simultaneously determines the other angles, ϕ_2, δ_1, and δ_2.

10 Calculate the elapsed times t_1 and t_2 for each satisfactory value of ϕ_1 from Equations [53] and [55].

11 Calculate the "circular" frequency of the vibration for ach ϕ_1 by means of the expression

$$\omega = \frac{2\pi}{t_1 + t_2} \quad \ldots\ldots\ldots\ldots\ldots\ldots\ldots\ldots [58]$$

12 Tabulate the sines of ϕ_1, ϕ_2, δ_1, δ_2 and determine the corresponding values of A_1, A_2, B_1, B_2, C_1, C_2, D_1, D_2 from Equations [43] through [50].

13 Substitute the amplitudes, phase angles, and times herein determined into Equations [11] through [14]. Check each pair of equations so obtained to see that all the basic conditions of the analysis are satisfied by these solutions. In general, not all of these solutions are satisfactory.

14 Repeat steps 6 through 13 for successive values of K until the desired ranges of frequencies or amplitudes are covered.

BIBLIOGRAPHY

1 "Vibration Problems in Engineering", by S. Timoshenko. D. Van Nostrand Company, New York, N. Y., 1937, pp. 114–150.

2 "Forced Vibrations With Nonlinear Spring Constants", by J. P. Den Hartog and S. J. Mikina Trans. ASME, vol. 54, 1932 paper APM-54-15.

3 "Forced Vibration in Nonlinear Systems With Various Combinations of Linear Springs," by J. P. Den Hartog and R. M. Heiles, JOURNAL OF APPLIED MECHANICS, Trans. ASME, vol. 58, 1936, p. A-127.

4 "Steady Oscillations of Systems With Nonlinear and Unsymmetrical Elasticity," by M. Rauscher, JOURNAL OF APPLIED MECHANICS, Trans. ASME, vol. 60, 1938, p. A-169.

Stresses and Deflections of Cylindrical Bodies in Contact With Application to Contact of Gears and of Locomotive Wheels

By H. PORITSKY,[1] SCHENECTADY, N. Y.

From the well-known Hertz theory of contact stresses, where contact is over a finite area, the more elementary two-dimensional case of contact between two cylinders with parallel generators may be obtained as a limiting case by allowing the contact area to become infinitely long in one direction. However, it is easier to obtain it directly; this is done in the paper.

1 Summary of Results

EQUATIONS are obtained for the two-dimensional stresses and deflections of two cylindrical bodies in contact under both normal and tangential reactions. These are expressed in the terms of proper Airy functions, from which either the case of plane stress or the case of plane strain can be obtained. The former applies to very thin plates in contact, the latter to contact between long cylinders.

Curves of constant principal stress difference $p - q$ (= twice maximum local shear) are given for a normal Hertz load, for a tangential load proportional to it, and for a superposition of these two loads corresponding to a coefficient of friction $\mu = 0.3$. These curves indicate the maximum shear and the point at which it occurs.

Applications are made to contact between gear teeth as well as to contact between rolling cylinders or a wheel rolling on a track both under the conditions of slip as well as under conditions of zero slip or locking of part of the contact area. It is shown that several different positions are possible for the area over which locking takes place relative to the contact area.

The distribution of the normal stress of the Hertz theory has to be modified slightly when there is also a tangential traction in case the two solids have unequal elastic constants $G_1/(1 - 2\sigma_1)$, $G_2/(1 - 2\sigma_2)$; in this case the tangential loads produce normal displacements which do not match, and therefore modify the normal load distribution and make it asymmetric. At the same time the width of the area of contact is slightly decreased.

A further generalization of the Hertz theory considered is in regard to the load distribution produced by arbitrary two-dimensional surface irregularities.

2 Concentrated Force Applied Along a Straight-Line Boundary

Consider the Airy function (1)[2]

$$H = (F/\pi)y\theta = (F/\pi)r\theta \sin\theta \quad \ldots\ldots\ldots\ldots [1]$$

(see Fig. 1). Differentiation yields for the stress components

$$\left.\begin{aligned} p_{rr} &= \frac{1}{r}\frac{\partial H}{\partial r} + \frac{1}{r^2}\frac{\partial^2 H}{\partial \theta^2} = \frac{2F}{\pi r}\cos\theta \\ p_{r\theta} &= \frac{1}{r^2}\frac{\partial H}{\partial \theta} - \frac{1}{r}\frac{\partial^2 H}{\partial r \partial \theta} = 0 \\ p_{\theta\theta} &= \frac{\partial^2 H}{\partial r^2} = 0 \end{aligned}\right\} \quad \ldots\ldots\ldots [2]$$

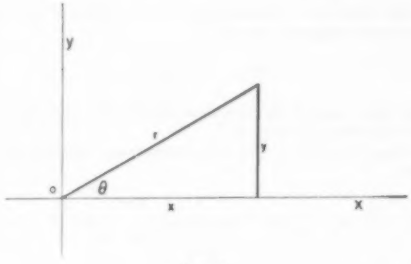

Fig. 1

From Equations [2] it follows that the lines of principal stress are the radial lines θ = const, and the circles r = const, and that the tangential principal stress component $p_{\theta\theta}$ vanishes. Thus Equation [1] can be applied to a half plane loaded at a point, or to a wedge of any angle loaded at the vertex. The components of force applied at the origin or vertex O are the negatives of the traction integrals over any path AB around the origin, hence the negatives of

$$F_x = \frac{\partial H}{\partial y}\Big]_A^B, \quad F_y = -\frac{\partial H}{\partial x}\Big]_A^B \quad \ldots\ldots\ldots [3]$$

where

$$\Big]_A^B$$

represents the increment along any path (see Fig. 2), from a point

[1] Engineering General Division, General Electric Company. Mem. ASME.

Contributed by the Applied Mechanics Division and presented at the Annual Meeting, New York, N. Y., November 27–December 2, 1949, of The American Society of Mechanical Engineers.

Discussion of this paper should be addressed to the Secretary, ASME, 29 West 39th Street, New York, N. Y., and will be accepted until July 10, 1950, for publication at a later date. Discussion received after the closing date will be returned.

Note: Statements and opinions advanced in papers are to be understood as individual expressions of their authors and not those of the Society. Paper No. 49—A-14.

[2] Numbers in parentheses refer to the Bibliography at the end of the paper.

A on one rectilinear boundary of the wedge of the half plane to a point B on the other rectilinear boundary.

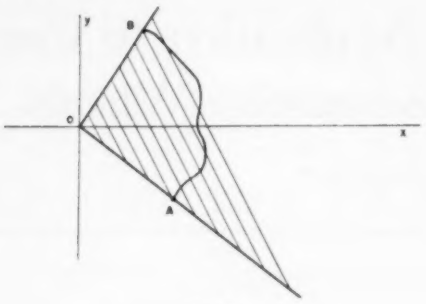

FIG. 2

In particular, for the half plane $x > 0$, Equations [1] and [3] yield

$$\left.\begin{aligned} F_x &= \frac{F}{\pi}\left(\theta + \frac{yx}{x^2+y^2}\right)\Bigg]_A^B = \frac{F}{\pi}(\theta + \sin\theta\cos\theta)\Bigg]_{\theta=-\pi/2}^{\pi/2} = F \\ F_y &= +\frac{F}{\pi}\left(\frac{y^2}{x^2+y^2}\right)\Bigg]_A^B = \frac{F}{\pi}(\sin^2\theta)\Bigg]_{-\pi/2}^{\pi/2} = 0 \end{aligned}\right\} \quad \ldots\ldots [4]$$

showing that the net traction across a path AB from the lower y-axis to the upper y-axis is (F, O); hence Equation [1] represents the stress due to tensile force $(-F, O)$ applied at the origin, while changing signs one obtains

$$H = -(F/\pi)y\theta \quad \ldots\ldots [5]$$

for the Airy function due to a compressive normal force F applied at the origin (see Fig. 3).

For the half plane $y < 0$, one obtains from Equation [5] (see Fig. 4)

$$\left.\begin{aligned} F_x &= -\frac{F}{\pi}(\theta + \sin\theta\cos\theta)\Bigg]_{\pi=-\pi}^{\theta=0} = -F \\ F_y &= -\frac{F}{\pi}(\sin^2\theta)\Bigg]_{\theta=-\pi}^{\theta=0} = 0 \end{aligned}\right\} \quad \ldots\ldots [6]$$

showing that Equation [5] represents the stress due to a shearing force F in the direction of positive x, applied at the origin, as shown in Fig. 3.

Turning to the displacements, we write Equation [5] in the form

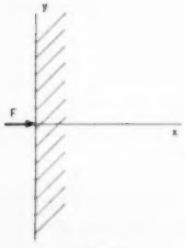

FIG. 3

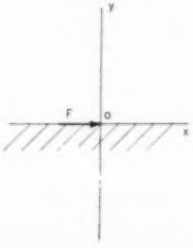

FIG. 4

$$H = R[\bar{z}g(z) + f(z)] \quad \ldots\ldots [7]$$

where

$$\left.\begin{aligned} g(z) &= -(F/2\pi)\ln z \\ f(z) &= (F/2\pi)z\ln z \end{aligned}\right\} \quad \ldots\ldots [8]$$

bar denoting conjugates, and R "the real part of." For plane strain the displacement (u, v) is given by [see (2)] Equations [2.10], [2.30].

$$G(u - iv) = (3 - 4\sigma)\bar{g} - f' - \bar{z}g' \quad \ldots\ldots [9]$$

where G is the shear modulus, σ Poisson's ratio. Applying to Equations [7] and [8] we shall evaluate the displacements along the free boundaries. There results

$$\begin{aligned} \frac{2\pi G}{F}(u - iv) &= -(3 - 4\sigma)\ln\bar{z} - \ln z - 1 + \bar{z}/z \\ &= -4(1-\sigma)\ln r - 1 + \cos 2\theta \\ &\quad - i\,[(4\sigma - 2)\theta + \sin 2\theta] \quad \ldots\ldots [10] \end{aligned}$$

Thus along the boundary $x = 0$ of Fig. 3, loaded normally with a compressive force F, the normal displacement in the direction of the force is given by (neglecting an additive constant)

$$u = -\frac{2F(1-\sigma)}{\pi G}\ln r \quad \ldots\ldots [11]$$

The tangential displacement along $x = 0$ is constant to each side of F and is given by

$$v = \left\{\begin{array}{ll} -\dfrac{F(1-2\sigma)}{2G} & \text{for } y > 0 \\ \dfrac{F(1-2\sigma)}{2G} & \text{for } y < 0 \end{array}\right\} \quad \ldots\ldots [12]$$

Comparing Equation [11] with the potential

$$V = -2e\ln r \quad \ldots\ldots [13]$$

due to a line charge of charge density e per unit length, it will be seen that the normal displacement along the free boundary has the same relation to the load F as the potential V has to the charge e except for the additional factor

$$(1 - \sigma)/\pi G \quad \ldots\ldots [14]$$

Equation [10] can also be used for the displacement of a half plane loaded by a tangential or shearing force F at a point, as in Fig. 4. Putting $\theta = -\pi$ and 0 one obtains from Equation [10] along $y = 0$ the same Equation [11] as given, except that now the right-hand member represents a displacement tangent to the boundary $y = 0$. Neglecting an additive constant, it will be seen that the displacement normal to the boundary is given by

$$v = \left\{\begin{array}{ll} -\dfrac{F(1-2\sigma)}{2G} & \text{for } x > 0 \\ \dfrac{F(1-2\sigma)}{2G} & \text{for } x < 0 \end{array}\right\} \quad \ldots\ldots [15]$$

thus indicating a relative constant displacement between one side of the load application and the other.

3 Contact Between Cylinders With Normal Traction—Normal Displacement Along Boundary

For contact between cylinders subject to normal tractions (see Fig. 5), to prevent interpenetration, it is necessary to produce

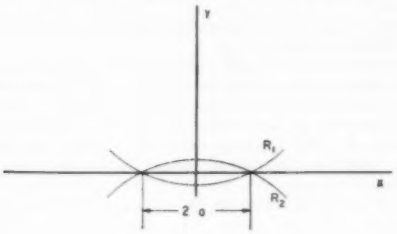

Fig. 5

over the contact band $-a < x < a$ a normal displacement on each cylinder whose sum is of the form

$$A' + C'x^2, \quad |x| < a \qquad [16]$$

where A', C' are constants, and

$$C' = -\frac{1}{2}\left(\frac{1}{R_1} + \frac{1}{R_2}\right) \qquad [17]$$

R_1, R_2 being the respective radii of curvature of the cylinders. The total normal compression force between the cylinders (per unit axial length) will be denoted by F. The radii of curvature will be assumed positive when both cylinders are convex as shown in Fig. 5.

To solve for the load distribution which will produce the parabolic displacement, [16], over the contact band $-a < x < a$ one could follow Hertz in using the analogy to the potential V of a uniform volume distribution of charge over an elliptic cylinder, then allow the minor axis of the latter to approach zero, the major axis approach a, while keeping the total charge constant, and in this way arrive at a charge density and load distribution varying as $\sqrt{a^2 - x^2}$. However, it will now be shown directly that a normal pressure over $y = 0$

$$\frac{2F}{\pi a^2}\sqrt{a^2 - x^2}, \quad |x| < a \qquad [18]$$

produces a normal displacement of the form [16], on either cylinder. In this proof, as is customary in the Hertz theory, it is assumed that (except near the contact band) the curvature of the cylinder's boundaries may be neglected, so that the spreading of stress takes place in the same manner as in a semi-infinite solid.

For definiteness, consider the solid $y > 0$ loaded by means of the pressure, [18]. Recalling Fig. 3, and Equation [10], it will be seen that the normal deflection along $y = 0$ in the direction the pressure is given by

$$v(x) = -\frac{2F}{\pi a^2}\frac{2(1-\sigma)}{\pi G}\int_{-a}^{a}\sqrt{a^2 - s^2}\ln r\, ds, \quad r = |x - s| \qquad [19]$$

While the foregoing applies only along $y = 0$, it is convenient to consider the right-hand member of Equation [19] for all x and y with $r = \sqrt{(x-s)^2 + y^2}$. Recalling the potential analogy and dropping the factor [14] from Equation [19], it will be seen that the function

$$V = -\frac{4F}{\pi a^2}\int_{-a}^{a}\sqrt{a^2 - s^2}\ln r\, ds \qquad [20]$$

represents the potential of a charge distribution of surface density ρ equal to the pressure [18]

$$\rho = \frac{2F}{\pi a^2}\sqrt{a^2 - x^2} \text{ over } y = 0, \ |x| < a \qquad [21]$$

After V has been evaluated, the displacement v on $y = 0$ is obtained from it by multiplication by the factor [14].

To evaluate Equation [20] we introduce confocal co-ordinates ξ, η by means of

$$\left.\begin{aligned} z = x + iy &= a\cosh(\xi + i\eta) = a\cosh\zeta \\ x &= a\cosh\xi\cos\eta \\ y &= a\sinh\xi\sin\eta \end{aligned}\right\} \qquad [22]$$

(see Figs. 6, 7). This maps the real axis of the z-plane into the boundary of the semi-infinite strip $DCBAE$ of the ζ-plane, the two foci $z = a$, $z = -a$ going into the corners at $\zeta = 0$, $\zeta = \pi i$.

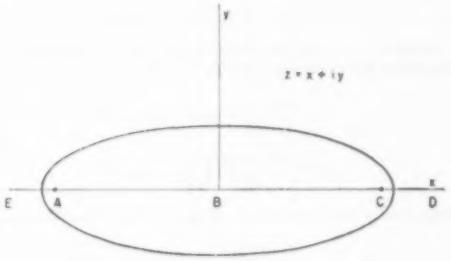

Fig. 6

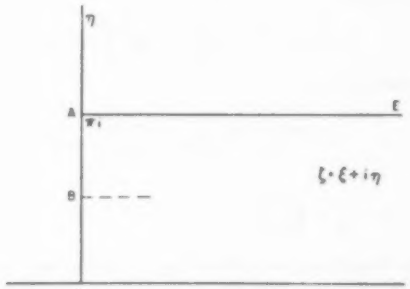

Fig. 7

The upper half z-plane is transformed into the inside of the strip $DCBAE$. The lower half, depending upon how one crosses $y = 0$, is transformed into a similar strip which is the image of $DCBAE$ in one of its rectilinear boundaries. If crossing over ABC is prohibited, all the images of the upper and lower z half planes lie in $\xi \geq 0$.

The transformation, Equations [22], is conformal and therefore transforms the harmonic function $V(x, y)$ into a harmonic

function in ξ, η. In terms of ξ, η the function V can be expressed in the relatively simple form

$$V = -A + B\xi + Ce^{-2\xi}\cos 2\eta \quad [23]$$

where A, B, C are proper constants. To prove this one must show that (for proper values of B, C) the function V given by Equation [23] satisfies the following conditions:

(*a*) V is single valued in the (x, y)-plane.

(*b*) V is continuous over ABC.

(*c*) V has a derivative $\partial V/\partial y$ which is continuous over $y = 0$, $|x| > a$, but is discontinuous over $y = 0$, $|x| < a$ as follows

$$\Delta\left(\frac{\partial V}{\partial y}\right)_{y=0} = \left\{\begin{array}{l} -4\pi\rho = -\dfrac{8F}{a^2}\sqrt{a^2 - x^2} \text{ for } |x| < a \\ 0 \text{ for } |x| > a \end{array}\right\} \quad [24]$$

(*d*) V behaves at infinity like

$$-2F \ln r \quad [25]$$

These four requirements on V are readily verified in Equation [23] (see Appendix) provided that

$$B = 2C,\ C = -F \quad [26]$$

Hence

$$V = A - F(2\xi + e^{-2\xi}\cos 2\eta) \quad [27]$$

Recalling the factor [14] there results for the displacement V along ABC, due to the load [18]

$$\left.\begin{aligned} v\Big|_{ABC} &= -\frac{F(1-\sigma)}{\pi G}(\cos 2\eta + \text{const}) \\ &= -\frac{2F(1-\sigma)}{\pi G}\left(\frac{x^2}{a^2} + \text{const}\right) \end{aligned}\right\} \quad [28]$$

while outside the loaded area, along CD there results similarly

$$v\Big|_{CD} = -\frac{F(1-\sigma)}{\pi G}(2\xi + e^{-2\xi}) + \text{const} \quad [29]$$

Replacing ξ by

$$\xi = \cosh^{-1}\frac{x}{a} = \log\left[\frac{x}{a} + \sqrt{\left(\frac{x}{a}\right)^2 - 1}\right] \quad [30]$$

Equation [29] yields

$$\left.\begin{aligned} v\Big|_{CD} &= -\frac{2F(1-\sigma)}{\pi G}\left[\log w + \frac{1}{2w^2}\right] + \text{const} \\ &\text{where} \\ w &= \frac{x}{a} + \sqrt{\left(\frac{x}{a}\right)^2 - 1} \end{aligned}\right\} \quad [31]$$

The foregoing applies to the solid $y > 0$. Denoting its elastic constants by G_1, σ_1, and those of the solid $y < 0$ by G_2, σ_2, one obtains for the net relative displacement which is to prevent interpenetration

$$-\frac{2F}{\pi}\frac{x^2}{a^2}\left(\frac{1-\sigma_1}{G_1} + \frac{1-\sigma_2}{G_2}\right) + \text{const} \quad [32]$$

Equating the coefficient of x^2 to C' in Equation [17], there results

$$\left.\begin{aligned} a^2 &= \frac{4F}{\pi}\left(\frac{1-\sigma_1}{G_1} + \frac{1-\sigma_2}{G_2}\right)\Big/\left(\frac{1}{R_1} + \frac{1}{R_2}\right) \\ &= \frac{8F}{\pi}\left(\frac{1-\sigma_1^2}{E_1} + \frac{1-\sigma_2^2}{E_2}\right)\Big/\left(\frac{1}{R_1} + \frac{1}{R_2}\right) \end{aligned}\right\} \quad [33]$$

A plot of the normal displacement given by Equations [28] and [31] is shown in Fig. 8.

It will be noted from Equations [31] that the displacement of the loaded region relative to the region at infinity becomes infinite. This is due primarily to the fact that the stresses at infinity decrease inversely as the distance $(x^2 + y^2)^{1/2}$ from the origin; the same statement applies to the strains. Hence the displacements, which are obtained by integration of the strains, vary logarithmically with $(x^2 + y^2)^{1/2}$. This phenomenon is also observed for the displacement due to a concentrated load, Equations [10], [11]. In practice, for a finite object, the displacement need only be evaluated relative to a point somewhere in its middle, rather than relative to the region at infinity. While this reference point is a little uncertain in any particular case, the logarithmic term increases rather slowly with distance, so that the net displacement obtained is not a sensitive function of the position of the reference point.

We conclude this section with the following integral

$$\left.\begin{aligned} \int_{-a}^{a}\sqrt{a^2 - s^2}\ln(z-s)ds &= \text{const} + \frac{\pi a^2}{4}(2\zeta + e^{-2\zeta}) \\ \zeta = \cosh^{-1}(z/a) &= \ln\left\{\frac{z}{a} + \left[\left(\frac{z}{a}\right)^2 - 1\right]^{1/2}\right\} \end{aligned}\right\} \quad [34]$$

which will be utilized in the following section. Indeed, both members of Equations [34] are analytic in z and ζ, and the equality of their real parts follows from Equations [20] and [27].

4 Airy Function for Stress in Contact Between Two Cylinders

We shall now obtain the Airy function for the half-plane $y > 0$ loaded as in the preceding section with a normal pressure given by [18].

Using the form Equation [5] for the Airy function of a point force F, but rotating axes through 90 deg corresponding to the change from Fig. 3 to Fig. 9, we start with the Airy function

$$H = \frac{F}{\pi}x\left(\theta - \frac{\pi}{2}\right) \quad [35]$$

or, since a first-degree polynomial may be omitted from the Airy's function,

$$\left.\begin{aligned} H &= \frac{F}{\pi}x\,\theta \\ &= \frac{F}{2\pi}I\,[(z+\bar{z})\ln z] \end{aligned}\right\} \quad [36]$$

where I denotes "the imaginary part of." The distributed load [18], by superposition of Equation [36], leads to the Airy function

$$\left.\begin{aligned} H &= \frac{F}{\pi^2 a^2}I\left\{\int_{-a}^{a}\sqrt{a^2 - s^2}\,[(z-s)\ln(z-s) + (\bar{z}-s)\ln(\bar{z}-s)]\,ds\right\} \\ &= \frac{F}{\pi^2 a^2}I\left\{(z+\bar{z})\int_{-a}^{a}\sqrt{a^2 - s^2}\ln(z-s)\,ds - 2\int_{-a}^{a}\sqrt{a^2 - s^2}\,s\ln(z-s)\,ds\right\} \end{aligned}\right\} \quad [37]$$

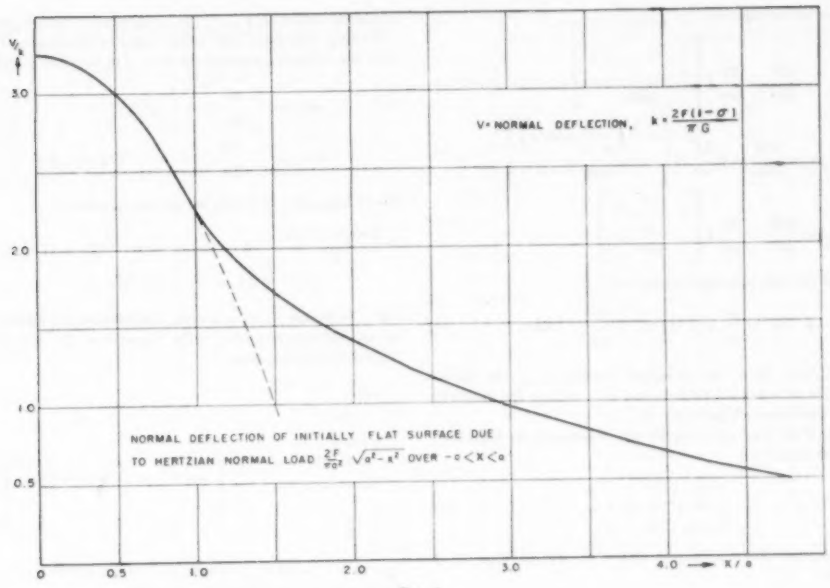

FIG. 8

The first integral in the right-hand member is evaluated in the preceding section Equation [34]. The second integral can be treated by similar methods, by interpreting its real part (along with the factor —2)

$$-2\int_{-a}^{a}\sqrt{a^2-s^2}\,s\ln r\,ds,\quad r=|z-s| \qquad [38]$$

as the potential of a charge distribution

$$\rho = x\sqrt{a^2-x^2},\ \text{over}\ |x|<a,\ y=0 \qquad [39]$$

over the strip ABC of Fig. 6. Introducing the transformation [22], one proves by similar methods that the integral Equation [38] differs from

$$\frac{\pi a^3}{2}\left(e^{-\zeta}\cos\eta - e^{-3\zeta}\cos 3\eta/3\right) \qquad [40]$$

at most by an additive constant. Hence

$$-2\int_{-a}^{a}\sqrt{a^2-s^2}\,s\ln(z-s)ds = \frac{\pi a^3}{2}\left(e^{-\zeta}-e^{-3\zeta}/3\right)+\text{const} \qquad [41]$$

Substituting from Equations [34] and [41] in Equation [37], one obtains for the Airy function

$$\left.\begin{aligned} H &= \frac{F}{2\pi}I\left[(z+z)(\zeta+e^{-2\zeta}/2)+a(e^{-\zeta}-e^{-3\zeta}/3)\right]\\ &= \frac{F}{2\pi}I\left[2x(\zeta+e^{-2\zeta}/2)+a(e^{-\zeta}-e^{-3\zeta}/3)\right]\end{aligned}\right\} \qquad [42]$$

FIG. 9

Differentiation of Equation [42] yields

$$\left.\begin{aligned}\frac{\partial H}{\partial x} &= \frac{F}{2\pi}I\left(2\zeta+\frac{4x}{a}e^{-\zeta}-e^{-2\zeta}\right)\\ \frac{\partial H}{\partial y} &= \frac{F}{2\pi}R\left(\frac{4x}{a}e^{-\zeta}-2e^{-2\zeta}\right)\end{aligned}\right\} \qquad [43]$$

and, further differentiation

$$\left.\begin{aligned} X_x &= \frac{\partial^2 H}{\partial y^2} = \frac{2F}{\pi a} I\left[\frac{\frac{x}{a}e^{-\zeta} - e^{-2\zeta}}{\sinh\zeta}\right] \\ X_y &= -\frac{\partial^2 H}{\partial x \partial y} = +\frac{2F}{\pi a} R\left[\frac{e^{-\zeta}\left(\frac{x}{a} - \cosh\zeta\right)}{\sinh\zeta}\right] \\ Y_y &= \frac{\partial^2 H}{\partial x^2} = \frac{2F}{\pi a} I\left[\frac{1 - \frac{x}{a}e^{-\zeta}}{\sinh\zeta}\right] \end{aligned}\right\} \quad \ldots [44]$$

The sum of the two principal stresses is

$$p + q = \frac{4F}{\pi a} I\,(e^{-\zeta}) = -\frac{4F}{\pi a} e^{-\xi}\sin\eta \quad \ldots\ldots [45]$$

The Mohr circle data, the principal stresses p, q, the photoelastic curves of constant retardation $p - q$, and the isoclinics are readily found from Equations [44].

Over $y = 0$ the traction integrals are obtained from Equations [43] by replacing x by

$$x = \begin{cases} a\cosh\xi \text{ for } x > a \\ a\cos\eta \text{ for } |x| < a \\ -a\cosh\xi \text{ for } x < -a \end{cases} \quad \ldots\ldots [46]$$

corresponding to the boundaries CD, CA, AE in Figs. 6, 7. There results

$$\frac{\partial H}{\partial y} = \frac{F}{\pi}, \frac{\partial H}{\partial x} = \frac{F}{2\pi}(2\eta - \sin 2\eta) = \frac{F}{2\pi}\begin{cases} 0, x > a \\ 2\eta - \sin 2\eta, |x| < a \\ 2\pi, x < -a \end{cases} \quad \ldots [47]$$

The applied tractions can be checked from Equation [47] by differentiations, or obtained directly from Equations [44] which yield for $y = 0$

$$X_x = -\frac{2F}{\pi a}\sin\eta,\ X_y = 0,\ Y_y = -\frac{2F}{\pi a}\sin\eta \quad \ldots [48]$$

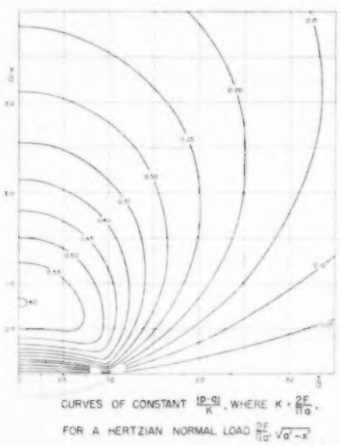

CURVES OF CONSTANT $\frac{|p-q|}{K}$, WHERE $K = \frac{2F}{\pi a}$, FOR A HERTZIAN NORMAL LOAD $\frac{2F}{\pi a}\sqrt{a^2 - x^2}$

FIG. 10

and these values of X_x, Y_y are in agreement with Equation [18].

Writing Equation [42] in the form of Equation [7], one obtains the following expressions for g, f in terms of ζ and z

$$\left.\begin{aligned} g(z) &= -\frac{iF}{2\pi}(\zeta + e^{-2\zeta}/2) \\ f(z) &= -\frac{iFa}{2\pi}(e^{-\zeta} - e^{-3\zeta}/3) + zg(z) \end{aligned}\right\} \quad \ldots\ldots [49]$$

Hence Equation [9] yields for the displacement

$$-\frac{2\pi G(iu + v)}{F} = (3 - 4\sigma)(\zeta + e^{-2\zeta}/2) + (\zeta + e^{-2\zeta}/2) + 2\{-e^{-2\zeta} + (2x/a)e^{-\zeta}\} \quad \ldots\ldots [50]$$

For $y = 0$ this yields a normal displacement v agreeing (except for an additive constant) with Equations [28] and [29], and a tangential displacement

$$\frac{u\pi G}{F(1 - 2\sigma)} = \begin{cases} 0 \text{ for } x > a \\ (\eta - \sin\eta\cos\eta) = \left[\cos^{-1}\frac{x}{a} - \frac{x}{a}\sqrt{1 - \left(\frac{x}{a}\right)^2}\right] \text{ for } |x| < a \\ \pi \text{ for } x < -a \end{cases} \quad \ldots\ldots [51]$$

Except for an additive constant, this agrees with the integrated displacement from Equations [12] and [18]

A plot of the curves of constant $p - q$ is given in Fig. 10.

For plane strain, if $w = 0$, then from $e_{zz} = 0$ follows

$$Z_z = -\sigma(X_x + Y_y) = \frac{4\sigma F}{\pi a} e^{-\xi}\sin\eta \quad \ldots\ldots [52]$$

The stresses for cylinders in contact have been obtained by Huber and Fuchs (3), as a limiting case of the general Hertz solution. In terms of the notation used in the foregoing their results are as follows

$$\left.\begin{aligned} Y_y &= \frac{2F}{\pi}\frac{y^3}{u^2 + a^2y^2}\sqrt{\frac{a^2 + u}{u}} \\ X_x &= \frac{2Fy}{\pi a^2}\left[\sqrt{\frac{a^2 + u}{u}}\left(2 - \frac{a^2y^2}{u^2 + a^2y^2}\right) - 2\right] \\ X_y &= \frac{2F}{\pi}\frac{xy^2}{u^2 + a^2y^2}\sqrt{\frac{u}{a^2 + u}} \\ Z_z &= \frac{4\sigma Fy}{\pi a^2}\left(\sqrt{\frac{a^2 + u}{u}} - 1\right) \end{aligned}\right\} \quad \ldots [53]$$

where

$$u = \frac{1}{2}\left[x^2 + y^2 - a^2 + \sqrt{(x^2 + y^2 - a^2)^2 + 4a^2y^2}\right]$$

These values may be shown to agree with Equations [44]. However, we believe that (especially for $y = 0$) these expressions are not as convenient as Equations [44].

5 Tangential Traction Between Cylinders

We consider next two cylinders in contact over $y = 0$, $|x| < a$, subject to a tangential traction proportional to [18] and given by

$$\frac{2T}{\pi a^2}\sqrt{a^2 - x^2}, \quad |x| < a \quad \ldots\ldots [54]$$

From Equations [5] and [54], one obtains for the Airy function

$$\left.\begin{aligned} H &= -\frac{2Ty}{\pi^2 a^2}\int_{-a}^{a}\sqrt{a^2-s^2}\,\theta_s\,ds,\ \theta_s = \tan^{-1} y/(x-s) \\ &= -\frac{2Ty}{\pi^2 a^2} I\left[\int_{-a}^{a}\sqrt{a^2-s^2}\ln(z-s)\,ds\right] \end{aligned}\right\} \quad [55]$$

Integrating by means of Equation [34], one obtains

$$\left.\begin{aligned} H &= -\frac{Ty}{2\pi} I\,(2\zeta + e^{-2\zeta}) \\ &= \frac{T}{4\pi} R\,[(z-\bar{z})\,(2\zeta + e^{-2\zeta})] \end{aligned}\right\} \quad [56]$$

This is of the form Equation [7] with

$$\left.\begin{aligned} g(z) &= -\frac{T}{4\pi}\,(2\zeta + e^{-2\zeta}) \\ f(z) &= \frac{T}{4\pi}\,(2\zeta + e^{-2\zeta}) \end{aligned}\right\} \quad [57]$$

The stress and displacement components may be found as in the preceding section; there results

$$\left.\begin{aligned} \frac{\partial H}{\partial x} &= -\frac{2Ty}{\pi a} I(e^{-\zeta}) \\ \frac{\partial H}{\partial y} &= -\frac{T}{\pi}\,[I(\zeta + e^{-2\zeta}/2) + 2(y/a)R(e^{-\zeta})] \end{aligned}\right\} \quad [58]$$

and hence

$$\left.\begin{aligned} X_x &= \frac{2T}{\pi a}\left[2R(e^{-\zeta}) + \frac{y}{a} I\left(\frac{e^{-\zeta}}{\sinh\zeta}\right)\right] \\ X_y &= \frac{2T}{\pi a}\left[I(e^{-\zeta}) - \frac{y}{a} R\left(\frac{e^{-\zeta}}{\sinh\zeta}\right)\right] \\ Y_y &= \frac{2Ty}{\pi a^2} I\left(\frac{e^{-\zeta}}{\sinh\zeta}\right) \end{aligned}\right\} \quad [59]$$

Equations [9] and [57] yield

$$\frac{4\pi G(-u+iv)}{T} = (3-4\sigma)\,(2\zeta + e^{-2\zeta}) + (2\zeta + e^{-2\zeta}) + 8ie^{-\zeta}(y/a) \quad [60]$$

In particular, for $y = 0$ there results

$$\frac{\pi G(-u+iv)}{T(1-\sigma)} = \left\{\begin{array}{l} 2\xi + e^{-2\xi} \text{ for } x > a \\ -i(\eta - \sin\eta\cos\eta) + \cos 2\eta \text{ for } |x| < a \\ 2\pi i + 2\xi + e^{-2\xi} \text{ for } x < -a \end{array}\right\} \quad [61]$$

Comparison of Equations [61] with [28], [29], [51] leads to a verification of the basic analogy indicated at the end of the second section, consisting in replacing along the plane boundary the normal tractions by tangential tractions, and the normal and tangential displacements by tangential and normal displacements, respectively, as shown in Table 1. A further relation between the loads and displacements will be indicated in the following section.

TABLE 1

Normal traction F	Normal displacement v	Tangential displacement u
Tangential traction T	Tangential displacement u	Normal displacement v

Over $|x| < a$ there results the displacement

$$u = -\frac{2T(1-\sigma)}{\pi G}\frac{x^2}{a^2} + \text{const, for } |x| < a \quad [62]$$

and hence there results the strain

$$e_{xx} = -\frac{4T(1-\sigma)}{\pi G}\,\frac{x}{a^2} \quad [63]$$

Fig. 11 contains the plot of the curves of constant $p - q$ for

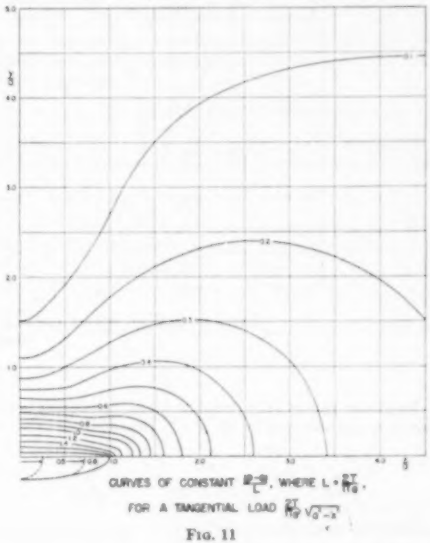

FIG. 11

the tangential loading [54], while Fig. 12 contains the shear curves for a loading which is the superposition of [18] and [54] with $T = 0.3\,F$, corresponding to a coefficient of friction $\mu = 0.3$.

6 Relations Between Loads and Displacements Along Boundary

As explained in the third section, one may arrive at the (normal) load distribution [18] required to produce the (normal) displacement [16] by means of the potential analogy utilized by Hertz. However, a more systematic method for the determination of $F(x)$ for arbitrary $v(x)$ is required, and will now be given.

Since actual solids are bounded not by ideal surfaces, but possess roughnesses corresponding to a certain degree of surface finish, it is of interest to determine the load distribution due to normal displacements corresponding to the surface irregularities over the contact area. To be sure, the assumed two-dimensional strains will represent only a special type of surface irregularity.

The results obtained for normal loads and displacements are also applicable to tangential tractions and displacements in view of the analogy indicated in Table 1, and applications of the results to locked contact surfaces will be given in the following section.

First consider normal loads only. From Equation [11] it follows that the normal displacement v along $y = 0$, due to concentrated loads $F_1, F_2, \ldots$ at $x = x_1, x_2, \ldots$, is given by the real part of

$$\left.\begin{aligned} &-\frac{2(1-\sigma)}{\pi G}\,\varphi(z) \\ \text{where}\quad &\varphi(z) = \sum_i F_i \ln(z - x_i) \end{aligned}\right\} \quad [64]$$

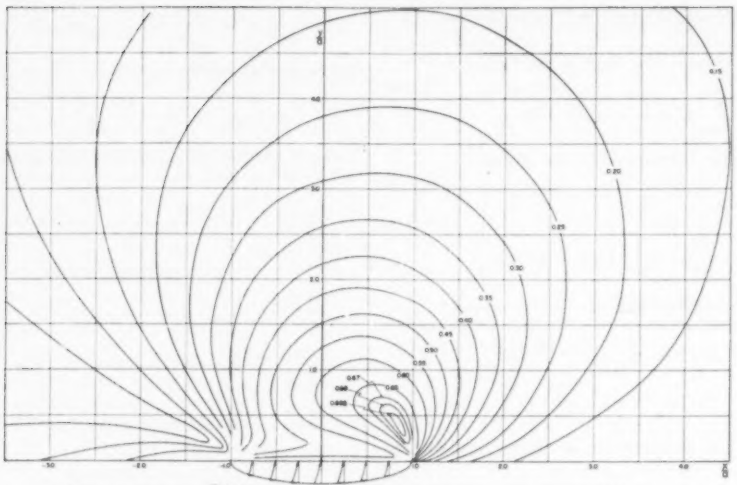

CURVES OF CONSTANT $\frac{p_{max}}{K}$ FOR SUPERPOSED NORMAL AND TANGENTIAL LOADS CORRESPONDING TO FIGURES 10, 11 WITH $T = .3F$

FIG. 12

The imaginary part of $\varphi(z)$, it will be noted, is constant between adjacent x_i, and decreases by πF_i at x_i. Hence

$$\lim_{y \to 0} \varphi(z) = -\frac{\pi G}{2(1-\sigma)} v + i\pi \sum_{x_i > x} F_i \quad \ldots\ldots [65]$$

Similarly, for distributed loads $F(x)$ per unit x, one introduces the analytic function for $y > 0$

$$\varphi(z) = \int_{-\infty}^{+\infty} F(s) \ln (z - s) ds \quad \ldots\ldots [66]$$

whereupon one proves

$$R[\varphi(z)] = -\frac{\pi G}{2(1-\sigma)} v \quad \ldots\ldots [67]$$

$$I[\varphi(z)] = \pi \int_x^{\infty} F(s) ds = \pi V(x), \; I[\varphi'(z)] = -\pi F(x). \quad [68]$$

Thus along $y = 0$ the integral of the load is proportional to the conjugate harmonic of the normal displacement.

Recalling familiar integral relations between the boundary value of the conjugate harmonic function $R[\varphi(z)]$, $I[\varphi(z)] = \pi V(x)$ along $y = 0$, one obtains, except for additive constants

$$\left.\begin{aligned} V(x) &= -\frac{G}{2(1-\sigma)} \int_{-\infty}^{+\infty} \frac{v(s)}{x - s} \, ds \\ v(x) &= \int_{-\infty}^{+\infty} \frac{V(s)}{x - s} \, ds \end{aligned}\right\} \quad \ldots\ldots [69]$$

where the singularity at $s = x$ is to be treated by using the Cauchy principal value

$$\int_{-\infty}^{+\infty} = \lim \left(\int_{-\infty}^{x-\epsilon} + \int_{x+\epsilon}^{+\infty} \right) \quad \ldots\ldots [70]$$

The second relation [69] follows, indeed, from [66] by integration by parts. The first relation [68] may be used to determine $V(x)$ and hence $F(x)$ when v is given.

More commonly, if there is continuous contact over a certain segment $|x| < a$ only, then v may be prescribed over it from known profiles of contacting solids, while for $|x| > a$ no contact occurs and $F = 0$ there. In this case the relations [68], [69] are relatively useless. The determination of the loads over $|x| < a$ and of the displacements over $|x| > a$ is carried out by utilizing the conformal mapping [22] of the half-plane $y > 0$ on the semi-infinite strip $DCBAE$ in Fig. 7. The requisite solution is obtained by expanding v along CA in a series

$$-\frac{Gv}{2(1-\sigma)} = \sum_{n=0}^{\infty} B_n \cos n\eta \quad \ldots\ldots [71]$$

whereupon it will be seen that

$$\varphi = B_0 + C(\xi + i\eta) + \sum_{n=1}^{\infty} B_n e^{-n\zeta} \quad \ldots\ldots [72]$$

and hence

$$V = -C\eta + \sum_{n=1}^{\infty} B_n e^{-n\xi} \sin n\eta \quad \ldots\ldots [73]$$

where C is a real constant related to the total load thus

$$V\Big]_{\zeta=0}^{\zeta=\pi i} = \pi C = \int_{-a}^{a} F(x) dx \quad \ldots\ldots [74]$$

The distribution of the load may now be determined from

$$F(x) = -\frac{dV}{dx}\bigg|_{CA} = \frac{\partial V}{\partial \eta} \Big/ \left|\frac{dz}{d\zeta}\right| = \frac{-C + \Sigma B_n n \cos n\eta}{a \sin \eta} \quad \ldots\ldots [75]$$

The displacement along $y = 0, x > a$ is given by

$$-\frac{Gv}{2(1-\sigma)} = B_0 + C\xi + \sum_{n=1}^{\infty} B_n e^{-n\xi} \quad \ldots\ldots [76]$$

As an example, the load distribution corresponding to a con-

stant displacement over $|x| < a$ is considered in the next section. Equation [71] yields $B_0 = \text{const}$, $B_n = 0$ for $n > 0$, and from Equation [75] it follows that $F(x)$ varies as $1/\sqrt{a^2 - x^2}$ (see Equation [104]).

Another example is furnished by the Hertzian load distribution given in previous sections. The displacement [16] leads to B_0, B_2 as the only nonvanishing coefficients in Equation [71].

A more difficult situation presents itself when surface irregularities are such that contact occurs not over one continuous area but over several "high spots". The resulting load distribution may be obtained by superposition of the foregoing solutions for each contact interval.

It must be borne in mind, however, that the load distribution which assures contact over one interval, also produces displacements over other potential contact intervals, and hence affects the interference there. Therefore the superposition is not a simple process, but involves successive corrections both in the division of the total load between several contact intervals, in the width of these intervals, and in the amount of interference and the load distribution over each interval.

Comparison of $V(x)$, defined by Equations [68], with the tangential displacement u under normal loads $F(x)$ along $y = 0$ (obtained by integration of Equations [12]), with proper allowance for interchange of x and y and u and v)

$$u|_{y=0} = -\frac{F(1-2\sigma)}{G}\int_{-\infty}^{x} F(s)ds + \text{const} \quad [77]$$

shows that u is proportional to $V(x)$, the integrated load up to x. If the elastic constants of the two contacting bodies are equal to each other, this displacement is the same for both bodies and causes no slip between the bodies as the normal load is applied. On the other hand, if the elastic constants are different, then the tangential displacements for the two solids are in proportion to their respective $(1 - 2\sigma)/G$, and slip must occur, unless it is prevented by the action of friction.

If, in addition to normal traction $F(x)$, tangential forces $T(x)$ also act over the contact area, then the calculation of the displacements due to the latter, both tangential and normal, may be found from $T(x)$ by means of the foregoing equations and the analogy displayed in Table 1. It must be kept in mind, however, that whereas the reaction of a pressure traction is still a pressure traction, the reaction of a positive drag or shear traction is a negative traction and causes a reversal of the tangential displacements along the boundary. On the other hand, if the elastic constants of the two solids are equal to each other, the normal displacements due to $T(x)$ do not interfere with the fit over the contact interval. If the elastic constants $G/(1 - 2\sigma)$ are not equal, then the effect of tangential tractions is to cause a redistribution of normal load, and is equivalent to a proper surface irregularity.

Over portions of the contacting solid boundaries $y = 0$ with (normal and) tangential tractions where there is no slip, the displacement u must match. The determination of $T(x)$ for given $u(x)$ is analogous to that of $F(x)$ for given $v(x)$, although the difference in sign of u indicated leads to a new situation. One such example is discussed in the following section.

Next, let us consider the redistribution of the normal load from its Hertzian expression [18] for contacting solids with unequal elastic constants $G_1/(1 - 2\sigma_1)$, $G_2/(1 - 2\sigma_2)$, subject to both normal and tangential tractions. It will be assumed that slip occurs over the contact area, so that only the normal displacements must be matched, and that the coefficient of friction μ is constant so that

$$T(x) = \mu F(x) \quad [78]$$

Superposition of the net normal displacements measured inward for each solid and utilization of Equations [11] and [15] yields for the net displacement

$$v_1 + v_2 = K_1\int_{-a}^{a} \ln r\, F(s)ds - K_2\int_{x}^{a} F(s)ds + \text{const} \quad [79]$$

where

$$K_1 = \frac{2}{\pi}\left[\frac{1-\sigma_1}{G_1} + \frac{1-\sigma_2}{G_2}\right], \quad K_2 = \left[\frac{1-2\sigma_1}{G_1} - \frac{1-2\sigma_2}{G_2}\right]$$

We now introduce $\varphi(z)$ as in Equation [66] and note that Equations [68] still hold. In place of Equation [67], however, we obtain from Equation [79]

$$v_1 + v_2 = K_1 R\,[\varphi(z)] + K_2 I\,[\varphi(z)] \quad [80]$$

The solution for $F(x)$ is again carried as in Equation [66] by means of the conformal mapping [22] by expanding φ as follows

$$\varphi = C_0\zeta + \Sigma\, C_n e^{-n\zeta}, \; C_n = A_n + i\,B_n \quad [81]$$

and similarly expanding v over the contact interval in a Fourier series in η. In particular, for smooth contacting solids, $v_1 + v_2$ as given by [16], [17], and [81] may be reduced to

$$\varphi(z) = i\,B_0\zeta + (A_2 + i\,B_2)e^{-2\zeta} \quad [82]$$

Replacing the left-hand member of Equation [80] by [16] yields

$$\left.\begin{aligned} A_2 &= C'a^2/2K_1(1 + K_2^2/K_1^2) \\ B_2 &= A_2K_2/K_1 \end{aligned}\right\} \quad [83]$$

and Equation [80] now leads to $A_0 = 0$ and to

$$F(x) = \frac{4A_2}{\pi a^2}\left(\sqrt{a^2 - x^2} + \frac{K_2}{K_1}x\right), \; A_2 = \frac{F}{2} \quad [84]$$

The term $x\,K_2/K_1$ constitutes the effect sought and leads to an asymmetric normal load distribution. At the same time Equation [33] which can be written in the form

$$a^3 = 4FK/\left(\frac{1}{R_1} + \frac{1}{R_2}\right) \quad [85]$$

is modified into

$$a^2 = 4FK/(1 + K_2^2/K_1^2)\left(\frac{1}{R_1} + \frac{1}{R_2}\right) \quad [86]$$

leading to a slight decrease in a.

7 Application to Cylinders in Sliding and Rolling Contact Under Normal and Tangential Traction

Rolling contact under normal load occurs in rail wheels, and under normal and tangential load in locomotive driving wheels and in braked rail wheels. In contact of gear teeth, rolling contact occurs at the pitch point, and possibly near it; elsewhere contact is of the sliding variety. The sliding or slip velocity between gear teeth when contact is at a point P on one of the gears is given by

$$V_s = d\omega(1 + R) \quad [87]$$

where, as shown in Fig. 13, $d(= PA)$ is the distance along the normal from P to its intersection A with the pitch circle, ω is the gear rotational velocity (in radians/sec), and $R = \omega'/\omega = n/n'$ is the speed ratio of the gear and its mating gear; primes refer to the latter, n to the number of teeth. In some cases this slip velocity may reach a value as high as 30 per cent of the rotational velocity at the pitch radius.

At slipping contact, if the coefficient of friction μ is constant and if the two cylinders possess the same elastic constants, the

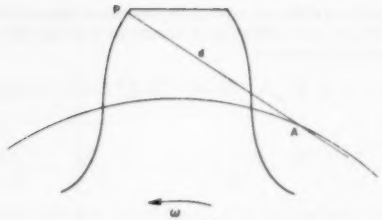

FIG. 13

state of stress for ideally smooth surfaces may be obtained by superposition of the solutions of sections 4 and 5, placing $T = \mu F$ in the latter. Indeed (neglecting tooth distortion and bending), the normal Hertz stress $F(x)$ produces normal displacements over the contact band $|x| < a$ which reduce the curvature and assure contact over that band. The tangential load distribution $T(x)$ also produces a normal displacement, but as indicated in the preceding section, for the same elastic constants between the cylinders, this does not affect the fit over the contact area; it merely causes the contact always to "run uphill." On the other hand, $T(x)$ also produces a tangential displacement, and this differs in sign for the two contacting surfaces, thus causing slip; however, this slip merely adds to the over-all assumed slip.

Generally, it is assumed that oil is squeezed out in gear contact over the Hertz contact area, and there is metal-to-metal contact there; hence the coefficient of friction μ over that area may be fairly high.

It is to be pointed out that the quantity $(1 - \mu)$ is not a measure of the gear efficiency, since the slip velocity against which the friction force μF operates is only a fraction of the rotational speed at the pitch point.

For cylinders in rolling contact under normal loads with torque transmission, slipping may take place over part of the contact where

$$T = \mu F \quad [88]$$

while over the rest of the contact area, where

$$T < \mu F \quad [89]$$

the two surfaces in contact are locked and no slipping takes place. We proceed to obtain $T(x)$ in this case.

First note from Equations [54], [62], and [63], that a tangential traction

$$\sqrt{a^2 - x^2} \text{ over } |x| < a,\ y = 0 \quad [90]$$

applied to $y < 0$ produces a displacement and strain

$$u = -\frac{1-\sigma}{G}\,x^2,\ e_{zz} = \frac{\partial u}{\partial x} = -\frac{2(1-\sigma)}{G}\,x \text{ over } y = 0,\ |x| < a \quad [91]$$

For the mating solid the corresponding traction as well as u, e_{zz} are reversed in sign. Next, superpose on [90] the traction

$$-\sqrt{b^2 - x^2} \text{ over } |x| < b,\ y = 0,\ b < a \quad [92]$$

leading to a traction shown by the solid curve in Fig. 14(a). Then over $x < b$ the extension vanishes

$$e_{zz} = 0,\ |x| < b \quad [93]$$

This corresponds to contact in which the normal load N is first applied, then a tangential load

$$D < \mu N \quad [94]$$

is applied. Slipping occurs over $b < |x| < a$, while over $|x| < b$, the surfaces are locked; b is given by

$$D = \mu N\left[1 - \frac{b^2}{a^2}\right] \quad [95]$$

The state of stress is obtained by starting with the solution of Sections 3 and 4, with F replaced by N, adding the solution of Section 5, with T replaced by D, and subtracting a similar solution with a replaced by b given by Equation [95], and T by Db^2/a^2.

Other possible distributions of $T(x)$ may be obtained for rolling contact if "creep" is allowed. It is necessary that the extension e_{zz} be constant over the locked area, although not the same constant for the two mating solids, since only in this way could rolling proceed, and any particular point move through the locked area without further slipping taking place. The difference in the constant values of e_{zz} leads to the "creeping" of one cylinder over the other one.

Note that if the semicircle of radius b in Fig. 14(a), be shifted to a center at $x = c$ without emerging from the semicircle of radius a, the resulting traction

$$\left[\sqrt{a^2 - x^2} - \sqrt{b^2 - (x-c)^2}\right],\quad c > 0,\quad c + b < a \quad [96]$$

shown as a solid curve in Fig. 14(b) leads to a constant strain over $|x - c| < b$

$$e_{zz} = \frac{2(1-\sigma)}{G}\,[-x + (x - c)] = -\frac{2(1-\sigma)c}{G},\ |x - c| < b \quad [97]$$

Over the mating solid (the track, if the foregoing refers to the wheel), the strain is the opposite of Equation [97]. The total drag $D = \int T dx$ is still given by Equation [95], but now, over the locked interval $|x - c| < b$, there is the strain difference $\Delta e_{zz} = 4(1 - \sigma)c/G$, and introducing a factor to yield the net drag D given by Equation [95]

$$|\Delta e_{zz}| = \frac{8(1-\sigma)c\mu N}{G\pi a^2} \quad [98]$$

and utilizing Equation [33], there results for the creep

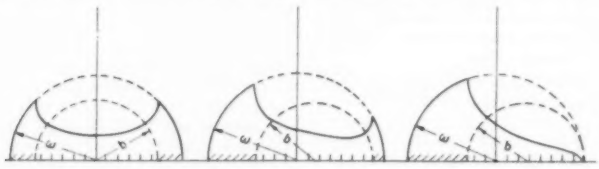

FIG. 14a FIG. 14b FIG. 14c

FIG. 14

$$\Delta e_{zz} = c\mu \left(\frac{1}{R_1} + \frac{1}{R_2} \right) \quad [99]$$

The foregoing solution holds for any $c < (a - b)$. The maximum value for the creep results when the semicircles of radius b, a are tangent to each other, as shown in Fig. 14(c).

For a driving wheel of a locomotive on a track, assuming for c its maximum value $a - b$, equating the track radius to infinity, there results

$$|\Delta e_{zz}| = \frac{a\mu}{R} \left(1 - \frac{b}{a} \right) \quad [100]$$

One may express b/a in terms of the ratio of the tractive effort D to the maximum possible tractive effort $D_m = \mu N$ by means of Equation [95] which yields

$$\frac{D}{D_m} = 1 - \frac{b^2}{a^2}, \quad \frac{b}{a} = \sqrt{1 - \frac{D}{D_m}} \quad [101]$$

Utilizing [33] once more there results

$$|\Delta e_{zz}| = \sqrt{\frac{8N}{\pi}} \frac{(1 - \sigma)R}{G} \left(1 - \sqrt{1 - D/D_m} \right) \quad [102]$$

Since e_{zz} represents an elongation, Equation [102] gives the creep rate as a ratio of the rotation rate of the wheel, and

$$1 + |\Delta e_{zz}| = \frac{2\pi R \cdot \text{number of wheel rotations}}{\text{length of track covered}} \quad [103]$$

It is not clear what determines physically the value of c in any one case.

The creep of wheels has been studied by Carter (4). He proposes the tractive stress distribution shown in Fig. 14(c); Equation [102] agrees with his results.

General contact between two rigid bodies under arbitrary tractions has been investigated by R. D. Mindlin (5), although he does not consider the two-dimensional case of cylinders in contact, and is primarily interested in compliances (approach of infinite regions). In the limiting case of two-dimensional stress distributions, the compliances obtained by Mindlin (5) become infinite, but limiting stress distributions may be utilized. The distribution of $T(x)$ obtained in this way agrees with that of Fig. 14(a). Reference should also be made to the work of C. Cattaneo (6).

Of some interest is the case of compression by means of a rigid die which forces a constant displacement v over $|x| < a$. It is readily shown from the analysis of the preceding section that in this case $F(x)$ is given by

$$F(x)/N = 1/\pi \sqrt{a^2 - x^2} \quad [104]$$

Similarly, if two solids are brought in contact over $|x| < a$ and subjected to a tangential load while slipping is prevented over $|x| < a$, the tangential traction varies as the right-hand member of Equation [104]. This case can also be obtained as a limiting case from Mindlin's paper (5).

The solution with creep may apply to gears at pitch-point contact. Elsewhere, slipping will take place all over the contact area.

In addition to the load carried by the gear teeth in direct contact over the region where the oil is squeezed out, part of the load may be carried by the oil due to the pressure that is developed in it as it is being dragged into the narrowing gap as the cylindrical surfaces move into closer contact. This oil pressure has been studied by Gatcombe (7) and Poritsky (8) on the basis of the assumption that no elastic distortion takes place over the cylinders. Actually, this theory should be modified to take account of the elastic distortion represented by Equation [31]. Furthermore, the elastic displacement due to the oil pressure should be taken into consideration in the oil-flow and pressure equations.

ACKNOWLEDGMENT

The author gratefully acknowledges the assistance of H. A. Beardslee, G. Horvay, and K. H. Weber in checking many of the equations, and in the construction of Figs. 8 and 10 to 12.

BIBLIOGRAPHY

1 "Elasticity," by A. E. Love, Dover Publications, New York, N. Y., fourth edition, 1944, pp. 210, 211.

2 "Application of Analytic Functions to Two-Dimensional Biharmonic Analysis," by H. Poritsky, Trans. American Mathematical Society, vol. 59, March, 1946, pp. 248–279.

3 "Spannungsverteilung bei der Berührung zweier elastischer Zylinder," by M. T. Huber and S. Fuchs, *Physikalische Zeitschrift*, vol. 15, 1914, p. 298.

4 "On the Action of Locomotive Driving Wheel," by F. W. Carter, Proceedings of the Royal Society, of London, series A, vol. 112, 1926, p. 151.

5 "Compliance of Elastic Bodies in Contact," by R. D. Mindlin JOURNAL OF APPLIED MECHANICS, Trans. ASME, vol. 71, September, 1949, pp. 259–268.

6 "Rendiconti," by C. Cattaneo, Accademia dei Lincei, series 6, vol. 27, 1938, pp. 342–348, 434–436, and 474–478.

7 "Lubrication Characteristics of Involute Spur Gears," by E. K. Gatcombe, Trans. ASME, vol. 67, 1945, pp. 177–185; discussions, pp. 185–188.

8 "Lubrication of Gears," by H. Poritsky, unpublished General Electric Company report.

Appendix

PROOF THAT EQUATION [27] REPRESENTS INTEGRAL [20]

The items to be proved are items (a)–(d) listed in the text following Equation [23].

To prove (a), note that the transformation [22] is periodic, and the strip $\xi > 0$, $-\pi < \eta < \pi$ covers the whole z-plane. Since Equation [23] is periodic in η, the function V is single-valued in the z-plane.

The values of V along ABC (see Figs. 6, 7), approached through positive y, and the values approached through negative y are obtained by letting ξ approach zero, first for $0 < \eta < \pi$, then for $-\pi < \eta < 0$, corresponding values of η at the same point on ABC being the negatives of each other. Since Equation [23] is even in η, the values of V are continuous along ABC. This completes the proof of (b).

Since V is even in η, $\partial V/\partial \eta$ vanishes for $\eta = 0$; it also vanishes for $\eta = \pi$. Hence $\partial V/\partial y$ vanishes along CD, EA. Along CD, $\partial V/\partial y$ does not vanish. Since V is symmetric in η, V is symmetric in y; hence

$$\Delta \left(\frac{\partial V}{\partial y} \right)_{ABC} = 2 \left. \frac{\partial V}{\partial y} \right|_{\substack{y=0^+ \\ ABC}} \quad [105]$$

Now the latter derivative may be computed from

$$\left. \frac{\partial V}{\partial y} \right|_{ABC} = \frac{\partial V}{\partial \xi} \Big/ \left| \frac{dz}{d\zeta} \right|_{\zeta = 0} \quad [106]$$

Substituting from Equations [27] and [22], there results

$$\left. \frac{\partial V}{\partial y} \right|_{ABC} = 2F \left(\frac{-1 + \cos 2\eta}{a \sin \eta} \right) = -\frac{4F}{a} \sin \eta$$

$$= -\frac{4F}{a^2} \sqrt{a^2 - x^2} \quad [107]$$

Recalling Equation [105], it will be noted that Equation [24] has been established, thus completing the proof of (c).

As regards (d), this follows from Equation [27], from which V behaves like $-2F\xi$ at infinity, when one notes from $\zeta = \cosh^{-1}(z/a)$ that $R(\zeta)$ behaves like $\ln |z| = \ln r$ at infinity.

On One-Term Approximations of Forced Nonharmonic Vibrations

By G. SCHWESINGER,[1] FORT MONMOUTH, N. J.

Steady forced vibrations of harmonically excited nonlinear systems deviate from a sinusoidal wave form, the magnitude of the deviation depending upon the frequency of the exciting force and the nature of the system concerned. Approximations by simple harmonic solutions suggested so far are either restricted to special vibration problems or generally fail to provide the desired accuracy without giving account of the errors committed. An improved general method is proposed and demonstrated, yielding the best accuracy attainable with harmonic solutions. This method, furthermore, gives the approximate root mean square of the error and thus allows for establishing dependable limits for its applicability.

Introduction

APART from the procedure of purely numerical or graphical integration, the methods of investigating the forced vibrations of systems with a nonlinear spring or damping or inertia force may be classified in three groups.

The first group treated in this paper is referred to as "one-term approximations." These solutions are based upon the assumption that the steady forced vibrations are harmonic when excited by an external harmonic force. A general simple method of this type was presented by Rüdenberg (1).[2,3] Although, with regard to the availability of advanced solutions, one-term approximations might appear now obsolete and uninteresting, the author dares to deal with them anew because they can be essentially improved and thus gain more usefulness.

The second group comprises the more adequate methods which take into account the deviation of the forced vibration from a simple sine wave. Solutions of this type are either obtained by applying the procedure of successive analytical or graphical approximation (2, 3) or by calculating very few members of a trigonometrical series which approximates or equals the Fourier series of the rigorous solution. The latter procedure can start from certain more or less arbitrary mathematical requirements (4), or from fundamental physical principles of energy (5). But unless a simple vibratory system, preferably without damping, is concerned, the solutions of this second group are rather cumbersome even if the desired accuracy may be achieved after only two approximating steps or with two series members. Some of these approximations are faced with difficulties when the nonlinear characteristic is a broken or discontinuous line.

Exact analytical solutions which constitute the third group were found so far only in a few special cases where damping is produced by dry friction (6) or where the spring characteristic consists of adjoining sections of straight lines (7). Advantage can be taken of those cases for comparing the accuracy of different approximate methods as shown later.

The lack of further rigorous solutions on one side and the inconvenience of handling multiple-term or multiple-step approximations on the other side often suggest the use of one-term approximations, though the inadequate and vigorously simplifying assumption of sinusoidal forced vibrations seems likely to preclude a satisfactory result at all. Indeed, one-term approximations are debatable. There are examples where the Rüdenberg method proved reliable and occasionally even better than certain two-term solutions (8), and other cases where it was found quite inaccurate (9). L. S. Jacobsen (10) gave a surprisingly good one-term solution for a system with linear spring and inertia force, but any arbitrary kind of damping, by substituting for the actual damping law an equivalent viscous damping on account of which an equal amount of energy is dissipated during one cycle. On the other hand, J. P. Den Hartog was less successful in trying to obtain an analogous one-term solution, namely, a solution based on a balance of energy of the vibrating body, for a symmetrical undamped system with nonlinear spring characterisitic. He found that his quarter-wave energy method sometimes furnished unsatisfactory results, but gave no explanation for this fact (4).

It is within the very nature of all one-term solutions that satisfactory results are achieved only as long as the wave form of the forced vibration is nearly sinusoidal. This fact readily explains the occasional failure of these approximations. Their usefulness would increase considerably if it were possible roughly to check their accuracy in any cases of doubt, so that more accurate solutions may be resorted to if the error is found to exceed an admissible limit. Besides that, none of the foregoing one-term approximations has both properties together, namely, a general applicability to all types of nonharmonic systems and sufficient accuracy without requiring much computing work.

In the present paper a one-term solution will be treated which fulfills the foregoing requirements. It will be shown that this general method comprises Jacobsen's solution (10) as a special case, and it will become clearer why Den Hartog's quarter-wave energy method proved unsuccessful. The new method is based upon the Ritz procedure which sometimes was suggested and applied to vibratory problems, yet without being used as a convenient one-term approximation, allowing estimation of the errors of the solution obtained. A paper of I. K. Silverman (5) in which some related results are deduced in another way will be discussed later

The New One-Term Approximation

The differential equation of the forced nonharmonic vibration may be written in the most general form

---

[1] Consultant, Signal Corps Engineering Laboratories.

[2] Numbers in parentheses refer to the Bibliography at the end of the paper.

[3] In some publications this method is ascribed to O. Martienssen who possibly did imply it, yet very loosely and apparently not aware of its potential scope (see *Elektrotechnische Zeitschrift*, 1910, pp. 204–206).

Presented at the National Meeting of the Applied Mechanics Division, Ann Arbor, Mich., June 13–15, 1949, of The American Society of Mechanical Engineers.

Discussion of this paper should be addressed to the Secretary, ASME, 29 West 39th Street, New York, N. Y., and will be accepted until July 10, 1950, for publication at a later date. Discussion received after the closing date will be returned.

Note: Statements and opinions advanced in papers are to be understood as individual expressions of their authors and not those of the Society. Paper No. 49—APM-17.

$$\frac{d}{dt}\,[m(x)\dot{x}] + D(\dot{x}) + f(x) = P \sin(\omega t + \varphi)$$

where $m(x)$ is the mass which may be a function of the displacement x. $D(\dot{x})$ is the damping force and $f(x)$ the spring force. The system is excited harmonically by the external force $P \sin(\omega t + \varphi)$, φ being the phase difference between the excitation and the fundamental harmonic of the resulting forced vibration. For the further investigation the foregoing differential equation may be written in a different form. The first member of this equation is differentiated and the particular resulting term which contains $\dot{x}^2$ is combined with the function $D(\dot{x})$ to another function $g(\dot{x})$. Thus

$$m(x)\ddot{x} + g(\dot{x}) + f(x) = P \sin(\omega t + \varphi) \quad \ldots\ldots [1]$$

Although not explicitly apparent, the notation $g(\dot{x})$ may imply that in the case of a variable mass g is also a function of the displacement x. It should further be noted that only the component $D(\dot{x})$ of the function g dissipates energy over a full cycle.

Neglecting the higher harmonics, i.e., assuming

$$x = A \sin \omega t \quad \ldots\ldots [2]$$

is equivalent to a disturbance of the vibrating body by a force

$$Q(t) = -m(x)\omega^2 A \sin \omega t + g(\dot{x}) + f(x) - P \sin(\omega t + \varphi) \ldots [3]$$

wherein x has to be replaced by the expression given in Equation [2]. The force Q alters the balance of energy during a certain interval of time by the quantity

$$E = \int_{x_1}^{x_2} Q\,dx = A\omega \int_{t_1}^{t_2} Q \cos \omega t\,dt$$

Den Hartog (4) has tried to obtain a satisfactory one-term approximation for symmetrical systems without damping by requiring the force Q not to perform work during a quarter-cycle between the limits $t_1 = 0$ and $t_2 = \pi/2\omega$. This requirement, though quite plausible and of course satisfied in the rigorous solution, sometimes yields worse results than Rüdenberg's assumption that the force Q is equal to zero at the end of every stroke. After having introduced the simplifying Assumption [2], the closest approximation of the actual vibratory curve by a single term will be characterized by a minimum amount of the integral which is taken of the square values of the disturbing force Q during one cycle, i.e.

$$I = \int_0^{2\pi} Q(t)^2\,d(\omega t) = \min \quad \ldots\ldots [4]$$

This minimum condition can be satisfied by proper choice of the unknown parameters A and φ, but in this form the evaluation in general leads to intricate equations which are hardly solvable. Convenient formulas are obtained by an artifice, that is, to consider the unknown amplitude A a quantity given in advance and, using the notation

$$P_1 = P \cos \varphi,\ P_2 = P \sin \varphi \quad \ldots\ldots [5]$$

to ask for the values of P_1 and P_2 satisfying the minimum condition which then can be written as follows

$$\frac{\partial I}{\partial P_1} = 0, \qquad \frac{\partial I}{\partial P_2} = 0$$

When putting

$$\tau = \omega t \quad \ldots\ldots [6]$$

one finds

$$\int_0^{2\pi} Q(\tau) \sin \tau\,d\tau = 0, \qquad \int_0^{2\pi} Q(\tau) \cos \tau\,d\tau = 0 \ldots [7]$$

If in Equations [7] Q is substituted by the Expression [3], then, with regard to the Assumption [2] implying symmetrical systems, some terms will vanish when integration is performed, simplifying the foregoing conditions to

$$\left.\begin{aligned} P_1 &= \frac{1}{\pi}\int_0^{2\pi}\left[f(x) - m(x)\omega^2 A \sin \tau + \frac{dm(x)}{dx}\,\omega^2 A^2 \cos^2 \tau\right]\sin \tau\,d\tau \\ P_2 &= \frac{1}{\pi}\int_0^{2\pi} g(\dot{x}) \cos \tau\,d\tau = \frac{1}{\pi}\int_0^{2\pi} D(\dot{x}) \cos \tau\,d\tau \end{aligned}\right\} \ldots [8]$$

Herein P_1 and P_2 appear dependent upon the unknown amplitude A which itself can be computed now from the relation

$$P_1^2 + P_2^2 = P^2 \quad \ldots\ldots [9]$$

The phase difference φ is given by

$$\varphi = \text{arc tan}\,\frac{P_2}{P_1} \quad \ldots\ldots [10]$$

The Equations [8], which permit all symmetrical systems to be solved easily, can be evaluated also numerically or graphically if the functions m, f, and g are not given in analytical terms.

Considering asymmetrical systems, the Assumption [2] has to be amplified by a further member B according to

$$x = A \sin \tau + B$$

Though this amplified assumption consists of two members, it shall also be called a "one-term approximation," because it contains only one harmonic component. The parameter B will minimize the integral, Equation [4], if it satisfies the condition

$$\frac{\partial I}{\partial B} = 0$$

from which in connection with Equations [7] the value of B can be computed. The correspondent general solution is omitted here, since in practice the most general case as represented by Equation [1] scarcely will occur. An example to be discussed later will show the practical procedure which is considerably less convenient than that of investigating symmetrical systems.

The foregoing developed solution approaches the exact one the closer, the more it was possible to reduce Q in magnitude by fulfilling the minimum condition, Equation [4]. The minimum amount of the integral I in Equation [4] may be considered a measure of the error of the solution due to the influence of Q. If I vanishes, the solution is exact.

As the conditions, Equations [7], express the fact that the periodic function $Q(\tau)$ does not contain the fundamental harmonic of the period 2π, the lowest harmonic of $Q(\tau)$ has a period $2\pi/n$, n being the lowest term but one in the Fourier series which represents the exact solution. When estimating roughly the error of the present approximation, the series terms of an order higher than n may be neglected in $Q(\tau)$, hence

$$Q(\tau) \approx P_n \sin(n\tau + \psi)$$

or, with regard to Equation [4]

$$Q(\tau) \approx \sqrt{\frac{I}{\pi}} \sin(n\tau + \psi) \quad \ldots\ldots [11]$$

Q has to be supposed a small quantity because otherwise the Assumption [2] would not furnish satisfactory results at all. Furthermore, the disturbing frequency $n\omega$ is supposed to be far enough away from "superharmonic" resonance. This term is

suggested in reference (11) for a vibratory motion in which a higher harmonic component of the order n is dominant over the other harmonics, including the fundamental one. Under these suppositions the small force Q, acting on the nonharmonic system, will produce an additional small deflection of the vibrating body of an amount A_n not too much different from what would occur if the same force Q would disturb a linear system with a spring constant $\bar{k}$ and a mass $\bar{m}$, both being certain intermediate values of the variable quantities $k = f'(x)$ and $m(x)$, respectively. Because damping may be neglected as having no essential influence on this estimation of errors, one obtains

$$A_n \approx \frac{\sqrt{\frac{I}{\pi}}}{\bar{k} - \bar{m}n^2\omega^2} \sin(n\tau + \psi) \quad \ldots\ldots [12]$$

and finally the mean error

$$\alpha \approx \pm \frac{\sqrt{\frac{I}{2\pi}}}{\bar{m}n^2\omega^2 - \bar{k}} \quad \ldots\ldots [13]$$

The choice of $\bar{m}$ and $\bar{k}$ is not critical as long as, in accordance with the foregoing supposition of avoiding superharmonic resonance, $n^2\omega^2$ is restricted to values considerably greater than $\bar{k}/\bar{m}$. Then the values $\bar{k}$, $\bar{m}$ may be taken equal to the mean values of k and m within the range between zero deflection and maximum deflection A or, still simpler and mostly sufficient, equal to the values at the middle deflection $^1/_2A$. The final choice should consider the inherent characteristics of the system; n has to be substituted by 2, in general, but by 3 in the case of symmetrical systems the solution of which is represented by a Fourier series with members of odd order.

The square of Equation [3] when expressed by the variable τ may be written

$$Q^2(\tau) = [-m(x)\omega^2 A \sin\tau + g(\dot{x}) + f(x)]^2 - 2Q(\tau)(P_1 \sin\tau + P_2 \cos\tau) - P_1^2 \sin^2\tau - P_2^2 \cos^2\tau - 2P_1P_2 \sin\tau \cos\tau$$

wherein x has to be replaced by $A \sin\tau$. Integration of this expression between the limits 0 and 2π results, with regard to the conditions, Equations [7] and [9], in the following relation which is useful for computing the numerator of Equation [13] for symmetrical systems

$$\frac{I}{2\pi} = \frac{1}{2\pi}\int_0^{2\pi} [-m(x)\omega^2 A \sin\tau + f(x) + g(\dot{x})]^2 d\tau - \frac{1}{2}P^2 \ldots [14]$$

The foregoing estimation aims at finding a reliable lower limit of the frequency ω down to which the suggested one-term solution may be used without exceeding a certain prescribed error. The possibility of establishing such a limit without much additional computing work is an essential attribute of the new solution. Its reliability will be demonstrated later.

Comparison With Other One-Term Approximations

It has been mentioned that the method treated in this paper comprises Jacobsen's procedure of equivalent viscous damping (10) as a special case which yields good one-term solutions for systems with straight spring characteristic and constant mass as represented by

$$m\ddot{x} + g(\dot{x}) + kx = P \sin(\omega t + \varphi) \quad \ldots\ldots [15]$$

Applying Equations [8] and [9] in this case furnishes

$$P_1 = \frac{1}{\pi}\int_0^{2\pi} (k - m\omega^2) A \sin^2\tau \, d\tau = (k - m\omega^2)A$$

$$P^2 = P_1^2 + P_2^2 = (k - m\omega^2)^2 A^2 + P_2^2,$$

from which

$$A = \frac{\sqrt{P^2 - P_2^2}}{k - m\omega^2} \quad \ldots\ldots [16]$$

Jacobsen's procedure first requires the determination of the dissipation of energy V by damping during one cycle. If the forced vibrations are assumed sinusoidal, it amounts to

$$V = \int_{\text{cycle}} g(\dot{x})\, dx = A\int_0^{2\pi} g(\dot{x}) \cos\tau \, d\tau$$

or, with respect to Equation [8], to

$$V = \pi A P_2 \quad \ldots\ldots [17]$$

This amount of energy has to equal the loss of energy V_0 of an equivalent system with viscous damping which obeys, as is well known, the differential equation

$$m\ddot{x} + c\dot{x} + kx = P \sin(\omega t + \varphi_0).$$

The equivalent energy dissipation is

$$V_0 = \int_0^{2\pi/\omega} c\dot{x}^2 \, dt = \pi c\omega A^2 \quad \ldots\ldots [18]$$

Equating V and V_0 furnishes the equivalent damping constant

$$c = \frac{P_2}{\omega A} \quad \ldots\ldots [19]$$

This value has to be inserted into the solution of the foregoing linear differential equation which gives the amplitude

$$A = \frac{P}{\sqrt{(k - m\omega^2)^2 + c^2\omega^2}} = \frac{P}{\sqrt{(k - m\omega^2)^2 + P_2^2/A^2}}$$

Solving for A, one obtains

$$A = \frac{\sqrt{P^2 - P_2^2}}{k - m\omega^2}$$

an equation identical with Equation [16]. Hereby it is verified that Jacobsen's solution is a special case of the new one-term approximation. It may be recalled that the latter was not deduced by considering the balance of energy of the nonharmonic system.

An attempt (4) to obtain in this way a useful one-term solution for systems with symmetrical nonlinear spring characteristics failed to give satisfactory results. In the case of such a system without damping, as investigated by den Hartog, the second Integral [7] always vanishes if $P_2 = 0$, that means, if the phase angle φ between the exciting force P and the forced vibration is zero or 180 deg. Then the force $Q(\tau)$ is an odd function of τ so that the first integral in Equations [7] is allowed to be evaluated between the limits zero and $\pi/2$ without changing the result. Thus the condition of best approximation for undamped systems becomes

$$\int_0^{\pi/2} Q(\tau) \sin\tau \, d\tau = 0 \quad \ldots\ldots [20]$$

while den Hartog required the force Q not to perform work during a quarter cycle, corresponding to

$$\int_0^{\pi/2} Q(\tau) \cos\tau \, d\tau = 0$$

Since the force Q contributes to the total amount of its work mainly when it covers great instantaneous displacements near the middle position of the vibrating body, the approximation achieved by the quarter-wave energy method will be close in that range near the abscissa axis. On the other hand, the new approximation eliminates the disturbing influence of Q rather in the range of large deflections x, wherefrom it may be concluded

that it always will furnish more accurate values of the amplitudes than the quarter-wave energy method. It also becomes rather plausible that Rüdenberg's approximation which assumes the forces to balance each other just at greatest deflection ($\tau = \pi/2, 3\pi/2, \ldots$) often proves nearly correct.

A simple and immediate physical explanation of the failure of the quarter-wave energy method is not readily at hand because the assumption it is based upon is fulfilled in the rigorous solution of the considered problem. One might object that other physical principles of energy of wider scope like Hamilton's principle are available, which can be applied also to systems with damping. In fact, if this principle is applied, one obtains the same results as derived in this paper in another way and expressed by Equations [7]. I. K. Silverman (5) first has used this principle to obtain excellent two-term approximations for the special case of undamped systems with nonlinear spring characteristic. Omitting the second term of his solution, the first term is found to be identical with Equation [20]. However, in comparison with applying Hamilton's principle, the method used in this paper seems more advantageous because immediately it permits an estimation of the errors.

Special Examples

It would be instructive to apply the method described to most different types of nonharmonic systems and to compare its results with both the exact solution and Rüdenberg's one-term approximation. Systems with nonlinear damping might be excluded from this consideration because, as shown before, the new method would furnish the same results as Jacobsen's procedure applied to such cases (10). But the scheme just outlined meets the difficulty that exact analytical solutions are known only for a few special cases and that comparable results of other papers on this subject, in general, refer to some simple basic systems the thorough investigation of which is still remarkably intricate. For these reasons the selection of examples was confined to the following three cases.

The first case deals with a symmetrical nonlinear-spring characteristic which has an initial set, as indicated by the solid line in Fig. 1, and consists of sections of straight lines so that, even if viscous damping is assumed, an exact periodic solution in closed form can be obtained in the way originated by Den Hartog.

The differential equation of this system is

$$m\ddot{x} + c\dot{x} + kx \pm F_0 = P \sin(\omega t + \varphi) \quad \ldots\ldots [21]$$

the plus sign being valid in the range

$$0 < x < A$$

and the minus sign in the range

$$-A < x < 0$$

Introducing new variables and parameters, namely

$$y = \frac{k}{P}x, \quad \gamma = \omega\sqrt{\frac{m}{k}}, \quad \delta = \frac{c}{2\sqrt{mk}}, \quad b = \frac{F_0}{P} \quad \ldots [22]$$

yields with respect to Equation [6]

$$\gamma^2\frac{d^2y}{d\tau^2} + 2\delta\gamma\frac{dy}{d\tau} + y \pm b = \sin(\tau + \varphi) \quad \ldots\ldots [23]$$

Now the conditions, Equations [8], have to be evaluated, as easily seen by comparing Equations [1] and [23], with the functions

$$f = y \pm b = A\sin\tau \pm b$$

$$g = 2\delta\gamma A\cos\tau$$

$$m\omega^2 = \gamma^2$$

Hence

$$P_1 = \frac{1}{\pi}\int_0^{\pi}[A(1-\gamma^2)\sin\tau + b]\sin\tau\,d\tau + \frac{1}{\pi}\int_{\pi}^{2\pi}[A(1-\gamma^2)\sin\tau - b]\sin\tau d\tau = A(1-\gamma^2) + \frac{4}{\pi}b$$

$$P_2 = \frac{1}{\pi}\int_0^{2\pi} 2\delta\gamma A\cos^2\tau\,d\tau = 2\delta\gamma A$$

and because of

$$P_1^2 + P_2^2 = 1$$

one obtains

$$[(1-\gamma^2)^2 + 4\delta^2\gamma^2]A^2 + \frac{8}{\pi}b(1-\gamma^2)A + \frac{16\,b^2}{\pi^2} = 1 \ldots [24]$$

$$A = \frac{\sqrt{(1-\gamma^2)^2 + 4\delta^2\gamma^2\left(1 - \frac{16}{\pi^2}b^2\right)} - \frac{4}{\pi}b(1-\gamma^2)}{(1-\gamma^2)^2 + 4\delta^2\gamma^2} \quad \ldots\ldots [25]$$

The expression, Equation [25], represents only one of the two roots of the quadratic Equation [24]. The other root differs from the first one by the opposite sign of the first member in the numerator and does not apply to the present problem. This appears from the fact that, when assuming the second root, the absolute static deflection ($\gamma = 0$) under a certain disturbing force would become greater than that of a linear system in which $b = 0$. This is doubtlessly impossible because the nonlinear system just considered has a greater restoring force. Since the second solution furnishes the same absolute value $|A|$ as obtained from Equation [25] after changing the sign of b, it must be concluded that the second root pertains to the dotted spring characteristic of Fig. 1.

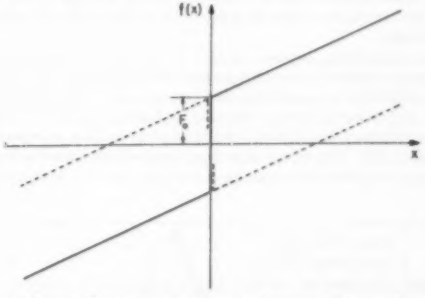

Fig. 1 System Incorporating Linear Springs With an Initial Tension

According to Equation [14]

$$\frac{I}{2\pi} = \frac{1}{2\pi}\int_0^{\pi}\{[A(1-\gamma^2)\sin\tau + b]^2 + (2\delta\gamma A)^2\cos^2\tau\}d\tau + \frac{1}{2\pi}\int_{\pi}^{2\pi}\{[A(1-\gamma^2)\sin\tau - b]^2 + (2\delta\gamma A)^2\cos^2\tau\}\,d\tau$$

$$-\frac{1}{2} = \frac{1}{2}A^2(1-\gamma^2)^2 + 2\delta^2\gamma^2A^2 + \frac{4}{\pi}b(1-\gamma^2)\,A + b^2 - \frac{1}{2}$$

or, with regard to Equation [24]

$$\frac{I}{2\pi} = \left(1 - \frac{8}{\pi^2}\right)b^2 \quad \ldots\ldots [26]$$

Since in the symmetrical system considered here the first superharmonic resonance may be expected when γ approaches the value $^1/_3$, it follows from Equation [13] after putting there

$$n = 3, \quad \bar{k} = 1, \quad \bar{m}\omega^2 = \gamma^2$$

$$|\alpha| \approx \frac{b\sqrt{1 - \frac{8}{\pi^2}}}{9\gamma^2 - 1} \qquad [27]$$

The Rüdenberg approximation, as can be easily verified, is expressed by a formula which is obtained from Equation [25] by replacing there the factors $4/\pi$ and $16/\pi^2$ by 1.

Instead of writing down now the somewhat lengthy exact solution of the foregoing problem, a numerical example may be given in Table 1 which is computed with the values $b = 0.25$ and $\delta = 0.2$. The figures in row I are the exact amplitudes while row II represents the new approximation, and row III the Rüdenberg solution. The last row gives the mean error $|\alpha|$ computed from Equation [27].

TABLE 1 NUMERICAL EXAMPLE

γ	0.5	0.75	0.9	1.0	1.2	1.5	2	4
I	0.824	1.336	1.978	2.358	1.815	0.916	0.417	0.0865
II	0.888	1.360	1.993	2.368	1.824	0.921	0.420	0.0872
III	0.973	1.477	2.109	2.420	1.769	0.880	0.399	0.0827
$\lvert\alpha\rvert$	0.087	0.027	0.017	0.013	0.009	0.006	0.003	0.0008

Table 1 shows that the errors of the Rüdenberg solution in average are about 7 times larger than those of the new approximation, and that the mean errors listed in the last row check surprisingly well with the actual errors of the latter approximation as long as γ does not too nearly approach the first superharmonic resonance. If, for instance, an error of 3 per cent is supposed admissible, then it might be concluded from the figures II and $|\alpha|$ without knowing the exact solution that the new one-term approximation may be applied if γ is not smaller than 0.7, and this conclusion would be quite in accordance with the actual conditions.

Fig. 2 shows the response curves I, II, and III pertaining to the numerical values. Curve I represents the exact deflection of the vibrating body midway between two consecutive zero positions. This mid-deflection is not identical with the greatest deflection if the vibratory velocity changes its sign more than once during a half cycle. The latter case just happens at superharmonic resonance and nearby, entailing the oscillations of curve I in that

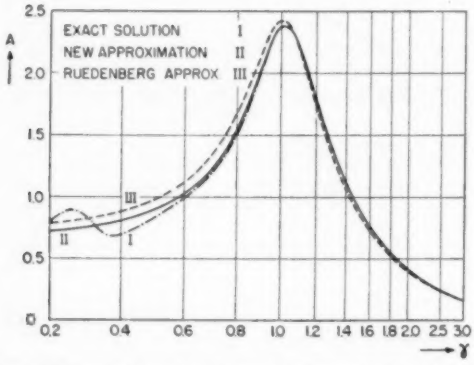

FIG. 2 RESPONSE CURVES OF A SYSTEM ACCORDING TO FIG. 1, WITH VISCOUS DAMPING

frequency range. Outside this range, the exact solution I and the new approximation II are so closely spaced as to appear fused whereas the Rüdenberg approximation III cle .rly deviates from the exact course over the whole frequency range of Fig. 2.

The second case is represented by the undamped system with

$$f(x) = k_0 x + k_1 x^3 \qquad [28]$$

which has been investigated by many authors, thus offering several approximate and also exact numerical solutions for comparative discussion. Substituting again

$$y = \frac{k_0 x}{P}, \quad \gamma = \omega\sqrt{\frac{m}{k_0}}, \quad a = \frac{k_1 P^2}{k_0^2} \qquad [29]$$

and regarding Equation [6], one obtains from the differential Equation [1]

$$\gamma^2 \frac{d^2y}{d\tau^2} + y + ay^3 = \sin(\tau + \varphi) \qquad [30]$$

Because no damping is involved, the conditions, Equations [8] and [9], furnish

$$P_1 = \frac{1}{\pi}\int_0^{2\pi} (A\sin\tau + aA^3\sin^3\tau - \gamma^2 A\sin\tau)\sin\tau d\tau$$

$$= \frac{3}{4}aA^3 + (1 - \gamma^2)A = 1 \qquad [31]$$

C. R. Wylie, Jr., (9) has discussed several approximate solutions of the undamped system, Equation [28], by comparing them with the exact numerical solution. In the following, reference is made to Fig. 3 of his paper which shows the response curves of this system pertaining to the value $a = 1$. The Rüdenberg approximation[4]

$$aA^3 + (1 - \gamma^2)A = 1$$

is contained in reference (9) as Equation [5] and plotted as curve ③ in Fig. 3 of that paper. It is stated there that this curve is "quite inaccurate." Drawing the curve corresponding to Equation [31] herewith, one will find that this curve closely coincides with curve ①, which results as first step of approximation from a rather inconvenient procedure suggested by A. Stodola and modified by M. Rauscher. This procedure is commented to "furnish quite accurate results." The comparison readily shows that the new approximation, though of about the same accuracy, is obtained in a much easier way.

On the assumption that the error of the amplitude is not to exceed an amount of 3 per cent, it appears from Fig. 3 of reference (9), that the Stodola-Rauscher approximation may be used as long as $\gamma > 0.8$. Inserting this frequency limit into Equation [31], one obtains the amplitude $A = 0.956$ and from that by using Equation [14]

$$\frac{I}{2\pi} = \frac{1}{2\pi}\int_0^{2\pi} (A\sin\tau + aA^3\sin^3\tau - \gamma^2 A\sin\tau)^2 d\tau - \frac{1}{2}$$

$$\frac{I}{2\pi} = \frac{1}{2}(1 - \gamma^2)^2 A^2 + \frac{3}{4}(1 - \gamma^2)A^4 + \frac{5}{16}A^6 - \frac{1}{2} = 0.0239$$

According to the differential Equation [30], the absolute value of the restoring force varies between zero and $A + aA^3$. The mean value $\bar{k}$ to be substituted into Equation [13], therefore may be taken equal to $1 + aA^2$, that is, equal to 1.9. After putting $n = 3$ and $m\omega^2 = \gamma^2$, one obtains from [13]

[4] In reference (9) the notation λ is used instead of γ.

$$\left|\frac{\alpha}{A}\right| \approx 4 \text{ per cent}$$

This error is a little greater than the assumed value of 3 per cent. In fact, when plotting in Fig. 3 of reference (9), the amplitude A according to Equation [31], one will find that the point pertaining to $\gamma = 0.8$ lies slightly farther off from the exact solution than the Stodola-Rauscher approximation.

Table 2 will show even more clearly the superiority of the new approximation over the Rüdenberg solution. Table 2 refers to the same spring characteristic, Equation [28], but pertains to the value $a = 0.5$ and gives the amplitudes A of the two-term Duffing solution in row I a, b, c, of the new approximation in row II a, b, c, and of the Rüdenberg approximation in row III a, b, c. The latter differs from the two-term approximation by amounts in average almost 6 times greater than those of the new approximation.

TABLE 2 EXAMPLE SHOWING SUPERIORITY OF NEW APPROXIMATION

γ	0.5	0.75	1.0	1.581	2	4
I a	0.976	1.145	1.423	2.341	3.074	6.579
II a	0.931	1.111	1.386	2.275	2.982	6.356
III a	0.880	1.031	1.260	2.000	2.603	5.510
I b	...	...	...	1.502	2.706	6.505
II b	...	...	...	1.484	2.642	6.289
III b	...	...	...	1.000	2.262	5.442
I c	...	...	...	0.793	0.338	0.066
II c	...	...	...	0.790	0.338	0.066
III c	...	...	...	1.000	0.340	0.067

The last example will be an asymmetrical system whose spring characteristic is straight but of different slope at positive and negative deflections, as illustrated in Fig. 3. Assuming the

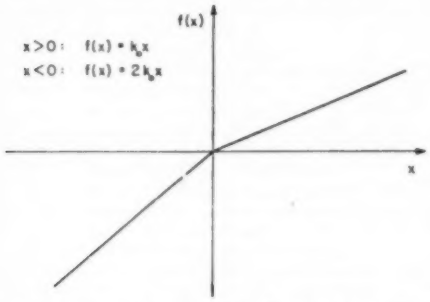

FIG. 3 ASYMMETRICAL SYSTEM WITH BROKEN SPRING CHARACTERISTIC

slope on the negative side to be twice as great as that on the positive side and using the Notation [29], the following differential equation of this system is obtained

$$\left.\begin{aligned} \gamma^2 \frac{d^2y}{d\tau^2} + y &= q \cos \tau, \quad \text{if } y > 0 \\ \gamma^2 \frac{d^2y}{d\tau^2} + 2y &= q \cos \tau, \text{ if } y < 0 \end{aligned}\right\} \quad \ldots\ldots [32]$$

The harmonic exciting force is expressed by a cosine function instead of a sine function (used in the preceding examples) because that is more convenient in the present case. The one-harmonic-term approximation may be written

$$y = A \cos \tau + B$$

or, with respect to Fig. 4

$$y = A(\cos \tau - \cos \epsilon) \ldots\ldots [33]$$

The integral to be minimized is now

$$I = 2 \int_0^{\epsilon} [A(1 - \gamma^2) \cos \tau - A \cos \epsilon - q \cos \tau]^2 \, d\tau + 2 \int_{\epsilon}^{\pi} [A(2 - \gamma^2) \cos \tau - 2A \cos \epsilon - q \cos \tau]^2 \, d\tau$$

By analogy, the first minimizing condition is

$$\frac{\partial I}{\partial q} = 0$$

As second minimizing parameter, ϵ can be chosen so that

$$\frac{\partial I}{\partial \epsilon} = 0$$

The evaluation of these conditions leads to following two equations between A, ϵ, q

$$A\left(\pi - \frac{\epsilon}{2} + \frac{1}{4} \sin 2\epsilon - \frac{\pi}{2} \gamma^2\right) - \frac{\pi}{2} q = 0$$

$$A[3 + (4\pi - 3\epsilon) \cot \epsilon - \gamma^2] - q = 0$$

the determinant of which has to vanish if A and q are supposed different from zero. Hence

$$\epsilon - \frac{1}{2} \sin 2\epsilon + \pi(4\pi - 3\epsilon) \cot \epsilon + \pi = 0 \ldots\ldots [34]$$

In the interval $0 < \epsilon < \pi$ Equation [34] has one root, namely, $\epsilon = 102.876$ deg, which is independent of γ. If the exciting force has the value P, then, with respect to Equations [29] and [32], q has to be taken equal to 1. Thus

$$A = \frac{1}{3 + (4\pi - 3\epsilon) \cot \epsilon - \gamma^2} = \frac{1}{1.3591 - \gamma^2} \ldots [35]$$

The Rüdenberg approximation is

$$A = \frac{1}{1.3333 - \gamma^2}$$

The rigorous solution of this problem shows that ϵ actually is variable and that a fundamental resonance occurs when $\gamma^2 = 8(3 - 2\sqrt{2}) = 1.3726$. Some numerical values of the amplitudes A are computed in Table 3 where row I gives the exact solution, row II the new approximation, and row III the Rüdenberg solution. The last row contains the estimated error $|\alpha|$ calculated from

$$|\alpha| \approx \frac{0.145\, A}{4\gamma^2 - 1.36} \ldots\ldots [36]$$

This formula is obtained from Equation [13] after evaluating the integral I and putting $n = 2$ because of asymmetry. The exact amplitudes listed are defined equal to the mean value of the absolute deflections at $\tau = 0$ and $\tau = \pi$ (see Fig. 4).

TABLE 3 NUMERICAL VALUES OF AMPLITUDES

γ	0.9	1.0	1.171	1.5	2	4
I	1.764	2.672	∞	1.137	0.3802	0.06835
II	1.822	2.785	74.0	1.122	0.3786	0.06830
III	1.911	3.000	25.4	1.091	0.3750	0.06818
$\lvert\alpha\rvert$	0.118	0.153	...	0.021	0.0037	0.0002

The figures in Table 3 show that the accuracy of the new approximation now is only 3 times better than that of the Rüdenberg solution, while it was 6 to 8 times better in the first and second examples. The estimated error $|\alpha|$ of the amplitudes also checks less well with the actual errors than previously, but it is still possible to determine the frequency limit for a pre-

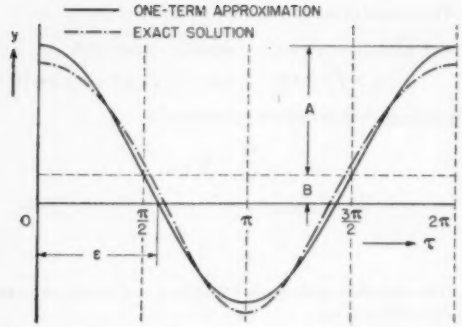

FIG. 4 ONE-TERM APPROXIMATION OF AN ASYMMETRICAL VIBRATION

scribed error $|\alpha/A|$ rather reliably. Assuming, for instance again, $|\alpha/A| = 3$ per cent, one finds from Equation [36] that γ should be greater than 1.24, while actually the limit is between 1.1 and 1.2. In comparison with symmetrical systems, the results indicate a loss of accuracy of the suggested one-term approximation applied to asymmetrical systems.

BIBLIOGRAPHY

1 "Einige unharmonische Schwingungsformen mit grosser Amplitude," by R. Rüdenberg, *Zeitschrift für Angewandte Mathematik und Mechanik*, vol. 3, 1923, p. 454.

2 "Erzwungene Schwingungen bei veränderlicher Eigenfrequenz," by G. Duffing, F. Vieweg, Braunschweig, 1918.

3 "Steady Oscillations of Systems With Nonlinear and Unsymmetrical Elasticity," by M. Rauscher, JOURNAL OF APPLIED MECHANICS, Trans. ASME, vol. 60, 1938, p. A-169.

4 "The Amplitudes of Non-Harmonic Vibrations," by J. P. Den Hartog, *Journal of The Franklin Institute*, vol. 216, 1933, pp. 459–473.

5 "On Forced Pseudo-Harmonic Vibrations," by I. K. Silverman, *Journal of The Franklin Institute*, vol. 217, 1934, pp. 743–745.

6 "Forced Vibrations With Combined Coulomb and Viscous Friction," by J. P. Den Hartog, Trans. ASME, vol. 53, 1931, Paper APM-53-9.

7 "Forced Vibrations With Non-Linear Spring Constants," by J. P. Den Hartog and S. J. Mikina, Trans. ASME, vol. 54, 1932, Paper APM-54-15.

8 "An Experimental Investigation of Forced Vibrations in a Mechanical System Having a Non-Linear Restoring Force," by C. A. Ludeke, *Journal of Applied Physics*, vol. 17, 1946, pp. 603–609.

9 "On the Forced Vibrations of Non-Linear Springs," by C. R. Wylie, Jr., *Journal of The Franklin Institute*, vol. 236, 1943, p. 273.

10 "Steady Forced Vibration as Influenced by Damping," by L. S. Jacobsen, Trans. ASME, vol. 52, 1930, Paper APM-52-15.

11 "Forced Vibrations of Systems With Non-Linear Restoring Force," by K. O. Friedrichs and J. J. Stoker, *Quarterly of Applied Mathematics*, Brown University, Providence, R. I., vol. 1, 1943, pp. 97–115.

Longitudinal and Torsional Impact in a Uniform Bar With a Rigid Body at One End[1]

By A. H. BURR,[2] ITHACA, N. Y.

A uniform bar carrying a rigid body at one end is analyzed for those cases where its other end is struck by a rigid body, and struck by a bar and body, also for the case of sudden application of force at either end. Recurrence formulas are derived in nondimensional form and applied to determine in a finite number of terms the stress equations for striking impact and for a constant-force impact. Some useful theorems and simplifications, applicable to other problems of this nature, are indicated. For striking impact by a rigid body, charts show the time-variation of stress and the maximum stress for a range of physical values of the bar and bodies. Application to the design of bars, helical springs, and shafts is discussed.

Nomenclature

The following nomenclature is used in the paper:

A = area of cross section of bar
$1/\alpha$ = bar ratio = W/W_{bar} for longitudinal impact (= I/I_{bar} for torsional impact)
c = velocity of longitudinal wave propagation = $\sqrt{E/\rho}$
c_t = velocity of torsional wave propagation = $\sqrt{G/\rho}$
d = bar or shaft diameter
E = modulus of elasticity of bar
G = modulus of elasticity in shear of spring or shaft
g = gravitational acceleration
γ = weight density of bar or shaft
ρ = mass density of bar or shaft = γ/g
$F(t)$, $F'(t)$ = forces, expressed as function of time t, applied to body W and body W', respectively
F_0' = constant force suddenly applied to body W'
I, I' = mass moments of inertia of bodies at ends $x = 0$ and $x = l$, respectively
I_{bar} = mass moment of inertia of bar or shaft
J = polar moment of inertia of area for bar or shaft
$K = -K' = (q + q')/(q - q') = (\lambda + 1)/(\lambda - 1)$
l = length of bar or shaft
λ = body ratio = W'/W for longitudinal impact (= I'/I for torsional impact)
Λ, Λ' = operators defined by Equations [15] and [16]
$q = gA\sqrt{E\rho}/W = 2\alpha/T$
$q' = gA\sqrt{E\rho}/W' = 2\alpha/\lambda T$
σ, σ' = total stresses
R, R' = dimensionless total stresses
s, s' = wave stresses
S, S' = dimensionless wave stresses
σ_0, τ_0 = initial normal and shearing stresses, respectively, in striking impact
t = time
T = period or interval = $2l/c$ for longitudinal impact (= $2l/c_t$ for torsional impact)
v, v' = particle or body velocities
V, V' = dimensionless particle or body velocities
v_0, ω_0 = linear and angular striking velocities, respectively
W, W' = weight of bodies at ends $x = 0$ and $x = l$, respectively
W_{bar} = weight of bar = $A\gamma l$
x = position along bar or shaft
z_m = dimensionless quantity = $-q(t - mT)$ = $-2\alpha\left(\frac{t}{T} - m\right)$
z_m' = dimensionless quantity = $-q'(t - mT)$ = $-\frac{2\alpha}{\lambda}\left(\frac{t}{T} - m\right)$

Introduction

In machinery, longitudinal impact may occur in hoisting rope, connecting rods, hammer-type power tools, and helical springs, torsional impact, in the rotating shafts of punches and shears, geared drives, clutches, brakes, and drills. The theoretical study reported in this paper was undertaken with the expectation that it would find application to such machinery. Although the principal derivations herein are in terms of longitudinal impact, the differential equations and their solutions, except for physical constants, are identical for torsional impact, and attention is given to making the results readily applicable to both cases. An adaptation for the longitudinal impact of helical springs is also given.

One kind of impact consists of a striking or collision of one metal part with another, as in the engagement of jaw clutches, in hammering actions, and in the taking-up of slack in rope and of clearances in bearings. This will be called *striking impact*. Another kind consists of the rapid application of force or torque, as in the sudden support of the weight of a body, and as friction torque in clutches and brakes. This will be called *force impact*. The two kinds of impact may occur simultaneously as during the sudden connection of two members, one of which has been accelerating under force or motor torque.

The physical system principally treated herein is that of a uniform elastic bar or shaft at each end of which there is a relatively rigid body with its center of mass on the axis of the bar. The mass of the bar is considered, but the bodies are treated as inelastic. At one end of the bar the body is permanently attached. At the other end, in the case of striking impact, the bar is struck by the body and is in contact with it until separation, Figs. 1(*a* and *b*); in the case of force impact the body may either be considered attached to or in contact with the bar, and force is suddenly applied to this body, Figs. 2(*a* and *b*). A briefer treatment is made of another system, that of the striking of two bars

---

[1] This paper is based upon a dissertation submitted by the author in partial fulfillment of the requirements for the degree of Doctor of Philosophy in the University of Michigan.

[2] Professor and Head, Department of Machine Design, Cornell University. Mem. ASME.

Contributed by the Applied Mechanics Division and presented at the Annual Meeting, New York, N. Y., November 27–December 2, 1949, of The American Society of Mechanical Engineers.

Discussion of this paper should be addressed to the Secretary, ASME, 29 West 39th Street, New York, N. Y., and will be accepted until July 10, 1950, for publication at a later date. Discussion received after the closing date will be returned.

Note: Statements and opinions advanced in papers are to be understood as individual expressions of their authors and not those of the Society. Paper No. 49—A-6.

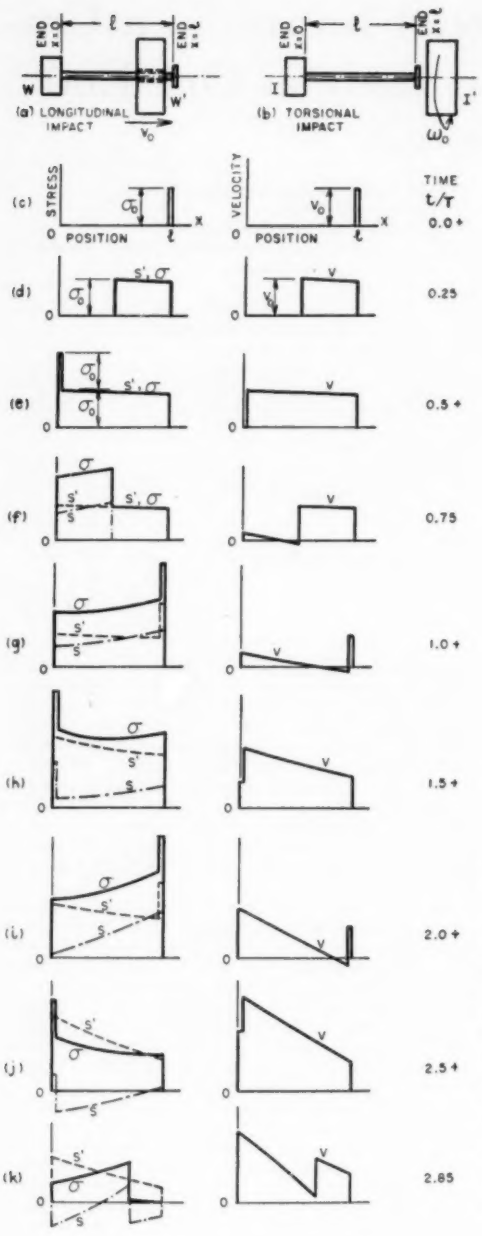

FIG. 1 STRIKING-IMPACT WAVE ACTION
(Plotted for $1/\alpha = W/W_{bar} = I/I_{bar} = 4$, $\lambda = W'/W = I'/I = 10$, and material steel.)

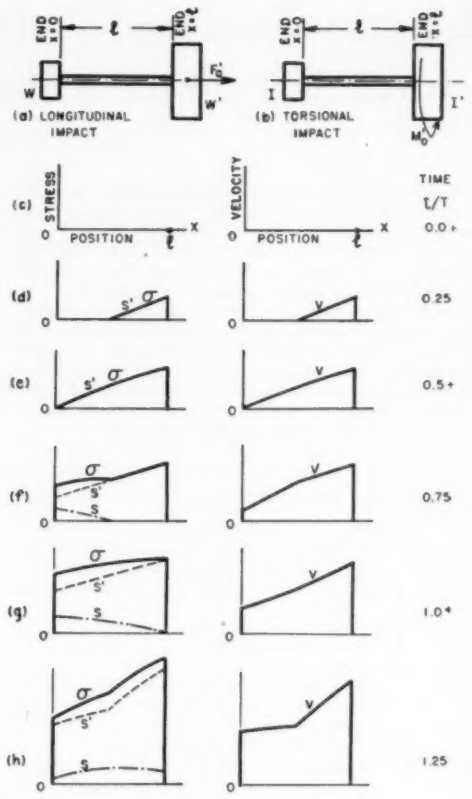

FIG. 2 FORCE-IMPACT WAVE ACTION

the nonstriking ends of which carry attached rigid bodies (Appendix 3 and Fig. 9).

The method essentially used in deriving recurrence equations is that which was presented by Donnell (1, 2)[3] in his solution of the bar fixed at one end and struck at the other. The equation of motion of an end body is written as an ordinary differential equation of first order and degree. By a consideration of the properties of wave propagation, solution of the equation is readily made for the stress value at the end of the bar. However, a new solution is required for each period or interval of time required for the wave front to travel the length of the bar and return. Hence there is derived a recurrence formula, a type used earlier in impact problems by Saint Venant (3, 4), and Boussinesq (5, 6). It is a formula which gives the solution for one interval in terms of that for the previous interval, including an integral and a constant of integration. Solutions are obtained in finite numbers of terms.

IMPACT WAVE ACTION IN BARS WITH FINITE BODIES AT EACH END

A longitudinal disturbance in a bar is propagated along the bar in an elastic wave traveling at the velocity of sound, a con-

[3] Numbers in parentheses refer to the Bibliography at the end of the paper.

stant propagation velocity $c = \sqrt{E/\rho}$, where E is the modulus of elasticity, and ρ the mass density of the material of the bar (7). A second and much smaller velocity is that of the particles, undergoing displacement and deformation throughout the bar. This is known as the particle velocity, in general, a variable quantity. In a wave propagated in the negative direction, particle velocity v_w' is related to stress s' by the formula $v_w' = s'/\sqrt{E\rho}$, (8). The particles move in the positive direction to cause a tensile or positive stress.[4] On the other hand, in a wave propagated in the positive direction the relation is $v_w = -s/\sqrt{E\rho}$, i.e., the particles must move in the negative direction to cause a positive or tensile stress. These two waves may superimpose, such that at any position x along the bar the *total stress* σ and the *net velocity* v are, respectively

$$\sigma = s' + s \quad \ldots\ldots [1]$$

and

$$v = \frac{1}{\sqrt{E\rho}}(s' - s) \quad \ldots\ldots [2]$$

When action is initiated by a rigid body striking the bar, there is a sudden change in the particle velocity at the position struck, a change which equals the relative *striking velocity* v_0, Fig. 1(*c*). By the previously stated relation between velocity and stress, the *initial stress* σ_0, which is suddenly induced at this position is[4]

$$\sigma_0 = v_0\sqrt{E\rho} \quad \ldots\ldots [3]$$

The stress which immediately follows the initial stress is a function of the mass of the body and of the cross-sectional area of the bar. In striking impact it is a decreasing stress, as the elastic force of the bar acts against the body, decreasing its velocity and hence the velocity of the adjacent particles of the bar.

The elastic force induced at an impact end, acting against the adjacent region, causes an acceleration of its particles and a propagation as a wave along the bar of the conditions at the impact end, Figs. 1(*d*, *e*). Damping neglected, the stress and velocity conditions travel unchanged to the other end of the bar. In Fig. 1 stress distribution is illustrated in the left-hand column, and velocity in the center column. The time of occurrence for each row is indicated in the right-hand column by the ratio t/T, where t is the time and $T = 2l/c$ is the period or time for propagation of a wave over the length of the bar and return. In the stress column, negatively propagated stress s', positively propagated stress s, and total stress σ are shown separately.

At the left-hand end of the bar, because the attached body is rigid and, having mass, cannot change its velocity suddenly, there occurs upon incidence of the wave, a reflection of the stress in the form of a wave s of the same kind, i.e., tensile or compressive, Fig. 1(*e*). The initial magnitude s of the reflected wave[5] is σ_0. The subsequent shape of the reflected wave, however, is affected by the motion of the attached body under the elastic force of the bar. The velocity v of the body increases, and reflected stress s is smaller than incident stress s', by Equation [2], Fig. 1(*f*).

In similar manner the wave s is reflected by the body now in contact at the right-hand end of the bar,[5] and the effect of the reflection is added to the wave s', Fig. 1(*g*). In striking impact, one or more reflections, Figs. 1(*h*, *i*, *j*), often many reflections, from each end of the bar occur before the stress again becomes zero in value, Fig. 1(*k*). When it becomes zero at the striking end, separation occurs.

If, instead of by striking, the action is initiated by a force suddenly applied to a rigid body in contact with the bar, the initial velocity of the body and adjacent particles is zero; hence the initial stress is zero, Fig. 2(*c*). The stress during the first interval is an increasing one as the continued action of the external force upon the body increases its velocity. The initial reflection is zero, Fig. 2(*e*). Likewise, for subsequent reflections, Fig. 2(*g*) the only discontinuity is in the slope of the stress curve.

Equations for torsional waves are derived in Appendix 1. Velocity of propagation along the axis is $c_t = \sqrt{G/\rho}$, where G is the modulus of elasticity in shear. The initial extreme-fiber stress in the striking impact of a circular shaft is

$$\tau_0 = \frac{\omega_0 d}{2}\sqrt{G\rho} \quad \ldots\ldots [4]$$

where ω_0 is the relative angular striking velocity, and d is the shaft diameter. These equations are similar to those for longitudinal impact, and for the torsional impacts illustrated in Figs. 1(*b*) and 2(*b*), the stress and velocity diagrams of Figs. 1 and 2 hold, except that c_t should be substituted for c and τ for σ.

Recurrence Formulas

The derivation which follows is for a system in which striking and force impact occur simultaneously, striking at one end and force at both ends, the most general case for a bar with bodies at both ends.

At both ends, stress is discontinuous at intervals of time equal to that required for a wave to travel the length of the bar and return, the period $T = 2l/c$. Hence subscript notation is required to indicate the interval for which an equation holds. For end $x = 0$, subscript n ($n = 1, 2, 3\ldots$), indicates the time interval $(n - 0.5)T \leqslant t < (n + 0.5)T$. Equations [1] and [2] for total stress σ and net velocity v may be rewritten, respectively, as

$$\text{End } x = 0 \begin{cases} \sigma_n = s_n'(t - 0.5T) + s_n(t) \quad \ldots\ldots [5] \\ v_n = \dfrac{1}{\sqrt{E\rho}}[s_n'(t - 0.5T) - s_n(t)] \quad \ldots\ldots [6] \end{cases}$$

The first term to the right of the equality sign is the stress value of the incident wave determined at the other end a time $0.5T$ earlier,[6] and the second term is the stress value of the reflected wave initiated at the beginning of the interval. Similar equations may be written for σ_n' and v_n' at the other end, valid for the time interval $(n - 1)T < t < nT$

$$\text{End } x = l \begin{cases} \sigma_n' = s_{n-1}(t - 0.5T) + s_n'(t) \quad \ldots\ldots [7] \\ v_n' = \dfrac{1}{\sqrt{E\rho}}[-s_{n-1}(t - 0.5T) + s_n'(t)] \quad \ldots\ldots [8] \end{cases}$$

The equation of motion for the attached body of weight W at end $x = 0$, is

$$A\sigma_n + F(t) = \frac{W}{g}\frac{dv_n}{dt} \quad \ldots\ldots [9]$$

where $A\sigma_n$ is the elastic force exerted by the bar, and $F(t)$ is the externally applied force, expressed as a function of time t. With

[4] The signs of the formulas are chosen to fit the system of Fig. 1(*a*) in which the body, traveling in the positive x-direction, i.e., with positive velocity v_0, gives, upon striking, an initial stress which is tensile. Thus by the formulas, a tensile stress will be indicated by a positive value, a compressive stress, by a negative value, in the conventional manner.

[5] Against a rigid body a discontinuity in the stress wave is reflected in full value regardless of the velocity of the body. By Equation [2], a sudden change in s or s' must be accompanied by the same change in s' or s, respectively. The total stress, $\sigma = s' + s$, is thereby suddenly changed by twice the value of the stress-wave discontinuity.

[6] The parenthetical expression $(t - 0.5T)$ indicates that $t - 0.5T$ is to be substituted for t in the equation for s_n'.

the substitution for s_n and σ_n by Equations [5] and [6], and for $gA\sqrt{E\rho}/W$ by the symbol q, there is obtained the equation

$$\frac{d}{dt}[s_n(t) - s_n'(t-0.5T)] + qs_n(t) + qs_n'(t-0.5T) = -q\frac{F(t)}{A}$$

With the addition to both sides of this equation of the term $-2qs_n'(t-0.5T)$, there is obtained an equation of the form

$$\frac{dy}{dt} + qy = Q$$

where $y = s_n(t) - s_n'(t-0.5T)$, q is a constant, and $Q = -2qs_n'(t-0.5T) - qF(t)/A$ is a function of t only. This is an ordinary linear differential equation of first order, and it may be integrated after multiplication throughout by the integrating factor e^{qt}. Its solution is

$$y = e^{-qt}\int e^{qt}Q dt + C_n e^{-qt}$$

where C_n is the constant of integration. After substitution for y and Q, the equation may be solved for the unknown reflected stress $s_n(t)$ in terms of the known incident stress $s_n'(t-0.5T)$ and the force function $F(t)$. Thus

$$s_n(t) = s_n'(t-0.5T) - 2qe^{-qt}\int e^{qt}s_n'(t-0.5T)dt - \frac{q}{A}e^{-qt}\int e^{qt}F(t)dt + C_n e^{-qt} \quad [10]$$

This is the *recurrence formula* for end $x = 0$. The constant of integration C_n is found from the equation

$$s_n[(n-0.5)T] = s_{n-1}[(n-0.5)T] + \sigma_0 \quad [11]$$

which expresses the phenomenon that at time $(n-0.5)T$, at the beginning of the nth interval, the reflected stress of the $(n-1)$th interval is suddenly increased by an amount σ_0 upon arrival of the discontinuity of value σ_0; also, that for force impact only ($\sigma_0 = 0$) there is no discontinuity in the value of s.

The equation of motion for the body of weight W' in contact with the bar at end $x = l$ is

$$-A\sigma_n' + F'(t) = \frac{W'}{g}\frac{dv_n'}{dt} \quad [12]$$

where $-A\sigma_n'$ is the elastic force exerted by the bar and $F'(t)$ is the externally applied force. By steps similar to those given, the recurrence formula for end $x = l$ is found to be

$$s_n'(t) = s_{n-1}(t-0.5T) - 2q'e^{-q't}\int e^{q't}s_{n-1}(t-0.5T)dt + \frac{q'}{A}e^{-q't}\int e^{q't}F'(t)\,dt + C_n' e^{-q't} \quad [13]$$

where $q' = gA\sqrt{E\rho}/W'$, and the constant of integration C_n' is found from the equation

$$s_n'[(n-1)T] = s'_{n-1}[(n-1)T] + \sigma_0 \quad [14]$$

A-Operations

Because application of the recurrence formulas becomes increasingly tedious with each succeeding integration, it is advantageous to seek every possible simplification. In the successive stress equations s_1', s_1, s_2', s_2, s_3' ..... there will be a repetition of terms of the type $Z(t) = z_m e^{qm}$, where $k = 0, 1, 2, \ldots$, and $z_m = -q(t - mT)$, where $m = 0.0, 0.5, 1.0, 1.5, 2.0, \ldots$ Substitution into Equation [10] of an expression for s_n' containing one or more $Z(t)$-terms means the following operation Δ will be performed upon each $Z(t)$-term

$$\Delta[Z(t)] = Z(t-0.5T) - 2qe^{-qt}\int e^{qt}Z(t-0.5T)dt \quad [15]$$

where the expression in parentheses indicates that $t - 0.5T$ is substituted for t in the term Z. Likewise, for use in Equation [13], there may be defined

$$\Delta'[Z(t)] = Z(t-0.5T) - 2q'e^{-q't}\int e^{q't}Z(t-0.5T)dt \quad [16]$$

Before application of the recurrence formulas it is advantageous to evaluate $\Delta[Z(t)]$ and $\Delta'[Z(t)]$ for several values of the exponent k. The results are listed in Table 2 of Appendix 2. Useful constants are K and K', defined as follows

$$K = -K' = \frac{q+q'}{q-q'} \quad [17]$$

Nondimensional Forms

Additional simplifications follow from separate treatments of striking impact and force impact and from nondimensional equation forms. In nondimensional form Equations [5], [6], [7], and [8] become, respectively

$$R_n = S_n'(t-0.5T) + S_n(t) \quad [18]$$

$$V_n = S_n'(t-0.5T) - S_n(t) \quad [19]$$

$$R_n' = S_{n-1}(t-0.5T) + S_n'(t) \quad [20]$$

$$V_n' = -S_{n-1}(t-0.5T) + S_n'(t) \quad [21]$$

For striking impact only, total stresses are $R_n = \sigma_n/\sigma_0$ and $R_n' = \sigma_n'/\sigma_0$, wave stresses $S_n = s_n/\sigma_0$ and $S_n' = s_n'/\sigma_0$, and body velocities $V_n = v_n/v_0$ and $V_n' = v_n'/v_0$. The recurrence formulas, Equations [10], [11], [13], and [14], respectively, become for striking impact only and in terms of the operators defined by Equations [15] and [16]

$$S_n(t) = \Delta[S_n'(t)] + B_n e^{q_0} \quad [22]$$

$$S_n[(n-0.5)T] = S_{n-1}[(n-0.5)T] + 1.0 \quad [23]$$

$$S_n'(t) = \Delta'[S_{n-1}(t)] + B_n' e^{q_0 t} \quad [24]$$

$$S_n'[(n-1)T] = S'_{n-1}[(n-1)T] + 1.0 \quad [25]$$

where B_n and B_n' are constants of integration.

For a force impact only caused by a constant force F_0' suddenly applied at end $x = l$, there may be defined the static stress $\sigma_{st} = F_0'/A$, whence $R_n = \sigma_n/\sigma_{st}$ and $R_n' = \sigma_n'/\sigma_{st}$, $S_n = s_n/\sigma_{st}$ and $S_n' = s_n'/\sigma_{st}$, and $V_n = v_n\sqrt{E\rho}/\sigma_{st}$ and $V_n' = v_n'\sqrt{E\rho}/\sigma_{st}$. Equations [10], [11], [13], and [14] become, respectively

$$S_n(t) = \Delta[S_n'(t)] + D_n e^{q_0} \quad [26]$$

$$S_n[(n-0.5)T] = S_{n-1}[(n-0.5)T] \quad [27]$$

$$S_n'(t) = \Delta'[S_{n-1}(t)] + 1 + D_n' e^{q_0 t} \quad [28]$$

$$S_n'[(n-1)T] = S'_{n-1}[(n-1)T] \quad [29]$$

where D_n and D_n' are constants of integration.

Stress Equations

The stress equations may now be determined. At the impact end, $x = l$, of the bar during the first time interval $n = 1$ following impact, no earlier stresses exist, and S_0 and S_0' are zero. Hence the recurrence formulas, Equations [24] and [25], or [28] and [29], may be applied to determine the expression for stress S_1', the stress during the first interval. Then Equations [22] and [23], or [26] and [27] may be applied to determine S_1, the reflected stress during the first interval at the other end, $x = 0$. In the same manner the recurrence formulas for the two ends may

be applied alternately to determine expressions for the reflected stresses S_2', S_2, S_2', S_3, of successive intervals. Resulting equations for several intervals are listed in Tables 3 and 5 of Appendix 2.

In the special case of end bodies of equal weight, $W' = W$, $q' = q$, the value of K (Equation [17]) becomes infinite, and the general stress equations cannot be used. However, if the recurrence formulas are applied to this case, K will not appear in the results. These results are added to Tables 3 and 5.

Equations for total stresses R_a and R_a', determined from Tables 3 and 5, and Equations [18] and [20], are listed in Tables 4 and 6.

It may be proved that the stress resulting from two or more simultaneous impacts, even though not initiated at the same instant, is obtained by adding the stresses for the impacts acting separately (9). This holds for striking or force impacts or a combination of the two kinds. Additions must be made with stresses $R\sigma_0$ and $R\sigma_{st}$, not with the dimensionless stresses R.

Characteristics of Striking Impact

Charts have been prepared to show the variation of stress and velocity with time, Figs. 3, 4, 5, and the variation of maximum stress with physical proportions, Figs. 6, 7. The computations can be shortened if it is observed that certain terms in the stress equations (Appendix 2) have in one interval the same numerical value as in the preceding interval at a time T earlier. Thus $e'^2 = e^{-q(t-2T)}$ at time $t = 2.5T$ has the same numerical value as $e'^1 = e^{-q(t-T)}$ at time $t = 1.5T$. Details of a method of calculation, including a rearrangement of the stress equations of Appendix 2 to utilize duplications of numerical values, are given

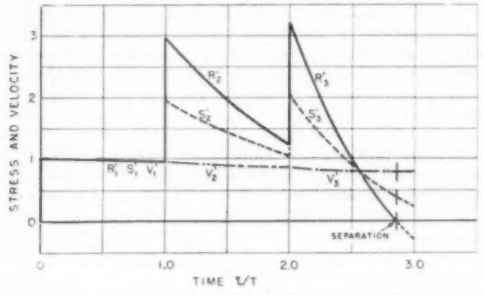

Fig. 3 At Striking End $x = l$ A Time Variation of Dimensionless Total Stress R', Wave Stress S', and Velocity V'
(For a bar ratio $1/\alpha = 4$, a body ratio $\lambda = 10$, and striking impact.)

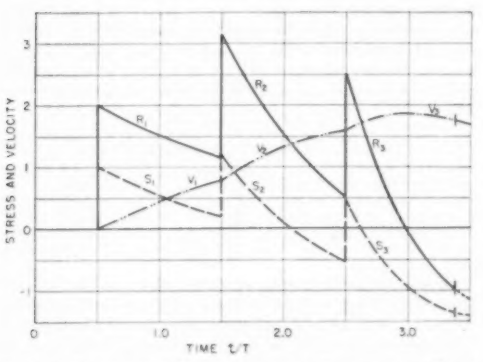

Fig. 4 At End $x = 0$ A Time Variation of Dimensionless Total Stress R', Wave Stress S', and Velocity V'
(For a bar ratio $1/\alpha = 4$, a body ratio $\lambda = 10$, and striking impact.)

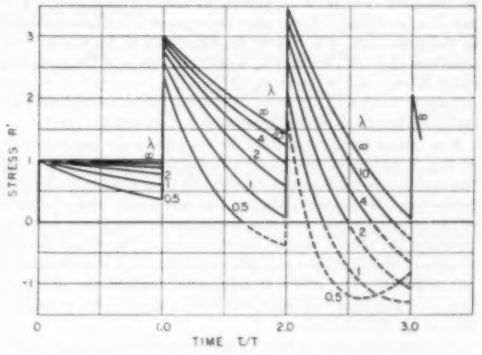

Fig. 5 At Striking End $x = l$ The Time Variation of Dimensionless Total Stress R' for Several Values of Body Ratio λ
(For a bar ratio $1/\alpha = 4$ and striking impact.)

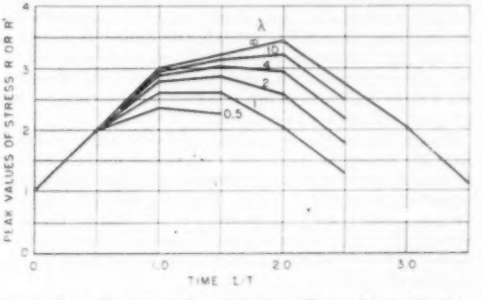

Fig. 6 Peak Values of Dimensionless Total Stress R or R' Plotted Against Time at Beginning of Each Interval
(For a bar ratio $1/\alpha = 4$ and striking impact.)

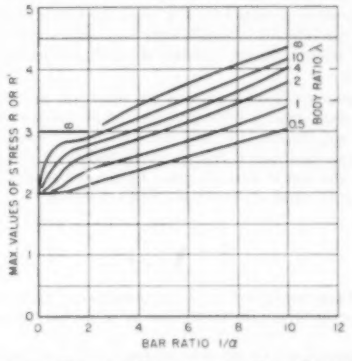

Fig. 7 Maximum Values of Dimensionless Total Stress Before Separation
(For striking impact and plotted as a function of bar ratio $1/\alpha$ and body ratio λ.)

elsewhere (10). A complete table of exponential values, such as given in reference (11), is also helpful.

Convenient nondimensional quantities are the body ratio λ and the bar ratio $1/\alpha$,[7] defined for longitudinal impact as $\lambda = W'/W$ and $1/\alpha = W/W_{bar}$, and for torsional impact as $\lambda = I'/I$ and $1/\alpha = I/I_{bar}$. Time may be expressed nondimensionally as the time ratio, t/T. Now the equations of Appendix 2 are functions of K, K', z_m, and z_m' only. In terms of the foregoing ratios $K = -K' = (\lambda + 1)/(\lambda - 1)$, $z_m = -q(t - mT) = -2\alpha(t/T - m)$, and $z_m' = z_m/\lambda$. Hence the stress and velocity ratios are functions of the three ratios λ, $1/\alpha$, and t/T, only.

Figs. 3 and 4 are constructed for the same body and bar ratios as Fig. 1, but show the time variation for the velocities of the two bodies and the reflected stresses and total stresses at the ends of the bar. Separation at the impact end occurs when the slope of the velocity curve, i.e., the acceleration of the body, becomes zero and the total stress R' becomes zero. The dotted line extension of the stress beyond this time holds only if separation is not possible. The effect of separation reaches the attached-body end at a time $0.5T$ later, and the stress curve R beyond that time is likewise dotted.

For striking impact it may be proved analytically that at each end of the bar, until at least the time of zero total stress, the total stress and the wave stress are continuously decreasing quantities throughout their intervals, with peak values at the beginnings of their intervals (12). This is illustrated in Fig. 5, plotted for several values of λ. Also, it may be proved analytically that the maximum stress before separation is located at an end[8] of the bar (13). Hence, to determine the maximum stress following a striking impact, it is sufficient to calculate the stresses R' and R at the beginnings of their respective time intervals, namely, $t = (n - 1)T$ and $t = (n - 0.5)T$.

Peak points for the two ends are plotted together in Fig. 6. Each line joining the points rises continuously until a maximum is reached, thereafter drops continuously, although the points are plotted alternately for each end. This same characteristic occurs for $1/\alpha = 0.5$, 1, 2, 4, and 10 with $\lambda = 0.5$, 1, 2, 4, 10, and infinity (∞). The maximum point of each peak-value curve is plotted in Fig. 7 to give maximum stress before separation as a function of $1/\alpha$ and λ.

As $1/\alpha$ increases, the maximum stress, the time of its occurrence, and the duration of impact increase. For an extension of Fig. 7 to higher values of $1/\alpha$, stress equations would be needed for more intervals than the three per end listed in Tables 3 and 4. The characteristic noted for Fig. 6 should prove useful in predicting the interval in which each maximum stress will occur, thereby minimizing the number of equations and calculations required.

By assuming that all parts of the bar reach maximum stress and the same velocity at the same instant, and neglecting the mass of the bar, Tuplin (15) uses the equation of conservation of momentum to obtain a velocity of the bodies after impact, then equates the loss of kinetic energy to the energy of strain. His equation, in terms of the ratios α and λ, becomes

$$R = \sqrt{\frac{\lambda}{\alpha(1 + \lambda)}} \quad \ldots\ldots\ldots\ldots\ldots [30]$$

A slight improvement in this approximate energy method is obtained by including the kinetic energy of the bar, whence

$$R = \sqrt{\frac{\lambda(1 + \alpha)}{\alpha(1 + \alpha + \lambda)}} \quad \ldots\ldots\ldots\ldots\ldots [31]$$

Because of its assumption of uniform stress the energy method will indicate a lower stress than will the wave method. For the range covered by Fig. 7, the energy method gives large errors, differing by more than 1.0 in absolute value, but decreasing with increasing values of $1/\alpha$. For the special case of a fixed end ($W = \infty$) the absolute error varies from 1.20 at $W'/W_{bar} = 4.0$ to 1.00 at $W'/W_{bar} = 64.0$, with corresponding relative errors of 37 per cent and 11 per cent.

Equations for the stress after separation have not been developed. However, it has been demonstrated (16) that the stress ratio after separation will not be greater than 3.0 for the $1/\alpha$ and λ-ranges of Fig. 7.

Design of Bars, Helical Springs, and Shafts

Maximum stress is rapidly determined by use of a chart such as Fig. 7. One need only compute the body ratio λ and bar ratio $1/\alpha$, then enter the chart to determine the stress ratio R. The maximum stress in pounds per square inch is this value of R, multiplied by the initial stress. For a bar, initial stress is given by Equation [3], which for steel becomes $\sigma_0 = 148\ v_0$, with v_0 in in. per sec. For a helical spring, initial shearing stress is $\tau_0 = K_w v_0 \sqrt{2G\rho/\cos\beta}$, where K_w is the Wahl factor, and β is the lead angle of the coil.[9] For steel, and taking $\cos\beta = 1.0$, $\tau_0 = 130\ K_w v_0$; and the weight of the spring, in pounds, is $W_{bar} = 0.70\ D_w^2 D_m N$, where D_w and D_m are wire and mean coil diameters, respectively, in inches, and N is the number of active coils. For a shaft in torsion, initial shearing stress is given by Equation [4], which for steel becomes $\tau_0 = 4.80\ n_0 d$, where n_0 is striking velocity in revolutions per minute and d is shaft diameter in inches.

If the design problem is to determine bar, spring, or shaft dimensions, given the end bodies, striking velocity, and allowable maximum stress, then the solution may be made by fitting equations to the maximum stress curves. Within the $1/\alpha$ range of Fig. 7 each curve may be approximately represented by a linear equation

$$R = a + b/\alpha \quad \ldots\ldots\ldots\ldots\ldots [32]$$

where a and b are given by Table 1. Substitution may be made for α in terms of the dimensions of the elastic member, and in the cases of the bar or of the spring, the equation may be solved for one of the dimensions such as diameter. For the shaft a trial-and-error solution is necessary. Some judgment must be used in proportioning the member to give it a reasonable or economical size, and in the case of the bar and the shaft there is a lower limit to the allowable stress which may be used, hence a restriction in the choice of material. Some guides are given elsewhere (17).

TABLE 1 CONSTANTS FOR EQUATION [32]

λ	a	b
0.5	1.9	0.11
1	2.1	0.13
2	2.3	0.15
4	2.5	0.15
10	2.6	0.16
∞	3.0	0.14

An analysis indicates that an elastic solid steel disk of usual proportions, firmly attached to a shaft, will give results but little different from those for a rigid disk. The effect of a more flexible machinery member may be seen by supposing the member re-

[7] The notation is chosen to be consistent with that of reference (1).

[8] If one of the bodies is infinite, the maximum stress at the infinite-body end of the bar is larger than the maximum stress at the finite body end. Also, an infinite striking body gives higher stresses than an infinite attached body, i.e., a "fixed-end" condition (14).

[9] This equation may be derived by the method of Appendix 1, or may be derived from Donnell's statement regarding k, page 166 of reference (1), and its Equation [11], and definition of symbols.

placed by a rigid body and a massless spring between the body and shaft. A discontinuity in an incident stress wave is not reflected in full because the velocity of the end *can* suddenly change by deflection of the spring. The change in the reflected stress will be less than the value of the incident discontinuity,[10] and the total-stress peak will be smaller than with full reflection. Similarly, the several other peaks, including the maximum, will be smaller than with a rigid body, and use of the preceding maximum-stress charts will be "on the safe side." This is likewise true for conditions which create sloping wave fronts, such as local deformation at a rounded impacting end.[11] Full reflection will not occur because of the time for some change of velocity in the reflecting body before the top of the wave arrives.

Acknowledgment

The author is indebted to Profs. J. Ormondroyd, R. V. Churchill, and H. M. Hansen of the University of Michigan, for their advice and criticism in connection with the writing of the doctoral dissertation upon which this paper is based.

BIBLIOGRAPHY

1 "Longitudinal Wave Transmission and Impact," by L. H. Donnell, Trans. ASME, vol. 52, 1930, paper APM-52-14, pp. 153–167.
2 "Theory of Elasticity," by S. Timoshenko, McGraw-Hill Book Company, Inc., New York, N. Y., 1934, pp. 389–395.
3 "Choc longitudinal de deux barres élastiques, dont l'une est extrêmement courte ou extrêmement roide par rapport à l'autre," by B. de Saint Venant, Comptes Rendus de l'Académie des Sciences, Paris, France, vol. 66, 1868, pp. 650–653.
4 "Solution, en termes finis, du problème du choc longitudinal le deux barres élastiques en forme de tronc de cône ou de pyramide," by B. de Saint Venant, Comptes Rendus de l'Académie des Sciences, Paris, France, vol. 66, 1868, pp. 877–881.
5 Reference to this work of Boussineeq is given by B. de Saint Venant in Comptes Rendus de l'Académie des Sciences, Paris, France, vol. 97, 1883, p. 129; also in the Note to Section 60 of the translation by Saint Venant and A. A. Flamant of Clebsch' "L'Élasticité des Corps Solides," Paris, France, 1883, pp. 480a–480gg.
6 "Application des Potentiels à l'étude de l'équilibre et du mouvement des solides élastiques," by J. Boussinesq, Gauthier-Villars, Paris, France, 1885, pp. 505–546.
7 Reference (2), p. 382.
8 Reference (2), p. 384.
9 "Longitudinal and Torsional Impact of a Uniform Bar With a Rigid Body at Each End, by Striking With or Suddenly Applying Force to One of the Bodies. Application to the Design of Shafts, Bars, and Helical Springs," by A. H. Burr, Ph.D. Dissertation, Graduate School, University of Michigan, Ann Arbor, Mich., 1947, pp. 46–50.
10 Reference (9), pp. 60–66.
11 "Tables of the Exponential Function e^x," by Federal Works Agency, Work Projects Administration, 1939, available through National Bureau of Standards, Washington 25, D. C.
12 Reference (9), pp. 101–107.
13 Reference (9), pp. 107–111.
14 Reference (9), pp. 141–144, 147–150.
15 "Torsional Vibrations," by W. A. Tuplin, John Wiley & Sons, Inc., New York, N. Y., 1934, pp. 302–313.
16 Reference (9), pp. 111–117.
17 Reference (9), pp. 91–100.
18 "Measurement of Impact Strains by a Carbon-Strip Extensometer," by R. Fanning and W. V. Bassett, Trans. ASME, Journal of Applied Mechanics, vol. 62, 1940, pp. A-24–A-28.
19 "Measurement of Dynamic Strain," by C. O. Dohrenwend and W. R. Mehaffey, Trans. ASME, vol. 65, 1943, Journal of Applied Mechanics, pp. A-85–A-92.

[10] Indicated by Equation [2]; see also footnote 5.

[11] Fanning and Bassett (18), likewise Dohrenwend and Mehaffey (19), in experiments with two free bars, used rounded ends to obtain uniform application of load. The modification of theory to account for the rounded ends indicated a sloping wave front and a longer duration of impact, but no appreciable difference in the height of the initial wave front. The theory was well checked experimentally. No experimental work is known to be available on bars with attached bodies or fixed ends.

Appendix 1

Torsional Waves in Bars of Circular Section

For the element of the bar of length dx, Fig. 8(*a*), the equation of motion is written

$$JG\left[\frac{\partial\varphi}{\partial x}+\frac{\partial^2\varphi}{\partial x^2}dx\right]-JG\frac{\partial\varphi}{\partial x}=Jdx\,\rho\frac{\partial^2\varphi}{\partial t^2}$$

whence

$$\frac{\partial^2\varphi}{\partial t^2}=\frac{G}{\rho}\frac{\partial^2\varphi}{\partial x^2}=c_t^2\frac{\partial^2\varphi}{\partial x^2}\qquad[33]$$

where $c_t=\sqrt{G/\rho}$. The general solution of this equation is

$$\varphi=f(x-c_tt)+f'(x+c_tt)\qquad[34]$$

It is seen that c_t is the speed with which conditions of displacement f, of stress $(Gd/2)(\partial f/\partial x)$, and of particle angular velocity $\partial f/\partial t$ are propagated in a *positive* direction without change in value, i.e., in a wave.[12] Likewise, c_t is the speed with which conditions f', $(Gd/2)(\partial f'/\partial x)$, and $\partial f'/\partial t$ are propagated in a *negative* direction without change.

Assume a constant torsional stress τ suddenly applied to an end of the bar. After a time interval t, a portion of length $l=c_tt=t\sqrt{G/\rho}$ will be under stress τ, Fig. 8(*b*). Now torsional moment $M_t=2\tau J/d$, where d is the diameter of the bar. The rotation

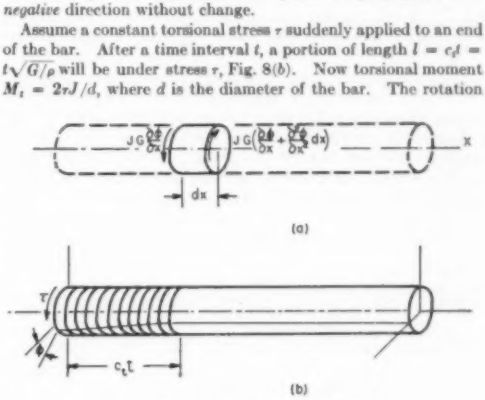

Fig. 8 Torsional Wave Propagation

of the end relative to the unstressed region is $\varphi=M_tl/JG=2\tau t/d\sqrt{G\rho}$. Since the stress wave is propagated at constant velocity, the angular velocity ω of the end is constant and equal to φ/t. Thus there is obtained the equation relating particle velocity to stress

$$\omega=\frac{2\tau}{d\sqrt{G\rho}}\qquad[35]$$

If a rigid body strikes the end of the bar with angular velocity ω_0, the end of the bar takes the velocity of the body, and from Equation [35], the initial stress is

$$\tau_0=\frac{\omega_0 d}{2}\sqrt{G\rho}\qquad[36]$$

Appendix 2

Tabulations of Equations

TABLE 2 A-OPERATION FORMULAS

(1) $A[e^{kx}]=e^{k'x+\alpha+\beta}\,(K')$

[12] A constant value of the argument $(x-c_tt)$ is maintained if, as t is increased by Δt, x increases by $\Delta x=c_t\Delta t$. Propagation velocity is $\Delta x/\Delta t=c_t$.

(2) $\Delta[2(K'z_m')e^{z_m'}] = e^{z'_{m+0.5}}(K')[(1 - K'^2) + (2K'z'_{m+0.5})]$

(3) $\Delta[2(K'z_m')^2e^{z_m'}] = e^{z'_{m+0.5}}(K')[-K'(1 + K')(1 - K'^2) + (1 - K'^2)2(K'z'_{m+0.5}) + 2(K'z'_{m+0.5})^2]$

(4) $\Delta[e^{z_m}] = e^{z_{m+0.5}}[1 + 2z_0]$

(5) $\Delta[(z_m)e^{z_m}] = e^{z_{m+0.5}}[z_{m+0.5} + z_0z_{2m+1}]$

(6)* $\Delta[z_m{}^k e^{z_m}] = e^{z_{m+0.5}} z^k{}_{m+0.5}\left[1 + \frac{2}{1+k} z_{m+0.5}\right]$

(7) $\Delta[\text{const}] = -[\text{const}]$

(1') $\Delta'[e^{z_m}] = e^{z_{m+0.5}}(K)$

(2') $\Delta'[2(Kz_m)e^{z_m}] = e^{z_{m+0.5}}(K)[(1 - K^2) + 2(Kz_{m+0.5})]$

(3') $\Delta'[2(Kz_m)^2e^{z_m}] = e^{z_{m+0.5}}(K)[-K(1 + K)(1 - K^2) + (1 - K^2)2(Kz_{m+0.5}) + 2(Kz_{m+0.5})^2]$

(4') $\Delta'[e^{z_m'}] = e^{z'_{m+0.5}}[1 + 2z_0']$

(5') $\Delta'[(z_m')e^{z_m'}] = e^{z'_{m+0.5}}[z'_{m+0.5} + z_0'z'_{2m+1}]$

(6')* $\Delta'[(z_m')^k e^{z_m'}] = e^{z'_{m+0.5}}(z'_{m+0.5})^k\left[1 + \frac{2}{1+k} z'_{m+0.5}\right]$

(7') $\Delta'[\text{const}] = -[\text{const}]$

* Formula 6 (or 6') will give a result differing from Formula 4 and 5 (or 4' and 5') by a constant which is accounted for in the evaluation of the constant of integration of the recurrence formulas.

TABLE 3 WAVE-STRESS EQUATIONS FOR STRIKING IMPACT

General:

End $x = l$

$S_1'(t) = e^{z_0'}$

$S_2'(t) = S_1'(t) + e^{z_1'}[(1 + K' - K'^2) + 2K'z_1'] + e^{z_1}(K)(1 + K)$

$S_3'(t) = S_2'(t) + e^{z_1'}[(1 + 2K' - 3K'^2 - 2K'^3 + 3K'^4) + 2(1 + K' - K'^2)2(K'z_2') + 2(K'z_2')^2] + e^{z_2}(K)(1 + K)[(2 + K - 3K^2) + 2(Kz_2)]$

End $x = 0$

$S_1(t) = e^{z_{0.5}}(1 + K) + e^{z'_{0.5}}(K')$

$S_2(t) = S_1(t) + e^{z_{1.5}}(1 + K)[(1 + K - 2K^2) + 2(Kz_{1.5})] + e^{z'_{1.5}}(K')[(2 + K' - 2K'^2) + 2(K'z'_{1.5})]$

$S_3(t) = S_2(t) + e^{z_{2.5}}(1 + K)[(1 + 2K - 5K^2 - 3K^3 + 6K^4) + (2 + 2K - 3K^2)2(Kz_{2.5}) + 2(Kz_{2.5})^2] + e^{z'_{2.5}}(K')[(3 + 3K' - 8K'^2 - 3K'^3 + 6K'^4) + (3 + 2K' - 3K'^2)2(K'z'_{2.5}) + 2(K'z'_{2.5})^2]$

Special Case $W' = W$:

End $x = l$

$S_1'(t) = e^{z_0}$

$S_2'(t) = S_1'(t) + e^{z_1}[1 + 4z_1 + 2z_1^2]$

$S_3'(t) = S_2'(t) + e^{z_1}\left[1 + 8z_1 + 12(z_1)^2 + \frac{16}{3}(z_1)^3 + \frac{2}{3}(z_1)^4\right]$

End $x = 0$

$S_1(t) = e^{z_{0.5}}[1 + 2z_{0.5}]$

$S_2(t) = S_1(t) + e^{z_{1.5}}\left[1 + 6z_{1.5} + 6(z_{1.5})^2 + \frac{4}{3}(z_{1.5})^3\right]$

$S_3(t) = S_2(t) + e^{z_{2.5}}\left[1 + 10z_{2.5} + 20(z_{2.5})^2 + \frac{40}{3}(z_{2.5})^3 + \frac{10}{3}(z_{2.5})^4 + \frac{4}{15}(z_{2.5})^5\right]$

TABLE 4 TOTAL-STRESS EQUATIONS FOR STRIKING IMPACT

General:

End $x = l$

$R_1' = e^{z_0'}$

$R_2' = R_1' + e^{z_1'}[(1 + 2K' - K'^2) + 2K'z_1'] + e^{z_1}(1 + K)^2$

$R_3' = R_2' + e^{z_2'}[(1 + 4K' - 2K'^2 - 4K'^3 + 3K'^4) + (2 + 3K' - 2K'^2)2K'z_2' + 2(K'z_2')^2] + e^{z_2}(1 + K)^2[(1 + 2K - 3K^2) + 2Kz_2]$

End $x = 0$

$R_1 = e^{z_{0.5}}(1 + K) + e^{z'_{0.5}}(1 + K')$

$R_2 = R_1 + e^{z_{1.5}}(1 + K)[(1 + 2K - 2K^2) + 2(Kz_{1.5})] + e^{z'_{1.5}}(1 + K')[(1 + 2K' - 2K'^2) + 2(K'z'_{1.5})]$

$R_3 = R_2 + e^{z_{2.5}}(1 + K)[(1 + 4K - 4K^2 - 6K^3 + 6K^4) + (2 + 3K - 3K^2)2Kz_{2.5} + 2(Kz_{2.5})^2] + e^{z'_{2.5}}(1 + K')[(1 + 4K' - 4K'^2 - 6K'^3 + 6K'^4) + (2 + 3K' - 3K'^2)2K'z'_{2.5} + 2(K'z'_{2.5})^2]$

Special Case $W' = W$:

End $x = l$

$R_1' = e^{z_0}$

$R_2' = R_1' + 2e^{z_1}[1 + 3z_1 + z_1^2]$

$R_3' = R_2' + 2e^{z_1}\left[1 + 7z_1 + 9(z_1)^2 + \frac{10}{3}(z_1)^3 + \frac{1}{3}(z_1)^4\right]$

End $x = 0$

$R_1 = 2e^{z_{0.5}}[1 + z_{0.5}]$

$R_2 = R_1 + 2e^{z_{1.5}}\left[1 + 5z_{1.5} + 4(z_{1.5})^2 + \frac{2}{3}(z_{1.5})^3\right]$

$R_3 = R_2 + 2e^{z_{2.5}}\left[1 + 9z_{2.5} + 16(z_{2.5})^2 + \frac{28}{3}(z_{2.5})^3 + 2(z_{2.5})^4 + \frac{2}{15}(z_{2.5})^5\right]$

TABLE 5 WAVE-STRESS EQUATIONS FOR CONSTANT-FORCE IMPACT

General:

End $x = l$

$S_1' = 1 - e^{-z_0'}$

$S_2' = S_1' + 1 + e^{z_1'}(-1 + K' + K'^2 - 2K'z_1') + e^{z_1}K(1 - K)$

End $x = 0$

$S_1 = -1 + e^{z_{0.5}}(1 - K) - e^{z'_{0.5}}K'$

$S_2 = S_1 - 1 + e^{z_{1.5}}(1 - K)(1 - K - 2K^2 + 2Kz_{1.5}) + e^{z'_{1.5}}K'(-2 + K' + 2K'^2 - 2K'z'_{1.5})$

Special Case $W' = W$:

End $x = l$

$S_1' = 1 - e^{z_0}$

$S_2' = S_1' + 1 - e^{z_1}(1 + 2z_1^2)$

End $x = 0$

$S_1 = -1 + e^{z_{0.5}}(1 - 2z_{0.5})$

TABLE 6 TOTAL-STRESS EQUATIONS FOR CONSTANT-FORCE IMPACT

General:

End $x = l$

$R_1' = 1 - e^{z_0'}$

$R_2' = R_1' + e^{z_1'}[-1 + K'^2 - 2(K'z_1')] + e^{z_1}(1 - K^2)$

End $x = 0$

$R_1 = e^{z_{0.5}}(1 - K) - e^{z'_{0.5}}(1 + K')$

$R_2 = R_1 + e^{z_{1.5}}(1 - K)(1 - 2K^2 + 2Kz_{1.5}) + e^{z'_{1.5}}(1 + K')(-1 + 2K'^2 - 2K'z'_{1.5})$

Special Case $W' = W$:

End $x = l$

$R_1' = 1 - e^{z_0}$

$R_2' = R_1' - e^{z_1}[2(z_1 + z_1^2)]$

End $x = 0$

$R_1 = e^{z_{0.5}}(-2z_{0.5})$

Appendix 3

Two Bars of the Same Material and Section With Rigid Bodies at Their Nonstriking Ends

Certain symbols are defined by Fig. 9 and Table 7. The time to travel twice the length of bar l' is $T' = 2l'/c$. Other symbols are defined in the Nomenclature.

TABLE 7 TIME INTERVALS

	End $x = 0$	End $x = l + l'$
n	t_n	t_n'
1	$0.5T \leqslant t < 0.5T + T'$	$0.5T' \leqslant t < 0.5T' + T$
2	$0.5T + T' \leqslant t < 1.5T + T'$	$0.5T' + T \leqslant t < 1.5T' + T$
3	$1.5T + T' \leqslant t < 1.5T + 2T'$	$1.5T' + T \leqslant t < 1.5T' + 2T$
.	. . . . .	. . . . .
.	. . . . .	. . . . .

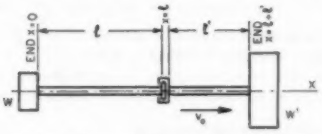

FIG. 9 STRIKING IMPACT OF TWO BARS CARRYING RIGID BODIES

The free end of the bar l' strikes the free end of the bar l with a positive velocity v_0. There ensue equal and opposite elastic forces in the two bars at their striking ends, and, because of equal sections and material, equal stresses and a common velocity of the two ends equal to the average of the two velocities before striking. The *change* of velocity of each bar end is one half the relative striking velocity, and the initial stress is one half that indicated by Equation [3] or [4]. Thus

$$\sigma_0 = \frac{1}{2} v_0 \sqrt{E\rho} \quad \ldots\ldots [37]$$

In both bars initial stress waves of constant value σ_0 are propagated away from the striking end. At time $0.5T$ the bar l is uniformly stressed, and the wave is incident at end $x = 0$. The reflected wave s_1 with front value σ_0 travels through the contacting surfaces at $x = l$ and is incident at end $x = l + l'$ at time $0.5T' + T$. Similarly, the initial wave in the bar l' is incident at $x = l + l'$ at time $0.5T'$, and the reflected wave s_1' is incident at end $x = 0$ at time $0.5T + T'$. Time intervals are defined in Table 7.

At each body there are two incident stress waves, the initial wave of constant value σ_0, and the wave with a value determined at the other body a time $0.5(T + T')$ earlier. These, added to the reflected wave, give the total stresses. At end $x = 0$

$$\sigma_n = s_n(t) + s'_{n-1}[t - 0.5(T + T')] + \sigma_0 \quad \ldots\ldots [38]$$

and at end $x = l + l'$

$$\sigma_n' = s_n'(t) + s_{n-1}[t - 0.5(T + T')] + \sigma_0 \quad \ldots\ldots [39]$$

From the equations of motion for each body, Equations [9] and [12] with $F(t) = F'(t) = 0$, there are obtained the recurrence formulas

$$s_n(t) = s'_{n-1}[t - 0.5(T + T')] - 2qe^{-qt} \int e^{qt} s'_{n-1}[t - 0.5(T + T')]dt - \sigma_0 + C_n e^{-qt} \quad \ldots\ldots [40]$$

and

$$s_n'(t) = s_{n-1}[t - 0.5(T + T')] - 2q'e^{-q't} \int e^{q't} s_{n-1}[t - 0.5(T + T')]dt - \sigma_0 + C_n' e^{-q't} \quad \ldots\ldots [41]$$

The formulas for determining the constants of integration are

$$s_n(t_n) = s_{n-1}(t_n) + \sigma_0 \quad \ldots\ldots [42]$$

and

$$s_n'(t_n') = s'_{n-1}(t_n') + \sigma_0 \quad \ldots\ldots [43]$$

where t_n and t_n' are defined by Table 7.

Equations for total stress at end $x = 0$ are listed in Table 8 in nondimensional form, where $R = \sigma/2\sigma_0$. Since σ_0 is one half that in the case of a single bar, for which $R = \sigma/\sigma_0$, a comparison for the two cases of the magnitudes of R is a comparison of the magnitudes of stress. It may be noticed that the equations written in pairs in the foregoing may be obtained one from the other by an interchange of primed and unprimed symbols. Hence stress equations for the end $x = l + l'$ may be obtained from Table 8 by substitution of primed for unprimed symbols R, K, q, and t_n and unprimed for primed.

TABLE 8 TOTAL-STRESS EQUATIONS FOR THE TWO-BAR SYSTEM

GENERAL CASE (W not equal to W') FOR END $x = 0$:

$R_1 = \sigma_1/2\sigma_0 = e^{-q(t-t_1)}$

$R_2 = \sigma_2/2\sigma_0 = R_1 + e^{-q(t-t_2)}(K) + e^{-q'(t-t_2)}(1 + K')$

$R_3 = \sigma_3/2\sigma_0 = R_2 + e^{-q(t-t_3)}[1 + K - K^2 - 2Kq(t - t_3)] + e^{-q'(t-t_3)}(K')(1 + K')$

Discussion

Analysis of a Single Stiffener on an Infinite Sheet[1]

R. E. Glover.[2] The integral equation developed by the author is based upon the assumption that the stiffener and plate maintain contact along a line. By integrating his Equation 4 with respect to y between the limits 0 and b, an influence function can be obtained which permits the loads transmitted to the plate of thickness t and modulus E by a stiffener of width b and length $2a$ to be uniformly distributed across the width b of the plate covered by the stiffener. The expression obtained in this way for the strain in the plate due to a load P_1 is

$$\epsilon_y(\bar{x}, 0) = -\frac{P_1}{2\pi btE}\left[\frac{(1+\mu)^2 w\bar{x}}{2(\bar{x}^2+w^2)} + (1-\mu^2)\tan^{-1}\frac{w}{\bar{x}}\right]$$

where $w = b/a$.

When this expression is used in the author's Equation [11], it expresses the requirement that the plate and stiffener maintain contact along both edges of the stiffener. When the stiffener has a width b, a section A, a length $2a$, and a modulus E_1, his Equation [11] becomes

$$\bar{p} = \frac{AE_1}{btE}\int_{-1}^{+1} K_1(\bar{x}, \bar{\xi})\,d\bar{p}$$

where

$$K_1(\bar{x}, \bar{\xi}) = -\frac{1}{2\pi}\left[\frac{(1+\mu)^2 w(\bar{x}-\bar{\xi})}{2((\bar{x}-\bar{\xi})^2+w^2)} + (1-\mu^2) + \tan^{-1}\frac{w}{(\bar{x}-\bar{\xi})}\right]$$

An interesting feature of the solution of this integral equation is the appearance of concentrated loads which are transmitted to the plate at the two ends of the stiffener. This occurs because the kernel $K_1(\bar{x}, \bar{\xi})$ has only a finite jump at $\bar{x} = \bar{\xi}$. The author's kernel jumps from $+\infty$ to $-\infty$ at this point and no concentrated loads are required. The physical reason for the concentrated loads, in the present case, when the stiffener is subjected to equal pulls at the two ends, is that the forces, transmitted to the plate by the stiffener between the ends, produce a compressive strain in the plate at the ends. The strain in the stiffener is, however, tensile at this point and therefore continuity can only be maintained if a part of the pull is transmitted immediately to the plate. Similar considerations will apply in the antisymmetrical case. An approximate solution can be obtained for the symmetrical case by assuming an expression of the form

$$p = \alpha + \beta\bar{x}^2 + \gamma\bar{x}^4$$

This expression may be substituted into the integral equation, the integrals evaluated, and the constants α, β, and γ determined to satisfy the integral, equation at the points $\bar{x} = 0$, $\bar{x} = 0.5$, and $\bar{x} = 1$. In so doing, allowance must be made for the concentrated loads $(1-\alpha-\beta-\gamma)$ at the two ends. For the case illustrated in the author's Fig. 2, using the data of his numerical example, applying to a 1-in-square stiffener 20 in. long attached to a $^1/_{10}$-in-thick sheet, the conditions at the three points are, respectively

$$\alpha = 0.996\beta + 0.758\gamma + 0.556(1-\alpha-\beta-\gamma)$$
$$\alpha + 0.250\beta + 0.0625\gamma = 0.695\beta + 0.963\gamma + 0.730(1-\alpha-\beta-\gamma)$$
$$\alpha + \beta + \gamma = -0.913\beta - 1.253\gamma + 2.420(1-\alpha-\beta-\gamma)$$

A solution to these equations gives

$$\alpha = 0.408 \qquad \beta = 0.139 \qquad \gamma = 0.090$$

Table 1 of this discussion gives values by which this solution can be compared to that given by the author. The concentrated loads at the ends are $0.363P$.

TABLE 1

$\bar{x}$	$\bar{p}$
0.0	0.408
0.2	0.424
0.4	0.432
0.6	0.470
0.8	0.534
1.0	0.637

These solutions are of interest in connection with the design of the welds which attach the stiffener to the sheet. If the stiffener is to be cut off square, then heavy shear-stress concentrations can be expected in the welds near the ends. Such concentrations may be mitigated by tapering the ends of the stiffener. In one case,[3] where square bars were to be welded to a scroll case to strengthen it, it was found that nearly all the pull would be transmitted to the bars in the tapered portion. An equitable distribution of shear stresses along the taper permitted the design of welds which would develop the full strength of the bar.

[1] By S. U. Benscoter, published in the Journal of Applied Mechanics, September, 1949, Trans. ASME, vol. 71, pp. 242–246.

[2] Bureau of Reclamation, Denver Federal Center, Denver, Colo.

[3] Computed by Messrs. W. T. Moody and F. W. Taylor, Engineers, Office of Design and Construction, Bureau of Reclamation.

Fatigue Under Combined Pulsating Stresses[1]

T. J. Dolan.[2] The authors are to be commended for having developed a machine suitable for combined-stress fatigue testing in which the relative magnitudes of the two principal stresses can be controlled and synchronized accurately. However, they have undertaken a rather difficult task in attempting to correlate and co-ordinate fatigue data from two entirely different types of testing machine. The writer's remarks are not to be construed as a criticism of the authors, but rather are intended to emphasize the complexity of fatigue phenomena and the lack of adequate, fundamental information from which to formulate a "theory of failure" under various states of combined alternating stresses.

For example, in addition to the initial mechanical properties of the metal (as controlled by composition, processing treatments, presence of inherent stresses, etc.,) the fatigue behavior of a member has been shown by various investigators to be influenced

[1] By H. Majors, Jr., B. D. Mills, Jr., and C. W. MacGregor, published in the September, 1949, issue of the Journal of Applied Mechanics, Trans. ASME, vol. 71, pp. 269–276.

[2] Research Professor of Theoretical and Applied Mechanics, University of Illinois, Urbana, Ill. Mem. ASME.

by (*a*) the state of stress; (*b*) the range of stress and type of stress cycle; (*c*) the frequency of stressing and the presence of rest periods; (*d*) the over-all size of member; (*e*) surface finish; (*f*) geometrical shape; (*g*) previous strain history; (*h*) the stability (of mechanical properties, residual stresses, and anisotropy) during the process of repeated stressing. Undoubtedly, several of these variables influenced the fatigue properties reported in the paper, and it becomes difficult to obtain a significant interpretation of the test data.

The rather ingenious mechanism and fixtures devised for producing pulses of loading in thin-walled tubes developed a strain history quite different from that in the rotating-beam test. The pulses were of short duration with very high (and fairly constant) strain rate, whereas in the rotating beam the strains were applied in a sinusoidally varying cycle with a strain rate decreasing to zero at peak stress. Most of the popular concepts of "a mechanical equation of state" for the structural behavior of materials indicate that the strain rate is an important consideration. These differences in strain rate and strain history make it difficult to visualize any simple or direct quantitative correlation of the two types of test. One would suspect that the differences in surface finish (honing versus polishing with fine abrasives) and differences in size of test specimen between the rotating beam and the tubular fatigue specimens would also affect the relative fatigue strengths observed.

It should be pointed out that if the distortion-energy theory is a good criterion for yielding in the tubular specimens, then all the tests under pulsating loads developed peak stresses above the yield point of the material. Any general plastic yielding accompanied by strain-hardening and redistribution of residual stresses would have acted to alter and to control the strength of the cylinders in a manner somewhat different from what is usually conceived to be the "fatigue" behavior. That is, after the first few cycles in the pulsating fatigue tests the subsequent stressing would not be governed by the same fatigue phenomena as those in the rotating-beam tests (for which the endurance limits were at stress levels below the yield point).

The wire strain gages in the circuits employed by the authors are capable of detecting "increments" of strain during each pulse of load application, but they do not integrate or summarize the total strain developed during a test. Hence plastic yielding in the tangential direction during the first few load applications would not be detectable by subsequent dynamic-strain observations. Any inelastic actions occurring during the pulsating fatigue tests would invalidate corrections of stress for different wall ratios or calculation of fiber stresses on the inside surface by the Lamé solution, since the Lamé formula assumes only elastic action.

The empirical Equations [5], [6], and [7] of the paper represent very rough approximations to some of the widely varied fatigue behavior observed for metals under different ranges of stress (i.e., for other than completely reversed cycles). In view of the numerous differences in influencing factors involved in the two types of test, it seems likely that it is only by chance that the computed values of pulsating fatigue strength from Equations [6] and [7], based on the rotating-beam tests, gave values closely approximating that obtained from the tube samples.

The writer would like to suggest that some of the foregoing difficulties might be minimized by repeating a similar series of tests on tubes of high yield strength (a heat-treated alloy steel) free from marked anisotropy and for which the fatigue strength is appreciably below the yield point. If the pulsator could be arranged to apply a sinusoidally varying stress cycle, and specimens of the same size and surface finish could be tested in rotating-beam machines, the data would yield information of a more comparable nature.

The marked anisotropy of the material tested violates the fundamental assumption on which theories of failure of elastic action are based; hence one would not expect close correlation with any of the popular theories (such as the distortion-energy theory). However, when dealing with fatigue-test data, it should be recognized that the phenomena associated with fatigue failure do not involve "general yielding" of a large portion of the member; therefore there is reason to suspect that the conditions leading to fatigue failure under states of combined stress might not be expressed adequately by any of the relationships which have been proposed as criteria for initiation of *general yielding*. A complete correlation may be possible only with the aid of new concepts that explain the process leading to (and the criteria for) "fracture" of a member subjected to repeated stressing.

S. J. Fraenkel.[2] A study of the paper reveals that the authors plotted their results in the manner made familiar in static multiaxial stress experiments. In doing this, dimensionless ratios of the two significant principal stresses to the corresponding uniaxial fatigue limit were employed. This latter quantity was taken from a biaxial fatigue test in which the longitudinal stress was only 2.5 per cent of the tangential component, so that the stress was essentially uniaxial in the tangential direction. This quantity, having a numerical value of 36,800 psi, was used in the authors' treatment as the uniaxial fatigue limit at 10,000,000 cycles for both directions, as can be seen by calculting the co-ordinates of the experimental points on the combined stress diagram in Fig. 16 of the paper. Reference to Table 1 of the paper shows, however, that the material was decidedly anisotropic. The endurance limit in the longitudinal direction exceeded that in the transverse direction by 15 per cent, an amount which agrees well with earlier findings on steel of nearly identical composition and heat-treatment. Unfortunately, no uniaxial pulsation tests were performed with the significant stress in the longitudinal direction, so that a measure of anisotropy in terms of uniaxial longitudinal fatigue strength at 10,000,000 cycles is not available. In the absence of such a figure, it appears reasonable to assume that the effect of anisotropy on fatigue limits at a large, though finite, number of cycles is the same as on the endurance limits. It is suggested, therefore, that a value of 1.15 times the tangential fatigue limit, or 42,300 psi, be used for the longitudinal fatigue limit at 10,000,000 cycles. If this is done and the co-ordinates of the experimental points are recalculated on this basis, better agreement with the shear-energy theory is obtained than is shown in the authors' Fig. 16.

It was further noted in the study of the paper that the strain-time curve of the specimens had a triangular shape. This raises the question of the significance of the wave shape in fatigue testing. If we compare, for example, a triangular and a rectangular wave, it is seen that in the former the peak stress exists for only a small part of the cycle, whereas, in the latter case, the peak stress exists very nearly during the complete cycle. In the authors' treatment the two cases would be considered the same; in the absence of proof to that effect, however, the thought cannot be dismissed that the fatigue limit, both uniaxial and multiaxial, may be affected by the percentage of the cycle during which the peak stress is present. As a parameter describing this condition, the ratio of the area under the strain-time curve to the duration of a complete cycle may be suggested.

This question, far from being academic, has considerable practical significance in the fatigue testing of entire assemblies. Whereas, the test arrangement usually permits the exercise of some control over the strain-time relation in the testing of small

[2] Supervisor, Structural Research Section, Armour Research Foundation, Chicago, Ill. Jun. ASME.

laboratory specimens, the fatigue testing of built-up units, such as of frames of vehicles, results in fatigue cycles of varying and nearly uncontrollable wave shape, which differ moreover from each other at various points in the structure. Therefore, doubts may be expressed as to whether results obtained with one type of wave form are applicable to other wave forms. It would be extremely desirable to extend studies of this type to include a variety of wave forms, varying from the triangular, sinusoidal, trapezoidal, to the rectangular shape, while holding the maximum stress constant. If these influences could be determined, the setting of fatigue and endurance limits on the basis of a variety of wave forms would be greatly facilitated.

Authors' Closure

The comments made by Professor Dolan and Mr. Fraenkel are well taken and appreciated. Answering comments are necessary for the paper may be misinterpreted.

The principal purpose of including the rotating-beam results was, as pointed out in the paper, to determine the degree of anisotropy originally present. Having these results, however, it was deemed of interest to determine, in spite of the difference in types of stress cycles, if the well-known empirical relations connecting endurance limit, yield point (or ultimate strength), and the fatigue limit (where the mean stress of the cycle was not zero) gave reasonable results here. As mentioned in the paper, it was not the purpose to make a detailed study of this since sufficient tests were not made for this purpose. As stated: "It was possible, however, at least to indicate the probable relationship involved for this material." Thus, contrary to expectations, test results indicated good agreement with either the modified Goodman or the Gerber-type relations as discussed. It is too early to generalize on this result, and while it is to be expected that the variable stress, the mean stress, the phase relationships, stress ratios, etc., are probably of greater significance than the shape of the stress cycle, the latter effect is unknown at present and can only be determined by further experimentation. The present results are only "indicative" of this effect.

However, since the value of σ_f, the fatigue limit under uniaxial stress for the same ratio of mean stress to maximum stress for the cycle, was determined likewise in the tube-pulsation tests, as well as by the uniaxial reversed bending and the empirical relations, regardless of the future proof or disproof of the effect of type of stress cycle, the latter concern does not affect the main results of the paper, namely, to show the influence of combined stresses on fatigue failure.

Some concern has been manifested that the results of the paper check so consistently in various instances with other well-established relations. Professor Dolan has listed various "factors" purportedly affecting the fatigue properties of the paper. It is to be noted that these either were held constant, were the variables under study, or can be shown to be of small effect, in the various cases. As an example, "the initial mechanical properties of the metal as controlled by composition, processing treatments, presence of inherent stresses etc.," is of no importance here as a variable for it is a constant. The "state of stress" was the main variable under study and this affected the results as presented. Because this investigation was under pulsating stresses, the ratio of mean stress to the maximum stress was established for the cycle for all stress ratios of principal stresses. Therefore this was not a variable. All tubular specimens experienced the same frequency of stressing (880 cycles per min), and shape of stress cycle, and the same rest period. These are not variables here. All of the tubular specimens were of the same size with significant dimensions varying only a few thousandths and had the same surface finishing. Surface finish was not a variable here.

The "previous strain history" effect for specimens at the fatigue limit for all pulsating-tube tests was basically no different from that present in all combined-stress tests conducted statically. All specimens were subjected to the same type of pressure wave and, due to the different but constant ratios of principal stresses during any one test, the strain existing to fracture is naturally different. The strain history of each tube is irrevocably tied up with the stress ratio employed—but this is the variable under study!

Professor Dolan has made a good point when comparing the tube tests with the uniaxial rotating-beam tests. It is of interest to consider some variables if one were to compare the tube tests with the uniaxial rotating beam. Mr. Dolan commented on the "over-all size of the member." It is to be noted that great care was taken to machine the small rotating-beam specimens (Krouse and R. R. Moore fatigue specimens) at the same radial distance from the center of the bar as the average tube radius for the combined stress specimens. The ratio of the R. R. Moore to the Krouse fatigue-specimen diameter is 2.50 and yet the endurance limits in the axial direction as shown in Table 1 of the paper are almost identical. Indeed, the larger specimen had a slightly larger endurance limit than the smaller specimen, which is in exactly the opposite direction to that expected if a "size effect" were present for the material used (SAE 1020 annealed). The ratio of the bore radius of the tube specimens to the R. R. Moore specimen is 3.33, hence, from the foregoing observations, "the over-all size of the member" is not an important variable here.

Similarly, due to the precaution used in producing polishing scratches in both tube and beam specimens in directions which do not precipitate cracks, the "surface finishes" (both very fine) are not variables here.

"Geometrical shape" as a factor affecting the test results is not a variable, since the strain measurements determined the stress ratios reported, no notches were present, and both specimens (uniaxial and biaxial) had large, curve tapers as is conventional practice.

It is not correct to base conclusions upon the static yield stress (stress for low rate of loading), because the magnitude of stress for first yielding is a function of rate of loading.[4] It is well known that yielding occurs as a progression of microscopic regions of plastic flow, due to unfavorable orientation or minute imperfections causing stress concentrations. Thus the strain magnitude depends upon the duration of stress, how many areas are yielding and rate of local yielding. Also, the rate of flow is a function, of applied stress.[5] It should be noted that owing to the type of stress cycle, the test is closely allied to a repeated impact-fatigue test. Even though the peak of the sharp triangular pulse were higher than the dynamic yield stress (stress for high loading rate), the magnitude of yielding per cycle will be small, and the areas suffering plastic flow distributed randomly through the metal so that measurement with ordinary strain gages would be difficult.

It should be observed that the nominal stresses were used throughout which is the usual procedure. Because a common structural material possesses a yield stress close to the endurance limit, it is not excluded from an experimental program of study. Since nominal stresses were used, the corrections as reported in the paper are valid by using the Lamé formula for different wall ratios than those used with the calibration tubes which were never stressed to yielding.

The criticism that it is "only by chance that the computed

[4] "The Effect of the Speed of Stretching and the Rate of Loading on the Yielding of Mild Steel," by E. A. Davis, Journal of Applied Mechanics, Trans. ASME, vol. 60, 1938, p. A-137.

[5] "High-Speed Tension Tests at Elevated Temperatures, Parts II and III," by A. Nadai and M. J. Manjoine, Journal of Applied Mechanics, Trans. ASME, vol. 63, 1941, p. A-91.

values of pulsating fatigue strength from Equations [6] and [7] of the paper, based upon the rotating-beam tests, gave values closely approximating that obtained from the tube samples" should be supported by experimental evidence. In the light of the previous remarks the results reported stand until test data refute them.

There is complete agreement with Mr. Dolan that it would have been interesting to repeat the tests using sinusoidal stress cycles and to perform another series of tests on a high yield strength.

Another comment that must be reiterated lest there be misinterpretation. Fig. 16 of the paper shows a comparison of the various strength theories. Under *static conditions* one would use the *yield stress for a uniaxial tension test*. Fig. 16 uses the same mathematical formulations, but a "dynamic quantity" (the endurance limit under uniaxial conditions but same ratio of maximum to mean stress as for the various stress ratios) in the place of a static quantity!

Recognizing Mr. Fraenkel's kind discussion, the authors were aware that the endurance limit in pulsation probably would be different in the tangential direction from that in the longitudinal direction, but felt that in the absence of the result, no assumption should be made.

One of the results of the experimental program has been to bring to light that very little work has been reported about the effect of the shape of the stress cycle, as Mr. Fraenkel clearly indicates, upon the endurance limit and fracture line.

Relation of Experiments to Mathematical Theories of Plasticity[1]

B. G. Johnston.[2] Just prior to his remarks on "The Case Against Isotropic Work-Hardening-Bauschinger Effect," the author states: "It is possible that in a limited region, e.g., the tension-tension region for two-dimensional states of stress, isotropic work-hardening will be a reasonable first approximation."

Results of extensive tests[3] on plate steels used in pressure vessels indicate that the foregoing may not be true, at least at the boundaries of this limited region. Fig. 1 of this discussion is typical of these test results. Similar stress-strain curves were obtained in the as-received condition both parallel with and transverse to the rolling direction. However, after tensile overstrain of 5 per cent, as shown in Fig. 1, a much greater strain-hardening has taken place parallel to the direction of overstrain than transverse to it. Hence an appreciable degree of anisotropic work-hardening has developed between the bounding limits of the tension-tension region.

Similar results were obtained for 10 per cent and for 1 per cent overstrain; in the latter case a lowering of the transverse yield-stress level occurred as in the Bauschinger effect for complete reversal of strain direction. Tests made transverse to the direction of overstrain may be thought of as a 90-deg rotation of strain direction whereas complete reversal is a 180-deg rotation. Correspondingly, a partial "Bauschinger effect" is obtained with a 90-deg rotation, intermediate between no change and a complete reversal of strain direction. If a material behaves as shown in Fig. 1 herewith, it is obvious that if a tensile strain of 5 per cent in a given direction is followed by a rotation of 90 deg in the direction of the principal stress, a considerable additional strain will be produced in the new direction if the stress magnitude is maintained constant. This will be due to anisotropic work-hardening and will not prove or disprove any particular theory.

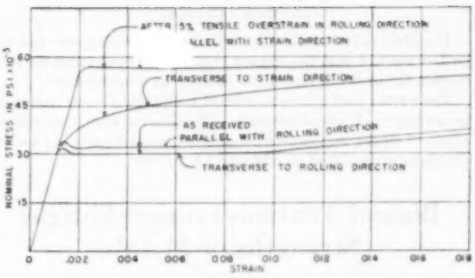

Fig. 1 Tensile Test Stress-Strain Curves for Sample of ASTM A-201 Steel

As the author points out, additional tests are needed to establish in what range isotropic work-hardening may be assumed as a reasonable first approximation for the incremental theory. On the other hand "isotropic behavior," when the directions of principal stress at a point do not change during flow, has more supporting evidence, is more limited in application, but is, nevertheless, useful information regarding a material.

Author's Closure

The data and analysis presented by Dr. Johnston show clearly that, as should be expected, work-hardening is not isotropic. However, an isotropic theory may still give fairly reasonable results for a meandering loading path in the tension-tension quadrant such as drawn in Fig. 9 of the paper. If there is an abrupt 90-deg change in the direction of the stress, as Dr. Johnston points out, a theory often will be required which takes into account anisotropy produced by plastic deformation. An introductory discussion of such theories is contained in another paper.[4]

Impact of a Mass on a Column[1]

R. Plunkett.[2] The writer has recently been working on the closely related problem of the vibration of nonuniform columns subjected to axial loads. Equation [5] of the paper shows that the relation between the axial load and the natural frequency squared is linear for the simply supported case, the frequency being zero when the axial load reaches the Euler load. It may be shown that the relation is almost linear for the fixed-end case. Thus it should be possible to extrapolate accurately to the actual elastic buckling load from a small number of experimental natural frequency determinations at different axial loads, regardless of the end fixity of the column. It has recently come to the writer's attention that this same procedure has been advocated in a Belgian volume.[3]

[1] By D. C. Drucker, published in the December, 1949, issue of the Journal of Applied Mechanics, Trans. ASME, vol. 71, pp. 349–357.

[2] Director, Frits Engineering Laboratory and Professor of Civil Engineering, Lehigh University, Bethlehem, Pa.

[3] "Effect of Plastic Strain and Heat Treatment on the Tensile and Notch Properties of a Rimmed and a Killed Steel," by C. J. Osborn, A. F. Scotchbrook, R. D. Stout, and B. G. Johnston, *The Welding Journal*, vol. 28, 1949, Research Supplement, pp. 337-s–353-s.

[4] "The Significance of the Criterion for Additional Plastic Deformation of Metals," by D. C. Drucker, Rheology Issue, *Journal of Colloid Science*, vol. 4, June, 1949.

[1] By W. H. Hoppmann, 2nd, published in the December, 1949, issue of the Journal of Applied Mechanics, Trans. ASME, vol. 71, pp. 370–374.

[2] The Rice Institute, Houston, Texas. Jun. ASME.

[3] "Les Relations Entre les Modes Normaux de Vibration," by G. Massonnet, Goemaere, Brussels, Belgium, 1940.

Author's Closure

The observation of Dr. Plunkett is an interesting one and the author concurs with his opinion that it may have value for estimating the buckling load in the manner that he describes.

The author also wishes to correct a numerical value occurring in the paper. Under Discussion of Results the stated increase of strain of 49 per cent caused by an axial load which is one half of the Euler critical load should read 17 per cent.

Biaxial Tension-Tension Fatigue Strengths of Metals[1]

F. B. Schneider.[2] The author refers to the accumulator A, Fig. 3, to maintain pressure, and to the gages H and L to measure the maximum and minimum pressures. While this will work at static conditions and up to a certain minimum number of fluctuations, it is not pointed out that the accumulator and the gages tend to respond to the average pressure at 300 fluctuations per min instead of to the maximum or minimum pressure. From the description given it would seem possible that the pressures could exceed the static test limits without noticeable indication on the gages, and the amount of liquid could decrease without corrective action from the accumulator as long as the average pressure remained within these limits. Perhaps the remark of the author that it was necessary to apply the low rate of 300 fluctuations per min to eliminate possible errors also refers to these conditions.

From Fig. 2 it appears that the connection to the pressure gages is in the piping leading to the test specimen. This assumes that the remainder of the piping to the test specimen must be in perfect order, since any leaks or air bubbles in this part of the piping would not register. Was there no possibility of air being trapped at the inlet connection to the test specimen even though the vent at the top of the specimen indicated no air? Why were the gages not connected to the specimen directly?

Between the gage connection and the gages is a tee with a pipe leading upward to the valve M. The vent on top of the test specimen cannot show whether the pipe to valve M contains trapped air. While this condition will not prevent the operation of the valve M, it will impair the maximum and minimum pressure readings of the gages at higher fluctuations. In other words, the test specimen will not be subjected to the extreme pressures as adjusted at static conditions, but will be exposed to pressures closer to the average pressure.

Considering Fig. 5 of the paper, with its peculiar crossing of curves, it could be that at the test of $R = 2.0$, air bubbles were present. Has the author an explanation for the crossing of these curves? Is it possible that at $R = 1.0$, a resonance condition shortens the life of the test specimen? The axial load is measured at a point far removed from the test specimen. While this is correct at static conditions, it is certain that the elastic system of the lever K will cause a time delay in the application of the load at the test specimen.

Since calculations have been made to ascertain the influence upon the value of the applied load of the error introduced by neglecting the inertia forces of the lever K, it would be interesting to know if similar calculations were made to check the influence of the elastic system of the lever K upon synchronism of the two principal loads. Synchronism has been adjusted statically only.

Since the presence of air bubbles together with the elasticity of the piping in the hydraulic system and the elasticity of the lever K in the mechanical system tend to destroy the desired synchronism in the test specimen, it would be interesting to learn whether it has been checked at the test specimen by electric gages. As a matter of record, Equation [1] of the paper should read

$$\sigma_1' = \frac{P'}{\pi dt} + \frac{p'd}{4t}$$

In the next paragraph of the paper, the ratios of the minimum to the maximum stresses, σ_1'''/σ_1' and σ_2'''/σ_2', were kept at about 0.10 to 0.30. The letters G_2, G_1, E_2, and C are not shown in Figs. 2 and 3. The eccentric E_1 is not shown in Fig. 3, but in Fig. 2.

The results of such tests are valuable to the designing engineer. They furnish him with the required data properly to design hydraulic apparatus with simultaneous fluctuating axial loads and hydraulic pressures. They caution him especially to strengthen the designs of apparatus where the maximum longitudinal stress is equal or one half the maximum circumferential stress.

Author's Closure

The author appreciates the comments made by Mr. Schneider. There are possible errors in the value of stresses calculated and in the synchronism of the stresses as indicated by Mr. Schneider. It has been assumed that with the rates of fluctuation used these errors are small. However, in a current project using the same testing machine, the biaxial dynamic strains will be measured on the specimen. In this way, the actual values of the stresses and the synchronism of these stresses will be determined.

Determination of the Buckling Load for Columns of Variable Stiffness[1]

G. Sonnemann.[2] The author points out a very good method by which problems of columns with variable stiffness can be solved. It is rather unfortunate that he did not go into greater detail to point out some very enlightening facts.

If one rewrites Equation [7a] of the paper in the manner suggested by the author, one would obtain

$$\mu_1 = \frac{\int_0^L (F_1'')^2 EI\,dx}{\int_0^L (F_1')^2 dx} \qquad [1]$$

This is the standard form of the Rayleigh quotient to give the critical buckling load for any column, as long as the shear deformation is negligible.

Similarly, if one rewrites Equation [7b] as suggested by the author, one obtains

$$\mu_2 = \frac{\int_0^L (F_1')^2 dx}{\int_0^L [(F_1)^2/EI]\,dx} \qquad [2]$$

This is the standard form suggested by Timoshenko to give a closer approximation of the critical load for any column with negligible shear deformation.

[1] By Joseph Marin, published in the December, 1949, issue of the Journal of Applied Mechanics, Trans. ASME, vol. 71, pp. 383–388.

[2] Locomotive Engineering Division, General Electric Company, Erie, Pa. Mem. ASME.

[1] By C. C. Miesse, published in the December, 1949, issue of the Journal of Applied Mechanics, Trans. ASME, vol. 71, pp. 406–410.

[2] Assistant Professor, Department of Mechanical Engineering, Drexel Institute of Technology, Philadelphia, Pa. Jun. ASME.

Thus one can think of the μ_1, μ_2, μ_3, etc., as the Rayleigh and Timoshenko quotients for the critical loads.

The author also derives the inequality to establish the lower bound. Unfortunately, he did not make use of the vibrating-string or sound-wave analog; that is, for the hinged column, for example, one can consider a wave as shown in Fig. 1 herewith.

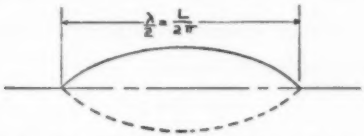

FIG. 1 FIRST HARMONIC, FUNDAMENTAL MODE OF VIBRATION

Notice then that the critical frequency of vibration will be inversely proportional to the wave length required or

$$\mu_{CR} = \frac{k}{\lambda^2} = k\,\frac{\pi^2}{L^2}$$

or using the present notation

$$P_{CR} = \frac{EI\,\pi^2}{L^2}$$

Hence

$$k = EI$$

and

$$\mu_{CR} = \frac{\pi^2}{L^2}\,EI$$

The second harmonic and third would look as shown in Figs. 2(*a*) and 2(*b*).

With these illustrations it is possible to determine the buckling load to be inserted in the inequality [16], or for this specific case into the inequality [5*a*] shown herewith, namely

$$\mu_2 - \frac{\mu_1 - \mu_2}{\dfrac{b}{\mu_2} - 1} \leqslant P_{CR} \leqslant \mu_2$$

It is pointed out that b is the lower bound on the "second buckling load." This, according to the author, is the second harmonic, which by inspection gives

$$b = \frac{k}{\lambda^2} = EI\,\frac{4\pi^2}{L^2}$$

However, the following fact has to be remembered: If the first assumed function F_1, called the generating function, F_0, F_2, F_3, and so on, also must, perforce, be symmetrical about the center. The second harmonic does not meet this specification, so that the third harmonic must be the lower bound on the "second buckling load" for the symmetrical case. Temple and Brickley[1] point out that this is true by means of an example. Also, the second harmonic cannot satisfy the boundary condition of zero slope of center of column.

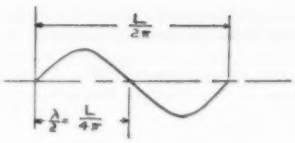

FIG. 2(*a*) SECOND HARMONIC

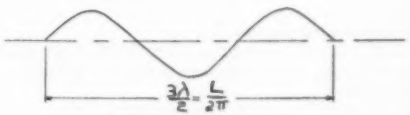

FIG. 2(*b*) THIRD HARMONIC

In general then, one could say that from the Euler critical-load formulas, for the hinged column, say

$$P_{CR} = (n+1)^2\,\frac{EI}{L^2}\,\pi^2$$

n must either be chosen as 0, 2, 4, - - - - or 1, 3, 5, depending on the choice of the generating function F. If example 1 of the paper is reworked, namely, assuming the 3rd harmonic as the lower bound of the second buckling load, then

$$b = \frac{9EI_0\,\pi^2}{4\,L^2}$$

and the lower bound would then be

$$1.821\,\frac{\pi^2 EI_0}{L^2} \leqslant P_{CR} \leqslant 1.830\,\frac{\pi^2 EI_0}{L^2}$$

This is a marked improvement of the author's result of

$$1.814\,\frac{\pi^2 EI_0}{L^2}$$

The same argument applies to the column built in at one end, free at the other. Then the wave shapes are shown in Fig. 3 (*a*, *b*, *c*), herewith.

Here again, the first harmonic is the same as the generating function, hence, b must be set equal to the third harmonic, or in other words

$$b = \frac{25}{4}\,\frac{EI\,\pi^2}{L^2}$$

[1] "Rayleigh's Principle and Its Applications," by G. Temple and W. Brickley, Oxford University Press, London, England, 1933, p. 98.

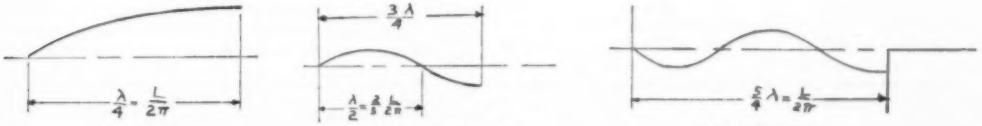

(*a*) Fundamental First harmonic (*b*) Second harmonic (*c*) Third harmonic

FIG. 3 WAVE SHAPES

For example 2 of the paper, the same thing applies, namely, b should be for the third harmonic which in that case is

$$b = 115.92 \frac{\overline{EI}\, x^2}{L^2}$$

Then the lower limit would be

$$17.85 \frac{EI_0}{L^2} \leqslant P_{CR} \leqslant 17.88 \frac{EI_0}{L^2}$$

Again a definite improvement.

All in all it should be noted that the method does give excellent results within very close tolerances which are acceptable for engineering purposes.

It may further be noted that this method is also applicable to the calculation of critical frequencies of rotating shafts.

Author's Closure

It is recognized that the method, presented in the subject paper, is a general method which is equally applicable to all eigenvalue problems whose equations meet certain requirements, and the author wishes to thank Professor Sonnemann for bringing this to the reader's attention. However, in the interest of brevity and simplicity, the broad implications and further applications of this method were omitted.

The functions, H_i, which were used to derive Inequality [16] in the Appendix of the subject paper, were required only to satisfy the boundary conditions of Equation [2]. It is noted that the second harmonic does satisfy these boundary conditions, as does any higher harmonic.

It is quite true, as Professor Sonnemann has pointed out, that any harmonic of higher order than the second will provide a lower bound on the second buckling load. Hence the third harmonic is a perfectly legitimate value for b, provided that it is greater than the last computed Rayleigh quotient, μ_{2i}, as pointed out in the line of text below Equation [32] of the subject paper.

Bending Vibration of a Rotating Blade Vibrating in the Plane of Rotation[1]

R. Plunkett.[2] The natural frequencies of a rotating propeller, in practice, are often estimated from the formula

$$\omega^2 = \omega_0^2 + k\Omega^2 \quad \ldots\ldots\ldots\ldots\ldots\ldots [1]$$

where ω_0 is the nonrotating natural frequency. This is a modification of a formula originally suggested by Southwell.[3] However, it should be realized that k depends not only upon the shape and physical characteristics of the blade, as it is often assumed, but also upon Ω^2 as is shown by this paper. The author in oral discussion pointed out that numerical values of k in the plane seem to be one less than k out of the plane. This may easily be seen from Equation [1] of the original paper, which may be rearranged to read

$$S_{n(in)} = \sum_{i=1}^{n} m_i y_i(\omega^2 + \Omega^2) - \sum_{i=1}^{n} m_i x_i \alpha_n \Omega^2$$

For vibration out of the plane

$$S_{n(out)} = \sum_{i=1}^{n} m_i y_i \omega^2 - \sum_{i=1}^{n} m_i x_i \alpha_n \Omega^2$$

Since all the other equations are identical and do not involve ω^2 or Ω^2

$$\omega^2_{(out)} = (\omega^2 + \Omega^2)_{in}$$

or from Equation [1] of this discussion

$$k_{out} = 1 + k_{in}$$

In step-by-step calculations of this type, a great deal of investigation is needed of the optimum number of steps for good accuracy and of the proper allocation of mass and rigidity to the different stations along the beam. Houbolt and Anderson[4] show a method of using parabolic integration instead of linear for increased accuracy, and Duncan[5] gives a method for extrapolating to an infinite number of steps. Many investigations, such as this very interesting one, are needed to find the best procedures to use in this relatively new field of step-by-step calculation of continuous problems.

Author's Closure

Professor Plunkett's comments and references are helpful, and his suggestions clarify a point in question. Before referring to his discussion regarding the values of k, some information might be added to that which was printed originally.

The relationship between the values of k in the plane and k out of the plane, in the equation

$$\omega_2 = \omega_0^2 + k\Omega^2$$

was very clearly shown in the data obtained from the example. Specifically, for the wedge-shaped blade taken as an example in the paper, when mounted on the small hub and rotating at 400 radians per sec, the value of k for vibration in the plane was 0.66 and for vibration out of the plane k became 1.66. Similarly, when mounted on the large hub and rotating at 200 radians per sec, k in the plane was 4.5 and k out of the plane became 5.5. That is,

$$k_{out} = 1 + k_{in}$$

When this relationship was first noted by the author (it was not anticipated), the first reaction was an attempt to determine whether it was a coincidence due to the shape of the blade. A solution was made for the natural frequencies of two rotating cantilever beams having shapes different than the wedge-shaped beam; both first and second natural frequencies were checked for one of the beams. Results showed that the relation was apparently general.

Professor Plunkett suggests a simple and welcome explanation for the k-relationship, based on a comparison of the equation for the shearing force in the beam for the case of vibration in the plane and the corresponding equation for vibration out of the plane. It might be pointed out that Equation [2], in the original paper, for the bending moment in the blade, contains ω^2 and Ω^2. However, this equation can also be rearranged into a form which

[1] By R. L. Sutherland, published in the December, 1949, issue of the Journal of Applied Mechanics, Trans. ASME, vol. 71, pp. 389–394.

[2] The Rice Institute, Houston, Texas. Jun. ASME.

[3] "Theory of Elasticity," by R. V. Southwell, Oxford Press, 1936, p. 483.

[4] "Calculation of Uncoupled Modes and Frequencies in Bending or Torsion of Nonuniform Beams," by J. C. Houbolt and R. A. Anderson, NACA Technical Note no. 1522, February, 1948.

[5] "Technique of the Step-by-Step Integration of Ordinary Differential Equations," by W. J. Duncan, College of Aeronautics, Cranfield, Report no. 4, February, 1947.

may be compared with the corresponding equation for vibration out of the plane. Again, it is shown that

$$\omega^2_{out} = (\omega^2 + \Omega^2)_{in}$$

The problems in selecting a suitable number of finite steps to consider in order to approximate accuracy sufficiently and in extrapolating results to an infinite number of steps are indeed interesting ones. The division of the blade used as an example in the paper was purely arbitrary and probably could be improved so as to approximate accuracy correspondingly, with less work, or more nearly to approximate accuracy with the same amount of work.

Book Reviews

Gas Turbines for Aircraft

GAS TURBINES FOR AIRCRAFT. By W. F. Godsey and L. A. Young. McGraw-Hill Book Company, New York, N. Y., 1949. Cloth, 6¼ × 9¼ in., 238 figs., 9 tables, charts, Appendix, xii and 355 pp., $4.50.

REVIEWED BY M. J. ZUCROW[1]

THE authors have produced one of the most valuable contributions to the literature on gas-turbine-type engines to appear in recent years. The authors get into their subject quickly and have succeeded in a book of only 355 pages in presenting an authoritative discussion of the problems, characteristics, and analysis of gas-turbine-type engines and their components. In general, the approach is that of the practicing engineer rather than that of the teacher.

The practicing engineer will find a large amount of material in this book that he can put to direct use; a significant fraction of the material has not previously appeared in the unclassified literature. The teacher of engineering, particularly of senior students, will not find the book as fully meeting his needs. It lacks the slow, more fundamental, and theoretical approach required in a text. But graduate students with some knowledge of the gas-turbine field should find the book a useful one. A criticism the reviewer feels justified in making is that the authors have not included a complete list of references to guide the interested reader who may desire more information on some of the topics and figures presented in the book.

The book is subdivided into eleven chapters and an appendix.

Chapter 1, Basic Aerodynamics of Aircraft. In 27 pages the authors discuss such topics as the properties of the atmosphere and the aerodynamic resistances of bodies to be propelled through the atmosphere, with and without compressibility. It would be difficult to do a better job in so few pages.

Chapter 2 on aircraft propulsion presents the fundamentals of aircraft propulsion, briefly reviews the important characteristics of the propeller, and discusses the propulsive and over-all efficiencies of thermal jet engines. The authors also introduce the concept of expansion efficiency. The chapter is brief, only 13 pages, but well presented. The average undergraduate will experience difficulty with this chapter because of the rapidity with which it moves.

Chapter 3, entitled Gas Flows, covers 51 pages. The authors have done a remarkable job of compressing a vast amount of material into a few pages. The practicing engineer will welcome this because of the many useful practical charts and equations he can apply to the solution of duct, nozzle, diffuser, shock, and flow with heat transfer problems. Few derivations of the equations are presented and the origin of some of the material is obscure. The college student will have difficulty with this chapter, but its utilitarian value cannot be questioned.

Chapter 4 deals with aircraft gas-turbine compressors. In 34 pages the authors present the theory and general characteristics of both the radial and the axial-flow compressors. At the expense of omitting derivations, the authors have done an excellent job of presenting the fundamental relationships for compressors, the factors influencing their selection, and the current problems.

Chapter 5 deals with fuels and burners and consists of 23 pages. In this chapter the authors present the method developed in Research Memorandum No. 6-44, Bureau of Ships, U. S. Navy Department, for calculating enthalpy and temperature changes for combustion of hydrocarbon fuels in moist air. Some descriptive material is presented on types of burners and spray nozzles, with discussion of the merits of the different devices. Combustion range and pressure losses due to combustion are also discussed. The treatment is primarily factual and a great deal of valuable information is compressed into a few pages.

Chapter 6 treats turbines and their characteristics and comprises 36 pages. To cover the subject matter adequately, the approach parallels that adopted in Chapter 4. The characteristics of impulse and reaction machines are presented. An excellent discussion of blade temperatures, and materials for turbine blades, disks, and exhaust systems is included. The effect of the variable-area exhaust nozzle is discussed briefly, and also supersonic exhaust nozzles.

Chapter 7, The Jet Nozzle (10 pages), is a discussion of the factors affecting the flow of the exhaust gases through final element of the engine. The influence of tailpipe length and nozzle shape on thrust are described. The supersonic exhaust nozzle is discussed, and general considerations governing the design and material selection for exhaust systems are presented.

Chapter 8 discusses gas-turbine cycles (61 pages) and Chapter 9 deals with variants of simple gas-turbine cycles (17 pages). The treatment is quite thorough but overly condensed even for one well-versed in the subject.

Chapter 10 deals with aircraft gas-turbine accessories and controls (15 pages). The chapter is entirely descriptive. Starters, lubrication systems, fuel systems, controls, windmilling characteristics, etc., are described. The references attached to some of the charts are incomplete and in a few cases lacking. It is a good chapter, nevertheless, and packs a lot of information in a short space.

Chapter 11, Present Development Status of Gas Turbines for Aircraft, is an interesting chapter. It contains a tabulation of data on current engines. Pictures of jet-propelled aircraft are presented and some of the problems associated with installing turbojet engines in aircraft are discussed. Curves are presented showing how the thrust per unit frontal area, specific fuel consumption, and engine specific weight have changed since 1942 and their expected values by 1952.

[1] Professor of Gas Turbines and Jet Propulsion, School of Mechanical Engineering, Purdue University, Lafayette, Ind. Mem. ASME.

The appendix consists mainly for the reproduction of thermodynamic charts and correction factor charts from the Bureau of Ships publication mentioned earlier.

In conclusion, it is the reviewer's opinion that this is an outstanding book and will be heartily welcomed by all practicing engineers interested in gas turbines. The book lacks, however, what Prof. J. H. Keenan terms the "pedestrial quality" of a college textbook.

Introduction to Statistical Mechanics

INTRODUCTION TO STATISTICAL MECHANICS. By Ronald W. Gurney. McGraw-Hill Book Company, Inc., New York, N. Y., 1949. Cloth 6¼ × 9¼ in., 59 figures, 17 tables, Appendix, vii and 268 pp., $5.

REVIEWED BY JOHN C. FISHER[2]

AN intuitive feeling for the principles and methods of statistical mechanics is of great value to anyone who wishes to make use of them in his own field, and it is toward the development of such an intuitive feeling that Professor Gurney directs his book. Starting from familiar concepts of chance and probability he leads gradually to the basic relationships of statistical mechanics, and to the interrelationship of statistical mechanics and classical thermodynamics, in a less mathematical and perhaps more physically significant manner than other writers generally have employed. Readers whose interest is largely experimental rather than theoretical should find the treatment particularly satisfying.

Metallurgists, in addition to physicists and chemists, will find the book of interest, for the treatment of solutions includes subjects such as solid solubility, order-disorder in crystals, and the influence of alloying upon the allotropic transformations in iron.

The book is what it purports to be, an introductory volume for students unfamiliar with the field. It is quite readable, with a gratifying fraction of the exposition in the written text, rather than in the mathematics which is kept at an adequate minimum. A few problems are included.

The book's defects are not serious. The readability would be greater if it were not necessary to refer so often to equations and figures in other chapters. An error in Fig. 3 at the very beginning of the book is disturbing. The brief discussion allotted to many interesting topics very probably is unavoidable in an introductory work of reasonable length.

Applied Mechanics

EINFÜHRUNG IN DIE TECHNISCHE MECHANIK. By Walter Kaufmann. Volume I, Statik starrer Körper. Springer, Berlin/Göttingen/Heidelberg, Germany, 1949 Paper, 6 × 9½ in., VI and 166 pp., 194 illustrations, 15 dm.

REVIEWED BY J. P. DEN HARTOG[3]

THIS book is one of the first postwar publications of the well-known publishing house of Julius Springer, and it appears in the same familiar prewar cover, except that the seat of the firm which was Berlin before 1944 is now stated as Berlin/Göttingen/Heidelberg. The quality of the printing, the figures, the paper, and the binding are as excellent as they were before the war, which is in striking contrast with the situation after World War I; all books printed between 1919 and 1925 were on paper of newsprint quality.

From 1932 on the author has been professor of mechanics at the Technische Hochschule in Munich and this book is the first volume of a series of four following his regular course in mechanics. The four volumes will deal with the subject matter of the four consecutive semesters in the freshman and sophomore years, as follows: Vol. 1, Statics; Vol. 2, Strength of Materials; Vol. 3, Dynamics; and Vol. 4, Fluid Mechanics.

The present volume on statics "avoids calculus as much as possible" because freshmen in Germany seem to be equally allergic to that as they are in the United States. However, numerous integral signs adorn the pages, and, in general, the course is more difficult and complete as is usual in this country. It covers the familiar subject matter, including funicular polygons, catenaries, trusses, and the method of virtual work. It does go deeper than that in a discussion of the general method of resolving an arbitrary force into its components along six arbitrary lines in space. As is usual in European textbooks no problems are included. The text is clearly written and well presented. The remaining three volumes of the series apparently have not yet been published.

Centrifugal and Axial Flow Pumps

CENTRIFUGAL AND AXIAL FLOW PUMPS. By A. J. Stepanoff. John Wiley & Sons, Inc., New York, N. Y., 1948. Cloth 6 × 9 in., x and 428 pp., 310 figs., $7.50.

REVIEWED BY A. I. PONOMAREFF[4]

THE rapid industrial expansion during the last two decades has brought about new practices and uses of centrifugal pumps. The introduction of these pumps into petroleum and chemical industries presented new mechanical and metallurgical problems involved in handling viscous and corrosive liquids often at highly elevated temperatures. Pumping water near or at the boiling point by the boiler feed or condensate pumps in a steam-power plant involves problems of cavitation and adequate vapor venting. The current trend toward higher pump-operating speeds accentuates the existing problems. The same trend resulted also in the development of a new pump of the propeller or axial-flow type. The existence of these new problems, brought about by the rapid progress in the design and application of centrifugal pumps, revealed the short-comings and inadequacy of the classical textbooks such as C. Pfleiderer's "Die Kreisel Pumpen," R. L. Daugherty's "Centrifugal Pumps," and others published some fifteen to twenty-five years ago.

The task of collecting and correlating the voluminous fragmentary information from the more recent publications on the various phases of pump design and application, thus projecting the classical pump theory into modern practice, was accomplished by Dr. Stepanoff. For many years a pump designer for the leading pump manufacturers and an author of many contributions to the technical literature on the pump design and the related subjects, Dr. Stepanoff is well qualified for such a task. Dr. Stepanoff's book is both a timely and welcome contribution to the technical literature.

The outstanding characteristic of the book is its unique hydraulic treatment of all pumps as one continuous series with the specific speed as an index number indicative of the type. This theoretical treatment is based on a single pattern of flow, identical reasoning, and similar procedure of impeller layout for centrifugal, mixed-flow, and axial-flow pumps. As a result of this, the author evolves a simple diagram, Fig. 9.16, page 185, which covers the essential design and performance features of pumps of all specific speeds. The co-ordinates of this diagram are well known

[2] Research Laboratory, General Electric Company, Schenectady, N. Y. Jun. ASME.

[3] Professor of Mechanical Engineering, Massachusetts Institute of Technology, Cambridge, Mass. Mem. ASME.

[4] Manager, Condenser Engineering Division, Westinghouse Electric Corporation, Philadelphia, Pa. Mem. ASME.

dimensionless head and capacity coefficients with the specific speeds and impeller discharge vane angles as parameters. It is to be expected that the construction of such a master diagram for a wide range of centrifugal, mixed-flow, and axial-flow pumps treated as one continuous series is based on certain limiting conditions. Among these, the most important is the author's acceptance of the forced vortex flow as the only pattern of head generation for all types of pumps. To correlate the actual pump performance with the forced vortex pattern of head generations, the author introduces a new concept of pressure energy exchange by "conduction" which takes place without actual mixing of streamlines in a manner similar to heat conduction.

The first chapters of the book are devoted to the classical theory of centrifugal pumps with its velocity diagrams and Euler's equation for theoretical head. As an introduction, the author discusses some selected topics from hydraulics, such as Bernoulli's equation, flow and losses in closed channels, and flow of water in a circular path, i.e., vortex motion. The author emphasizes the limitations of these fundamental laws of hydraulics when applied to flow in a revolving channel of a pump. Chapters devoted to pump design cover adequately such topics as impeller and casing design, hydraulic and mechanical losses, and the general characteristics of pump performance. In hydraulic treatment of all pumps, centrifugal, mixed-flow, and axial-flow, as one continuous and consistent series, the author assumes the forced vortex flow as the most efficient flow pattern and uses the mean effective impeller discharge diameter to represent the characteristics of all pumps in his master diagram. As the result of this treatment, the chapter on axial-flow pumps does not measure up to the high standard of the book as a whole. The recent developments of axial-flow compressors, for instance, indicate that some other flow patterns such as free vortex are at least equally efficient as the forced vortex pattern advocated by the author. Some of the author's illustrations, such as Fig. 8.3, page 146, showing the effect of number of impeller vanes on axial-flow pump efficiency is in conflict with the more recent findings. The last chapters of the book discuss special operating conditions, instability of head-capacity characteristics, and other problems encountered in the actual operation of pumps. Considerable attention is given to the design and operating features of hot-oil and boiler-feed pumps.

Dr. Stepanoff's book is a well-arranged and illustrated book. Each chapter of the book gives a very large number of references, most of which are selected from the recent publications.

Pump designers, consultants, and advanced students in the field of hydraulics will find this book an indispensable reference for the solution of their daily problems.

The Extrapolation, Interpolation, and Smoothing of Stationary Time Series

THE EXTRAPOLATION, INTERPOLATION, AND SMOOTHING OF STATIONARY TIME SERIES, WITH ENGINEERING APPLICATION. By Norbert Wiener. The Technology Press of The Massachusetts Institute of Technology and John Wiley and Sons, New York, N. Y., 1949. Cloth, 6¼ × 9¼ in., ix and 163 pp., Appendix. $4.

REVIEWED BY EUGENE W. PIKE[5]

THIS book is another illustration of the fact that in science, the by-products are often the most valuable results of a development. Nine years ago, Professor Wiener was asked to solve an important but specific wartime problem: "How can optimum properties for servomechanisms be formulated and specified?" This book is his answer to that problem, written in 1941, and only recently declassified. By stating his problem mathematically in terms of ensembles of stationary random processes,[6] Professor Wiener not only made possible a general solution of his original problem, but also won profound insights into the nature of communication, which have opened new horizons for research in fields as apparently unrelated as mental disease, chemical process control, economics, and the theory of information. These insights, presented more philosophically in his recent book "Cybernetics,"[7] appear in the "Time Series" only as casual asides, or as brief comments on the mathematics.

Having stated the problem, Professor Wiener proceeds to define "optimum properties" as those which minimize the mean-square error of response for the specified or expected conditions of operation. These conditions, in turn, are defined by the auto- and cross-correlation functions[8] of the various wanted and unwanted inputs, and by the required lead or lag in time between the output and the input signals. These combine to form an integral equation for the optimum frequency response, whose solution, by a tour de force of analysis, occupies four fifths of the book.

Although the book is addressed to "the working communication engineer and the working statistician," only those with a complete command of the concepts *and the conventions* of Fourier transforms, complex variables, probability and measure theory, and advanced calculus will find this book easy reading. Others will probably find themselves (like this reviewer) slowed to a two-pages-a-day pace, as much by the unexplained conventions and the undefined symbols as by any difficulty in grasping the fundamental concepts. It is to be hoped that a second edition will permit a pedagogical editing, commensurate with the importance and difficulty of the theory, which circumstances forbade in this first edition.

Although Professor Wiener's solution leads to explicit, general formulas covering every important case, actual engineering-design practice has usually made use of more or less ad hoc approximate solutions of the integral equations. Some of these methods are described in the appendixes, to this book, by Professor Levinson, and others in James, Nichols, and Phillips' "Servomechanisms,"[9] but much of the information in this field is either oral or classified.

The demonstration, by Professor Wiener, of the basically statistical nature of communication opens great opportunities to the statistician, the communication engineer, and the expositor alike. For the statistician, such operations as quality control reveal themselves as servomechanisms, while the communications designer can draw on the great body of work on inference from statistical series, which has already been accomplished by the mathematical economists and others, to solve some of those

[5] Raytheon Manufacturing Co., Waltham, Mass.

[6] A stationary random process is a sequence of variable events, each one dependent only statistically on its predecessors, whose average properties are the same everywhere along the sequence. The sequence of heads or tails resulting from repeated flipping of a coin is a stationary random sequence; so is the sequence of births, marriages, and deaths in a static population.

[7] "Cybernetics," by N. Wiener, John Wiley and Sons, Inc., New York, N. Y., 1949.

[8] If f_t is the t-th in a sequence of values then

$$\varphi(\lambda) = \lim_{N \to \infty} \frac{1}{2N+1} \sum_{t=-N}^{t=N} f_t \cdot f_{t-\lambda}$$

is the autocorrelation function of the sequence f_t; it is defined for all integer values of the lag λ. If f_t is a continuous function of t, then the sum becomes an integral.

[9] "Servomechanisms," by H. M. James, N. B. Nichols, and R. S. Phillips, Radiation Laboratory Series No. 25, McGraw-Hill Book Co., Inc., New York, N. Y., 1947.

problems which are not readily set up in terms of correlation functions.

The Mechanical Properties of Wood

THE MECHANICAL PROPERTIES OF WOOD. By Frederick F. Wangaard. John Wiley & Sons, Inc., New York, N. Y., 1950. Cloth, $5^1/_2 \times 8^1/_4$ in., xii and 388 pp., illus., $6.

REVIEWED BY ALBERT G. H. DIETZ[10]

THE author has completely rewritten and reworked the book of the same title originally written by Dean George A. Garratt of the Yale School of Forestry and first published in 1931. In the intervening years great progress has been made in the study of the mechanical properties of wood and a considerable volume of published material has appeared in many different technical publications. Professor Wangaard has sifted this material, added to it material of his own, and has organized the result into a logical, coherent discussion of the mechanical properties of wood and the methods employed to evaluate them.

The book is divided into four parts dealing, respectively, with the stress-strain relationships of wood, the factors affecting mechanical properties, working stresses for structural lumber, and methods of timber testing.

The first part, dealing with stress-strain relationships, first develops the necessary elements of applied mechanics as applied to wood and assumes that some readers may not be acquainted with these elementary principles. It also briefly notes the orthotropic nature of wood and presents extensive tables of the basic mechanical properties of the species found in the United States. Types of failures under various stress conditions are described and analyzed.

Part 2 deals with the various natural and man-made causes which affect the mechanical properties of wood. This includes a careful account of such influences as defects including knots, splits of various kinds, cross grain, fungi, cross breaks, compression wood, pitch accumulations, seasoning defects, injuries caused by animal organisms, frost, and wane; and other factors such as density, rate of growth, position in the tree, age, conditions of growth, microstructure, moisture content, preservative treatment, and duration of stress.

Part 3 develops the methods employed to determine working stresses for structural lumber. These are based upon the original work of such men as T. R. C. Wilson and today embodied in the grading procedures of the producers of structural lumber, starting with basic stresses for clear wood and proceeding to allowable stresses for actual timbers. It includes a short but welcome section on glued-laminated lumber.

Part 4 is largely an exposition of the methods of testing timber as originally developed largely at the U. S. Forest Products Laboratory and embodied in the standard methods of the American Society for Testing Materials. This section can well be used as a manual for classes in timber testing.

Because the book is not intended for students of advanced wood technology as related to mechanical properties, it does not attempt to develop the mathematical theory of orthotropic materials; neither does it cover such topics as the theory of bending behavior nor the behavior of plywood under stress. The exposition of the basic mechanical properties of wood is exceedingly well done.

[10] Professor of Structural Engineering, Department of Building Engineering and Construction, Massachusetts Institute of Technology, Cambridge, Mass. Mem. ASME.